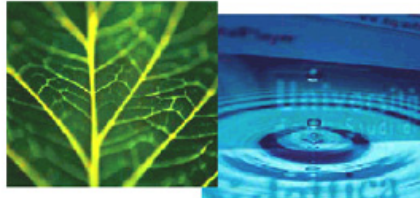


PhD Dissertation



International Doctorate School in Information and
Communication Technologies

DISI - University of Trento

COMPUTATIONAL INVERSE SCATTERING
VIA QUALITATIVE METHODS

Riccardo Aramini

Advisors:

Prof. Andrea Massa, Università degli Studi di Trento

Prof. Michele Piana, Università degli Studi di Genova

Co-Advisors:

Prof. Luca Formaggia, Politecnico di Milano

Prof. Housseem Haddar, École Polytechnique, Palaiseau Cedex

May 2011

Abstract

This Ph.D. thesis presents a threefold revisitation and reformulation of the linear sampling method (LSM) for the qualitative solution of inverse scattering problems (in the resonance region and in time-harmonic regime):

- 1. from the viewpoint of its implementation (in a 3D setting), the LSM is recast in appropriate Hilbert spaces, whereby the set of algebraic systems arising from an angular discretization of the far-field equation (written for each sampling point of the numerical grid covering the investigation domain and for each sampling polarization) is replaced by a single functional equation. As a consequence, this ‘no-sampling’ LSM requires a single regularization procedure, thus resulting in an extremely fast algorithm: complex 3D objects are visualized in around one minute without loss of quality if compared to the traditional implementation;*
- 2. from the viewpoint of its application (in a 2D setting), the LSM is coupled with the reciprocity gap functional in such a way that the influence of scatterers outside the array of receiving antennas is excluded and an inhomogeneous background inside them can be allowed for: then, the resulting ‘no-sampling’ algorithm proves able to detect tumoural masses inside numerical (but rather realistic) phantoms of the female breast by inverting the data of an appropriate microwave scattering experiment;*
- 3. from the viewpoint of its theoretical foundation, the LSM is physically interpreted as a consequence of the principle of energy conservation (in a lossless background). More precisely, it is shown that the far-field equation at the basis of the LSM (which does not follow from physical laws) can be regarded as a constraint on the power flux of the scattered wave in the far-field region: if the flow lines of the Poynting vector carrying this flux verify some regularity properties (as suggested by numerical simulations), the information contained in the far-field constraint is back-propagated to each point of the background up to the near-field region, and the (approximate) fulfilment of such constraint forces the L^2 -norm of any (approximate) solution of the far-field equation to behave as a good indicator function for the unknown scatterer, i.e., to be ‘small’ inside the scatterer itself and ‘large’ outside.*

Keywords

Qualitative methods for inverse scattering, linear sampling method, microwave imaging, breast cancer detection.

Contents

Preface	ix
1 Introduction	1
1.1 The context	1
1.2 The problems	4
1.3 The solutions	6
1.4 Innovative aspects	8
1.5 Structure of the thesis	9
2 A fully no-sampling 3D formulation of the LSM	11
2.1 State of the art	11
2.2 The problem	12
2.2.1 Plan of the following sections	14
2.3 The far-field equation	14
2.4 The discretization of the far-field equation and the LSM	17
2.5 A no-sampling implementation of the LSM	22
2.6 Numerical applications	28
2.7 First-order discretization	33
2.8 Conclusions and hints for future developments	37
2.9 Addendum to Chapter 2	39
3 The RGF_M for breast cancer detection	43
3.1 State of the art in breast cancer detection	43
3.2 The problem	45
3.2.1 Plan of the following sections	49
3.3 Notations	49
3.4 The inverse scattering problem: an analysis of the RGF equation	52
3.5 The visualization algorithm	68

3.6	Applications to data	71
3.7	Conclusions and hints for future developments	73
3.8	Addenda to Chapter 3	75
3.8.1	Complementary theorems	75
3.8.2	The interior transmission problem	76
4	The LSM explained by energy conservation	83
4.1	The problem	84
4.2	State of the art	87
4.2.1	FM-based approaches	88
4.2.2	Physics-based approaches	89
4.3	Outline of our approach	93
4.3.1	Plan of the following sections	94
4.4	The power flux of the scattered field and the far-field equation	95
4.5	Behaviour of the flow lines	104
4.6	A new version of the general theorem: $z \in D$	106
4.7	A new version of the general theorem: $z \notin D$	110
4.8	Tikhonov regularization and numerical validation	116
4.9	Conclusions and hints for future developments	119
4.10	Addenda to Chapter 4	119
4.10.1	A technical result about the discrepancy	119
4.10.2	Continuity properties of scattered fields	121
4.10.3	A technical detail concerning relations (4.71)	125
5	Figures and tables	129
5.1	[2.6] Numerical applications	130
5.2	[2.7] First-order discretization	134
5.3	[3.3] Notations	136
5.4	[3.6] Applications to data	136
5.5	[4.5] Behaviour of the flow lines	139
5.6	[4.6] A new version of the general theorem: $z \in D$	146
5.7	[4.7] A new version of the general theorem: $z \notin D$	147
	Bibliography	151

List of Tables

5.1 Values of the regularization parameter α provided by the generalized discrepancy principle in the traditional and the no-sampling LSM for the three previous experiments. First row: interval $[\alpha_{\min}^*, \alpha_{\max}^*]$ defined by the minimum and maximum values of α for all sampling points in the traditional implementation. Second row: the unique value α^* of α in the no-sampling implementation. 133

List of Figures

- 5.1 Visualization performance of the 3D no-sampling LSM: (a) the scatterer; (b) application of active contours to the restriction of the indicator function to the plane of Cartesian equation $x_2 = 0$ (white line: initialization; black line: final profile); (c) visualization provided by the no-sampling LSM in around 90 s of CPU time (the threshold value for the surface equation is computed by using (2.84)); (d) visualization provided by the traditional LSM in around 1600 s of CPU time (the threshold value for the surface equation is obtained by means of a heuristic trial-and-error procedure). . . 130
- 5.2 Comparison between the traditional and the no-sampling LSM for the scatterer shown in Figure 5.1(a): (a) visualization provided by the traditional LSM; (b) visualization provided by the no-sampling LSM. In both cases the threshold value for the surface equation is obtained by means of a heuristic trial-and-error procedure. The difference between the two visualizations is negligible. 131
- 5.3 Visualization performance of the 3D no-sampling LSM: (a) the scatterer; (b) application of active contours to the restriction of the indicator function to the plane of Cartesian equation $x_2 = 0.9$ (white line: initialization; black line: final profile); (c) visualization provided by the no-sampling LSM in around 90 s of CPU time (the threshold value for the surface equation is computed by using (2.84)); (d) visualization provided by the traditional LSM in around 1600 s of CPU time (the threshold value for the surface equation is obtained by means of a heuristic trial-and-error procedure). . . 132

5.4	Visualization of two objects with different permittivity by means of the no-sampling LSM: (a) the two scattering objects; (b) visualization obtained by using a unique threshold value $C = C_1$ computed as in (2.84) by cutting the non-connected scatterer with the plane $x_1 = -0.75$; (c) visualization obtained by using a unique threshold value $C = C_2$ computed as in (2.84) by cutting the non-connected scatterer with the plane $x_1 = 0.75$; (d) visualization obtained by using the two different threshold values C_1 and C_2 for the two objects. In each case, the visualization time is around 90 s of CPU time.	133
5.5	Visualization performance of the 3D no-sampling LSM: (a) the scatterer; (b) non-uniform triangular mesh formed on the unit sphere by the 144 views chosen to implement a first-order discretization of the far-field equation; (c) no-sampling LSM visualization of the scatterer.	134
5.6	Visualization performance of the 3D no-sampling LSM: (a) exact geometry of the scatterer (perfectly conducting teapot); (b) uniform triangular mesh formed on the unit sphere by the 252 views chosen to implement a first-order discretization of the far-field equation; (c) no-sampling LSM visualization of the teapot.	135
5.7	Scheme of the 2D microwave tomography experiment for breast cancer detection.	136
5.8	(a) Phantom of the breast: a circular tumour, centred at $(-2.00, -1.00) \cdot 10^{-2}$ m and with a diameter of $1.00 \cdot 10^{-2}$ m, is placed in the fat tissue. (b) Visualization provided by the RGM.	136
5.9	(a) Phantom of the breast: a circular tumour, centred at $(-2.00, -1.00) \cdot 10^{-2}$ m and with a diameter of $1.00 \cdot 10^{-2}$ m, is placed in the fat tissue; a square scatterer, centred at $(-8.20, 8.20) \cdot 10^{-2}$ m and with a side of $2.75 \cdot 10^{-2}$ m is put outside the breast. (b) Visualization provided by the RGM.	137
5.10	(a) Phantom of the breast: two circular tumours, with the same diameter of $1.50 \cdot 10^{-2}$ m, are placed in the fat tissue: one is centred at $(-2.00, -1.00) \cdot 10^{-2}$ m, the other in $(1.00, 0.00) \cdot 10^{-2}$ m. (b) Visualization provided by the RGM.	137

5.11	(a) Phantom of the breast: the healthy fat is perturbed with components randomly drawn from a uniform distribution within 10% around the unperturbed values; moreover, six veins and one gland are added inside the fat tissue. A circular tumour, centred at $(-2.00, -1.00) \cdot 10^{-2}$ m and with a diameter of $1.50 \cdot 10^{-2}$ m is also placed in the breast. (b) Visualization provided by the RGMF.	138
5.12	(a) Phantom of the breast: the healthy fat is perturbed with components randomly drawn from a uniform distribution within 10% around the unperturbed values; moreover, six veins and one gland are added inside the fat tissue. A circular tumour, centred at $(-2.00, -1.00) \cdot 10^{-2}$ m and with a diameter of $1.00 \cdot 10^{-2}$ m is also placed in the breast. (b) Visualization provided by the RGMF.	138
5.13	Implementation of the LSM: (a) visualization of an elliptic scatterer with, superimposed, its true profile (solid black line); (b) values of the discretized discrepancy $d(z)$	139
5.14	Behaviour of the unit vector field $\hat{\mathcal{S}}_z^{s,\epsilon}$ for a sampling point z (represented by a red bullet) placed at the centre of the ellipse.	140
5.15	Behaviour of the unit vector field $\hat{\mathcal{S}}_z^{s,\epsilon}$ for a sampling point z (represented by a red bullet) placed at the top of the ellipse.	141
5.16	Implementation of the LSM: (a) visualization of a double-elliptic scatterer with, superimposed, its true profile (solid black lines); (b) values of the discretized discrepancy $d(z)$	142
5.17	Behaviour of the unit vector field $\hat{\mathcal{S}}_z^{s,\epsilon}$ for a sampling point z (represented by a red bullet) placed at the centre of the upper ellipse.	143
5.18	Behaviour of the unit vector field $\hat{\mathcal{S}}_z^{s,\epsilon}$ for a sampling point z (represented by a red bullet) placed at the top of the upper ellipse.	144
5.19	Behaviour of the unit vector field $\hat{\mathcal{S}}_z^{s,\epsilon}$ for a sampling point z (represented by a red bullet) placed at the bottom of the upper ellipse.	145
5.20	Geometric construction considered in the proof of Theorem 4.6.1, for a point $z_n \in D$ approaching $z^* \in \partial D$	146
5.21	Behaviour of the unit vector field $\hat{\mathcal{S}}_z^{s,\epsilon}$ for a sampling point z (represented by a red bullet) placed outside the scatterer. Two ramification points (square boxes) are detectable.	147
5.22	Behaviour of the unit vector field $\hat{\mathcal{S}}_z^{s,\epsilon}$ for a sampling point z (represented by a red bullet) placed outside the scatterer. Two ramification points (square boxes) are detectable.	148

5.23 Behaviour of the unit vector field $\hat{\mathcal{S}}_z^{s,\epsilon}$ for a sampling point z (represented by a red bullet) placed outside the scatterer. 149

Preface

This Ph.D. thesis presents a detailed report of my research activity during the last three years, as a student of the International Doctoral School in Information and Communication Technology (ICT) at the Department of Information Engineering and Computer Science, University of Trento. Referring to Chapter 1 for a short and introductory overview of the topics treated in the thesis, here I would like to briefly explain some structural and typographical criteria I tried to meet in writing it.

Each chapter (except the first and the last one) is essentially a revised and enlarged version of one of the papers written by me, together with my advisors and/or colleagues, and published in the period 2007-2010. Accordingly, the chapters are very different from each other in many respects, and this might create more heterogeneity than is desirable in a Ph.D. thesis if considered as whole. However, this heterogeneity never becomes confusion or chaos, since there is a common theme underlying all chapters, i.e., the linear sampling method (LSM), which is an algorithm for the qualitative solution of inverse scattering problems. In fact, Chapter 2 presents an alternative implementation, named ‘no-sampling’, of the LSM. In Chapter 3 another qualitative method is formulated by matching the LSM itself with the so-called ‘reciprocity gap functional’. Chapter 4 investigates the open issue concerning the theoretical foundation of the LSM and tries to explain why or how this method works. As a result, each one of these chapters is essentially self-contained¹, as the paper whence it has been drawn; on the other hand, all of them focus on the LSM, although from very different perspectives. Summarizing, and if it did not sound too pretentious, I could borrow a musical metaphor to say that this thesis can be regarded as a set of variations on a theme: the latter is represented by the LSM, while the variations correspond to Chapters 2-4.

As far as the logical and typographical structure of the thesis is concerned, I obviously

¹This is also the reason why I maintained some differences in notations between Chapter 2, where a vector notation is used (in a three-dimensional setting), and Chapters 3-4, where, in agreement with most of the literature on the LSM, an ‘analytic’ or ‘scalar-wise’ notation is adopted (in a two-dimensional setting): no confusion can arise from these two notational conventions.

adopted the proper template provided by the ICT doctoral school: however, I introduced some changes whenever I deemed it necessary or useful. For example, I created a specific chapter (i.e., the last one, no. 5) to collect all the figures and tables of the thesis. For the sake of clarity, also this chapter is subdivided into sections: each of them contains the figures and tables referred to in a specific section of Chapters 2-4 and has just the same title (and, between square brackets, the same number) of such section. This choice avoids fragmentation in the main text, allows a better displacement of figures and enables the interested user to print them (possibly on a colour printer) as a separate folder to look at while reading, in parallel, the main text itself.

Acronyms and symbols

Throughout the thesis, a few acronyms are used. For the reader's convenience and for possible reference, they are listed in the following:

- CPU: central processing unit;
- f.f.a.: for almost all;
- FM: factorization method;
- LSM: linear sampling method;
- MRI: magnetic resonance imaging;
- PC: personal computer;
- RGF: reciprocity gap functional;
- RGFM: reciprocity gap functional method;
- TM: transverse magnetic;
- 2D: two-dimensional, two dimensions;
- 3D: three-dimensional, three dimensions.

Moreover, the black square, i.e., the symbol \blacksquare , denotes the end of the proof of a theorem, while the empty square, i.e., the symbol \square , denotes the end of a remark.

Acknowledgements

I wish to thank

- my advisors, Prof. Andrea Massa and Prof. Michele Piana, for their help and for having allowed me to follow my research interests;
- Dr Massimo Brignone, for his invaluable help in many different situations: PC maintenance and repair, implementation of several numerical simulations, scientific discussions, etc.;

- a few (former or not) Ph.D. students, colleagues and co-workers, such as Manuel Benedetti, Giovanni Bozza, Fabrice Delbary, Giovanni Giorgi and Luca Manica for their important contribution to our common research activities;
- Prof. Giacomo Caviglia and Prof. Enrico Pagani, for their kindness and for having helped me to investigate and clarify some interesting scientific problems;
- Prof. Housseem Haddar for having provided the direct scattering data for the perfectly conducting teapot considered at the end of Section 2.7.

Finally, and more generally, I wish to express my gratitude to my parents and to all my friends not cited above: although not directly involved in my research activity, they have often helped me with their (not only psychological) support.

Trento, May 5th, 2011

Chapter 1

Introduction

1.1 The context

Generally speaking, scattering is a physical phenomenon whereby a particle or a wave travelling in a given background (e.g., free space) impinges upon an obstacle or an inhomogeneity. The present Ph.D. thesis deals with electromagnetic scattering: in this case, an incident electromagnetic wave is scattered by a portion of a physical medium, which can be either penetrable or impenetrable; however, most of the following considerations equally hold for acoustic scattering. As a consequence of the principle of superposition, the value of the total electromagnetic field at any point in physical space is equal to the sum of the values of the incident and the scattered fields at the same point. Now, if the incident field, as well as the geometric and physical properties of the background medium and of the scatterer, are known, we can formulate the *direct electromagnetic scattering problem* as that of determining the scattered field. Conversely, when the incident field and the background are known, and the scattered field is measured at a certain number of points suitably located in the space outside the target, the problem of retrieving as much information as possible about the target itself is referred to as the *inverse electromagnetic scattering problem*.

Owing to their ill-posedness (in the sense of Hadamard) and their non-linearity¹, inverse scattering problems are hard to solve. The most significant drawback caused by ill-posedness is the non-continuous dependence of the solution on the data: this means, in particular, that a small variation of the data themselves (for example, their typical perturbation due to the noise affecting the procedure of measurement) undergoes an uncontrolled propagation during the computational process performed to determine the

¹See e.g. [4, 13, 15, 20, 35, 48, 59, 89].

solution, so that the latter proves meaningless, being overwhelmingly blurred by wild oscillations. This ‘pathology’ can be cured by a suitable ‘therapy’, i.e., by the *theory of regularization*, whose powerful tools, however, are better known and more effective when applied to linear inverse problems. Unfortunately, several scattering problems of interest (e.g., microwave tomography for breast cancer detection) are genuinely non-linear. The mathematical efforts made during the last fifty years to face this additional difficulty have given rise to three families of procedures (i.e., a), b), c) soon below): the first two can be regarded as ‘traditional’, since they have been known for a long time, and are based on a quantitative approach, in that their algorithms aim to compute the point values of the electrical parameters of the scatterer; the third family is much more recent and is based on a qualitative approach, in that its algorithms only aim to visualize the location and shape of the unknown target.

a) *Non-linear optimization algorithms* [13, 48, 59]: they consist of an iterative procedure whereby, starting from an initial guess concerning the geometric and physical properties of the scatterer, the solution searched for is progressively approached by increasing the number of iterations. Although such techniques can produce very precise reconstructions, they suffer from two major drawbacks: first, their computational burden is often very heavy, so that their implementation requires a long time; second, the initial guess must be quite accurate, i.e., close enough to the solution to be determined, but in many applications (like medical imaging) this *a priori* information is in general unavailable. However, some recent advances have given rise to much faster and robust algorithms [57].

b) *Methods based on a weak scattering approximation* [48, 56]: they consist in replacing the original problem with an approximate linear version of it. Obviously, any approximation is physically realistic only if some conditions are satisfied: for example, *Born approximation* is viable when the incident wavelength is larger than the maximum linear dimension of the target and the latter is a penetrable scatterer whose physical properties do not differ very much from those of the background. Another common approximation is *physical optics*: it can be adopted when the incident wavelength is much smaller than the minimum linear dimension of the target, which has to be impenetrable. Of course, a necessary condition for any approximation to be made is the *a priori* knowledge (not always available) of the kind of scattering: this means knowing *a priori* whether the target is penetrable or not and, if not, what conditions the total field verifies at its boundary. However, such *a priori* knowledge is, in general, not sufficient: e.g., when trying to detect a tumour in the breast, the penetrable nature of the scatterer can be assumed, but in microwave tomography (as well as in many other applications) no linearizing approxima-

tion can be realistically performed. This impossibility is strictly related to the significant diffraction effects involved by the physical interaction between microwaves and biological tissues: in breast fat, the wavelength of microwaves (at a frequency of around 5 GHz) is characterized by an order of magnitude equal to that of the linear dimensions of the tumour to be detected (i.e., 1 cm), and it can be shown that in this physical situation, referred to as *resonance* [48], multiple scattering inside the target cannot be neglected; as a consequence, no term in the equation describing the scattering phenomenon can be dropped or simplified by means of approximations.

*c) Qualitative methods*² [35, 44, 69]: they have been conceived to overcome, to some extent, the drawbacks affecting the previous two families of techniques. From a chronological viewpoint, the first qualitative method (1997) is the *linear sampling method* (LSM) [47, 52], but since then other approaches adopting the same perspective have been proposed. In general, the mathematical formulation and justification of each qualitative method vary with the different physical conditions in which scattering phenomena may occur, but its numerical implementation is largely independent of the material properties of the target (that can be either penetrable or impenetrable, or even formed by different connected components characterized by different values of permittivity and/or conductivity). This is a common feature of qualitative methods, since their core idea is to give up determining the point values of the physical parameters of the scatterer, and to aim at providing a visualization of its shape and location only, i.e., of its support. Such visualization is obtained by computing and plotting a suitable *indicator function*, whose values are small inside the scatterer itself and large outside (or, equivalently and more frequently, vice versa: some plots of this kind can be seen, e.g., in [4, 6]). Following this approach, the original inverse scattering problem is actually given a new and weaker formulation, since its solution is now characterized by a much lower information content. The main advantage of this ‘reduced’ version of the problem is its genuine linearity: more precisely, the computation of the indicator function is performed by numerically solving an integral equation that, although ill-posed, is linear (and then allows using the standard techniques of regularization theory for linear problems) and does not derive from approximations of any kind; the data acquired during the scattering experiment form the discretized integral kernel of this equation. Of course, the indicator function (defined, in principle, everywhere in physical space) can be plotted only if it is restricted to a finite domain: as a consequence, the only (very weak) *a priori* knowledge needed is that the scatterer is located inside a given bounded region. Moreover, by virtue of its linearity, the

²In this Ph.D. thesis, the expression ‘qualitative methods’ is a shorthand for ‘non-iterative qualitative methods’. *Level sets* [84] can be considered as an example of iterative qualitative method.

numerical procedure adopted to determine the indicator function requires short computational times: for example, the no-sampling implementation of the LSM [6, 7, 27] allows visualizing 2D and 3D scatterers respectively in around 1 s and 90 s only.

Of course, qualitative methods are not necessarily alternative to the reconstruction algorithms widely used for computing the point values of the refractive index of the unknown scatterer. On the contrary, the fast visualization provided by a qualitative method can be used (in case, after a post-processing procedure, as in [6]) to obtain an accurate initialization for an optimization algorithm: examples of this ‘hybrid’ approach can be found in [22, 23, 25, 28, 29].

The mathematical and computational efforts outlined at the previous points a)-c) are motivated not only by the deep and difficult theoretical issues involved by inverse scattering problems, but also by their great importance from the viewpoint of real-world applications, such as:

- *medical imaging*: e.g., using microwaves to detect bone marrow cancer (leukaemia) or breast cancer;
- *subsurface imaging*: e.g., mine removal, oil detection, archaeological investigations, etc.;
- *radar imaging*: e.g., detecting the number, the shapes and the dimensions of some moving objects, like airplanes, ships, etc.;
- *non-destructive testing*: e.g., detecting cracks inside objects, identifying dangerous materials (like explosives) in luggage, etc.

Hence, any new and effective approach to inverse scattering, as well as any improvement in the existing techniques or in their matching, can actually be of interest to a wide and heterogeneous scientific community.

1.2 The problems

In the framework of qualitative methods, the present Ph.D. thesis faces three main problems:

1. increasing the computational effectiveness of the LSM for 3D problems;
2. optimizing the application of the reciprocity gap functional method (RGFM) [36, 44] to the case of microwave tomography for breast cancer detection;

3. investigating the theoretical foundation of the LSM.

More precisely, we can describe the previous three problems as follows:

1. in [7] a no-sampling formulation³ of the LSM is proposed, whereby the visualization of the scatterer is obtained in a much shorter time than in the traditional implementation, without impairing its quality. In [6] this no-sampling visualization is post-processed by means of an edge-detection algorithm in order to automatically select the profile of the scatterer. However, both papers [6, 7] deal with 2D scatterers: then, a generalization to the 3D case is desirable, all the more that the issue of computational times is much more important in a 3D framework than in a 2D one;
2. the problem of detecting tumoural masses inside the female breast by using microwaves can be formulated as an inverse scattering one, with inhomogeneous background: this means that the scatterer searched for, i.e., the tumour, is located inside a medium with non-constant electrical parameters. This medium is not only the healthy breast, but, in principle, any other physical object that can influence the

³For the reader's convenience, we briefly recall the essential features of the no-sampling approach in a 2D setting. The traditional version of the LSM consists of selecting a computational grid \mathcal{Z} of L points $z_l \in \mathbb{R}^2$ covering the region where the scatterer is located, and of solving, for each z_l , a linear algebraic system obtained as an angle-discretized version of a linear and ill-posed integral equation of the first kind, called the *far-field equation*. The integral kernel of the latter is formed by the far-field patterns scattered in all directions by the target when illuminated by a plane wave for each incidence direction, while its right-hand side is the (analytically known) far-field pattern of the background Green's function, i.e., of the field radiated by the elementary source placed at the sampling point z_l in the absence of the scatterer. Then, the Tikhonov regularized solution of the discretized far-field equation (with a z_l -dependent regularization parameter, chosen by means of the generalized discrepancy principle) has a (discretized) L^2 -norm that is small if z_l is inside the scatterer, grows up when z_l approaches its boundary and remains even larger when z_l is outside. Of course, this L^2 -norm can be directly used as an indicator function, but often, for visualization purposes, other choices are preferred (e.g., the opposite of its logarithm). Now, the key-idea of no-sampling consists in treating the L ill-conditioned and algebraic systems solved by the method as a whole, i.e., as a unique and larger system in vector spaces of higher dimensions; then, it is possible to realize that such an approach naturally allows an infinite thickening of the sampling grid \mathcal{Z} , which thus becomes, for instance, a rectangle T in \mathbb{R}^2 . Of course, this requires that the infinitely many algebraic systems that would arise from a 'naive' implementation of the procedure are actually incorporated into a single functional equation, set in suitable $L^2(T)$ -based spaces. As a result, the indicator function can now be analytically determined in all T by a single regularization procedure: in particular, the regularization parameter is computed only once, by means of the usual generalized discrepancy principle, but now recast in the $L^2(T)$ -based spaces. This allows a notable decrease in the computational times: the visualization of 2D scatterers is performed by the no-sampling LSM in around 1 s only, and without loss of quality if compared to the traditional implementation.

results of the scattering experiment (e.g., the pieces of furniture or the walls of the room where the experimental set-up is placed). The LSM, originally formulated for a homogeneous background [47, 52], can be adapted to allow for an inhomogeneous one [36, 49, 50], provided that the Green's function of the latter is known. Since, in general, this knowledge is hardly available, another qualitative method has been conceived in order to (partly) overcome this drawback, i.e., the RGFM [36, 44], which allows neglecting all the physical bodies outside the spatial region T enclosed by the receiving antennas. For the sake of simplicity, in the two papers [36, 44] the background inside T is assumed to be homogeneous; however, the healthy female breast is far from being so. Hence, a first task here is to explicitly formulate the RGFM by taking into account the proper Green's function (so far, in a 2D setting). Moreover, independently of mammography applications, it is interesting to formulate a no-sampling approach to the RGFM, and to check whether it is so effective as in the case of the LSM;

3. qualitative methods are based on equations that are artificially formulated, i.e., do not derive from physical laws. This lack of a physical foundation seems to be responsible for at least one of the open problems [34, 35] concerning, in particular, the LSM⁴. Indeed, the far-field equation at the basis of the method is known to admit approximate solutions whose L^2 -norms behave as good indicator functions for the support of the scatterer (i.e., functions bounded inside and arbitrarily large outside the unknown object), but there is *a priori* no reason why computing the L^2 -norm of a (Tikhonov) regularized solution of the far-field equation, as required by the implementation of the LSM, should provide one of these indicator functions. However, many numerical applications, in very different scattering conditions, show that this is actually what happens⁵: the problem is then to explain why.

1.3 The solutions

The approaches pursued in this Ph.D. thesis to tackle the previous problems can be shortly described as follows:

⁴The same problem also affects the RGFM, but we shall not address this issue in the present Ph.D. thesis.

⁵This does not mean that for any fixed frequency and for any possible scatterer, the visualization provided by the LSM is good, but for the moment this is a minor point: we shall briefly discuss such issue in Subsection 4.2.2, p. 89.

1. a fully no-sampling formulation of the LSM in the 3D case can be achieved by taking into account that the far-field equation at the basis of the method is parameterized not only over a set of sampling points, but also over a set of sampling polarizations for the Green's function of the background. Accordingly, the functional framework conceived in [7] for the 2D case can be generalized to the 3D one, provided that a) the sampling point is regarded as a variable in the investigation domain, as in [7], and b) the sampling polarization is regarded as a variable in the unit sphere of directions in \mathbb{R}^3 . As regards the edge-detection problem, we do not pursue a genuinely 3D approach, although this is certainly the first choice. The point is that a three-step algorithm, whereby the edge-detection process is performed in a 2D setting, is much faster. As a first step, the indicator function provided by the no-sampling implementation of the LSM is restricted to a plane in \mathbb{R}^3 containing a slice of the scatterer⁶. Second, a 2D active-contour technique is applied to such restriction: the result of this procedure is a plane curve. The third step consists of computing the average value of the indicator function over this curve, and of choosing such value as the threshold level C for the indicator function itself. As a result, the C -level surface of the latter function can be plotted in \mathbb{R}^3 to visualize the scatterer. The output of our investigation in this field has been published in the papers [26, 27], which are the source for chapter 2 of the present Ph.D. thesis;
2. as regards the RGM, its theoretical framework is rebuilt in order to take into account, from the very beginning, the possible inhomogeneity of the background enclosed by the receiving antennas. This inhomogeneity is encoded into an appropriate Green's function, which must be known *a priori*: however, numerical simulations show that the resulting algorithm is rather robust with respect to unknown perturbations of the background. Moreover, this algorithm is formulated according to the no-sampling approach conceived in [7]. The results of our investigation in this field have been published in the paper [55], which is the source for chapter 3;
3. as regards the theoretical foundation of the LSM, we propose a physical interpretation of the far-field equation in terms of electromagnetic energy conservation in a lossless and homogeneous background. Specifically, we consider the conservation of power flux along the flow strips of the Poynting vector associated with the scattered field whose far-field pattern is one of the two terms in the far-field equation. The

⁶Of course, this requires some (rather weak) *a priori* information on the location of the scatterer; should this information be unavailable, the only possibility would consist in adopting a genuinely 3D approach.

behaviour of these flow lines is numerically investigated and theoretically described (but not predicted). Appropriate assumptions on the flow lines, based on the numerical results, allow characterizing a set of approximate solutions of the far-field equation that can be used to visualize the boundary of the scatterer in the framework of the LSM. In particular, under the same assumptions, we can show that Tikhonov regularized solutions belong to this set of approximate solutions for appropriate choices of the regularization parameter. The results of our investigation in this field have been published in the paper [9], which is the source for chapter 4.

1.4 Innovative aspects

The elements of innovation introduced by our approaches and methods can be shortly described, point by point, as follows:

1. in the traditional implementation of the LSM, a computational grid of sampling points covering the investigation domain needs to be chosen (cf. footnote no. 3 at p. 5): then, the problem arises of how to choose this grid, i.e., its thickness, the geometry of its elementary cell (if any), etc. Moreover, in a 3D setting, for each choice of the artificial polarization of the background Green's function, an *a priori* different visualization of the scatterer is obtained: accordingly, another issue must be addressed, i.e., how to choose the polarizations and how to combine the corresponding visualizations. Both problems are simply removed by our fully no-sampling approach: no grid and no polarization need to be chosen, since the Tikhonov regularized solution of the new functional far-field equation is analytically known as a function of both the sampling point $z \in \mathbb{R}^3$ and the sampling polarization in the unit sphere of directions in \mathbb{R}^3 . In particular, the indicator function can be analytically determined on the investigation domain as a continuous superposition of the infinitely many indicator functions corresponding to all possible polarizations, thus motivating the traditional heuristic procedure of choosing three independent polarizations and somehow averaging the three corresponding indicator functions. Moreover, on a commercial laptop with a 1.6 GHz CPU, the determination of the unique regularization parameter only takes around 2s, while no more than 85s are spent for the edge-detection algorithm and the visualization procedure together: as a result, our no-sampling approach can provide an almost automatic visualization of the scatterer in around 90s, thus turning out to be, as far as we know, the fastest inversion algorithm for inverse scattering problems in the resonance region;

2. for the first time, the RGFM is formulated taking into explicit account an inhomogeneous background and is implemented according to the no-sampling approach. As a consequence, the method can be applied to the visualization of tumoural masses inside the female breast by means of a very fast post-processing of microwave scattering data (the computational time for a single visualization is around 1 s only). Some interesting features emerge from the preliminary simulations presented here: first, as theoretically foreseen, the visualization is insensitive to the presence of scatterers outside the array of receiving antennas; second, although the implementation of the method requires the knowledge of the background Green's function, the results are rather robust with respect to unknown (but reasonably small) perturbations of the background itself; third, the visualization can be considered satisfactory even in absence of the coupling medium that is typically interposed between skin and antennas [16, 17, 72, 78] in order to favour the penetration of the incident wave into the breast;
3. the possibility of regarding the LSM as an indirect consequence of electromagnetic energy conservation was never considered before. The resulting framework allows establishing a link between the performance of the LSM and the behaviour of the flow lines of the Poynting vector associated with the scattered field. This link is formalized in terms of sufficient conditions: if the flow lines fulfil them, a good performance of the LSM is ensured. However, insofar as the behaviour of the flow lines is only numerically observed *a posteriori* and not theoretically predicted (by relying on the knowledge of the physical and geometric properties of the scatterer), our approach is incomplete: indeed, in this perspective, a mathematical justification of the LSM could only be achieved by proving *a priori* that the flow lines of interest behave in the proper way.

1.5 Structure of the thesis

The three points characterizing the previous sections also determine the structure of the thesis. Then, Chapter 2 is devoted to a detailed description of the fully no-sampling and 3D formulation of the LSM, post-processed by an edge-detection algorithm (based on active contours) to automatically determine the profile of the unknown scatterer. In Chapter 3 we formulate the RGFM in the case of an inhomogeneous background, we describe its no-sampling implementation and we investigate its application to breast cancer detection. Chapter 4 is concerned with a physical interpretation of the LSM in terms of

electromagnetic energy conservation in a lossless background. Finally, as claimed in the Preface, all the figures and tables of the thesis have been collected in Chapter 5.

Chapter 2

A fully no-sampling 3D formulation of the LSM

2.1 State of the art

The traditional implementation of the linear sampling method (LSM) has been recalled (for the 2D case) in footnote no. 3, p. 5 of Chapter 1 and will not be repeated here: for a detailed description of the LSM, we refer e.g. to [4, 7, 35, 52]. We only point out that this implementation requires choosing a grid \mathcal{Z} of sampling points $z_l \in \mathbb{R}^2$ covering the investigation domain $T \subset \mathbb{R}^2$ and then, for each z_l , solving (typically, by Tikhonov regularization) a linear system obtained as a discretized and noisy version of the far-field equation: thus, in particular, the problem arises of how to choose the grid \mathcal{Z} (i.e., number, distance and geometry of the sampling points). Too coarse a grid, indeed, would impair the visualization of the scatterer, while a too thick one would increase the computational cost of the algorithm without improving the visualization itself.

This problem is removed by the so-called no-sampling approach, introduced in [4, 7], whereby the z_l -parametrized family of algebraic linear systems recalled above is replaced by a single functional equation set in a direct sum of $L^2(T)$ -spaces, which is solved by a unique Tikhonov regularization procedure: as a consequence, the indicator function, whose plot visualizes the scatterer, turns out to be analytically known with respect to the continuous spatial variable $z \in T$, and no grid needs to be chosen. As a by-product, the computational time of the no-sampling LSM algorithm is very short, since the regularization is performed only once: visualizations of 2D scatterers are obtained in around 1 s, whereas the traditional implementation requires some minutes for providing an almost identical result.

Of course, for both sampling and no-sampling approaches, as well as for both 2D and 3D scatterers, a common issue is that of formulating a criterion to decide whether the value of the indicator function at a certain point $z \in T$ is large or small, i.e., whether z is inside or outside the scatterer. The simplest (but very heuristic) approach consists in choosing the threshold value by a trial-and-error procedure, i.e., until the ‘best visual reconstruction’ is obtained: however, this is only possible when the *a priori* information on the scatterer is rather detailed. Another possibility is to perform some preliminary experiments with known reference scatterers and to choose for the indicator functions the threshold values providing the best visualizations: then, these values are combined (e.g., somehow averaged, or tuned ‘by hand’) to obtain the cut-off value also for an unknown scatterer (cf. e.g. [51]).

A less heuristic and more general approach consists of using an edge-detection algorithm to post-process the visualization provided by the LSM. An example of this application (for 2D scatterers) is given in [6]: here, the knowledge of the analytic expression of the indicator function, made possible by the no-sampling implementation, enables a direct application of an iterative algorithm, based on deformable models, to the indicator function itself, rather than to the pixelized image obtained as a plot of the latter. The result is an automatic identification of the profile of the unknown scatterer: we refer to [4, 6] and references therein for details.

The next step is clearly to extend the no-sampling LSM, as well as its post-processing by edge-detection techniques, to the case of 3D scatterers: in particular, reducing the computational costs of the algorithms is even more important in a 3D than in a 2D setting.

2.2 The problem

In order to address the 3D case (for an anisotropic electromagnetic inverse scattering problem), two important critical issues must be accounted for. In the traditional implementation of the LSM for Maxwell’s equations, the regularized solution of the far-field equation depends on both the sampling point and the sampling polarization of the Green’s function of the background. Therefore, in principle, a different regularization parameter should be selected not only for each point of a computational grid in a volume containing the scatterer, but also for each vector in a set of polarizations. To avoid such increase of the computational effort, heuristic procedures can be introduced, although in [45] it is pointed out that the visualization depends on the choice of the polarization vector: in particular, in [45, 46] it is observed that the best visualizations are obtained by combining (with the

same weight) the three indicator functions computed for three independent polarizations. The unifying approach followed in this chapter allows replacing the two-parameters family of far-field equations with a single functional equation whose regularization occurs independently of both the sampling point and the sampling polarization, thus removing any problem in choosing the number and/or the distance of the sampling points, as well as in selecting the sampling polarizations and combining the corresponding indicator functions. The resulting algorithm provides visualizations of complex 3D objects from their scattering data in a computational time that, as far as we know, is faster than any other inverse scattering method working in the resonance region.

The second technical issue is concerned with the optimal selection of the scatterer surface. In the LSM, a point on the boundary forces the norm of the regularized solution of the far-field equation to grow up. As recalled above, in [6] (in a 2D setting) an edge-detection technique is realized by means of deformable models in order to highlight the contour of the scatterer. In principle, this technique could be extended to surfaces in 3D but, although active contours are reasonably fast, active surfaces [41] require a notable computational effort to converge to the boundary of the scatterer. The result of this procedure would be that the time saved by using the no-sampling implementation would be partly lost by the visualization process based on deformable volumes. Therefore in the present chapter we prefer a different approach: the indicator function is restricted to an appropriate plane in \mathbb{R}^3 and the points of the scatterer surface belonging to this plane¹ are determined by applying a 2D deformable model, just as in [6]. Then we compute the average value of the indicator function over this profile and the result is chosen as the threshold value identifying the level surface (of the indicator function itself) that is used to visualize the boundary of the scatterer. This method is easily adapted to the case in which a non-connected scatterer consists of connected components characterized by different physical parameters: it suffices to consider restrictions of the indicator function to regions containing only one connected component and to select a different cut-off value for each region.

The implementation of the no-sampling LSM presented in this chapter is significantly more general than that described in [7] for the 2D case. In particular, here the far-field equation is discretized in such a way that even situations with non-uniform placement of the emitting/receiving antennas and/or with limited aperture data can be naturally dealt with. Furthermore, an analytic computation of the generalized discrepancy function is performed, which allows a fast and accurate computation of the optimal value of the regularization parameter.

¹Cf. footnote no. 6, p. 7.

Summarizing, we present here a visualization method for 3D electromagnetic inverse scattering where no sampling is performed over the volume points or the polarization vectors and the profile of the scatterer is detected by means of an effective automatic thresholding of an analytically known indicator function. The result is an extremely fast algorithm: objects that are visualized in around half an hour by traditional linear sampling on a PC equipped with a 1.6 GHz processor and 1 GB RAM, are visualized with comparable accuracy by this fully no-sampling automatic procedure in around one minute.

2.2.1 Plan of the following sections

The remainder of this chapter provides a detailed explanation of our approach to the issues introduced above. More precisely, in Section 2.3 we shortly summarize some results of [46], i.e., we introduce the far-field equation and recall the general theorem concerned with its approximate solution. In Section 2.4 we first perform a rather general, zero-order discretization of the far-field equation: the meshes arising from the discretization of the incidence and the observation directions, although formed by latitude-longitude rectangles on the unit sphere, do not need to be uniform or equal to each other; then, we describe the traditional formulation of the LSM. Section 2.5 introduces the new formulation: with respect to [7], the generalization consists not only in passing from a 2D to a 3D framework and taking into account the sampling polarizations, but also in considering more general discretization meshes. Section 2.6 exploits the computational tools provided by [6] to perform some numerical examples illustrating the notable effectiveness of the new approach. In Section 2.7 we propose an alternative, first-order discretization of the far-field equation, based on triangular meshes: in this framework, we test our no-sampling algorithm on a scattering experiment already considered in the previous section, as well as on the visualization of the perfectly conducting teapot first considered in [46]. Finally, Section 2.9 is an addendum where a technical result of importance in our implementation of the LSM is proved.

2.3 The far-field equation

A very general electromagnetic inverse scattering problem [46, 48] is concerned with an incident time-harmonic field $\vec{E}^i = \vec{E}^i(\vec{x})$, solution of

$$\text{curl curl } \vec{E}^i(\vec{x}) - k^2 \vec{E}^i(\vec{x}) = 0, \quad \vec{x} \in \mathbb{R}^3 \setminus D_{\vec{J}}, \quad (2.1)$$

where $D_{\vec{J}}$ is the support of the source current density \vec{J} . This wave is scattered by an inhomogeneous and possibly anisotropic target, whose support is represented, in a Cartesian coordinate system, by a bounded domain $\bar{D} \subset \mathbb{R}^3$, such that D is an open and Lipschitz domain of \mathbb{R}^3 with connected complement. The physical properties of the scatterer are described by a 3×3 symmetric matrix $N = N(\vec{x})$ (representing the possibly anisotropic index of refraction), whose entries are bounded and complex-valued functions defined in \mathbb{R}^3 and such that N is the identity matrix outside \bar{D} . The relationship between the scatterer and the total electric field $\vec{E} = \vec{E}(\vec{x})$ is expressed by the equation

$$\operatorname{curl} \operatorname{curl} \vec{E}(\vec{x}) - k^2 N(\vec{x}) \vec{E}(\vec{x}) = 0, \quad \vec{x} \in \mathbb{R}^3 \setminus D_{\vec{J}}, \quad (2.2)$$

where

$$\vec{E}(\vec{x}) = \vec{E}^s(\vec{x}) + \vec{E}^i(\vec{x}), \quad \vec{x} \in \mathbb{R}^3, \quad (2.3)$$

and the scattered field $\vec{E}^s = \vec{E}^s(\vec{x})$ satisfies the Silver-Müller² radiation condition

$$\lim_{|\vec{x}| \rightarrow \infty} \left(\operatorname{curl} \vec{E}^s \times \vec{x} - ik|\vec{x}| \vec{E}^s \right) = 0 \quad (2.4)$$

uniformly in $\hat{x} = \frac{\vec{x}}{|\vec{x}|}$.

In the following, we shall assume that the electric incident field is a plane wave propagating along the direction \hat{d} and polarized along $\vec{p} \in \mathbb{R}^3$ ($\vec{p} \cdot \hat{d} = 0$), i.e.,

$$\vec{E}^i(\vec{x}) = \vec{p} e^{ik\vec{x} \cdot \hat{d}}, \quad \vec{x} \in \mathbb{R}^3. \quad (2.5)$$

The Stratton-Chu formula³ implies that the radiating solutions \vec{E}^s to the scattering problem have the asymptotic behaviour⁴

$$\vec{E}^s(\vec{x}) = \frac{e^{ikr}}{r} \left\{ \vec{E}_\infty(\hat{x}; \hat{d}, \vec{p}) + O\left(\frac{1}{r}\right) \right\} \quad \text{as } r = |\vec{x}| \rightarrow \infty, \quad (2.6)$$

where the far-field pattern $\vec{E}_\infty(\cdot; \hat{d}, \vec{p})$ is defined on the unit sphere $\Omega := \{\vec{x} \in \mathbb{R}^3, |\vec{x}| = 1\}$. It is worth noting that $\vec{E}_\infty(\cdot; \hat{d}, \vec{p})$ is a tangential vector field, i.e., it belongs to $L_t^2(\Omega) := \{\vec{f}(\cdot) \in [L^2(\Omega)]^3 \mid \vec{f}(\hat{x}) \cdot \vec{\nu}(\hat{x}) = 0 \forall \hat{x} \in \Omega\}$, where $\vec{\nu}(\hat{x})$ is the normal unit vector to Ω in \hat{x} and $\vec{f}(\hat{x}) \cdot \vec{\nu}(\hat{x})$ is the usual scalar product in \mathbb{C}^3 between $\vec{f}(\hat{x})$ and $\vec{\nu}(\hat{x})$. The set of functions $L_t^2(\Omega)$ is a Hilbert space with the scalar product defined by

$$\left(\vec{f}_1(\cdot), \vec{f}_2(\cdot) \right)_{L_t^2(\Omega)} := \int_{\Omega} \vec{f}_1(\hat{d}) \cdot \vec{f}_2(\hat{d}) ds(\hat{d}) \quad \forall \vec{f}_1(\cdot), \vec{f}_2(\cdot) \in L_t^2(\Omega). \quad (2.7)$$

²See e.g. [48], p. 160.

³See e.g. [48], p. 156.

⁴See e.g. [48], p. 164.

Let us now introduce the *far-field equation* in the unknown $\vec{g}_{\vec{z},\vec{q}}(\cdot)$ for the 3D vector case [46]:

$$\int_{\Omega} \vec{E}_{\infty}(\hat{x}; \hat{d}, \vec{g}_{\vec{z},\vec{q}}(\hat{d})) ds(\hat{d}) = \vec{E}_{e,\infty}(\hat{x}; \vec{z}, \vec{q}). \quad (2.8)$$

Here \vec{z} and \vec{q} are respectively the sampling point in \mathbb{R}^3 and the sampling polarization; $\vec{E}_{\infty}(\hat{x}; \hat{d}, \vec{g}_{\vec{z},\vec{q}}(\hat{d}))$ denotes the far-field pattern of the field scattered by the target along the direction \hat{x} when it is illuminated by a plane wave impinging from the direction \hat{d} and polarized along $\vec{g}_{\vec{z},\vec{q}}(\hat{d})$; the function $\vec{g}_{\vec{z},\vec{q}}(\cdot)$ is in $L_t^2(\Omega)$ for each $\vec{z} \in \mathbb{R}^3$ and $\vec{q} \in \mathbb{R}^3$; finally, $\vec{E}_{e,\infty}(\hat{x}; \vec{z}, \vec{q})$ is the far-field pattern of an elementary dipole located in \vec{z} and oriented along \vec{q} :

$$\vec{E}_{e,\infty}(\hat{x}; \vec{z}, \vec{q}) := \frac{ik}{4\pi} (\hat{x} \times \vec{q}) \times \hat{x} e^{-ik\hat{x} \cdot \vec{z}}. \quad (2.9)$$

We now observe that, owing to the linear dependence of the far-field patterns on the polarizations (see, e.g., (2.9)) and to the linearity of the far-field equation (2.8), we can assume $|\vec{q}| = 1$ without loss in generality; hence in the following we shall consider $\vec{q} = \hat{q} \in \Omega$. Then, if we introduce the *far-field operator* $F : L_t^2(\Omega) \rightarrow L_t^2(\Omega)$ defined by

$$[F\vec{g}(\cdot)](\hat{x}) := \int_{\Omega} \vec{E}_{\infty}(\hat{x}; \hat{d}, \vec{g}(\hat{d})) ds(\hat{d}), \quad (2.10)$$

the far-field equation (2.8) can be written as

$$[F\vec{g}_{\vec{z},\hat{q}}(\cdot)](\hat{x}) = \vec{E}_{e,\infty}(\hat{x}; \vec{z}, \hat{q}). \quad (2.11)$$

The LSM is based on the following *general theorem* [46].

Theorem 2.3.1. (General theorem) *Let us assume that k is not a transmission eigenvalue and let F be the far-field operator (2.10); moreover, let \hat{q} be any element of Ω . Then we have:*

1) *if $\vec{z} \in D$, for every $\epsilon > 0$ there exists a solution $\vec{g}_{\vec{z},\hat{q}}(\cdot) \in L_t^2(\Omega)$ of the inequality*

$$\left\| [F\vec{g}_{\vec{z},\hat{q}}(\cdot)](\cdot) - \vec{E}_{e,\infty}(\cdot; \vec{z}, \hat{q}) \right\|_{L_t^2(\Omega)} < \epsilon, \quad (2.12)$$

such that, for all $z^ \in \partial D$,*

$$\lim_{\vec{z} \rightarrow z^*} \|\vec{g}_{\vec{z},\hat{q}}(\cdot)\|_{L_t^2(\Omega)} = \infty; \quad (2.13)$$

2) *if $\vec{z} \notin D$, for every $\epsilon > 0$ and $\delta > 0$ there exists a solution $\vec{g}_{\vec{z},\hat{q}}(\cdot) \in L_t^2(\Omega)$ of the inequality*

$$\left\| [F\vec{g}_{\vec{z},\hat{q}}(\cdot)](\cdot) - \vec{E}_{e,\infty}(\cdot; \vec{z}, \hat{q}) \right\|_{L_t^2(\Omega)} < \epsilon + \delta, \quad (2.14)$$

such that, for all $z^ \in \partial D$,*

$$\lim_{\delta \rightarrow 0} \|\vec{g}_{\vec{z},\hat{q}}(\cdot)\|_{L_t^2(\Omega)} = \infty. \quad (2.15)$$

Analogous theorems hold for scattering problems formulated for conductors or partially coated objects: in addition to [46], see [35] and references therein.

2.4 The discretization of the far-field equation and the LSM

The aim of the present section is to perform an angular discretization of the far-field equation that allows dealing with very general scattering situations, such as non-uniform displacement of the emitting and receiving antennas and limited aperture data. The first step towards such a discretization is to project the far-field patterns onto some particular basis. A possible choice is the spherical basis $\{\hat{r}(\hat{w}), \hat{\theta}(\hat{w}), \hat{\varphi}(\hat{w})\}$ (with $\hat{r}(\hat{w}) = \hat{w}$) intrinsic to the generic direction \hat{w} . Since the far-field pattern $\vec{E}_\infty(\cdot; \hat{d}, \vec{p})$ belongs to $L_t^2(\Omega)$, it has no component along $\hat{r}(\hat{x})$ and we can write⁵

$$\vec{E}_\infty(\hat{x}; \hat{d}, \vec{p}) = E_\infty^\theta(\hat{x}; \hat{d}, \vec{p}) \hat{\theta}(\hat{x}) + E_\infty^\varphi(\hat{x}; \hat{d}, \vec{p}) \hat{\varphi}(\hat{x}), \quad (2.16)$$

where $E_\infty^\theta(\hat{x}; \hat{d}, \vec{p}) := \vec{E}_\infty(\hat{x}; \hat{d}, \vec{p}) \cdot \hat{\theta}(\hat{x})$ and $E_\infty^\varphi(\hat{x}; \hat{d}, \vec{p}) := \vec{E}_\infty(\hat{x}; \hat{d}, \vec{p}) \cdot \hat{\varphi}(\hat{x})$. Moreover, since $\vec{p} \cdot \hat{d} = 0$, then \vec{p} can be decomposed as⁶

$$\vec{p} = p^\theta \hat{\theta}(\hat{d}) + p^\varphi \hat{\varphi}(\hat{d}), \quad (2.17)$$

where $p^\theta := \vec{p} \cdot \hat{\theta}(\hat{d})$ and $p^\varphi := \vec{p} \cdot \hat{\varphi}(\hat{d})$. Hence, exploiting the linearity of the far-field pattern with respect to \vec{p} , it is possible to write

$$E_\infty^\theta(\hat{x}; \hat{d}, \vec{p}) = p^\theta E_\infty^{\theta\theta}(\hat{x}; \hat{d}) + p^\varphi E_\infty^{\theta\varphi}(\hat{x}; \hat{d}), \quad (2.18)$$

$$E_\infty^\varphi(\hat{x}; \hat{d}, \vec{p}) = p^\theta E_\infty^{\varphi\theta}(\hat{x}; \hat{d}) + p^\varphi E_\infty^{\varphi\varphi}(\hat{x}; \hat{d}), \quad (2.19)$$

where

$$E_\infty^{\theta\theta}(\hat{x}; \hat{d}) := E_\infty^\theta(\hat{x}; \hat{d}, \hat{\theta}(\hat{d})), \quad (2.20)$$

$$E_\infty^{\theta\varphi}(\hat{x}; \hat{d}) := E_\infty^\theta(\hat{x}; \hat{d}, \hat{\varphi}(\hat{d})), \quad (2.21)$$

$$E_\infty^{\varphi\theta}(\hat{x}; \hat{d}) := E_\infty^\varphi(\hat{x}; \hat{d}, \hat{\theta}(\hat{d})), \quad (2.22)$$

$$E_\infty^{\varphi\varphi}(\hat{x}; \hat{d}) := E_\infty^\varphi(\hat{x}; \hat{d}, \hat{\varphi}(\hat{d})). \quad (2.23)$$

⁵It is worth noting that in decomposition (2.16) the spherical basis elements $\hat{\theta}(\hat{x})$ and $\hat{\varphi}(\hat{x})$ can be replaced by any pair of orthogonal unit vectors $\hat{\xi}_1(\hat{x})$ and $\hat{\xi}_2(\hat{x})$ spanning the tangent plane to Ω in \hat{x} .

⁶As before, in decomposition (2.17) the spherical basis elements $\hat{\theta}(\hat{d})$ and $\hat{\varphi}(\hat{d})$ can be replaced by any pair of orthogonal unit vectors $\hat{\xi}_1(\hat{d})$ and $\hat{\xi}_2(\hat{d})$ spanning the tangent plane to Ω in \hat{d} . All the computations in the following can be trivially adapted to account for this more general choice.

Analogously to (2.16), the far-field pattern $\vec{E}_{e,\infty}(\cdot; \vec{z}, \hat{q}) \in L_t^2(\Omega)$, defined by (2.9), can be written in terms of $\hat{\theta}(\hat{x})$ and $\hat{\varphi}(\hat{x})$ as

$$\vec{E}_{e,\infty}(\hat{x}; \vec{z}, \hat{q}) = E_{e,\infty}^\theta(\hat{x}; \vec{z}, \hat{q}) \hat{\theta}(\hat{x}) + E_{e,\infty}^\varphi(\hat{x}; \vec{z}, \hat{q}) \hat{\varphi}(\hat{x}), \quad (2.24)$$

where $E_{e,\infty}^\theta(\hat{x}; \vec{z}, \hat{q}) := \vec{E}_{e,\infty}(\hat{x}; \vec{z}, \hat{q}) \cdot \hat{\theta}(\hat{x})$ and $E_{e,\infty}^\varphi(\hat{x}; \vec{z}, \hat{q}) := \vec{E}_{e,\infty}(\hat{x}; \vec{z}, \hat{q}) \cdot \hat{\varphi}(\hat{x})$. As a consequence, the vector equation (2.11) can be split into two scalar ones:

$$[F\vec{g}_{\vec{z},\hat{q}}(\cdot)](\hat{x}) \cdot \hat{\theta}(\hat{x}) = E_{e,\infty}^\theta(\hat{x}; \vec{z}, \hat{q}), \quad (2.25)$$

$$[F\vec{g}_{\vec{z},\hat{q}}(\cdot)](\hat{x}) \cdot \hat{\varphi}(\hat{x}) = E_{e,\infty}^\varphi(\hat{x}; \vec{z}, \hat{q}), \quad (2.26)$$

i.e., recalling definition (2.10) and decompositions (2.16), (2.18), (2.19),

$$\int_{\Omega} \left[g_{\vec{z},\hat{q}}^\theta(\hat{d}) E_\infty^{\theta\theta}(\hat{x}; \hat{d}) + g_{\vec{z},\hat{q}}^\varphi(\hat{d}) E_\infty^{\theta\varphi}(\hat{x}; \hat{d}) \right] ds(\hat{d}) = E_{e,\infty}^\theta(\hat{x}; \vec{z}, \hat{q}), \quad (2.27)$$

$$\int_{\Omega} \left[g_{\vec{z},\hat{q}}^\theta(\hat{d}) E_\infty^{\varphi\theta}(\hat{x}; \hat{d}) + g_{\vec{z},\hat{q}}^\varphi(\hat{d}) E_\infty^{\varphi\varphi}(\hat{x}; \hat{d}) \right] ds(\hat{d}) = E_{e,\infty}^\varphi(\hat{x}; \vec{z}, \hat{q}). \quad (2.28)$$

In real experiments, the far-field pattern is measured at large distances from the scatterer⁷ for $L_{\hat{x}} = T_{\hat{x}} F_{\hat{x}}$ observation directions and $L_{\hat{d}} = T_{\hat{d}} F_{\hat{d}}$ incidence directions. The observation directions are denoted as

$$\hat{x}_{\ell_{\hat{x}}(i,j)} = (\sin \theta_i^{\hat{x}} \cos \varphi_j^{\hat{x}}, \sin \theta_i^{\hat{x}} \sin \varphi_j^{\hat{x}}, \cos \theta_i^{\hat{x}}) \in \Omega, \quad (2.29)$$

where, for all integers $i = 0, \dots, T_{\hat{x}} - 1$ and $j = 0, \dots, F_{\hat{x}} - 1$, we have put

$$\ell_{\hat{x}}(i, j) := iF_{\hat{x}} + j, \quad \theta_i^{\hat{x}} \in (0, \pi), \quad \varphi_j^{\hat{x}} \in [0, 2\pi); \quad (2.30)$$

analogously, the incidence directions are denoted as

$$\hat{d}_{\ell_{\hat{d}}(i,j)} = (\sin \theta_i^{\hat{d}} \cos \varphi_j^{\hat{d}}, \sin \theta_i^{\hat{d}} \sin \varphi_j^{\hat{d}}, \cos \theta_i^{\hat{d}}) \in \Omega, \quad (2.31)$$

where, for all integers $i = 0, \dots, T_{\hat{d}} - 1$ and $j = 0, \dots, F_{\hat{d}} - 1$, we have put

$$\ell_{\hat{d}}(i, j) := iF_{\hat{d}} + j, \quad \theta_i^{\hat{d}} \in (0, \pi), \quad \varphi_j^{\hat{d}} \in [0, 2\pi). \quad (2.32)$$

As a consequence, equations (2.27) and (2.28) can be discretized by requiring that, for all $\ell_{\hat{x}} = 0, \dots, L_{\hat{x}} - 1$,

$$\sum_{\ell_{\hat{d}}=0}^{L_{\hat{d}}-1} \left[g_{\vec{z},\hat{q}}^\theta(\hat{d}_{\ell_{\hat{d}}}) E_\infty^{\theta\theta}(\hat{x}_{\ell_{\hat{x}}}; \hat{d}_{\ell_{\hat{d}}}) + g_{\vec{z},\hat{q}}^\varphi(\hat{d}_{\ell_{\hat{d}}}) E_\infty^{\theta\varphi}(\hat{x}_{\ell_{\hat{x}}}; \hat{d}_{\ell_{\hat{d}}}) \right] \Delta s_{\ell_{\hat{d}}} = E_{e,\infty}^\theta(\hat{x}_{\ell_{\hat{x}}}; \vec{z}, \hat{q}), \quad (2.33)$$

$$\sum_{\ell_{\hat{d}}=0}^{L_{\hat{d}}-1} \left[g_{\vec{z},\hat{q}}^\theta(\hat{d}_{\ell_{\hat{d}}}) E_\infty^{\varphi\theta}(\hat{x}_{\ell_{\hat{x}}}; \hat{d}_{\ell_{\hat{d}}}) + g_{\vec{z},\hat{q}}^\varphi(\hat{d}_{\ell_{\hat{d}}}) E_\infty^{\varphi\varphi}(\hat{x}_{\ell_{\hat{x}}}; \hat{d}_{\ell_{\hat{d}}}) \right] \Delta s_{\ell_{\hat{d}}} = E_{e,\infty}^\varphi(\hat{x}_{\ell_{\hat{x}}}; \vec{z}, \hat{q}), \quad (2.34)$$

⁷For an operative definition of ‘far-field region’, see e.g. [87], p. 24.

where, for all $i = 0, \dots, T_{\hat{d}} - 1$ and $j = 0, \dots, F_{\hat{d}} - 1$, we have defined

$$\Delta s_{\ell_{\hat{d}}} := \sin \theta_i^{\hat{d}} \Delta \theta_i^{\hat{d}} \Delta \varphi_j^{\hat{d}} > 0, \quad (2.35)$$

with $\Delta \theta_i^{\hat{d}} := \theta_{i+1}^{\hat{d}} - \theta_i^{\hat{d}} > 0$ and $\Delta \varphi_j^{\hat{d}} := \varphi_{j+1}^{\hat{d}} - \varphi_j^{\hat{d}} > 0$. In particular, in the case of uniform discretization we have $\Delta \theta_i^{\hat{d}} = \pi/T_{\hat{d}}$ and $\Delta \varphi_j^{\hat{d}} = 2\pi/F_{\hat{d}}$.

Remark 2.4.1. According to equations (2.33) and (2.34), the integral (2.10) on the unit sphere Ω is approximated, in the numerical implementation, by a zero-order discretization, whereby the mesh on Ω is formed by (not necessarily equal) latitude-longitude rectangles⁸, i.e., portions of sphere delimited by two lines of longitude and two lines of latitude. Then, the value of the integrand function is regarded as *constant* on each one of these rectangles and all the resulting contributions are summed, thus forming the left-hand side of equations (2.33) and (2.34). In Section 2.7 we shall introduce an alternative approach, whereby the far-field equation is discretized at the first order on a triangular mesh. \square

Equations (2.33) and (2.34) can be written in a more compact form by using the matrix notation, i.e.,

$$\mathbf{E}_{\infty} \Delta \mathbf{S}_{\hat{d}} \mathbf{G}_{\vec{z}, \hat{q}} = \mathbf{E}_{e, \infty}(\vec{z}, \hat{q}), \quad (2.36)$$

where we have defined $\Delta \mathbf{S}_{\hat{d}}$ as the diagonal and positive-definite matrix of $2L_{\hat{d}} \times 2L_{\hat{d}}$ elements

$$\Delta \mathbf{S}_{\hat{d}} := \begin{pmatrix} \Delta \mathbf{s}_{\hat{d}} & \mathbf{0} \\ \mathbf{0} & \Delta \mathbf{s}_{\hat{d}} \end{pmatrix}, \quad (2.37)$$

with $\Delta \mathbf{s}_{\hat{d}} := \text{diag}(\Delta s_{\ell_{\hat{d}}})_{\ell_{\hat{d}}=0, \dots, L_{\hat{d}}-1}$; $\mathbf{G}_{\vec{z}, \hat{q}}$ as the column vector of length $2L_{\hat{d}}$

$$\mathbf{G}_{\vec{z}, \hat{q}} := \begin{pmatrix} \mathbf{g}_{\vec{z}, \hat{q}}^{\theta} \\ \mathbf{g}_{\vec{z}, \hat{q}}^{\varphi} \end{pmatrix}, \quad (2.38)$$

with $\mathbf{g}_{\vec{z}, \hat{q}}^{\theta} := (g_{\vec{z}, \hat{q}}^{\theta}(\hat{d}_{\ell_{\hat{d}}}))_{\ell_{\hat{d}}=0, \dots, L_{\hat{d}}-1}$, $\mathbf{g}_{\vec{z}, \hat{q}}^{\varphi} := (g_{\vec{z}, \hat{q}}^{\varphi}(\hat{d}_{\ell_{\hat{d}}}))_{\ell_{\hat{d}}=0, \dots, L_{\hat{d}}-1}$; $\mathbf{E}_{e, \infty}(\vec{z}, \hat{q})$ as the column vector of length $2L_{\hat{x}}$

$$\mathbf{E}_{e, \infty}(\vec{z}, \hat{q}) := \begin{pmatrix} \mathbf{E}_{e, \infty}^{\theta}(\vec{z}, \hat{q}) \\ \mathbf{E}_{e, \infty}^{\varphi}(\vec{z}, \hat{q}) \end{pmatrix}, \quad (2.39)$$

⁸They are not *spherical* rectangles: indeed, in general, spherical polygons are figures made of arcs of great circles. Now, lines of longitude are great circles, but lines of latitude are not (except for the equator). For small variations in latitude, i.e., with the notations used in (2.35), for small $\Delta \theta_i^{\hat{d}}$, the area of a latitude-longitude rectangle is well approximated by the quantity $\Delta s_{\ell_{\hat{d}}}$ defined in (2.35).

with $\mathbf{E}_{e,\infty}^\theta(\vec{z}, \hat{q}) := (E_{e,\infty}^\theta(\hat{x}_{\ell_{\hat{x}}}; \vec{z}, \hat{q}))_{\ell_{\hat{x}}=0,\dots,L_{\hat{x}}-1}$, $\mathbf{E}_{e,\infty}^\varphi(\vec{z}, \hat{q}) := (E_{e,\infty}^\varphi(\hat{x}_{\ell_{\hat{x}}}; \vec{z}, \hat{q}))_{\ell_{\hat{x}}=0,\dots,L_{\hat{x}}-1}$; finally, the $2L_{\hat{x}} \times 2L_{\hat{d}}$ matrix \mathbf{E}_∞ is defined as

$$\mathbf{E}_\infty := \begin{pmatrix} \mathbf{E}_\infty^{\theta\theta} & \mathbf{E}_\infty^{\theta\varphi} \\ \mathbf{E}_\infty^{\varphi\theta} & \mathbf{E}_\infty^{\varphi\varphi} \end{pmatrix}, \quad (2.40)$$

with

$$\mathbf{E}_\infty^{\theta\theta} := \left(E_\infty^{\theta\theta}(\hat{x}_{\ell_{\hat{x}}}; \hat{d}_{\ell_{\hat{d}}}) \right)_{\ell_{\hat{x}}=0,\dots,L_{\hat{x}}-1; \ell_{\hat{d}}=0,\dots,L_{\hat{d}}-1}, \quad (2.41)$$

$$\mathbf{E}_\infty^{\theta\varphi} := \left(E_\infty^{\theta\varphi}(\hat{x}_{\ell_{\hat{x}}}; \hat{d}_{\ell_{\hat{d}}}) \right)_{\ell_{\hat{x}}=0,\dots,L_{\hat{x}}-1; \ell_{\hat{d}}=0,\dots,L_{\hat{d}}-1}, \quad (2.42)$$

$$\mathbf{E}_\infty^{\varphi\theta} := \left(E_\infty^{\varphi\theta}(\hat{x}_{\ell_{\hat{x}}}; \hat{d}_{\ell_{\hat{d}}}) \right)_{\ell_{\hat{x}}=0,\dots,L_{\hat{x}}-1; \ell_{\hat{d}}=0,\dots,L_{\hat{d}}-1}, \quad (2.43)$$

$$\mathbf{E}_\infty^{\varphi\varphi} := \left(E_\infty^{\varphi\varphi}(\hat{x}_{\ell_{\hat{x}}}; \hat{d}_{\ell_{\hat{d}}}) \right)_{\ell_{\hat{x}}=0,\dots,L_{\hat{x}}-1; \ell_{\hat{d}}=0,\dots,L_{\hat{d}}-1}. \quad (2.44)$$

Remark 2.4.2. The positive-definite matrix $\Delta\mathbf{S}_{\hat{d}}$ given in (2.37) defines a (weighted) scalar product $(\cdot, \cdot)_{L_{\hat{d}}}$ in $\mathbb{C}^{2L_{\hat{d}}}$, obtained from a $L_{\hat{d}}$ -angular discretization of the scalar product (2.7). If \mathbf{w}_1 and \mathbf{w}_2 are two column vectors in $\mathbb{C}^{2L_{\hat{d}}}$, we have

$$(\mathbf{w}_1, \mathbf{w}_2)_{L_{\hat{d}}} := \mathbf{w}_1^T \Delta\mathbf{S}_{\hat{d}} \bar{\mathbf{w}}_2, \quad (2.45)$$

where \mathbf{w}_1^T denotes the transpose of \mathbf{w}_1 and $\bar{\mathbf{w}}_2$ the complex conjugate of \mathbf{w}_2 . The scalar product (2.45) induces a norm, denoted by $\|\cdot\|_{L_{\hat{d}}}$, in $\mathbb{C}^{2L_{\hat{d}}}$; we shall write $(\mathbb{C}^{2L_{\hat{d}}}, (\cdot, \cdot)_{L_{\hat{d}}})$ to denote the vector space $\mathbb{C}^{2L_{\hat{d}}}$ endowed with the scalar product $(\cdot, \cdot)_{L_{\hat{d}}}$. In a completely analogous way, we can consider the space $(\mathbb{C}^{2L_{\hat{x}}}, (\cdot, \cdot)_{L_{\hat{x}}})$, by simply replacing the weight matrix (2.37) with its analogous $\Delta\mathbf{S}_{\hat{x}}$, defined in terms of $\Delta s_{\ell_{\hat{x}}} := \sin \theta_i^{\hat{x}} \Delta \theta_i^{\hat{x}} \Delta \varphi_j^{\hat{x}} > 0$. \square

In real applications, the far-field patterns are blurred by the noise affecting the measurement processes, so that only a noisy version $\mathbf{E}_\infty^{\mathbf{H}}$ of the far-field patterns is available, i.e.,

$$\mathbf{E}_\infty^{\mathbf{H}} := \mathbf{E}_\infty + \mathbf{H}, \quad (2.46)$$

where \mathbf{H} is the noise matrix. Then, we can define the linear operator

$$\begin{aligned} \mathcal{F}^h : (\mathbb{C}^{2L_{\hat{d}}}, (\cdot, \cdot)_{L_{\hat{d}}}) &\rightarrow (\mathbb{C}^{2L_{\hat{x}}}, (\cdot, \cdot)_{L_{\hat{x}}}) \\ \mathbf{x} &\mapsto \mathbf{E}_\infty^{\mathbf{H}} \Delta\mathbf{S}_{\hat{d}} \mathbf{x}; \end{aligned} \quad (2.47)$$

h is used as a superscript to distinguish \mathcal{F}^h from the corresponding noise-free version \mathcal{F} and also to denote the noise bound $h \geq \|\mathcal{F}^h - \mathcal{F}\|$, where $\|\cdot\|$ indicates the operator norm. By virtue of (2.47), $\mathbf{E}_\infty^{\mathbf{H}} \Delta\mathbf{S}_{\hat{d}} =: \mathbf{F}^h$ is the matrix representation of the linear operator \mathcal{F}^h ;

moreover, remembering (2.36), we can now write the noisy and discretized version of the far-field equation (2.8) in the form

$$\mathbf{F}^h \mathbf{G}_{\vec{z}, \hat{q}} = \mathbf{E}_{e, \infty}(\vec{z}, \hat{q}). \quad (2.48)$$

The ill-conditioning of equation (2.48) requires a regularization procedure; in particular, Tikhonov regularization method [89] consists in determining

$$\mathbf{G}_{\vec{z}, \hat{q}; \alpha} = \operatorname{argmin}_{\mathbf{G} \in \mathbb{C}^{2L_{\hat{d}}}} \left\{ \|\mathbf{F}^h \mathbf{G} - \mathbf{E}_{e, \infty}(\vec{z}, \hat{q})\|_{L_{\hat{x}}}^2 + \alpha \|\mathbf{G}\|_{L_{\hat{d}}}^2 \right\}. \quad (2.49)$$

Given (2.49), the optimal regularized solution is obtained by choosing for the regularization parameter α the value $\alpha^*(\vec{z}, \hat{q})$ determined by the generalized discrepancy principle, i.e., by finding the zero of the generalized discrepancy function $\rho : (0, +\infty) \rightarrow \mathbb{R}$ defined as⁹

$$\rho(\alpha) := \|\mathbf{F}^h \mathbf{G}_{\vec{z}, \hat{q}; \alpha} - \mathbf{E}_{e, \infty}(\vec{z}, \hat{q})\|_{L_{\hat{x}}}^2 - h^2 \|\mathbf{G}_{\vec{z}, \hat{q}; \alpha}\|_{L_{\hat{d}}}^2. \quad (2.50)$$

An explicit form for this regularized solution can be determined by using the singular representation¹⁰ of the linear operator \mathcal{F}^h , whose singular system is related to that of the matrix \mathbf{F}^h according to Theorem 2.9.1 in Section 2.9, p. 39. If we denote by $\{\sigma_p^h, \mathbf{u}_p^h, \mathbf{v}_p^h\}_{p=0}^{r^h-1}$ (where $\sigma_0^h \geq \sigma_1^h \geq \dots \geq \sigma_{r^h-1}^h$ and $r^h := \operatorname{rank} \mathbf{F}^h$) the singular system of \mathcal{F}^h and if $\alpha^*(\vec{z}, \hat{q})$ is the zero of the generalized discrepancy function (2.50), it turns out that the optimal Tikhonov regularized solution of (2.48) is given by¹¹

$$\mathbf{G}_{\vec{z}, \hat{q}; \alpha^*(\vec{z}, \hat{q})} = \sum_{p=0}^{r^h-1} \frac{\sigma_p^h}{(\sigma_p^h)^2 + \alpha^*(\vec{z}, \hat{q})} (\mathbf{E}_{e, \infty}(\vec{z}, \hat{q}), \mathbf{v}_p^h)_{L_{\hat{x}}} \mathbf{u}_p^h. \quad (2.51)$$

Then, inspired by Theorem 2.3.1, the LSM allows visualizing the scatterer profile by performing the following steps:

- take a grid of points $\mathcal{Z} \subset \mathbb{R}^3$ covering the scatterer and choose a sampling polarization \hat{q} ;
- for each grid point $\vec{z} \in \mathcal{Z}$, determine the optimal Tikhonov regularized solution (2.51);
- for each grid point $\vec{z} \in \mathcal{Z}$, consider the quantity $\|\mathbf{G}_{\vec{z}, \hat{q}; \alpha^*(\vec{z}, \hat{q})}\|_{L_{\hat{d}}}$ or a suitable combination of the analogous quantities obtained for different choices of \hat{q} [46];

⁹See e.g. chapter 1 of [89].

¹⁰For basic concepts and notations, see e.g. Subsection 1.5.1 at pp. 16-20 of [4].

¹¹Cf. [4], p. 41 and p. 136.

- visualize the profile of the scatterer as the set of grid points in which the previous combination becomes mostly large or small, depending on the analytical form chosen for the combination itself.

It is worth noting that $\|\mathbf{G}_{\vec{z}, \hat{q}; \alpha^*(\vec{z}, \hat{q})}\|_{L_{\hat{d}}}^2$ can be explicitly computed, by using (2.51), as

$$\|\mathbf{G}_{\vec{z}, \hat{q}; \alpha^*(\vec{z}, \hat{q})}\|_{L_{\hat{d}}}^2 = \sum_{p=0}^{r^h-1} \frac{(\sigma_p^h)^2}{[(\sigma_p^h)^2 + \alpha^*(\vec{z}, \hat{q})]^2} \left| (\mathbf{E}_{e, \infty}(\vec{z}, \hat{q}), \mathbf{v}_p^h)_{L_{\hat{x}}} \right|^2. \quad (2.52)$$

In this implementation the optimal regularization parameter $\alpha^*(\vec{z}, \hat{q})$ explicitly depends on the grid point \vec{z} and the prefixed \hat{q} and therefore it must be computed a number of times equal to the product of the number of grid points times the number of polarizations sampled in Ω .

Remark 2.4.3. The discretization introduced in this section is much more general than that adopted for the 2D formulation in [7] and easily allows dealing with non-uniform positions of emitters and receivers, as well as with the case of limited aperture data. In fact, it suffices to consider $\theta_i^{\hat{d}} \in (\bar{\theta}_1^{\hat{d}}, \bar{\theta}_2^{\hat{d}}) \subset (0, \pi)$ for $i = 0, \dots, T_{\hat{d}} - 1$; $\varphi_j^{\hat{d}} \in [\bar{\varphi}_1^{\hat{d}}, \bar{\varphi}_2^{\hat{d}}) \subset [0, 2\pi)$ for $j = 0, \dots, F_{\hat{d}} - 1$; $\theta_i^{\hat{x}} \in (\bar{\theta}_1^{\hat{x}}, \bar{\theta}_2^{\hat{x}}) \subset (0, \pi)$ for $i = 0, \dots, T_{\hat{x}} - 1$; $\varphi_j^{\hat{x}} \in [\bar{\varphi}_1^{\hat{x}}, \bar{\varphi}_2^{\hat{x}}) \subset [0, 2\pi)$ for $j = 0, \dots, F_{\hat{x}} - 1$. \square

2.5 A no-sampling implementation of the LSM

The key-idea of no-sampling is to replace the discrete grid \mathcal{Z} with a continuous one $T := [-c_1, c_1] \times [-c_2, c_2] \times [-c_3, c_3] \subset \mathbb{R}^3$ and, furthermore, to replace a finite set of sampled polarizations with the whole unit sphere Ω . This approach, whose purpose is to increase the computational effectiveness and the automation degree of the traditional LSM, amounts to regarding expression (2.52) as a sampled version of a function defined over $T \times \Omega$. The critical issue in this process is that, while the dependence of $\|\mathbf{G}_{\vec{z}, \hat{q}; \alpha^*(\vec{z}, \hat{q})}\|_{L_{\hat{d}}}^2$ on \vec{z} and \hat{q} is explicitly known for the term $\mathbf{E}_{e, \infty}(\vec{z}, \hat{q})$ (see (2.9), (2.24), (2.39), (2.52)), this is not true for the optimal value of the regularization parameter, since $\alpha^*(\vec{z}, \hat{q})$ can only be computed numerically as the zero of the generalized discrepancy function (2.50). This problem can be solved by setting the formulation of the method in a new mathematical framework, which enables us to consider as a unique functional equation the infinitely many algebraic linear systems

$$\mathbf{F}^h \mathbf{G}(\vec{z}, \hat{q}) = \mathbf{E}_{e, \infty}(\vec{z}, \hat{q}) \quad \forall \vec{z} \in T, \forall \hat{q} \in \Omega \quad (2.53)$$

that would arise from (2.48) if, with a ‘naive’ procedure, the unknown vector $\mathbf{G}_{\vec{z}, \hat{q}}$ were simply regarded as an unknown function $\mathbf{G}(\vec{z}, \hat{q})$ of the continuous parameters \vec{z} and \hat{q} .

The new mathematical setting requires the introduction of two functional spaces. Given the total number $L_{\hat{d}}$ of incidence directions, let us consider the Hilbert space $[L^2(\mathcal{B})]^{2L_{\hat{d}}} := \bigoplus_{i=1}^{2L_{\hat{d}}} L^2(\mathcal{B})$, with $\mathcal{B} := T \times \Omega$, equipped with the (weighted) scalar product

$$(\mathbf{f}(\cdot), \mathbf{g}(\cdot))_{2, L_{\hat{d}}} := \sum_{\ell_{\hat{d}}=0}^{L_{\hat{d}}-1} \Delta s_{\ell_{\hat{d}}} (f_{\ell_{\hat{d}}}(\cdot), g_{\ell_{\hat{d}}}(\cdot))_{L^2(\mathcal{B})} + \sum_{\ell_{\hat{d}}=0}^{L_{\hat{d}}-1} \Delta s_{\ell_{\hat{d}}} (f_{L_{\hat{d}}+\ell_{\hat{d}}}(\cdot), g_{L_{\hat{d}}+\ell_{\hat{d}}}(\cdot))_{L^2(\mathcal{B})} \quad (2.54)$$

for all $\mathbf{f}(\cdot) := \{f_t(\cdot)\}_{t=0}^{2L_{\hat{d}}-1}$, $\mathbf{g}(\cdot) := \{g_t(\cdot)\}_{t=0}^{2L_{\hat{d}}-1} \in [L^2(\mathcal{B})]^{2L_{\hat{d}}}$, where the weights $\Delta s_{\ell_{\hat{d}}}$ are defined in (2.35) and $(\cdot, \cdot)_{L^2(\mathcal{B})}$ denotes the usual scalar product in $L^2(\mathcal{B})$; moreover, we shall denote by $\|\cdot\|_{2, L_{\hat{d}}}$ the induced norm, i.e.,

$$\|\mathbf{f}(\cdot)\|_{2, L_{\hat{d}}} := \sqrt{\int_{\mathcal{B}} \|\mathbf{f}(\vec{z}, \hat{q})\|_{L_{\hat{d}}}^2 d\vec{z} ds(\hat{q})}. \quad (2.55)$$

In a completely analogous way we can define the Hilbert space $[L^2(\mathcal{B})]^{2L_{\hat{x}}}$, where $L_{\hat{x}}$ is the total number of observation directions.

We can now introduce the following linear operator, whose aim is that of enabling the operator \mathcal{F}^h , defined in (2.47), to act on $2L_{\hat{d}}$ -uples of functions, rather than on $2L_{\hat{d}}$ -uples of complex numbers.

Definition 2.5.1. *The linear operator $\mathbf{F}^h : [L^2(\mathcal{B})]^{2L_{\hat{d}}} \rightarrow [L^2(\mathcal{B})]^{2L_{\hat{x}}}$ is defined as*

$$[\mathbf{F}^h \mathbf{G}(\cdot)](\cdot) := \left\{ \sum_{t=0}^{2L_{\hat{d}}-1} (\mathbf{F}^h)_{st} G_t(\cdot) \right\}_{s=0}^{2L_{\hat{x}}-1}, \quad (2.56)$$

where $\mathbf{G}(\cdot) := \{G_t(\cdot)\}_{t=0}^{2L_{\hat{d}}-1} \in [L^2(\mathcal{B})]^{2L_{\hat{d}}}$, and $(\mathbf{F}^h)_{st}$ are the elements of the matrix \mathbf{F}^h .

Theorem 2.5.1. *The following properties for the linear operator \mathbf{F}^h hold:*

- i) *it is continuous, but not compact;*
- ii) *its kernel $\mathcal{N}(\mathbf{F}^h)$ is given by¹²*

$$\mathcal{N}(\mathbf{F}^h) = \left\{ \mathbf{G}(\cdot) \in [L^2(\mathcal{B})]^{2L_{\hat{d}}} \mid \mathbf{G}(\vec{z}, \hat{q}) \in \mathcal{N}(\mathbf{F}^h) \text{ f.a.a. } (\vec{z}, \hat{q}) \in \mathcal{B} \right\}; \quad (2.57)$$

¹²In relation (2.57), the acronym ‘f.a.a.’ means ‘for almost all’.

iii) if $\mathbf{G}(\cdot) \in [L^2(\mathcal{B})]^{2L_{\hat{d}}}$ is such that $\mathbf{G}(\vec{z}, \hat{q}) \in \mathcal{N}(\mathbf{F}^h)^\perp$ for almost all $(\vec{z}, \hat{q}) \in \mathcal{B}$, then $\mathbf{G}(\cdot) \in \mathcal{N}(\mathbf{F}^h)^\perp$, where the orthogonality must be intended with respect to the scalar product of the corresponding vector space.

Proof. These properties can be proved in full analogy with Theorem 3.2 and Remark 3.3 in [7]. ■

The non-compactness of \mathbf{F}^h does not prevent us from using the singular representation of the linear operator \mathcal{F}^h . Hence, we obtain the following expression for \mathbf{F}^h :

$$[\mathbf{F}^h \mathbf{G}(\cdot)](\cdot) = \left\{ \sum_{p=0}^{r^h-1} \sigma_p^h v_{p,s}^h (\mathbf{G}(\cdot), \mathbf{u}_p^h)_{L_{\hat{d}}} \right\}_{s=0}^{2L_{\hat{x}}-1} \quad \forall \mathbf{G}(\cdot) \in [L^2(\mathcal{B})]^{2L_{\hat{d}}}, \quad (2.58)$$

where $v_{p,s}^h$ is the s -th component of \mathbf{v}_p^h and $(\mathbf{G}(\cdot), \mathbf{u}_p^h)_{L_{\hat{d}}}$ is defined as the element in $L^2(\mathcal{B})$ such that

$$(\mathbf{G}(\cdot), \mathbf{u}_p^h)_{L_{\hat{d}}} : \mathcal{B} \ni (\vec{z}, \hat{q}) \mapsto (\mathbf{G}(\vec{z}, \hat{q}), \mathbf{u}_p^h)_{L_{\hat{d}}} \in \mathbb{C}. \quad (2.59)$$

If we denote by \mathbf{F} the corresponding noise-free version of \mathbf{F}^h , by using representation (2.58) for \mathbf{F}^h and the analogous one for \mathbf{F} , we can easily prove that

$$\|\mathbf{F}^h - \mathbf{F}\| = \|\mathcal{F}^h - \mathcal{F}\| = |\sigma_0^h - \sigma_0| \leq h, \quad (2.60)$$

where σ_0 is the largest singular value of \mathcal{F} : this means that the bounds on the levels of noise affecting \mathcal{F}^h and \mathbf{F}^h are the same, i.e., equal to h .

We can now use the operator \mathbf{F}^h to collect the infinitely many algebraic systems (2.53) into the following single functional equation, written in $[L^2(\mathcal{B})]^{2L_{\hat{x}}}$ for the unknown $\mathbf{G}(\cdot) \in [L^2(\mathcal{B})]^{2L_{\hat{d}}}$:

$$[\mathbf{F}^h \mathbf{G}(\cdot)](\cdot) = \mathbf{E}_{e,\infty}(\cdot), \quad (2.61)$$

where $\mathbf{E}_{e,\infty}(\cdot)$ is the element of $[L^2(\mathcal{B})]^{2L_{\hat{x}}}$ obtained from $\mathbf{E}_{e,\infty}(\vec{z}, \hat{q})$ by simply regarding the sampling pair (\vec{z}, \hat{q}) as a variable on \mathcal{B} . It is now clear that the regularization of the previous equation (2.61) requires a single-step procedure, thus providing a single value α^* for the regularization parameter, which is independent of both \vec{z} and \hat{q} (however, in general, α^* may depend on the choice of the investigation domain T). Then, the next problem to be solved is how to compute the Tikhonov regularized solution of equation (2.61): this task is accomplished by the following theorem, which shows that, for a generic α , both the generalized and the regularized solutions of (2.61) are obtained from the generalized and regularized solutions of (2.53) by simply regarding the sampling pair (\vec{z}, \hat{q}) as a variable on \mathcal{B} .

Theorem 2.5.2. *The generalized and Tikhonov regularized solutions of equation (2.61) are respectively given by*

$$\mathbf{G}^{h\dagger}(\cdot) = \sum_{p=0}^{r^h-1} \frac{1}{\sigma_p^h} (\mathbf{E}_{e,\infty}(\cdot), \mathbf{v}_p^h)_{L_{\hat{x}}} \mathbf{u}_p^h \quad (2.62)$$

and

$$\mathbf{G}_\alpha(\cdot) = \sum_{p=0}^{r^h-1} \frac{\sigma_p^h}{(\sigma_p^h)^2 + \alpha} (\mathbf{E}_{e,\infty}(\cdot), \mathbf{v}_p^h)_{L_{\hat{x}}} \mathbf{u}_p^h. \quad (2.63)$$

Proof. We prove the result for the generalized solution (the result for the Tikhonov regularized solution can be shown in an analogous way¹³). Since the generalized solution $\mathbf{G}^{h\dagger}(\vec{z}, \hat{q})$ of equation (2.53) is its (unique) least-squares solution of minimum norm, then for any $\mathbf{G}(\cdot) \in [L^2(\mathcal{B})]^{2L_{\hat{a}}}$ and for almost all $(\vec{z}, \hat{q}) \in \mathcal{B}$ it holds that

$$\left\| \mathbf{F}^h \mathbf{G}^{h\dagger}(\vec{z}, \hat{q}) - \mathbf{E}_{e,\infty}(\vec{z}, \hat{q}) \right\|_{L_{\hat{x}}}^2 \leq \left\| \mathbf{F}^h \mathbf{G}(\vec{z}, \hat{q}) - \mathbf{E}_{e,\infty}(\vec{z}, \hat{q}) \right\|_{L_{\hat{x}}}^2, \quad (2.64)$$

and then

$$\int_{\mathcal{B}} \left\| \mathbf{F}^h \mathbf{G}^{h\dagger}(\vec{z}, \hat{q}) - \mathbf{E}_{e,\infty}(\vec{z}, \hat{q}) \right\|_{L_{\hat{x}}}^2 d\vec{z} ds(\hat{q}) \leq \int_{\mathcal{B}} \left\| \mathbf{F}^h \mathbf{G}(\vec{z}, \hat{q}) - \mathbf{E}_{e,\infty}(\vec{z}, \hat{q}) \right\|_{L_{\hat{x}}}^2 d\vec{z} ds(\hat{q}). \quad (2.65)$$

It is now useful to observe that, by virtue of definition (2.56), for any $\mathbf{G}(\cdot) \in [L^2(\mathcal{B})]^{2L_{\hat{a}}}$ it holds that

$$\mathbf{F}^h \mathbf{G}(\vec{z}, \hat{q}) = [\mathbf{F}^h \mathbf{G}(\cdot)](\vec{z}, \hat{q}); \quad (2.66)$$

as a consequence, we can rewrite the previous inequality (2.65) as

$$\begin{aligned} \int_{\mathcal{B}} \left\| [\mathbf{F}^h \mathbf{G}^{h\dagger}(\cdot)](\vec{z}, \hat{q}) - \mathbf{E}_{e,\infty}(\vec{z}, \hat{q}) \right\|_{L_{\hat{x}}}^2 d\vec{z} ds(\hat{q}) &\leq \\ &\leq \int_{\mathcal{B}} \left\| [\mathbf{F}^h \mathbf{G}(\cdot)](\vec{z}, \hat{q}) - \mathbf{E}_{e,\infty}(\vec{z}, \hat{q}) \right\|_{L_{\hat{x}}}^2 d\vec{z} ds(\hat{q}), \end{aligned} \quad (2.67)$$

having denoted by $\mathbf{G}^{h\dagger}(\cdot)$ the element of $[L^2(\mathcal{B})]^{2L_{\hat{a}}}$ defined in (2.62) and simply obtained from $\mathbf{G}^{h\dagger}(\vec{z}, \hat{q})$ when the sampling pair (\vec{z}, \hat{q}) is regarded as a variable on \mathcal{B} . Recalling definition (2.55) and considering its analogous for $[L^2(\mathcal{B})]^{2L_{\hat{x}}}$, we can rewrite inequality (2.67) as

$$\left\| [\mathbf{F}^h \mathbf{G}^{h\dagger}(\cdot)](\cdot) - \mathbf{E}_{e,\infty}(\cdot) \right\|_{2,L_{\hat{x}}}^2 \leq \left\| [\mathbf{F}^h \mathbf{G}(\cdot)](\cdot) - \mathbf{E}_{e,\infty}(\cdot) \right\|_{2,L_{\hat{x}}}^2, \quad (2.68)$$

¹³See [4], pp. 151-153.

whence we immediately get

$$\mathbf{G}^{h\dagger}(\cdot) = \operatorname{argmin} \left\| [\mathbf{F}^h \mathbf{G}(\cdot)](\cdot) - \mathbf{E}_{e,\infty}(\cdot) \right\|_{2,L_{\hat{x}}}^2, \quad (2.69)$$

since inequality (2.68) holds for all $\mathbf{G}(\cdot)$ in $[L^2(\mathcal{B})]^{2L_{\hat{x}}}$.

Relation (2.69) states that $\mathbf{G}^{h\dagger}(\cdot)$ is a least-squares solution of equation (2.61); to show that its norm is minimum (and, consequently, that it is the generalized solution of (2.61)), we recall that $\mathbf{G}^{h\dagger}(\vec{z}, \hat{q}) \in \mathcal{N}(\mathbf{F}^h)^\perp$ for all (\vec{z}, \hat{q}) in \mathcal{B} : then, by virtue of statement iii) in Theorem 2.5.1, we find that $\mathbf{G}^{h\dagger}(\cdot) \in \mathcal{N}(\mathbf{F}^h)^\perp$. This concludes the proof. ■

The final step is now to fix the optimal value of the regularization parameter α , which, in expression (2.63), is still generic. This task can be accomplished by using the generalized discrepancy principle in the new functional context, i.e., by finding the zero of the new generalized discrepancy function

$$\rho(\alpha) = \left\| [\mathbf{F}^h \mathbf{G}_\alpha(\cdot)](\cdot) - \mathbf{E}_{e,\infty}(\cdot) \right\|_{2,L_{\hat{x}}}^2 - h^2 \|\mathbf{G}_\alpha(\cdot)\|_{2,L_{\hat{x}}}^2, \quad (2.70)$$

which, by virtue of (2.55), (2.58) and (2.63), can be written as

$$\rho(\alpha) = \sum_{p=0}^{r^h-1} \frac{\alpha^2 - h^2(\sigma_p^h)^2}{[\alpha + (\sigma_p^h)^2]^2} \int_{\mathcal{B}} \left| (\mathbf{E}_{e,\infty}(\vec{z}, \hat{q}), \mathbf{v}_p^h)_{L_{\hat{x}}} \right|^2 d\vec{z} ds(\hat{q}). \quad (2.71)$$

Remembering that $\mathcal{B} = T \times \Omega$ and exploiting the linearity of $\mathbf{E}_{e,\infty}(\vec{z}, \hat{q})$ with respect to \hat{q} (see (2.9), (2.24), (2.39)), it follows that¹⁴

$$\int_{\mathcal{B}} \left| (\mathbf{E}_{e,\infty}(\vec{z}, \hat{q}), \mathbf{v}_p^h)_{L_{\hat{x}}} \right|^2 d\vec{z} ds(\hat{q}) = \frac{4\pi}{3} \sum_{j=1}^3 \int_T \left| (\mathbf{E}_{e,\infty}(\vec{z}, \hat{e}_j), \mathbf{v}_p^h)_{L_{\hat{x}}} \right|^2 d\vec{z}, \quad (2.72)$$

where $\{\hat{e}_j : j = 1, 2, 3\}$ is the canonical basis of \mathbb{R}^3 . Now, taking into account the explicit expression of $\mathbf{E}_{e,\infty}(\vec{z}, \hat{q})$, as given by (2.9), (2.24) and (2.39), we can analytically compute the integral on T appearing in equality (2.72). To this end, for any $j \in \{1, 2, 3\}$ we introduce the complex vector $\mathbf{w}_j \in \mathbb{C}^{L_{\hat{x}}}$ whose $\ell_{\hat{x}}$ -th component, $\forall \ell_{\hat{x}} = 0, \dots, L_{\hat{x}} - 1$, is defined as

$$w_{j,\ell_{\hat{x}}} := v_{p,\ell_{\hat{x}}}^h \Delta s_{\ell_{\hat{x}}} [(\hat{x}_{\ell_{\hat{x}}} \times \hat{e}_j) \times \hat{x}_{\ell_{\hat{x}}}] \cdot \hat{\theta}(\hat{x}_{\ell_{\hat{x}}}) + v_{p,\ell_{\hat{x}}+L_{\hat{x}}}^h \Delta s_{\ell_{\hat{x}}} [(\hat{x}_{\ell_{\hat{x}}} \times \hat{e}_j) \times \hat{x}_{\ell_{\hat{x}}}] \cdot \hat{\varphi}(\hat{x}_{\ell_{\hat{x}}}), \quad (2.73)$$

where $v_{p,\ell_{\hat{x}}}^h$ is the $\ell_{\hat{x}}$ -th component of the singular vector $\mathbf{v}_p^h \in \mathbb{C}^{2L_{\hat{x}}}$, $\Delta s_{\ell_{\hat{x}}}$ is defined at the end of Remark 2.4.2 and $\hat{x}_{\ell_{\hat{x}}}$ is given by (2.29); then, after some computations, we find

$$\int_T \left| (\mathbf{E}_{e,\infty}(\vec{z}, \hat{e}_j), \mathbf{v}_p^h)_{L_{\hat{x}}} \right|^2 d\vec{z} = \mathbf{w}_j^T \mathbf{S} \bar{\mathbf{w}}_j, \quad (2.74)$$

¹⁴For details concerning the following relations (2.72)-(2.76), see [20], pp. 104-107.

where \mathbf{S} is the square real matrix of $L_{\hat{x}} \times L_{\hat{x}}$ elements defined as

$$\mathbf{S}_{\ell_{\hat{x}}^1 \ell_{\hat{x}}^2} := \frac{k^2}{2\pi^2} \prod_{j=1}^3 c_j \operatorname{sinc} \left[\frac{kc_j}{\pi} \left(\hat{x}_{\ell_{\hat{x}}^1} - \hat{x}_{\ell_{\hat{x}}^2} \right) \cdot \hat{e}_j \right] \quad \forall \ell_{\hat{x}}^1, \ell_{\hat{x}}^2 = 0, \dots, L_{\hat{x}} - 1. \quad (2.75)$$

We recall that in equality (2.75) the positive numbers c_j are the half-lengths of the sides of the parallelepiped $T = \prod_{j=1}^3 [-c_j, c_j]$ representing our domain of investigation. Hence, from equations (2.72) and (2.74) it follows that

$$\int_{\mathcal{B}} \left| (\mathbf{E}_{e,\infty}(\vec{z}, \hat{q}), \mathbf{v}_p^h)_{L_{\hat{x}}} \right|^2 d\vec{z} ds(\hat{q}) = \frac{4\pi}{3} \sum_{j=1}^3 \mathbf{w}_j^T \mathbf{S} \bar{\mathbf{w}}_j. \quad (2.76)$$

By inserting this result into (2.71), we obtain an explicit analytical expression for the generalized discrepancy $\rho(\alpha)$ (differently from [7], where a discretized version for the discrepancy is exploited). The analytical form for $\rho(\alpha)$ determined here allows a faster computation of its zero α^* , as well as an *a priori* estimate of an interval where α^* is to be found (an information that can be useful when the solution is numerically computed). Indeed, the integrals appearing in (2.71) are all non-negative: then (excluding the trivial case of an identically zero $\rho(\alpha)$), if $\alpha^* > 0$ verifies $\rho(\alpha^*) = 0$, it is easy to realize that there must exist two indices p_1 and p_2 , with $p_2 \geq p_1$, such that

$$\frac{(\alpha^*)^2 - h^2 (\sigma_{p_1}^h)^2}{[\alpha^* + (\sigma_{p_1}^h)^2]^2} \leq 0 \Leftrightarrow \alpha^* \leq h\sigma_{p_1}^h \quad \text{and} \quad \frac{(\alpha^*)^2 - h^2 (\sigma_{p_2}^h)^2}{[\alpha^* + (\sigma_{p_2}^h)^2]^2} \geq 0 \Leftrightarrow \alpha^* \geq h\sigma_{p_2}^h, \quad (2.77)$$

whence we have $\alpha^* \in [h\sigma_{p_2}^h, h\sigma_{p_1}^h]$. On the other hand, the inequalities $\sigma_{p_2}^h \geq \sigma_{r^h-1}^h$ and $\sigma_{p_1}^h \leq \sigma_0^h$ are clearly true: accordingly, we conclude that $\alpha^* \in [h\sigma_{r^h-1}^h, h\sigma_0^h]$.

By using the value α^* for the regularization parameter α in (2.63), we find the following representation for the optimal regularized solution of the functional problem (2.61):

$$\mathbf{G}_{\alpha^*}(\cdot) = \sum_{p=0}^{r^h-1} \frac{\sigma_p^h}{(\sigma_p^h)^2 + \alpha^*} (\mathbf{E}_{e,\infty}(\cdot), \mathbf{v}_p^h)_{L_{\hat{x}}} \mathbf{u}_p^h. \quad (2.78)$$

The most general indicator function we can now consider is $J(\Psi)$, where $J : [0, +\infty) \rightarrow \mathbb{R}$ is any appropriate monotonic function and

$$\begin{aligned} \Psi(\vec{z}) &:= \int_{\Omega} \|\mathbf{G}_{\alpha^*}(\vec{z}, \hat{q})\|_{L_{\hat{x}}}^2 ds(\hat{q}) = \\ &= \frac{4\pi}{3} \sum_{j=1}^3 \sum_{p=0}^{r^h-1} \frac{(\sigma_p^h)^2}{[(\sigma_p^h)^2 + \alpha^*]^2} \left| (\mathbf{E}_{e,\infty}(\vec{z}, \hat{e}_j), \mathbf{v}_p^h)_{L_{\hat{x}}} \right|^2 \quad \forall \vec{z} \in T. \end{aligned} \quad (2.79)$$

The analytic form (2.79) of Ψ , which represents the core of the indicator function, justifies the name ‘no-sampling’ for our approach: indeed, α^* does not depend on the sampling pair (\vec{z}, \hat{q}) , the term $\mathbf{E}_{e,\infty}(\vec{z}, \hat{e}_j)$ is analytically known and the singular system $\{\sigma_p^h, \mathbf{u}_p^h, \mathbf{v}_p^h\}_{p=0}^{r^h-1}$ of the operator \mathcal{F}^h is determined from the far-field patterns that have been measured. Moreover, as highlighted by (2.72) and (2.79), in our approach the three independent polarizations \hat{e}_j naturally play an equally important role in forming the indicator function: as a consequence, the heuristic procedure adopted in [46] to average the contributions of the three polarizations \hat{e}_j is automatically incorporated in the new rigorous formalism.

Of course, Theorem 2.5.2 now inspires a new implementation of the LSM, whereby the contour of the scatterer is detected by all points in which the indicator function $J(\Psi)$ becomes mostly large or small, depending on the choice of J .

2.6 Numerical applications

In this section we want to show that our no-sampling implementation yields visualizations that are very similar to those obtained by means of the traditional approach based on a sampling in the physical and polarization spaces, but in an extremely reduced amount of time and in a completely automatic fashion. In general, the 3D visualization of the scatterer is obtained by plotting the C -level surface of the indicator function $J(\Psi)$, i.e., the surface described by the Cartesian equation

$$J[\Psi(\vec{z})] = C, \quad \vec{z} \in T, \quad (2.80)$$

where $C \in [\min_{\vec{z} \in T} J[\Psi(\vec{z})], \max_{\vec{z} \in T} J[\Psi(\vec{z})]]$ is set to obtain the optimal visualization. Our aim is now to give a recipe to fix in an automatic way the C -level surface of $J(\Psi)$. An effective approach is the following three-step algorithm:

1. consider the 2D indicator function $J(\beta)$, where β is the 2D map

$$\beta : \mathbb{R}^2 \ni (u_1, u_2) \mapsto \Psi[\xi(u_1, u_2)] \in \mathbb{R} \quad (2.81)$$

and $\xi : \mathbb{R}^2 \ni (u_1, u_2) \mapsto (a_{11}u_1 + a_{12}u_2 + c_1, a_{21}u_1 + a_{22}u_2 + c_2, a_{31}u_1 + a_{32}u_2 + c_3) \in \mathbb{R}^3$ is the parametric equation of a plane in \mathbb{R}^3 containing a slice of the scatterer; such a plane can be found by using the (rather weak) *a priori* information on the scatterer suggesting where the scatterer is in the imaging volume¹⁵;

¹⁵Cf. footnote no. 6, p. 7.

2. apply an active-contour technique to $J(\beta)$ as in [6], i.e., among all (regular) plane curves described by a parametric equation of the form $\gamma : [0, 1] \rightarrow \mathbb{R}^2$, find a curve γ^* minimizing the energy functional

$$\mathcal{E}(\gamma) := \int_0^1 \left\{ \frac{1}{2} [w_1(s) \|\gamma'(s)\|_{\mathbb{R}^2} + w_2(s) \|\gamma''(s)\|_{\mathbb{R}^2}] + E_{ext}[\gamma(s)] \right\} ds, \quad (2.82)$$

where

$$E_{ext} := - \|\nabla J(\beta)\|_{\mathbb{R}^2}^2; \quad (2.83)$$

3. since active contours generate profiles that are close to level curves, the value of the indicator function on one of these profiles is almost constant. Therefore we choose

$$C := \int_0^1 J\{\Psi[\xi(\gamma^*(t))]\} dt, \quad (2.84)$$

i.e., the mean value of $J(\Psi)$ evaluated over the points of $\xi(\gamma^*)$.

The computation of the active contour in step no. 2 is accomplished as in [6, 40]. The external force in (2.83) can be determined by computing $\nabla J(\beta)$ numerically or analytically: in the former approach, starting from the knowledge of $J(\beta)$ on a prefixed grid of points, the gradient $\nabla J(\beta)$ is computed once for all on the same grid by means of finite differences and used (with interpolation) to deform the contours obtained at each iteration, while in the latter the knowledge of the analytical form of the indicator function $J(\Psi)$ allows computing the numerical value of $\nabla J(\beta)$ time by time on a finite number of points exactly belonging to the contours obtained at each iteration. We tested both procedures, but since the differences in the visualization quality are negligible, we shall illustrate only the results obtained when $\nabla J(\beta)$ is computed by means of finite differences: indeed, the latter procedure turns out to be faster, owing to the analytical form of $\nabla J(\beta)$, which is now more complicated than in the genuine 2D case discussed in [6].

Remark 2.6.1. In principle, the previous three-step algorithm can be implemented even for the traditional LSM: however, in this case the determination of C through (2.84) would require a notably greater computational effort. Indeed, in general, the 3D grid \mathcal{Z} of sampling points \vec{z} on which the indicator function $J(\Psi)$ is computed has nothing to do with the 2D grid \mathcal{G} used to implement the active-contour technique on a plane section of the scatterer: as a consequence, $J(\Psi)$ should be computed also on \mathcal{G} , then the final contour resulting from the edge-detection technique should be either deformed by interpolation and discretized on a proper number of points belonging to \mathcal{G} itself, or even discretized in an *ad hoc* set of points, on which $J(\Psi)$ should be computed separately. If

we now remember that in the traditional implementation of the LSM the regularization procedure needs to be repeated for each sampling pair (\vec{z}, \hat{q}) , we can easily understand that this approach is rather heavy from a computational viewpoint. \square

We now present and discuss three numerical experiments: in each one of them, the discretization described in Section 2.4 is adopted by using the same uniform 9×18 angular mesh on the unit sphere for both the observation and the incidence directions: more precisely, we choose the observation angles as

$$\theta_i^{\hat{x}} = \frac{\pi}{T_{\hat{x}}} \left(i + \frac{1}{2} \right) \quad \forall i = 0, \dots, T_{\hat{x}} - 1, \quad \text{with } T_{\hat{x}} = 9, \quad (2.85)$$

$$\varphi_j^{\hat{x}} = \frac{2\pi}{F_{\hat{x}}} j \quad \forall j = 0, \dots, F_{\hat{x}} - 1, \quad \text{with } F_{\hat{x}} = 18, \quad (2.86)$$

and the incidence angles as

$$\theta_i^{\hat{d}} = \frac{\pi}{T_{\hat{d}}} \left(i + \frac{1}{2} \right) \quad \forall i = 0, \dots, T_{\hat{d}} - 1, \quad \text{with } T_{\hat{d}} = 9, \quad (2.87)$$

$$\varphi_j^{\hat{d}} = \frac{2\pi}{F_{\hat{d}}} j \quad \forall j = 0, \dots, F_{\hat{d}} - 1, \quad \text{with } F_{\hat{d}} = 18. \quad (2.88)$$

The far-field patterns forming the matrix \mathbf{E}_{∞} defined in (2.40) are computed by using a code based on the method of moments [81]; each entry of \mathbf{E}_{∞} is then affected by 7% Gaussian noise. The scatterers are all isotropic and located in vacuum: this means that the index of refraction is given by [46]

$$N(\vec{x}) = n(\vec{x})I, \quad (2.89)$$

$$n(\vec{x}) = \frac{1}{\varepsilon_0} \left[\varepsilon_0 \varepsilon_r(\vec{x}) + i \frac{\sigma(\vec{x})}{\omega} \right], \quad (2.90)$$

where $i = \sqrt{-1}$, I is the 3×3 identity matrix, ε_0 is the dielectric constant in vacuum, $\varepsilon_r(\vec{x})$ and $\sigma(\vec{x})$ are the relative permittivity and the conductivity of the scatterer at the point \vec{x} , and finally $\omega = 2\pi\nu$ is the angular frequency. All no-sampling visualizations are realized by choosing $J(t) = t^{-1} \forall t \in \mathbb{R}^+ \cup \{0\}$ and taking as domain of investigation a cube of side 3 m, i.e., $T = [-1.5, 1.5]^3$. In all numerical tests, the forward scattering problem has been solved by using a method of moments code based on a stabilized biconjugated-gradient fast Fourier transform [90]. The computation domain has been discretized into cubical subdomains of side about $\lambda/20$, λ being the wavelength of the incident field in vacuum.

The first numerical example we consider is the visualization of the ‘U-shaped’ scatterer in Figure 5.1(a): this object is characterized by constant $\varepsilon_r = 1.8$ and $\sigma = 0.02 \text{ S/m}$.

The frequency used to perform this experiment is $\nu = 300$ MHz, corresponding to a wavelength $\lambda = 1.0$ m in vacuum. In order to determine the threshold value C in equation (2.80), we follow the previously described scheme. More precisely, if we refer \mathbb{R}^3 to the usual Cartesian coordinate system (x_1, x_2, x_3) , as shown in Figure 5.1(a), we restrict the indicator function $J(\Psi)$ to the plane of Cartesian equation $x_2 = 0$; an axial view of the 2D map visualizing this restriction is represented in Figure 5.1(b). Then, the active-contour technique is applied to the previous visualization map starting from a suitable initial guess (the white circle in Figure 5.1(b)), and the converging profile (also shown in Figure 5.1(b) as a black line) is used as the argument of the function $J\{\Psi[\xi(\cdot)]\}$ in equation (2.84). The resulting estimate of C is inserted into equation (2.80) and the corresponding visualization of the scatterer, represented in Figure 5.1(c), is obtained after 90.1 s of computational time with a 1.6 GHz CPU. In Figure 5.1(d) we show the visualization provided by the traditional implementation of the LSM (as explained in [46]) after 1590.1 s of computational time: in this case we have uniformly discretized the investigation domain T with a sampling grid \mathcal{Z} of $30 \times 30 \times 30$ points and combined the three indicator functions corresponding to the three independent polarizations $\hat{e}_1 = (1, 0, 0)$, $\hat{e}_2 = (0, 1, 0)$, $\hat{e}_3 = (0, 0, 1)$; different cut-off values C have been used until the ‘best visual reconstruction’, shown in Figure 5.1(d), has been obtained. The only difference with respect to [46] is that here, in order to make a consistent comparison with our no-sampling indicator function $J(\Psi) = 1/\Psi$, we choose

$$\Theta(\vec{z}) := \left[\frac{1}{3} \sum_{j=1}^3 \left\| \mathbf{G}_{\vec{z}, \hat{e}_j; \alpha^*(\vec{z}, \hat{e}_j)} \right\|_{L_{\hat{d}}}^2 \right]^{-1} \quad \forall \vec{z} \in \mathcal{Z} \quad (2.91)$$

as sampled indicator function, instead of

$$\Theta(\vec{z}) := \frac{1}{3} \sum_{j=1}^3 \left\| \mathbf{G}_{\vec{z}, \hat{e}_j; \alpha^*(\vec{z}, \hat{e}_j)} \right\|_{L_{\hat{d}}}^{-1} \quad \forall \vec{z} \in \mathcal{Z}, \quad (2.92)$$

where $\left\| \mathbf{G}_{\vec{z}, \hat{e}_j; \alpha^*(\vec{z}, \hat{e}_j)} \right\|_{L_{\hat{d}}}^2$ is given by (2.52) for each $j \in \{1, 2, 3\}$.

The following three considerations must be accounted for:

- all the input parameters in the active-contour algorithm are optimally fixed by choosing them in the ranges that, according to the theory, assure the convergence of the iteration [40];
- the visualization in Figure 5.1(c) provided by the no-sampling formulation coupled with deformable models is less accurate than the visualization in Figure 5.1(d) provided by linear sampling coupled with a heuristic choice of the threshold value C

based on a visual comparison with the true scatterer (supposed known). However, as many numerical tests proved, this difference in accuracy is not due to no-sampling but to a non-optimal performance of the edge-detection technique employed: indeed, applying heuristic thresholding to no-sampling would lead to visualizations that are essentially identical to those provided by traditional linear sampling. As an example, we show in Figure 5.2(b) the result obtained, in the no-sampling framework, by choosing for C the best visual value: a comparison with Figure 5.2(a), which is provided by the usual sampling algorithm and reproduces exactly Figure 5.1(d) for the reader's convenience, can hardly highlight any difference between the two visualizations;

- in the overall computational time of the no-sampling implementation, most of the time (around 80 s) is spent for the edge-detection procedure in Figure 5.1(b) and for the visualization process, while the determination of the unique regularization parameter only takes around 2 s. On the contrary, in the sampling formulation most of the time is devoted to the construction of the indicator function.

The second test is concerned with the non-connected scatterer in Figure 5.3(a), characterized by constant $\varepsilon_r = 2.0$ and $\sigma = 0.0 \text{ S/m}$ for both the U-forms and the sphere in between. The frequency chosen for this experiment is $\nu = 286 \text{ MHz}$, corresponding to a wavelength $\lambda = 1.05 \text{ m}$ in vacuum. The scatterer is first cut by the plane in \mathbb{R}^3 of Cartesian equation $x_2 = 0.9$ and the usual deformable model is applied to the corresponding visualization shown in Figure 5.3(b) together with the initial guess (white ellipse) and the reconstructed profile (black contour). The cut-off value C is then computed by means of equation (2.84) and the resulting surface (2.80) is plotted in Figure 5.3(c). In Figure 5.3(d) we show the result obtained by using the traditional LSM with the same choices for the parameters and the indicator function and the same heuristic procedure for estimating C as in the previous numerical experiment. The computational times for both visualizations are around the same ones as for the corresponding visualizations in Figure 5.1.

Finally, the third numerical experiment is performed by using the non-connected scatterer in Figure 5.4(a) at a frequency $\nu = 300 \text{ MHz}$: the parallelepiped on the left is centred at $(-0.75, 0, 0)$ and characterized by constant $\varepsilon_r = 2.1$ and $\sigma = 0.0 \text{ S/m}$, while that on the right is centred at $(0.75, 0, 0)$ and characterized by constant $\varepsilon_r = 1.5$ and $\sigma = 0.0 \text{ S/m}$. In this case we only adopt the no-sampling approach, but with three different strategies. In the first strategy, the scatterer is cut by the plane $x_1 = -0.75$ and the threshold C is determined as usual to obtain the visualization in Figure 5.4(b). In the second strategy,

we use the plane $x_1 = 0.75$, which provides the visualization in Figure 5.4(c). Finally, if we split the domain of investigation T into $T_a := [-1.5, 0] \times [-1.5, 1.5] \times [-1.5, 1.5]$ and $T_b := [0, 1.5] \times [-1.5, 1.5] \times [-1.5, 1.5]$, intersect T_a with $x_1 = -0.75$, T_b with $x_1 = 0.75$ and use the two corresponding threshold values to visualize the two objects with different ε_r , we obtain the visualization shown in Figure 5.4(d): this last procedure allows better preserving the original size of the two objects in the non-connected scatterer.

Remark 2.6.2. We proved in Section 2.5 (cf. inequalities (2.77)) that the unique value α^* of the regularization parameter in the no-sampling implementation must lay in the interval $[h\sigma_{r^h-1}^h, h\sigma_0^h]$. By elaborating the expression (2.50) of the discrepancy, as occurs in the traditional implementation of the LSM, and by using the same arguments as in (2.77), it is easy to prove that also each one of the many optimal values $\alpha^*(\vec{z}, \hat{q})$ of the regularization parameter must belong to the same interval. However, in our experience, for each numerical experiment, α^* is always in the interval $[\alpha_{\min}^*, \alpha_{\max}^*]$, where α_{\min}^* and α_{\max}^* are respectively the minimum and the maximum optimal regularization parameters obtained in the traditional implementation: in particular, as far as the examples in the current section are concerned, these values are shown in Table 5.1. The fact that $\alpha^* \in [\alpha_{\min}^*, \alpha_{\max}^*]$ is reasonable, since α^* can be intuitively regarded as a sort of average of all the values $\alpha^*(\vec{z}, \hat{q})$. \square

2.7 First-order discretization

In general, the positions of the emitting antennas on the unit sphere may be chosen in such a way that the rectangular mesh used in Section 2.4 to discretize the integral (2.10) on the unit sphere (cf. Remark 2.4.1) is neither the easiest, nor the most convenient way of ordering these positions. On the contrary, given a generic set of points on the unit sphere, the simplest approach is to create a mesh of plane triangles, whose vertices are the points themselves: this can be done automatically, by implementing a Delaunay-type algorithm [66] for triangular mesh generation. Moreover, triangular meshes naturally inspire a first-order discretization, whereby the integrand function on each triangle is approximated linearly, rather than by a constant value. Let us focus on this point in detail.

Let $A_1, B_1, C_1 \in \mathbb{R}^3$ be the three vertices of a triangle and let $T_1 \subset \mathbb{R}^3$, with $|T_1| := \text{mis}(T_1) > 0$, be the plane and closed region delimited by its three sides A_1B_1 , A_1C_1 and B_1C_1 . Moreover, let $f : T_1 \rightarrow \mathbb{R}$ be a continuous function: we are interested in determining a numerical approximation of the integral $\int_{T_1} f d\sigma$ by adopting a linear interpolation of f over T_1 and using only the values $f(A_1)$, $f(B_1)$, $f(C_1)$ that f takes on the three vertices

A_1, B_1, C_1 . To this end, we observe that, since $|T_1| > 0$, the two vectors $\overrightarrow{C_1A_1}$ and $\overrightarrow{C_1B_1}$ are linearly independent and span the plane containing T_1 . Then, by using a Cartesian coordinate system (x_1, x_2, x_3) in \mathbb{R}^3 and setting $A_1 = (x_1^{A_1}, x_2^{A_1}, x_3^{A_1})$, $B_1 = (x_1^{B_1}, x_2^{B_1}, x_3^{B_1})$, $C_1 = (x_1^{C_1}, x_2^{C_1}, x_3^{C_1})$, we can describe the plane region T_1 by means of the following parametric representation $\tilde{T}_1 : E_1 \rightarrow \mathbb{R}^3$, with $E_1 := \{(s, t) \in \mathbb{R}^2 : 0 \leq s \leq 1 - t, 0 \leq t \leq 1\}$:

$$\tilde{T}_1 : \begin{cases} x_1(s, t) = (x_1^{A_1} - x_1^{C_1})s + (x_1^{B_1} - x_1^{C_1})t + x_1^{C_1} \\ x_2(s, t) = (x_2^{A_1} - x_2^{C_1})s + (x_2^{B_1} - x_2^{C_1})t + x_2^{C_1} \\ x_3(s, t) = (x_3^{A_1} - x_3^{C_1})s + (x_3^{B_1} - x_3^{C_1})t + x_3^{C_1} \end{cases} \quad \text{for } (s, t) \in E_1. \quad (2.93)$$

Indeed, for a fixed value $t_0 \in [0, 1]$ of t , the map $\tilde{T}_1|_{t=t_0} : [0, 1 - t_0] \rightarrow \mathbb{R}^3$ is the parametric representation of a segment that is parallel to $\overrightarrow{C_1A_1}$ and connects a point of $\overrightarrow{C_1B_1}$ to a point of $\overrightarrow{A_1B_1}$, since

$$\tilde{T}_1(0, t_0) = ((x_1^{B_1} - x_1^{C_1})t_0 + x_1^{C_1}, (x_2^{B_1} - x_2^{C_1})t_0 + x_2^{C_1}, (x_3^{B_1} - x_3^{C_1})t_0 + x_3^{C_1}) \in \overrightarrow{C_1B_1}, \quad (2.94)$$

and

$$\tilde{T}_1(1 - t_0, t_0) = ((x_1^{B_1} - x_1^{A_1})t_0 + x_1^{A_1}, (x_2^{B_1} - x_2^{A_1})t_0 + x_2^{A_1}, (x_3^{B_1} - x_3^{A_1})t_0 + x_3^{A_1}) \in \overrightarrow{A_1B_1}. \quad (2.95)$$

Moreover, it is clear that as t_0 varies in $[0, 1]$, the point $\tilde{T}_1(0, t_0)$ spans the whole segment $\overrightarrow{C_1B_1}$: this suffices to conclude that \tilde{T}_1 is a parametric representation of T_1 .

Now, let $f_1 : T_1 \rightarrow \mathbb{R}$ be the linear function we want to use as a first-order approximation of f , in order to estimate $\int_{T_1} f d\sigma$: since the parametric representation (2.93) of T_1 is also linear¹⁶, the composite function $\tilde{f}_1 := f_1 \circ \tilde{T}_1 : E_1 \rightarrow \mathbb{R}$ is linear too, i.e., of the form

$$\tilde{f}_1(s, t) = a_1s + a_2t + a_3. \quad (2.96)$$

The three unknown coefficients a_1, a_2 and a_3 can be easily determined by imposing that f_1 and f take the same values on the three vertices A_1, B_1 and C_1 , i.e.,

$$f_1(A_1) = f(A_1), \quad f_1(B_1) = f(B_1), \quad f_1(C_1) = f(C_1). \quad (2.97)$$

By noting that $A_1 = \tilde{T}_1(1, 0)$, $B_1 = \tilde{T}_1(0, 1)$ and $C_1 = \tilde{T}_1(0, 0)$, conditions (2.97) can be substituted into (2.96) to obtain

$$a_1 + a_3 = f(A_1), \quad a_2 + a_3 = f(B_1), \quad a_3 = f(C_1), \quad (2.98)$$

¹⁶With a slight abuse of language, here we call ‘linear’ maps that are actually affine, owing to the presence of a known term, such as a_3 in (2.96).

i.e.,

$$a_1 = f(A_1) - f(C_1), \quad a_2 = f(B_1) - f(C_1), \quad a_3 = f(C_1). \quad (2.99)$$

Hence, according to our first-order approximation, we can write

$$\begin{aligned} \int_{T_1} f d\sigma &\approx \int_{T_1} f_1 d\sigma = \int_{E_1} \tilde{f}_1(s, t) \left| \frac{\partial \tilde{T}_1}{\partial s}(s, t) \wedge \frac{\partial \tilde{T}_1}{\partial t}(s, t) \right| ds dt = \\ &= \int_0^1 dt \int_0^{1-t} (a_1 s + a_2 t + a_3) \left| \overrightarrow{C_1 A_1} \wedge \overrightarrow{C_1 B_1} \right| ds = \\ &= 2|T_1| \int_0^1 \left[a_1 \frac{s^2}{2} + a_2 t s + a_3 s \right]_{s=0}^{1-t} dt = \\ &= |T_1| \frac{a_1 + a_2 + 3a_3}{3}, \end{aligned} \quad (2.100)$$

having observed that $\left| \overrightarrow{C_1 A_1} \wedge \overrightarrow{C_1 B_1} \right|$ is twice the area $|T_1|$ of the triangle T_1 . If we now substitute relations (2.99) into (2.100), we find the desired result:

$$\int_{T_1} f d\sigma \approx \frac{|T_1|}{3} [f(A_1) + f(B_1) + f(C_1)]. \quad (2.101)$$

We can now make a further step and consider, more generally, a regular surface S approximated by a triangular mesh formed by L triangles T_j , with $j = 1, \dots, L$. If we denote by A_j , B_j and C_j the three vertices of the triangle T_j , we can easily generalize the approach described above to find

$$\int_S f d\sigma \approx \sum_{j=1}^L \int_{T_j} f_j = \sum_{j=1}^L \frac{|T_j|}{3} [f(A_j) + f(B_j) + f(C_j)]. \quad (2.102)$$

An alternative version of (2.102) can be obtained by summing over the vertices, rather than over the triangles, as described in the following. First, we note that each point A_j , B_j and C_j is, in general, a vertex of more than one triangle: e.g., it can hold $A_2 = B_1$, $C_1 = B_3$, and so on. Then, the distinct vertices on the mesh are less than $3 \times L$, say N . In order to avoid repetitions, let us denote by P_1, \dots, P_N these distinct vertices and, for each point P_n , let us define the index set

$$J_n := \{j \in \{1, \dots, L\} : P_n \in T_j\} \quad \forall n = 1, \dots, N. \quad (2.103)$$

The set J_n clearly identifies all the triangles having P_n as one of their vertices. Hence, if we introduce the weights¹⁷

$$\omega_n := \frac{1}{3} \sum_{j \in J_n} |T_j| \quad \forall n = 1, \dots, N, \quad (2.104)$$

¹⁷Cf. relation (50) p. 861 in [36].

we can rearrange the sum in (2.102) as

$$\int_S f d\sigma \approx \sum_{n=1}^N \omega_n f(P_n). \quad (2.105)$$

We now have all the ingredients to come back to the far-field equation (2.11) and its first-order discretization. The integral on the left-hand side of (2.11) is made over the unit sphere Ω , and the vertices of the triangular mesh approximating Ω are identified by the incidence unit vectors $\hat{d}_{\ell_{\hat{d}}}$, with $\ell_{\hat{d}} = 0, \dots, L_{\hat{d}} - 1$. Notably, the sums in equations (2.33) and (2.34), which follow from our previous zero-order discretization of the integral on Ω in (2.11), are performed just on the incidence directions $\hat{d}_{\ell_{\hat{d}}}$, in the same spirit as in (2.105). Therefore, the new and first-order discretized far-field equation is obtained from (2.33) and (2.34) by simply replacing the weights $\Delta s_{\ell_{\hat{d}}}$, defined in (2.35), with the new ones $\omega_{\ell_{\hat{d}}}$, defined as in (2.104) (with the index n replaced by $\ell_{\hat{d}}$). The final result is then

$$\sum_{\ell_{\hat{d}}=0}^{L_{\hat{d}}-1} \left[g_{\vec{z}, \hat{q}}^{\theta}(\hat{d}_{\ell_{\hat{d}}}) E_{\infty}^{\theta\theta}(\hat{x}_{\ell_{\hat{x}}}; \hat{d}_{\ell_{\hat{d}}}) + g_{\vec{z}, \hat{q}}^{\varphi}(\hat{d}_{\ell_{\hat{d}}}) E_{\infty}^{\theta\varphi}(\hat{x}_{\ell_{\hat{x}}}; \hat{d}_{\ell_{\hat{d}}}) \right] \omega_{\ell_{\hat{d}}} = E_{e, \infty}^{\theta}(\hat{x}_{\ell_{\hat{x}}}; \vec{z}, \hat{q}), \quad (2.106)$$

$$\sum_{\ell_{\hat{d}}=0}^{L_{\hat{d}}-1} \left[g_{\vec{z}, \hat{q}}^{\theta}(\hat{d}_{\ell_{\hat{d}}}) E_{\infty}^{\varphi\theta}(\hat{x}_{\ell_{\hat{x}}}; \hat{d}_{\ell_{\hat{d}}}) + g_{\vec{z}, \hat{q}}^{\varphi}(\hat{d}_{\ell_{\hat{d}}}) E_{\infty}^{\varphi\varphi}(\hat{x}_{\ell_{\hat{x}}}; \hat{d}_{\ell_{\hat{d}}}) \right] \omega_{\ell_{\hat{d}}} = E_{e, \infty}^{\varphi}(\hat{x}_{\ell_{\hat{x}}}; \vec{z}, \hat{q}). \quad (2.107)$$

Hence, from an implementation viewpoint, the only difference between the zero-order and the first-order discretization of the far-field equation consists in the weights defining the scalar product on $\mathbb{C}^{2L_{\hat{d}}}$ (cf. Remark 2.4.2): instead of $\Delta s_{\ell_{\hat{d}}}$, we now have $\omega_{\ell_{\hat{d}}}$. In particular, this means that the computational times of the regularization procedure will be the same in both cases.

As regards the scalar product on $\mathbb{C}^{2L_{\hat{x}}}$, it depends on how we order the observation directions $\hat{x}_{\ell_{\hat{x}}}$: we can either maintain the rectangular mesh of Section 2.4 and the corresponding weights $\Delta s_{\ell_{\hat{x}}}$, or adopt a triangular mesh and use the new weights $\omega_{\ell_{\hat{x}}}$, defined analogously to $\omega_{\ell_{\hat{d}}}$. Of course, different scalar products induce different norms (cf. e.g. definition (2.55)), and this can in principle affect, for instance, the choice of the optimal value α^* of the regularization parameter, since the generalized discrepancy (2.70) is defined in terms of such norms.

It is now interesting to test our no-sampling formulation of the LSM by using the first-order discretized far-field equation given by (2.106), (2.107). As a first example, we consider again the non-connected scatterer of Figure 5.3(a) (reproduced in Figure 5.5(a)) in the same physical conditions: however, the set of incidence directions, coincident with the set of observation directions, is now chosen so to form a non-uniform triangular mesh

with 146 vertices, shown in Figure 5.5(b). The visualization provided by the no-sampling LSM, plotted in Figure 5.5(c), is obtained in less than 30 s by the same procedure described in Section 2.6: in particular, only around 1 s is taken by the regularization algorithm, while the remaining time is due to the edge-detection algorithm and the visualization process¹⁸. No significant difference can be noticed between the two visualizations shown in Figure 5.3(c) and in Figure 5.5(c).

The second example is concerned with the visualization of the perfectly conducting scatterer shown in Figure 5.6(a) and contained in a parallelepiped $T = [-0.4, 0.4] \times [-0.4, 0.4] \times [-0.2, 0.4]$. The direct far-field data, computed by using CESC solver¹⁹, are just those used in [46]; moreover we corrupt each value by 7% Gaussian noise. The wave number is $k = 56 \text{ m}^{-1}$ and the 252 incidence/observation directions are uniformly distributed on the unit sphere as shown in the triangular mesh of Figure 5.6(b). In order to determine the threshold value C for the indicator function, we follow the scheme described in Section 2.6. More precisely, referring \mathbb{R}^3 to the usual Cartesian coordinate system (x_1, x_2, x_3) , we restrict the indicator function $1/\Psi$ to the plane of Cartesian equation $x_3 = 0.05$ and fix the value C by applying an active-contour technique to this restricted visualization map. The corresponding C -level surface of $1/\Psi$ provides the visualization of the scatterer, which is shown in Figure 5.6(c). The regularization algorithm is performed in around 10 s, while the overall visualization procedure is completed in less than 3 minutes.

2.8 Conclusions and hints for future developments

In the present chapter we have introduced a no-sampling version of the LSM for 3D electromagnetic inverse scattering problems. According to this approach, the indicator function is analytically known, which allows a fast and essentially automatic visualization of the scatterers from the knowledge of their far-field patterns.

We can now make some comments and suggestions for future work.

1) *About the post-processing of the LSM by edge-detection algorithms.* It is certainly

¹⁸We cannot assure that the PC (a common laptop in any case) used for the two experiments of this section is the same as that used for the simulations of the previous section, so any comparison in computational times might be improper. However, it is worth noting that the regularization algorithm is always very fast: around 2 s in Section 2.6, with 9×18 incidence/observation angles, and around 1 s here, with 146 angles. The edge-detection and visualization procedure is rather faster in this experiment (less than 30 s) than in the analogous experiment of Section 2.6 (around 80 s), but this may also depend on a different thickness of the visualization grid.

¹⁹Prof. Housseem Haddar is gratefully acknowledged for having provided these data.

possible to consider scatterers that are much more complex than those chosen here to illustrate the advantages of the no-sampling formulation of the LSM: for example, we could consider anisotropic, inhomogeneous and non-connected scatterers, with connected components that are very close to each other (with respect to the wavelength λ) and, consequently, hard to separate in the visualization. In these more difficult cases, the most suitable approach for post-processing the indicator function is probably an iterative procedure based on level sets (see [84] and references therein): indeed, level sets can easily detect non-connected objects starting from a connected initial guess, since their formulation (unlike the active-contour technique used in this chapter) enables an automatic splitting of the profiles obtained during the iterations; moreover, the final result provided by such a procedure does not need to be a level surface of the indicator function, thus allowing a further degree of freedom that can be useful to improve the visualization quality²⁰. Implementing a level-set-based technique for a post-processing of the no-sampling LSM is beyond the purposes of this chapter; however, we point out that, in principle, the analytical knowledge of the indicator function can be very useful also for such a technique.

2) *About the ‘hybridization’ of the LSM with reconstruction methods.* In many applications, the information content provided by the mere visualization of the scatterer may be too poor, and a pointwise reconstruction of its material parameters may be necessary or desirable. In this case, an iterative reconstruction algorithm should be used: however, the visualization of the scatterer, as obtained by post-processing the LSM via edge-detection techniques, can be very useful to properly initialize the algorithm itself, thus reducing the risk that the latter converges to false solutions. Examples of this ‘hybrid’ approach (in the sense that a qualitative method is used to initialize a quantitative one) can be found in [22, 23, 25, 28, 29]. Of course, the need for short computational times pertains not only to the LSM and its post-processing, but also to the last step, i.e., the reconstruction procedure, which is typically the most expensive: anyway, some recent multiscale algorithms [57] can provide their final output in short or reasonable computational times.

3) *About the optimal number of emitters and receivers.* For any qualitative method, an interesting open issue is concerned with its optimal implementation, i.e., an implementation allowing the best visualization quality with the minimum amount of data. The simplest possible explanation of this problem is the following. In the LSM, $L_{\hat{d}}$ different directions are chosen for the incident plane wave and, for each incidence direction, the far-field pattern of the field scattered by the target is measured in $L_{\hat{x}}$ different observation

²⁰This can be important in cases where a level surface of the indicator function can hardly capture all the information needed for a good visualization (e.g., strongly inhomogeneous and/or non-connected scatterers: cf. the third numerical example of Section 2.6, soon before Remark 2.6.2).

directions, so that the total number of measurements is $S := L_{\hat{d}} \times L_{\hat{x}}$. Of course, if S is too small, no satisfactory visualization of the unknown scatterer can be achieved; on the other hand, intuition suggests (and numerical experiments confirm) that increasing S can improve the visualization quality only up to an optimal value S_o , above which no further improvement is obtained. In principle, S_o depends at least on the maximum linear dimension M of the scatterer, on the incident wavelength λ and on the intensity n of the noise affecting the measurement procedures. If we consider that any $S > S_o$ uselessly increases both the duration of the process of data acquisition²¹ and the computational time required by the regularization algorithm to invert the data themselves, it proves interesting to find a criterion allowing an assessment of S_o in terms of an *a priori* knowledge or estimate of M , λ and n . To this end, a good starting point could consist in performing an appropriate number of numerical simulations in various scattering conditions and trying to link the S_o experimentally determined with the number N of degrees of freedom [30] of a scattered field under the same scattering conditions: some examples of such an approach can be found in [37]. However, for any incident wave, N is the minimum number of probes that are necessary to collect *all* the information transported by the scattered field. On the other hand, the LSM, as well as any other qualitative method, only exploits the information concerning the *geometry* of the scatterer, and neglects the information about its *physical properties*. Then, in the framework of qualitative methods, it would be very interesting to investigate the possibility of splitting these two kinds of information and to distinguish between a ‘geometric’ and a ‘physical’ number of degrees of freedom: of course, only the former should be related to the optimal number S_o of probes to be used. In any case, reasoning in terms of N can provide an upper bound for S_o ; moreover, if the same scattering data are to be used at a later stage for a reconstruction algorithm, the whole information content carried by the field needs to be collected, and then the number of probes expressed in terms of N becomes optimal.

2.9 Addendum to Chapter 2

Let M and N be two positive integers; let the $M \times M$ matrix $\Delta \mathbf{S}_M$ and the $N \times N$ matrix $\Delta \mathbf{S}_N$ be diagonal and positive-definite; let the vector spaces \mathbb{C}^M and \mathbb{C}^N be equipped with the scalar products $(\cdot, \cdot)_{\Delta \mathbf{S}_M}$ and $(\cdot, \cdot)_{\Delta \mathbf{S}_N}$ described by $\Delta \mathbf{S}_M$ and $\Delta \mathbf{S}_N$ respectively, i.e.,

$$(\mathbf{x}_1, \mathbf{x}_2)_{\Delta \mathbf{S}_M} := \mathbf{x}_1^T \Delta \mathbf{S}_M \bar{\mathbf{x}}_2, \quad (\mathbf{y}_1, \mathbf{y}_2)_{\Delta \mathbf{S}_N} := \mathbf{y}_1^T \Delta \mathbf{S}_N \bar{\mathbf{y}}_2, \quad (2.108)$$

²¹This is a crucial issue for 3D real scattering experiments: see e.g. [60].

where $\mathbf{x}_1, \mathbf{x}_2 \in \mathbb{C}^M$ and $\mathbf{y}_1, \mathbf{y}_2 \in \mathbb{C}^N$ are generic column vectors. Let the linear operator $\mathcal{T} : (\mathbb{C}^M, (\cdot, \cdot)_{\Delta \mathbf{S}_M}) \rightarrow (\mathbb{C}^N, (\cdot, \cdot)_{\Delta \mathbf{S}_N})$ be represented by the $N \times M$ matrix \mathbf{T} . We denote by $(\Sigma, \mathbf{U}, \mathbf{V})$ the singular system of \mathcal{T} , such that

$$\mathbf{T}\mathbf{U} = \mathbf{V}\Sigma, \quad \mathbf{T}^* \mathbf{V} = \mathbf{U}\Sigma, \quad (2.109)$$

with the orthonormality properties

$$\mathbf{U}^T \Delta \mathbf{S}_M \bar{\mathbf{U}} = \mathbf{I}_r, \quad \mathbf{V}^T \Delta \mathbf{S}_N \bar{\mathbf{V}} = \mathbf{I}_r, \quad (2.110)$$

where \mathbf{I}_r is the $r \times r$ identity matrix, r is the rank of \mathbf{T} and \mathbf{T}^* is the matrix representing the adjoint operator \mathcal{T}^* . Then the following theorem holds.

Theorem 2.9.1. *Let $(\tilde{\Sigma}, \tilde{\mathbf{U}}, \tilde{\mathbf{V}})$ be the singular system of the matrix*

$$\tilde{\mathbf{T}} := (\Delta \mathbf{S}_N)^{\frac{1}{2}} \mathbf{T} (\Delta \mathbf{S}_M)^{-\frac{1}{2}}. \quad (2.111)$$

Then the triple $(\Sigma, \mathbf{U}, \mathbf{V})$ defined by

$$\Sigma := \tilde{\Sigma}, \quad \mathbf{U} := (\Delta \mathbf{S}_M)^{-\frac{1}{2}} \tilde{\mathbf{U}}, \quad \mathbf{V} := (\Delta \mathbf{S}_N)^{-\frac{1}{2}} \tilde{\mathbf{V}} \quad (2.112)$$

is the singular system of the operator \mathcal{T} .

Proof. The fact that $(\tilde{\Sigma}, \tilde{\mathbf{U}}, \tilde{\mathbf{V}})$ is the singular system of the matrix $\tilde{\mathbf{T}}$ defined in (2.111) means that

$$\tilde{\mathbf{T}}\tilde{\mathbf{U}} = \tilde{\mathbf{V}}\tilde{\Sigma}, \quad \tilde{\mathbf{T}}^T \tilde{\mathbf{V}} = \tilde{\mathbf{U}}\tilde{\Sigma}, \quad (2.113)$$

with the orthonormality properties

$$\tilde{\mathbf{U}}^T \tilde{\mathbf{U}} = \mathbf{I}_r, \quad \tilde{\mathbf{V}}^T \tilde{\mathbf{V}} = \mathbf{I}_r. \quad (2.114)$$

Now, by virtue of (2.111), (2.112), (2.113), we have

$$\begin{aligned} \mathbf{T}\mathbf{U} - \mathbf{V}\Sigma &= \mathbf{T} (\Delta \mathbf{S}_M)^{-\frac{1}{2}} \tilde{\mathbf{U}} - (\Delta \mathbf{S}_N)^{-\frac{1}{2}} \tilde{\mathbf{V}}\tilde{\Sigma} = \\ &= (\Delta \mathbf{S}_N)^{-\frac{1}{2}} \left[(\Delta \mathbf{S}_N)^{\frac{1}{2}} \mathbf{T} (\Delta \mathbf{S}_M)^{-\frac{1}{2}} \tilde{\mathbf{U}} - \tilde{\mathbf{V}}\tilde{\Sigma} \right] = \\ &= (\Delta \mathbf{S}_N)^{-\frac{1}{2}} \left[\tilde{\mathbf{T}}\tilde{\mathbf{U}} - \tilde{\mathbf{V}}\tilde{\Sigma} \right] = \mathbf{0}, \end{aligned} \quad (2.115)$$

so that the first of relations (2.109) is satisfied. Recalling now (2.108), we have:

$$(\mathbf{T}^* \mathbf{y}, \mathbf{x})_{\Delta \mathbf{S}_M} = (\mathbf{T}^* \mathbf{y})^T \Delta \mathbf{S}_M \bar{\mathbf{x}} = \mathbf{y}^T (\mathbf{T}^*)^T \Delta \mathbf{S}_M \bar{\mathbf{x}} \quad (2.116)$$

and

$$(\mathbf{y}, \mathbf{T}\mathbf{x})_{\Delta\mathbf{S}_N} = \mathbf{y}^T \Delta\mathbf{S}_N \overline{(\mathbf{T}\mathbf{x})} = \mathbf{y}^T \Delta\mathbf{S}_N \overline{\mathbf{T}\mathbf{x}}. \quad (2.117)$$

By comparing (2.116) with (2.117), we find:

$$(\mathbf{T}^*)^T \Delta\mathbf{S}_M = \Delta\mathbf{S}_N \overline{\mathbf{T}} \Rightarrow (\mathbf{T}^*)^T = \Delta\mathbf{S}_N \overline{\mathbf{T}} \Delta\mathbf{S}_M^{-1}, \quad (2.118)$$

and then

$$\mathbf{T}^* = \Delta\mathbf{S}_M^{-1} \overline{\mathbf{T}}^T \Delta\mathbf{S}_N. \quad (2.119)$$

A computation analogous to (2.115) now shows that $\mathbf{T}^* \mathbf{V} - \mathbf{U}\Sigma = \mathbf{0}$, i.e., also the second of relations (2.109) is satisfied. Finally, the orthonormality properties (2.110) are immediately proved by taking into account the analogous properties (2.114) and definitions (2.112). ■

Chapter 3

The RGF_M for breast cancer detection

3.1 State of the art in breast cancer detection

Nowadays, the prospective existence of tumoural masses in the female breast is usually investigated by means of X-ray mammography: this approach relies on the possibility of detecting portions of biological tissues whose density¹ is different from that of the background surrounding them. Such imaging technique can be adopted for both diagnostic purposes (i.e., to investigate the origin of dubious changes occurring in the patient's breast, like pain or lumps) and screening plans (i.e., to detect breast cancer before any symptom is developed or any clinical sign is noticed).

However, the approach just outlined suffers from some drawbacks, which are among the main reasons for the persistence of the disease itself. In particular:

- (1) X-rays are ionizing radiations, which entails a degree of invasiveness potentially harmful to the patient's health and, consequently, limits the frequency of this kind of check-up;
- (2) producing X-rays for medical purposes requires physical devices that are rather big, heavy and expensive, so they can be neither bought by all hospitals, nor easily transported: this hampers the spread of screening plans even in the European Union²;

¹See e.g. [15], p. 195.

²At the end of the year 2006, nationwide mammographic screening was available in eleven Member States only: see e.g. the *European Parliament resolution on breast cancer in the enlarged European*

- (3) the reliability of X-ray tests is limited by the fact that the density of the tumoural masses in the female breast does not differ very much from that of the healthy tissue surrounding them. Such a low physical contrast in density gives rise to possibly faulty results, which can then be either false-positive [58] (i.e., the tumour does not exist, but it is detected) or false-negative³ [67] (i.e., the tumour exists, but it is not detected).

In the framework of the techniques currently available, a certain number of improved and/or comparative approaches, also involving magnetic resonance imaging (MRI) for high risk women, have been conceived in order to enable radiologists to detect breast cancer more accurately and at an earlier stage. However, to this end, also some completely different methods have been proposed: they belong to a family of alternative and, so far, prototypal tomographies, like electrical impedance [19, 39], optical [12], ultrasound [80] and microwave⁴ tomography [31, 32, 68, 85], whose common feature, unlike X-ray tomography or nuclear magnetic resonance, is the non-linear link between the measured data and the physical quantities to be reconstructed.

In particular, using microwaves [3] to detect breast cancer seems to be a promising complementary technique to X-rays, for at least three reasons:

- (1') microwaves are negligibly invasive (i.e., essentially harmless);
- (2') producing and measuring low power microwaves for medical applications requires physical devices that are relatively cheap, easily available and transportable;
- (3') microwaves can detect portions of biological tissues whose electrical parameters (permittivity and conductivity, instead of density) are different from those of the background and, in particular, the electrical contrast between the tumoural masses and the healthy tissue surrounding them is much larger than the corresponding contrast in density[16]: hence, by using microwaves, the reliability of cancer detection should even increase with respect to current standards.

All three previous points are necessary starting conditions to face the current challenges and trends concerning diagnostic and/or monitoring systems⁵, which should be

Union', text adopted on Wednesday, 25th October 2006 in Strasbourg, available online at the web page <www.europarl.europa.eu/sides/getDoc.do?type=TA&reference=P6-TA-2006-0449&language=EN>.

³This kind of error mainly occurs for younger (i.e., premenopausal) women: the interior part of their breast is largely taken up by the milk ducts, whose density is the same as that of a solid tumoural mass.

⁴It is worth noting that the tomographic approach is not the only way to exploit microwaves for breast cancer detection: also ultra-wide-band radar techniques have been studied [18, 64], but they are far from the main focus of this Ph.D. thesis and then will not be considered here.

⁵Cf. the web page <http://ec.europa.eu/information_society/activities/health/research/

lightweight, portable, reliable and suited for easy and frequent home usage by the patient him/herself or his/her informal carers (such as relatives or friends). As a second step, it should be possible to link these user-friendly devices up to the Internet for a real-time external and professional assistance (when needed), or to store the data collected by them in a suitable electronic format: in such a way, the results of the domestic check-up could be easily sent e.g. by e-mail to hospitals and/or (personal) physicians. It is worth pointing out that, in general, the aim of this new generation of medical portable systems is not to replace, but rather to flank, complement and support (in a different context of usage) the current or future diagnostic devices that, owing to their costs, dimensions and complexity, are or will be available in hospitals only. As far as microwave tomography is concerned, at present it is impossible to be sure that a small and efficient portable tomograph will be realized in the next future. In any case, even a bigger prototype would represent a new kind of diagnostic and monitoring system that could be placed and used in hospitals (or also in travelling medical vans, such as the tomograph constructed by Prof. Paul M. Meaney and his staff⁶) to increase the effectiveness of the techniques currently adopted for breast cancer detection, as well as the number of women kept under observation.

Summarizing, we can say that the state of the art for breast cancer detection, as well as the current trends and challenges proposed by the European work programs concerning healthcare, seem to indicate that making microwave tomography an effective diagnostic technique would represent a significant medical achievement. Then, given the main focus of the current Ph.D. thesis, it is interesting to see how qualitative methods can play an important role in addressing such an issue. To this end, in the next section we consider a specific microwave scattering problem and describe a processing technique of its data in order to visualize tumoural masses inside the female breast.

3.2 The problem

Qualitative methods for inverse scattering problems have been usually formulated for time-harmonic waves, i.e., for fixed-frequency fields, and we shall maintain this ‘historical’ choice⁷. More specifically, for a tomographic imaging of the breast, a fixed-frequency

fp7phs/index.en.htm> in the Thematic Portal of Europe’s Information Society, whose home page is <http://ec.europa.eu/information_society/index.en.htm>.

⁶Cf. the web page <http://www-nml.dartmouth.edu/biomedprg/MIS/ClinicalSystems_Gen2.html> in the web site of ‘The Microwave Imaging and Spectroscopy (MIS) group’, whose home page is <<http://www-nml.dartmouth.edu/biomedprg/MIS/Main.html>>.

⁷However, it is worth noting that, insofar as the frequency is generic, a wise use of Fourier transform also enables a multi-frequency approach [74]; moreover, a linear sampling method working directly in the

microwave signal is transmitted from different positions and the diffracted field is collected by different antennas surrounding the breast itself. Furthermore, it is intuitive that both to reduce the dimensions of the experimental apparatus (i.e., the tomograph) and to increase the information content of the data⁸, the scattered field should be measured as close as possible to the breast: in other terms, near-field measurements of the scattered field should be used as input data.

A first possibility is to consider the linear sampling method (LSM) in its near-field formulation [36, 49, 50]. However, as a non-negligible drawback, this method requires the knowledge of the Green's function of the background, and the latter consists of all the physical bodies that are different from the scatterer (i.e., the tumour) and can influence the scattering experiment: these include not only the healthy tissues of the breast, but also the objects, the walls and the people of the room where the measurements are performed. An experimental device usually adopted to shield the breast from the multiple reflections of external scatterers consists in immersing the breast itself and the emitting/receiving antennas in an appropriate coupling medium (typically, saline [77], or glycerine-saline mixtures [78], or corn syrup [16, 17]). Indeed, this medium should meet the following requirements:

1. it should not be too lossy, so that the field radiated by the emitting antennas actually reaches the breast, is diffracted by it and can be measured by the receivers as a non-zero signal;
2. it should be 'lossy enough to permit the assumption that all fields propagate to infinity without reflection'⁹ from outer scatterers;
3. its electrical properties should be as similar as possible to those of the healthy breast, in order to favour the penetration of the incident wave into the breast itself, i.e., to reduce the reflection across the interface between skin and surrounding medium [16, 17, 72, 78].

When such a coupling medium is used, the simplest assumption that can be made to apply the LSM is that the entire background consists of a homogeneous and infinite medium having the same electrical properties of the coupling medium itself. In this case, however, the visualization provided by the method would highlight any tissue (not only the tumour) whose electrical properties differ from those of the background: then, the visualization

time domain (and then avoiding integral transforms) has been recently proposed in [38].

⁸Cf. e.g. [15], p. 211.

⁹Quoted from [76], p. 137.

should be post-processed by a quantitative algorithm computing the point values of the refractive index, in order to discriminate between healthy and cancerous tissues¹⁰. A more refined possibility is to assume the (approximate) knowledge¹¹ of the healthy breast: then, the latter, together with the surrounding (and infinite) coupling medium, would form the reference background and the LSM would only visualize the tumoural mass.

Of course, for numerical purposes, one can also consider idealized situations where the breast is surrounded by free space: this is the approach pursued e.g. in [21, 24]. If there is no object around the breast¹², no shielding from exterior reflections is needed: in this case, the only role of the coupling medium would be that of favouring the penetration of the incident wave, as described at the previous point no. 3. Then, testing an inversion method without using the coupling medium represents a ‘worst-case’ scenario: if the reconstructions obtained in this way are satisfactory, in principle they should be even more so when such medium is added.

According to point no. 2 above, the coupling medium physically cancels out or reduces the influence of outer objects on the scattering experiment. However, such a physical shielding can also be replaced by a ‘numerical’ one, i.e., overcome by an inversion method whose performance is insensitive to the presence of outer scatterers. This alternative possibility is offered by the reciprocity gap functional method (RGFM) [36, 44]: of course, there is a price to be paid, i.e., the fact that both the electric and magnetic fields need to be measured (while only the former or, less frequently, the latter is exploited in most scattering experiments). In the present chapter, we want to explore the possibility of using this method for breast cancer detection (in a 2D setting). Then, we shall use no coupling medium¹³ and sometimes add an exterior scatterer in order to show that the method is insensitive to it. Moreover, we want to extend the no-sampling approach, already developed for the LSM, to the RGFM.

However, one of the hypotheses assumed to formulate the RGFM is that the incident and the scattered fields are respectively emitted and measured inside a homogeneous

¹⁰It is worth recalling (cf. Section 2.8 of Chapter 2) that, in any case, the visualization provided by the LSM (or by any other qualitative method), possibly post-processed by an edge-detection technique, can always be used as initial guess for an iterative algorithm to compute the point values of the electrical parameters inside the investigation domain: examples of this ‘hybrid’ approach can be found in [22, 23, 25, 28, 29].

¹¹Obtained, for example, by a previous clinical MRI exam.

¹²For the moment, receiving antennas are considered as ideal probes, i.e., probes that measure the field without modifying it. However, if necessary, it would not be difficult to include the antennas, whose geometric and physical properties are known, into the background.

¹³Incidentally, we point out that using no coupling medium could help to simplify and downsize the experimental apparatus, thus reducing its cost.

background embedding the target: but the latter, in our application, is just the tumour, then the background is inhomogeneous, being formed, to a first approximation, by fat tissue, a thin layer of skin and the medium (free space) interposed between the patient's body and the emitting/receiving antennas¹⁴ (glands, ligaments or impurities could be considered later, in more refined models of the breast, or also as one of the noise sources perturbing the measurements). Then, we need to modify and generalize the RGFM with respect to its original formulation, in order to allow for an inhomogeneous background.

Now, the standard RGFM does not require the knowledge of the Green's function of the (homogeneous) background medium and this is one of its attractive features. The only possible way to adapt the RGFM to breast microwave tomography is probably to introduce in its formulation the Green's function of the inhomogeneous background¹⁵ surrounding the tumour, but this requires the knowledge of the physical and geometric properties of the background itself. If (a model of) the latter is simple enough, the Green's function can be analytically determined, otherwise it can be numerically computed, but in practice the problem is how to get such information on the background. We shall not discuss this issue in detail; we only outline two approaches (not alternative to each other):

- as regards the electrical parameters of the breast, the patient could undergo (at least in a screening plan) a preliminary MRI test providing detailed information on the structural properties of her breast; then, this information could be used as a landmark for several future tests performed by means of microwave tomography;
- as regards the geometric parameters of the breast, instead of letting the breast freely dangle under the action of its own weight, it could be softly modelled by inserting it into a cup of suitable dimension and material, i.e., into a sort of 'tomographic bra' smoothly enforcing a regular (essentially hemispherical) geometry.

Summarizing, in this chapter we generalize the RGFM introduced by [36, 44] in order to visualize tumoural masses inside the female breast. The generalization consists in taking explicitly into account the heterogeneity of the background medium¹⁶ enclosed by the array of receiving antennas: in other terms, the information on the healthy breast is encoded in the computation of the Green's function. Moreover, the implementation of the algorithm is realized by means of the no-sampling scheme already introduced for the

¹⁴When the RGFM is applied, the background outside the antennas is irrelevant.

¹⁵This possibility is explicitly suggested in [36].

¹⁶In particular, since skin and fat are lossy media, this approach gives rise to an interior transmission problem involving complex wave numbers, which deserves a careful discussion.

LSM, which allows a remarkable rapidity in the visualization process (2D maps of the inner breast are obtained in around 1 s with a conventional PC).

3.2.1 Plan of the following sections

The remainder of this chapter is devoted to explaining in detail our approach to the issues highlighted above. More precisely, Section 3.3 introduces some notations frequently used throughout this chapter. In Section 3.4 we formulate the inverse scattering problem of microwave tomography and we prove the general theorem at the basis of our visualization method. Section 3.5 describes the visualization algorithm and its implementation. Section 3.6 contains some numerical applications with synthetic but realistic scattering data. Our conclusions and hints for future work are presented in Section 3.7. Finally, Section 3.8 is a kind of appendix where we prove some complementary theorems used throughout this chapter: in particular, we discuss the properties of an interior transmission problem of interest for the study of the RGF equation introduced in Section 3.4.

3.3 Notations

The 2D scattering problem modelling a microwave tomography experiment for breast cancer detection is depicted in Fig. 5.7. We consider an idealized geometric model of the breast, whereby its axial view consists of a disk representing the fatty tissue, surrounded by a thin layer representing the skin. Embedded in the fat, the tumour takes up a spatial region assumed to be a bounded Lipschitz domain D such that the open complement of D is connected. In the space surrounding the breast, Γ and C denote two closed curves which are the boundaries of the bounded Lipschitz domains Ω and V respectively, with $\bar{\Omega} \subset V$. In the acquisition step, the receiving antennas will be placed on Γ and the emitting antennas will be placed on C . Since we work at a fixed (angular) frequency ω , in the following we shall not indicate the dependence on ω for the various physical quantities involved; we just observe that $\omega = k_0 c$, where k_0 and c are the wave number and the speed of light in free space respectively. We recall that the electrical properties of a generic medium are coded in the refractive index $\mathbf{n}(x)$, which is related to the electrical permittivity $\varepsilon(x)$ and conductivity $\sigma(x)$ by the definition¹⁷

$$\mathbf{n}(x) := \frac{1}{\varepsilon_0} \left[\varepsilon(x) + i \frac{\sigma(x)}{\omega} \right], \quad (3.1)$$

¹⁷See e.g. [48], p. 251.

and to the wave number $\mathbf{k}(x)$ by the definition $\mathbf{k}^2(x) := k_0^2 \mathbf{n}(x)$.

In this 2D model of the breast, several different refractive indices and wave numbers can be defined. First of all, in general, we shall use the subscripts 0, 1 and 2 applied to electrical permittivity, electrical conductivity, refractive index and wave number to indicate their constant value in free space (or coupling medium), fat and skin, respectively. In particular, we shall assume $\sigma_0 = 0$ and $\text{Im}\{n_j\} > 0$ for $j = 1, 2$. Then, $n_\Omega(x)$ and $k_\Omega(x)$ will denote the piecewise constant refractive index and wave number of the healthy medium contained in Ω (with $k_\Omega^2 = k_0^2 n_\Omega(x)$ for $x \in \Omega$). Outside Ω , the background $E := \mathbb{R}^2 \setminus \bar{\Omega}$ is formed by free space and several possible scatterers (e.g., walls, instrumentation) and is characterized by refractive index $n_E(x)$ and wave number $k_E(x)$. Therefore, in the case of a healthy breast, the refractive index and the wave number of the inhomogeneous medium in \mathbb{R}^2 are

$$n_b(x) := \begin{cases} n_\Omega(x) & x \in \Omega \\ n_E(x) & x \in E \end{cases} \quad \text{and} \quad k_b(x) := \begin{cases} k_\Omega(x) & x \in \Omega \\ k_E(x) & x \in E. \end{cases} \quad (3.2)$$

On the other hand, if a tumour D is present inside the fat, the refractive index and wave number of the medium in \mathbb{R}^2 are

$$\tilde{n}_b(x) := \begin{cases} n_D(x) & x \in D \\ n_b(x) & x \in \mathbb{R}^2 \setminus \bar{D} \end{cases} \quad \text{and} \quad \tilde{k}_b(x) := \begin{cases} k_D(x) & x \in D \\ k_b(x) & x \in \mathbb{R}^2 \setminus \bar{D}, \end{cases} \quad (3.3)$$

where $n_D(x)$ is the refractive index of the tumour and $k_D(x)$ is the corresponding wave number. Finally, for reasons related to the following computations, two auxiliary refractive indices and two auxiliary wave numbers are introduced, i.e.,

$$n(x) := \begin{cases} n_\Omega(x) & x \in \Omega \\ 1 & x \in E \end{cases} \quad \text{and} \quad k(x) := \begin{cases} k_\Omega(x) & x \in \Omega \\ k_0 & x \in E, \end{cases} \quad (3.4)$$

and

$$\tilde{n}(x) := \begin{cases} n_D(x) & x \in D \\ n(x) & x \in \mathbb{R}^2 \setminus \bar{D} \end{cases} \quad \text{and} \quad \tilde{k}(x) := \begin{cases} k_D(x) & x \in D \\ k(x) & x \in \mathbb{R}^2 \setminus \bar{D}. \end{cases} \quad (3.5)$$

Accordingly to these different wave numbers, for each $y \in \mathbb{R}^2$ different Green's functions can be defined. We denote by $G_b(\cdot, y)$ the Green's function for the equation describing the wave propagation in the entirely healthy background: in other terms, $G_b(\cdot, y)$ satisfies the equation $\Delta G_b(x, y) + k_b^2(x)G_b(x, y) = -\delta(x - y)$ in \mathbb{R}^2 . Here $k_b(x)$ is assumed to be bounded everywhere and such that $k_b(x) = k_0$ for $|x| > R$ with R large enough. The Green's function corresponding to $k(x)$ is denoted by $G(\cdot, y) = G_y$ and, by superposition,

$$G_b(x, y) = G(x, y) + u_b^s(x, y) \quad \forall x, y \in \mathbb{R}^2, \quad x \neq y, \quad (3.6)$$

where $u_b^s(x, y)$ is the field scattered in x by the objects outside Ω when the pointlike source is located in y and only the media inside Ω are included in the background. As we shall see, one of the strengths of our visualization method is that the only Green's function we need to know in order to implement the algorithm is G_y . Finally, $\tilde{G}_b(x, y)$ is the Green's function corresponding to $\tilde{k}_b(x)$.

Throughout this chapter, we shall assume that all the propagation media are linear, i.e., characterized in time-harmonic regime by constitutive relations of the form¹⁸

$$D_i(x) = \sum_{k=1}^3 \varepsilon_{ik}(x) E_k(x), \quad B_i(x) = \sum_{k=1}^3 \mu_{ik}(x) H_k(x), \quad i = 1, 2, 3, \quad (3.7)$$

under the further hypothesis that the tensors $\varepsilon_{ik}(x)$ and $\mu_{ik}(x)$ are symmetrical for each x . Such assumptions are not restrictive, since the vast majority of natural media (even inhomogeneous or anisotropic), and certainly those involved in a microwave tomography of the breast, enjoy these properties. In this case, the reciprocity principle holds¹⁹: in our framework, it can be stated as a symmetry property of the Green's functions, i.e.,

$$G(x, y) = G(y, x), \quad G_b(x, y) = G_b(y, x), \quad \tilde{G}_b(x, y) = \tilde{G}_b(y, x), \quad \forall x \neq y. \quad (3.8)$$

Finally, we introduce the notations for some functional spaces we shall use in the next sections:

$$H_\Delta^s(D) := \{u \in H^s(D) : \Delta u \in L^2(D)\}, \quad \text{for } s = 0, 1; \quad (3.9)$$

$$K_1^s := \{u \in H^s(D) : \Delta u + k_1^2 u = 0 \text{ in } D\}, \quad \text{for } s = 0, 1; \quad (3.10)$$

$$K_D^s := \{u \in H^s(D) : \Delta u + k_D^2(x) u = 0 \text{ in } D\}, \quad \text{for } s = 0, 1. \quad (3.11)$$

We can easily realize that the following inclusions hold:

$$K_1^1 \subset K_1^0, \quad K_D^1 \subset K_D^0, \quad K_1^s \subset H_\Delta^s(D), \quad K_D^s \subset H_\Delta^s(D), \quad \text{for } s = 0, 1. \quad (3.12)$$

Furthermore, the spaces $H_\Delta^s(D)$, K_1^s and K_D^s equipped with the norm defined as

$$\|u\|_{H_\Delta^s(D)}^2 := \|u\|_{H^s(D)}^2 + \|\Delta u\|_{L^2(D)}^2, \quad \text{for } s = 0, 1, \quad (3.13)$$

are Hilbert spaces (the completeness derives from using the graph norm²⁰). Moreover, it can be shown that for the spaces K_1^s and K_D^s the $H_\Delta^s(D)$ -norm is equivalent to the $H^s(D)$ -norm. Finally, following the same approach as that of Theorem 4.2 in [83], it can be proved that K_1^1 is dense in K_1^0 with respect to the $L^2(D)$ -norm.

¹⁸In (3.7) we use standard letters to denote the electromagnetic field and its Cartesian components.

¹⁹See e.g. [70], pp. 308-309.

²⁰See e.g. [54], p. 38.

3.4 The inverse scattering problem: an analysis of the RGF equation

Let us assume that $k_D \in L^\infty(D)$ and that there exists a positive real number c_D such that $\text{Im}\{n_D(x)\} \geq c_D > 0$ for almost all (f.a.a.) $x \in D$. In the case of a TM-polarized time-harmonic incident wave $u^i = u^i(\cdot, x_0)$ chosen as the Green's function $G_b(\cdot, x_0)$ for $x_0 \in \mathbb{R}^2 \setminus \bar{D}$, the spatial part $u = u(\cdot, x_0)$ of the total electric field satisfies the forward problem [44]

$$\begin{cases} \Delta u + \tilde{k}_b^2(x)u = 0 & \text{in } \mathbb{R}^2 \setminus \{x_0\} \\ u = u^s + u^i \\ \lim_{r \rightarrow \infty} \sqrt{r}(\partial_r u^s - ik_0 u^s) = 0, \end{cases} \quad (3.14)$$

where $\partial_r := \frac{\partial}{\partial r}$. Problem (3.14) can be equivalently expressed in integral form by means of the Lippmann-Schwinger equation: then, by following an approach analogous to that of chapter 8 in [48], it can be shown that, for each $x_0 \in \mathbb{R}^2 \setminus \bar{D}$, there exists a unique solution $u = u(\cdot, x_0) \in H_{loc}^1(\mathbb{R}^2 \setminus \{x_0\})$ of problem (3.14). We observe that this solution is the Green's function $\tilde{G}_b(\cdot, x_0)$: in particular, by virtue of (3.8), we have the reciprocity property $u(x, x_0) = u(x_0, x)$ for all $x_0 \in \mathbb{R}^2 \setminus \bar{D}$ and $x \in \mathbb{R}^2 \setminus \{x_0\}$.

The inverse scattering problem considered in this chapter is that of inferring information on $\tilde{k}_b^2(x)$ and, in particular, on $n_D(x)$, from the knowledge of $u(x, x_0)$ (and its normal derivative²¹ $\partial_\nu u(x, x_0)$) at different (discretized) x -locations, for a suitable number of emitting antennas placed at different x_0 -locations and sending the known fields $u^i(\cdot, x_0)$. For theoretical purposes, we shall also consider the scattered field $u^s(x, x_0)$, which is obtained from the total field $u(x, x_0)$ by remembering that $u^s = u - u^i$, as stated in the second relation of system (3.14). This inverse scattering problem is ill-posed in the sense of Hadamard and, at microwave frequencies, it is highly non-linear²². We shall address such problem by means of a qualitative approach, which will be able to visualize the support \bar{D} of the tumour without providing any information on the point values of $n_D(x)$.

²¹Here "normal" is to be understood with respect to the circle $\Gamma = \partial\Omega$ where receivers are placed. We recall that u^i , u^s and u respectively denote the non-zero component of the incident, scattered and total electric fields, which are perpendicular to the slice of the breast under exam. As a consequence, computations similar to those sketched at the beginning of Section 4.4, p. 95, show that the magnetic field vector lies in the plane of the slice and that its tangential (with respect to Γ) component is directly proportional to $\partial_\nu u$.

²²See e.g. [15], p. 214; [48], p. 105 and p. 140.

For two functions u, v in $H^1_\Delta(\Omega)$, the Reciprocity Gap Functional (RGF) is defined as

$$\mathcal{R}(u, v) := \int_\Gamma [u(x)\partial_\nu v(x) - v(x)\partial_\nu u(x)] ds(x), \quad (3.15)$$

where $\partial_\nu := \frac{\partial}{\partial \nu}$, ν being the unit normal vector to $\Gamma = \partial\Omega$, directed into the exterior of Ω . The visualization method utilized for the microwave tomography application in this chapter is based on the analysis of the family of RGF equations (parameterized over the sampling point $z \in \Omega$) [44]

$$\mathcal{R}(u(\cdot, x_0), s_g) = \mathcal{R}(u(\cdot, x_0), G_z) \quad \forall x_0 \in C, \quad (3.16)$$

where the unknown is a function $g \in H^{-1/2}(C)$, $G_z = G(\cdot, z)$, s_g is the single-layer potential of density g

$$s_g(x) := \int_C G(x, y)g(y)ds(y), \quad x \in \mathbb{R}^2 \setminus C, \quad (3.17)$$

and, as above, $u(\cdot, x_0)$ is the unique solution to problem (3.14) when the incident wave is sent by a point $x_0 \in C$; for future reference, we introduce the set U of all such solutions, i.e.,

$$U := \{u(\cdot, x_0) : x_0 \in C\}. \quad (3.18)$$

In order to perform the analysis of the family of RGF equations (3.16), we need to introduce the following three operators:

$$F : H^{-\frac{1}{2}}(C) \rightarrow L^2(C), \quad g \xrightarrow{F} [x_0 \mapsto \mathcal{R}(u(\cdot, x_0), s_g)], \quad (3.19)$$

$$H : H^{-\frac{1}{2}}(C) \rightarrow K_1^0, \quad g \xrightarrow{H} s_g|_D, \quad (3.20)$$

$$P : K_1^0 \rightarrow L^2(C), \quad v \xrightarrow{P} \left[x_0 \mapsto \int_D [k_1^2 - k_D^2(x)] v(x)u(x, x_0)dx \right]. \quad (3.21)$$

The aim of this section is to study some relevant properties of these operators, according to a plan consisting of the following main points:

Point 1: we show that F can be written as the product of $-P$ and H (Theorem 3.4.1);

Point 2: we prove that H is injective with dense range (Theorem 3.4.2);

Point 3: we prove that P is injective with dense range (Theorem 3.4.6), which, together with points 1 and 2, implies that F is injective with dense range (Corollary 3.4.7);

Point 4: we give an exact characterization of D via the range of P (Theorem 3.4.8);

Point 5: we prove the general theorem qualitatively characterizing D in terms of the behaviour of approximate solutions to the family of RGF equations (Theorem 3.4.9): this theorem will inspire the visualization algorithm described in the next section.

We now discuss these five points in detail.

Point 1.

Theorem 3.4.1. *The operator F is compact and can be factored as $F = -PH$.*

Proof. From definitions (3.15) and (3.19), it easily follows that F is an integral operator with regular kernel $S : C \times C \rightarrow \mathbb{C}$ defined as $S(x_0, y) := \mathcal{R}(u(\cdot, x_0), G(\cdot, y))$. In particular, the range of F is a subset of $H^1(C)$, which is compactly embedded²³ in $L^2(C)$: this shows the compactness of F .

As regards the factorization $F = -PH$, for any $g \in H^{-\frac{1}{2}}(C)$ let us define $v \in H_{\Delta}^1(\Omega)$ as $v := s_g|_{\Omega}$. Then, from (3.17) and (3.19), we get

$$Fg(x_0) = \mathcal{R}(u(\cdot, x_0), s_g) = \mathcal{R}(u(\cdot, x_0), v) \quad \forall x_0 \in C, \quad (3.22)$$

so that, remembering definition (3.15),

$$Fg(x_0) = \int_{\Gamma} u(x, x_0) \partial_{\nu} v(x) ds(x) - \int_{\Gamma} v(x) \partial_{\nu_x} u(x, x_0) ds(x) \quad \forall x_0 \in C. \quad (3.23)$$

Since both $u(\cdot, x_0)|_{\Omega}$, $v \in H_{\Delta}^1(\Omega)$ satisfy in $\Omega \setminus \bar{D}$ the equation

$$\Delta u + k^2(x)u = 0, \quad (3.24)$$

applying the second Green's identity in $\Omega \setminus \bar{D}$ to the right-hand side of (3.23) gives:

$$Fg(x_0) = \int_{\partial D} u(x, x_0) \partial_{\nu} v(x) ds(x) - \int_{\partial D} v(x) \partial_{\nu_x} u(x, x_0) ds(x) \quad \forall x_0 \in C. \quad (3.25)$$

Then, if we observe that $u(\cdot, x_0)|_D \in K_D^1$ and $v|_D \in K_1^1$, we can still apply the second Green's identity in D and rewrite equality (3.25) as:

$$Fg(x_0) = - \int_D [k_1^2 - k_D^2(x)] u(x, x_0) v(x) dx \quad \forall x_0 \in C, \quad (3.26)$$

i.e., by remembering definitions (3.20) (in particular, $v|_D = Hg$) and (3.21),

$$Fg(x_0) = -PHg(x_0) \quad \forall x_0 \in C. \quad (3.27)$$

This concludes the proof. ■

Point 2.

²³See e.g. [75], p. 87.

Theorem 3.4.2. *The operator H is injective and has a dense range with respect to the $L^2(D)$ -norm.*

Proof. We split the proof into three steps.

Step 1: H is injective. Suppose that $g \in H^{-\frac{1}{2}}(C)$ is such that $Hg = 0$. Then, remembering definition (3.20), we have that $s_g = 0$ in D . Moreover, since $s_g \in H^1(V)$ verifies equation (3.24) in V , we have $s_g = 0$ in V by virtue of the unique continuation principle²⁴. Hence, also the trace on $C = \partial V$ of s_g is zero, i.e., $S_C g = 0$, where $S_C : H^{-1/2}(C) \rightarrow H^{1/2}(C)$ such that $g \mapsto S_C g := s_g|_C$ is the single-layer operator²⁵ on C . Since, as stated before, we assume that $\text{Im}\{n_j\} > 0$ for $j = 1, 2$, it is possible to prove (see Theorem 3.8.2 in Subsection 3.8.1) that S_C is injective. Then, $S_C g = 0$ implies $g = 0$.

Step 2: \tilde{H} has a dense range. Let us introduce the auxiliary operator

$$\tilde{H} : H^{-\frac{1}{2}}(C) \rightarrow H^{\frac{1}{2}}(\partial D), \quad g \mapsto s_g|_{\partial D}, \quad (3.28)$$

and prove that it has a dense range: this amounts to proving that the transpose operator

$${}^t\tilde{H} : H^{-\frac{1}{2}}(\partial D) \rightarrow H^{\frac{1}{2}}(C), \quad f \mapsto \int_{\partial D} G(x, y) f(y) ds(y), \quad x \in C, \quad (3.29)$$

is injective. We note that for all $f \in H^{-\frac{1}{2}}(\partial D)$, ${}^t\tilde{H}f$ is the trace on C of the single-layer potential of density f on ∂D (cf. definition (3.17)). Now, let us suppose that $f \in H^{-\frac{1}{2}}(\partial D)$ is such that ${}^t\tilde{H}f = 0$: we want to prove that $f = 0$. To this end, let us consider the single-layer potential v of density f on ∂D , i.e.,

$$v(x) := \int_{\partial D} G(x, y) f(y) ds(y), \quad x \in \mathbb{R}^2 \setminus \partial D. \quad (3.30)$$

Of course, v is a radiating solution of equation (3.24) in $\mathbb{R}^2 \setminus \bar{D}$. Moreover, the assumption ${}^t\tilde{H}f = 0$ means that v vanishes identically on $C = \partial V$: hence, by virtue of Theorem 3.8.1 in Subsection 3.8.1, we have $v = 0$ in $\mathbb{R}^2 \setminus \bar{V}$ and then the unique continuation principle ensures that $v = 0$ in $\mathbb{R}^2 \setminus \bar{D}$. As a consequence, we get $S_{\partial D} f = 0$, where $S_{\partial D} : H^{-1/2}(\partial D) \rightarrow H^{1/2}(\partial D)$ is the single-layer operator on ∂D . Analogously to the end of the previous Step 1, we can now conclude that $f = 0$ by using the injectivity of $S_{\partial D}$.

Step 3: H has a dense range. We want to show that for any $w \in K_1^0$ and $\epsilon > 0$, there exists $g \in H^{-1/2}(C)$ such that

$$\|Hg - w\|_{L^2(D)} < \epsilon. \quad (3.31)$$

²⁴See e.g. [71], pp. 64-69.

²⁵See e.g. [75], p. 203.

To this end, we first recall that K_1^1 is dense in K_1^0 with respect to the $L^2(D)$ -norm: hence, there exists $v \in K_1^1$ such that

$$\|v - w\|_{L^2(D)} < \frac{\epsilon}{2}. \quad (3.32)$$

Then, we observe that the continuous dependence of the solution of a strongly elliptic equation on the boundary data²⁶ implies the existence of a constant $\alpha > 0$ such that for all $\psi \in K_1^1$ it holds that

$$\|\psi\|_{H^1(D)} \leq \alpha \|\psi|_{\partial D}\|_{H^{\frac{1}{2}}(\partial D)}. \quad (3.33)$$

Now, remembering the previous Step No. 2, we can choose $g \in H^{-\frac{1}{2}}(C)$ such that

$$\left\| \tilde{H}g - v|_{\partial D} \right\|_{H^{\frac{1}{2}}(\partial D)} < \frac{\epsilon}{2\alpha}. \quad (3.34)$$

Moreover, since both $Hg = s_g|_D \in H^1(D)$ and $v \in K_1^1$ (and consequently $Hg - v$) solve equation $\Delta\psi + k_1^2\psi = 0$ in D , by virtue of inequalities (3.33) and (3.34) we have

$$\|Hg - v\|_{H^1(D)} \leq \alpha \|(Hg - v)|_{\partial D}\|_{H^{\frac{1}{2}}(\partial D)} = \alpha \left\| \tilde{H}g - v|_{\partial D} \right\|_{H^{\frac{1}{2}}(\partial D)} < \frac{\epsilon}{2}. \quad (3.35)$$

Hence, by using the triangle inequality together with relations (3.32), (3.35) and remembering that the $L^2(D)$ -norm is bounded by the $H^1(D)$ -norm, we obtain relation (3.31), which concludes the proof. ■

Point 3.

In order to establish the main result of this point 3, i.e., Theorem 3.4.6, we first need to prove the following three lemmas.

Lemma 3.4.3. *The set $U_D = \{u|_D : u \in U\}$ is dense in K_D^1 with respect to the $L^2(D)$ -norm.*

Proof. Let $v \in U_D^\perp$: this means that $v \in K_D^1$ is such that $(u, v)_{L^2(D)} = 0$ for all $u \in U_D$, i.e.,

$$\int_D u(x, x_0)\bar{v}(x)dx = 0 \quad \forall x_0 \in C. \quad (3.36)$$

As already observed, for all $x_0 \in \mathbb{R}^2 \setminus \bar{D}$, in $\mathbb{R}^2 \setminus \{x_0\}$ it holds that $u(\cdot, x_0) = \tilde{G}_b(\cdot, x_0)$, where $\tilde{G}_b(\cdot, x_0)$ is the Green's function for the first equation in problem (3.14), which takes into account the presence of the tumour. Now, let us define

$$w(x) := \int_D \tilde{G}_b(y, x)\bar{v}(y)dy \quad \forall x \in \mathbb{R}^2. \quad (3.37)$$

²⁶See e.g. [75], pp. 128-129.

In particular, by virtue of the previous observation, we have

$$w(x) = \int_D u(y, x) \bar{v}(y) dy \quad \forall x \in \mathbb{R}^2 \setminus \bar{D} \quad (3.38)$$

and, as a consequence of (3.36), $w(x_0) = 0 \quad \forall x_0 \in C$. Moreover, $w = w(x)$ is clearly a radiating solution of $\Delta w + \tilde{k}_b^2(x)w = 0$ in $\mathbb{R}^2 \setminus \bar{D}$ and, as just stated, it vanishes on $C = \partial V$; hence, by applying Theorem 3.8.1 in Subsection 3.8.1, we have $w = 0$ in $\mathbb{R}^2 \setminus V$ and, by virtue of the unique continuation principle, $w = 0$ in $\mathbb{R}^2 \setminus \bar{D}$: in particular, it holds that $w|_{\partial D} = 0$, $\partial_\nu w|_{\partial D} = 0$. Moreover, as a direct consequence of definition (3.37), w verifies $\Delta w + \tilde{k}_b^2(x)w = -\bar{v}$ in D . From the latter equation, we immediately get

$$\int_D (\Delta w)(x)v(x)dx + \int_D \tilde{k}_b^2(x)w(x)v(x)dx = -\|v\|_{L^2(D)}^2, \quad (3.39)$$

i.e., by virtue of the second Green's identity²⁷,

$$\begin{aligned} \int_D (\Delta v)(x)w(x)dx - \int_{\partial D} w(x)\partial_\nu v(x)ds(x) + \\ + \int_{\partial D} v(x)\partial_\nu w(x)ds(x) + \int_D \tilde{k}_b^2(x)w(x)v(x)dx = -\|v\|_{L^2(D)}^2 \end{aligned} \quad (3.40)$$

or, remembering that $w|_{\partial D} = 0$, $\partial_\nu w|_{\partial D} = 0$,

$$\int_D \left[\Delta v(x) + \tilde{k}_b^2(x)v(x) \right] w(x)dx = -\|v\|_{L^2(D)}^2. \quad (3.41)$$

But $v \in K_D^1$, then, by virtue of definitions (3.2) and (3.11), the left-hand side of (3.41) is zero: hence, we have $\|v\|_{L^2(D)}^2 = 0$, i.e., $v = 0$. This concludes the proof. ■

Lemma 3.4.4. *The following operator:*

$$M : H^{\frac{1}{2}}(\partial D) \rightarrow L^2(C), \quad v \mapsto \int_{\partial D} v(x)\partial_{\nu_x} u(x, x_0)ds(x), \quad (3.42)$$

with $x_0 \in C$ and $u(\cdot, x_0) \in U$, has a dense range.

Proof. It suffices to prove that the transpose operator

$${}^t M : L^2(C) \rightarrow H^{-\frac{1}{2}}(\partial D), \quad \varphi \mapsto \int_C \varphi(x_0)\partial_{\nu_x} u(x, x_0)ds(x_0) \quad (3.43)$$

(with $x \in \partial D$) is injective. Let $\varphi \in L^2(C)$ be such that ${}^t M\varphi = 0$. For each $x \in \mathbb{R}^2$, we can define the function v as

$$v(x) := \int_C \varphi(x_0)u(x, x_0)ds(x_0). \quad (3.44)$$

²⁷See e.g. [75], p. 118.

Since $u(\cdot, x_0)$ verifies (3.14), it follows that v satisfies $\Delta v + \tilde{k}_b^2(x)v = 0$ in $\mathbb{R}^2 \setminus C$; moreover, according to (3.14), $u = u^i + u^s$, where the incident field is $u^i(x, x_0) := G_b(x, x_0)$ and $u^s(x, x_0)$ is the corresponding scattered field. Then, v can be regarded as the total field $v = v^i + v^s$ resulting from the sum of the incident field

$$v^i(x) := \int_C \varphi(x_0) G_b(x, x_0) ds(x_0) \quad \forall x \in \mathbb{R}^2, \quad (3.45)$$

which is the single-layer potential of density φ and satisfies

$$\Delta v + k_b^2(x)v = 0 \quad (3.46)$$

in $\mathbb{R}^2 \setminus C$, and the scattered field

$$v^s(x) := \int_C \varphi(x_0) u^s(x, x_0) ds(x_0) \quad \forall x \in \mathbb{R}^2, \quad (3.47)$$

which verifies (3.46) in $\mathbb{R}^2 \setminus \bar{D}$. Moreover, by virtue of (3.43) and (3.44), it holds that $\partial_\nu v = {}^t M \varphi$, but ${}^t M \varphi = 0$ by assumption: then, it turns out that the function v given by (3.44) is the unique solution of the following boundary value problem:

$$\begin{cases} \Delta v + k_D^2(x)v = 0 & \text{in } D \\ \partial_\nu v = 0 & \text{on } \partial D. \end{cases} \quad (3.48)$$

Hence $v = 0$ in D and by the unique continuation principle $v = 0$ in V , i.e., $v^s = -v^i$ in V . If we now define \tilde{v}^s in \mathbb{R}^2 as $\tilde{v}^s(x) := v^s(x)$ for $x \in \mathbb{R}^2 \setminus \bar{D}$ and $\tilde{v}^s(x) := -v^i(x)$ for $x \in \bar{D}$, we can easily see that \tilde{v}^s is an entire radiating solution of (3.46). As a consequence²⁸, we have $\tilde{v}^s = 0$ in \mathbb{R}^2 , and then $v^i = 0$ in V . In particular, the single-layer potential of density φ is null on C , and since the single-layer operator is injective (see Theorem 3.8.2), then $\varphi = 0$, ${}^t M$ is injective and M has a dense range. ■

Lemma 3.4.5. *For each $f \in H^{\frac{1}{2}}(\partial D)$, the set $E_f := \{\partial_\nu u : u \in H_\Delta^1(D) \text{ and } u|_{\partial D} = f\}$ is dense in $H^{-\frac{1}{2}}(\partial D)$.*

Proof. We first observe that E_f is an affine space, i.e., $E_f = E_0 + \partial_\nu u_f$, where $u_f \in H_\Delta^1(D)$ is the unique solution of the following boundary value problem:

$$\begin{cases} \Delta u = 0 & \text{in } D \\ u = f & \text{on } \partial D. \end{cases} \quad (3.49)$$

²⁸See [48], p. 20: the motivation presented there for a constant k also holds in our case, provided that the proper versions of the second Green's identity and Green's representation formula are used: see e.g. [75], p. 118 and p. 237.

Then, in order to prove that E_f is dense in $H^{-\frac{1}{2}}(\partial D)$, it suffices to show this property for E_0 . Indeed, let us assume that E_0 is dense in $H^{-\frac{1}{2}}(\partial D)$ and let v be any element of $H^{-\frac{1}{2}}(\partial D)$: then, $v - \partial_\nu u_f \in H^{-\frac{1}{2}}(\partial D)$. Hence, for every $\epsilon > 0$, there exists $w^\epsilon \in E_0$ such that

$$\|w^\epsilon - (v - \partial_\nu u_f)\|_{H^{-\frac{1}{2}}(\partial D)} = \|v - (w^\epsilon + \partial_\nu u_f)\|_{H^{-\frac{1}{2}}(\partial D)} < \epsilon, \quad (3.50)$$

i.e., we have found $w^\epsilon + \partial_\nu u_f \in E_f$ that approximates $v \in H^{-\frac{1}{2}}(\partial D)$.

Now, in order to show that E_0 is dense, it suffices to prove the density of the range of the operator T defined as:

$$T : L^2(D) \rightarrow H^{-\frac{1}{2}}(\partial D), \quad \varphi \xrightarrow{T} \partial_\nu u_\varphi, \quad (3.51)$$

where, for all $\varphi \in L^2(D)$, $u_\varphi \in H^1_\Delta(D)$ is the unique solution of the boundary value problem

$$\begin{cases} \Delta u = \varphi & \text{in } D \\ u = 0 & \text{on } \partial D. \end{cases} \quad (3.52)$$

We can prove the density of the range of T by proving that its transpose tT is injective: to this end, we have to explicitly determine tT , defined by the condition

$$\int_{\partial D} g(x)(T\varphi)(x)ds(x) = \int_D ({}^tTg)(x)\varphi(x)dx \quad \forall g \in H^{\frac{1}{2}}(\partial D), \quad \forall \varphi \in L^2(D). \quad (3.53)$$

Then, we now want to show that tT is given by

$${}^tT : H^{\frac{1}{2}}(\partial D) \rightarrow L^2(D), \quad g \xrightarrow{{}^tT} w_g, \quad (3.54)$$

where $w_g \in H^1_\Delta(D)$ is the unique solution of the following problem:

$$\begin{cases} \Delta w = 0 & \text{in } D \\ w = g & \text{on } \partial D. \end{cases} \quad (3.55)$$

Indeed, let $\varphi \in L^2(D)$ and $g \in H^{\frac{1}{2}}(\partial D)$. Then, by taking into account the equations and boundary conditions in (3.52), (3.55), as well as the expressions (3.51), (3.54) for T and tT , and by using the second Green's identity in D , we obtain:

$$\begin{aligned} \int_{\partial D} g(x)(T\varphi)(x)ds(x) &= \int_{\partial D} w_g(x)\partial_\nu u_\varphi(x)ds(x) = \int_D w_g(x)\varphi(x)dx = \\ &= \int_D ({}^tTg)(x)\varphi(x)dx \quad \forall g \in H^{\frac{1}{2}}(\partial D), \quad \forall \varphi \in L^2(D), \end{aligned} \quad (3.56)$$

so that condition (3.53) is verified, i.e., expression (3.54) for tT is correct. Now, let us consider $g \in H^{\frac{1}{2}}(\partial D)$ such that ${}^tTg = 0$. Then, by uniqueness of the solution to the

Laplace equation for a Dirichlet boundary condition on ∂D (i.e., problem (3.55), with $g = 0$), we have that $g = 0$. Hence tT is injective and consequently T has a dense range. This concludes the proof. ■

The following theorem makes use of notations, concepts and results described in Subsection 3.8.2, which concerns an interior transmission problem. Accordingly, we shall often highlight the dependence of the index of refraction on the generic wave number k in free space.

Theorem 3.4.6. *The operator P is bounded. Moreover, if k_0 is not a transmission eigenvalue of the following problem*

$$\begin{cases} \Delta v + k^2 n_1(k)v = 0 & \text{in } D \\ \Delta u + k^2 n_D(k)(x)u = 0 & \text{in } D \\ (v - u) = 0 & \text{on } \partial D \\ \partial_\nu(v - u) = 0 & \text{on } \partial D, \end{cases} \quad (3.57)$$

then the operator P is injective and has a dense range.

Proof. We split the proof into three steps.

Step 1: P is bounded. Let us denote by $u(\cdot, \cdot)$ the function obtained from $u(\cdot, x_0) \in U$ when $x_0 \in C$ is regarded as a variable: since $u(\cdot, x_0)$ is singular only for $x = x_0$, we have that $u(\cdot, \cdot) \in L^\infty(D \times C) \subset L^2(D \times C)$. Then, remembering definition (3.21), the boundedness of $k_D \in L^\infty(D)$ and the Cauchy-Schwarz inequality, we have:

$$\begin{aligned} \|Pv\|_{L^2(C)}^2 &= \int_C \left| \int_D [k_1^2 - k_D^2(x)] v(x)u(x, x_0) dx \right|^2 dx_0 \leq \\ &\leq \|k_1^2 - k_D^2\|_{L^\infty(D)}^2 \|v\|_{L^2(D)}^2 \|u\|_{L^2(D \times C)}^2. \end{aligned} \quad (3.58)$$

We observe that since the $L^2(D)$ -norm is bounded by the $H_\Delta^0(D)$ -norm, the inequality in (3.58) shows the boundedness of P whichever of the two norms is chosen for its domain K_1^0 .

Step 2: P is injective. Let $v \in K_1^0$ be such that $Pv = 0$. Then, recalling definition (3.21), we have:

$$\int_D [k_1^2 - k_D^2(x)] u(x, x_0)v(x) dx = 0 \quad \forall x_0 \in C. \quad (3.59)$$

By Lemma 3.4.3, the set $U = \{u(\cdot, x_0) : x_0 \in C\}$ is dense in K_D^1 with respect to the $L^2(D)$ -norm: from (3.59) and the continuity of the scalar product in L^2 , we then have

$$\int_D [k_1^2 - k_D^2(x)] u(x)v(x) dx = 0 \quad \forall u \in K_D^1. \quad (3.60)$$

For the same $v \in K_1^0$, consider now the unique solution $w \in H_\Delta^1(D)$ of

$$\begin{cases} \Delta w + k_D^2(x)w = [k_1^2 - k_D^2(x)]v & \text{in } D \\ w = 0 & \text{on } \partial D. \end{cases} \quad (3.61)$$

Since $u \in K_D^1$ and w verifies the first of (3.61), by virtue of (3.60) we can show that

$$-\int_D \Delta u(x)w(x)dx + \int_D \Delta w(x)u(x)dx = \int_D [k_1^2 - k_D^2(x)] u(x)v(x)dx = 0 \quad \forall u \in K_D^1. \quad (3.62)$$

Then, the second Green's identity in D , with $w = 0$ on ∂D by (3.61), yields

$$\int_{\partial D} u(x)\partial_\nu w(x)ds(x) = 0 \quad \forall u \in K_D^1. \quad (3.63)$$

We now observe that the following problem

$$\begin{cases} \Delta u + k_D^2(x)u = 0 & \text{in } D \\ u = f & \text{on } \partial D \end{cases} \quad (3.64)$$

has a unique solution $u_f \in K_D^1$ for each $f \in H^{\frac{1}{2}}(\partial D)$. As a consequence, $\{u|_{\partial D} : u \in K_D^1\} = H^{\frac{1}{2}}(\partial D)$ and then, by virtue of (3.63), we get

$$\int_{\partial D} f(x)\partial_\nu w(x)ds(x) = 0 \quad \forall f \in H^{\frac{1}{2}}(\partial D), \quad (3.65)$$

which proves that $\partial_\nu w = 0$. Consider now the function $u \in H_\Delta^0(D)$ defined as $u := w + v$. Remembering that w is the solution of (3.61), $\partial_\nu w = 0$ and $v \in K_1^0$, it is easy to realize that v and u satisfy the homogeneous transmission problem (3.57) for $k = k_0$. Since we have supposed that k_0 is not a transmission eigenvalue, this implies that $u = v = 0$; then P is injective.

Step 3: P has a dense range. Let $h \in L^2(C)$ and $\epsilon > 0$: by virtue of Lemma 3.4.4, there exists $f \in H^{\frac{1}{2}}(\partial D)$ such that

$$\|Mf - h\|_{L^2(C)} < \frac{\epsilon}{2}. \quad (3.66)$$

Moreover, the operator Q defined as

$$Q : H^{-\frac{1}{2}}(\partial D) \rightarrow L^2(C), \quad v \stackrel{Q}{\mapsto} \left[x_0 \mapsto \int_{\partial D} v(x)u(x, x_0)dx \right] \quad (3.67)$$

(with $u(\cdot, x_0) \in U$) is easily seen to be bounded. By virtue of Lemma 3.4.5, there exists a function $q \in H_\Delta^1(D)$ such that $q|_{\partial D} = f$ and

$$\|\partial_\nu q\|_{H^{-\frac{1}{2}}(\partial D)} < \frac{\epsilon}{2\|Q\|}. \quad (3.68)$$

Since we have supposed that k_0 is not a transmission eigenvalue (see Subsection 3.8.2), there exist $\tilde{v}, \tilde{w} \in H_{\Delta}^0(D)$ such that $\tilde{v} - \tilde{w} \in H_{\Delta}^1(D)$ and

$$\begin{cases} \Delta \tilde{v} + k_0^2 n_1(k_0) \tilde{v} = 0 & \text{in } D \\ \Delta \tilde{w} + k_0^2 n_D(k_0)(x) \tilde{w} = 0 & \text{in } D \\ (\tilde{v} - \tilde{w}) = q & \text{on } \partial D \\ \partial_{\nu}(\tilde{v} - \tilde{w}) = \partial_{\nu} q & \text{on } \partial D. \end{cases} \quad (3.69)$$

Let $\tilde{u} := \tilde{v} - \tilde{w}$. Then $\tilde{u} \in H_{\Delta}^1(D)$ and, as a simple consequence of the first two equations in (3.69), we have

$$\Delta \tilde{u} + k_D^2(x) \tilde{u} = -[k_1^2 - k_D^2(x)] \tilde{v} \quad \text{in } D. \quad (3.70)$$

Then, by using (3.70) and the second Green's identity in D , easy computations show that for all $u \in K_D^1$ it holds that

$$\int_D [k_1^2 - k_D^2(x)] u(x) \tilde{v}(x) dx = \int_{\partial D} \tilde{u}(x) \partial_{\nu} u(x) ds(x) - \int_{\partial D} u(x) \partial_{\nu} \tilde{u}(x) ds(x), \quad (3.71)$$

i.e., remembering that $\tilde{u} = \tilde{v} - \tilde{w}$, $q|_{\partial D} = f$ and recalling the boundary conditions in (3.69),

$$\int_D [k_1^2 - k_D^2(x)] u(x) \tilde{v}(x) dx = \int_{\partial D} f(x) \partial_{\nu} u(x) ds(x) - \int_{\partial D} u(x) \partial_{\nu} q(x) ds(x). \quad (3.72)$$

If we now remember definitions (3.21), (3.42) and (3.67), we can rewrite (3.72) as

$$(Pv)(x_0) = (Mf)(x_0) - (Q\partial_{\nu}q)(x_0) \quad \forall x_0 \in C; \quad (3.73)$$

then, by using the triangle inequality and recalling relations (3.66), (3.68), we get:

$$\|Pv - h\|_{L^2(C)} \leq \|Mf - h\|_{L^2(C)} + \|Q\| \|\partial_{\nu}q\|_{L^2(\partial D)} < \epsilon, \quad (3.74)$$

which shows that P has a dense range, since h is arbitrarily chosen in $L^2(C)$. ■

Corollary 3.4.7. *If k_0 is not a transmission eigenvalue of problem (3.57), then the operator $F = -PH$ is injective and has a dense range.*

Proof. The injectivity of F is obvious. As regards the denseness of its range, let us consider any $w \in L^2(C)$: by using the triangle inequality, the linearity and the boundedness of the operator P (see Theorem 3.4.6), and remembering that both P and H have a dense range, it turns out that for each $\epsilon > 0$ we can find $g \in H^{-\frac{1}{2}}(C)$ (and an auxiliary $v \in K_1^0$) such that the following chain of inequalities holds:

$$\begin{aligned} \|w - (-PHg)\|_{L^2(C)} &\leq \|w - Pv\|_{L^2(C)} + \|P(v + Hg)\|_{L^2(C)} < \\ &< \frac{\epsilon}{2} + \|P\| \|v + Hg\|_{L^2(D)} < \frac{\epsilon}{2} + \|P\| \frac{\epsilon}{2\|P\|} = \epsilon. \end{aligned} \quad (3.75)$$

This concludes the proof. ■

Point 4.

In order to characterize the range of P , for each $z \in \Omega$ we introduce the function $\Lambda_z \in L^2(C)$ defined as

$$\Lambda_z : C \rightarrow \mathbb{C}, \quad x_0 \mapsto \mathcal{R}(u(\cdot, x_0), G_z). \quad (3.76)$$

Then the following theorem, again based on results in Subsection 3.8.2, holds.

Theorem 3.4.8. *Suppose that k_0 is not a transmission eigenvalue of problem (3.57). Then, for all $z \in \Omega$, $\Lambda_z \in \text{range}(P)$ if and only if $z \in D$.*

Proof. 1) Let $z \in D$ and let us consider a function $\beta \in C^\infty(\Omega)$ such that²⁹ $\beta = 0$ in a neighbourhood of z and $\beta = 1$ in a neighbourhood of ∂D : then $\beta G_z \in H_\Delta^1(D)$. Since k_0 is not a transmission eigenvalue of problem (3.57), there exist (see Subsection 3.8.2) $\tilde{v}, \tilde{w} \in H_\Delta^0(D)$ such that $\tilde{v} - \tilde{w} \in H_\Delta^1(D)$ and

$$\begin{cases} \Delta \tilde{v} + k_0^2 n_1(k_0) \tilde{v} = 0 & \text{in } D \\ \Delta \tilde{w} + k_0^2 n_D(k_0)(x) \tilde{w} = 0 & \text{in } D \\ (\tilde{v} - \tilde{w}) = \beta G_z & \text{on } \partial D \\ \partial_\nu(\tilde{v} - \tilde{w}) = \partial_\nu(\beta G_z) & \text{on } \partial D. \end{cases} \quad (3.77)$$

Since $\beta = 1$ in a neighbourhood of ∂D , the factor β can be omitted in the boundary conditions of (3.77). Moreover, since $z \in D$, both G_z and $u(\cdot, x_0) \in U$ are in $H_\Delta^1(\Omega \setminus \bar{D})$ and satisfy equation (3.24) in $\Omega \setminus \bar{D}$; hence, if we set $\tilde{u} := \tilde{v} - \tilde{w}$, by applying the second Green's identity in $\Omega \setminus \bar{D}$ and remembering definition (3.21), as well as the boundary conditions of (3.77), we get:

$$\begin{aligned} \mathcal{R}(u(\cdot, x_0), G_z) &= - \int_{\partial D} G_z(x) \partial_{\nu_x} u(x, x_0) ds(x) + \int_{\partial D} u(x, x_0) \partial_{\nu_x} G_z(x) ds(x) = \\ &= - \int_D [k_1^2 - k_D^2(x)] u(x, x_0) \tilde{v}(x) dx = -(P\tilde{v})(x_0) \quad \forall x_0 \in C, \end{aligned} \quad (3.78)$$

i.e., recalling definition (3.76), $\Lambda_z(x_0) = [P(-\tilde{v})](x_0)$ for all $x_0 \in C$: this means that $\Lambda_z \in \text{range}(P)$.

2) Let us now suppose that $z \in \Omega \setminus \bar{D}$ and, by contradiction, that $\Lambda_z \in \text{range}(P)$. By definition (3.15) and recalling from (3.14) that $u = u^s + u^i$ with $u^i(\cdot, x_0) = G_b(\cdot, x_0)$, for

²⁹See e.g. [75], p. 64.

all $x_0 \in C$ we have

$$\begin{aligned} \mathcal{R}(u(\cdot, x_0), G_z) &= \int_{\Gamma} [u(x, x_0) \partial_{\nu_x} G(x, z) - G(x, z) \partial_{\nu_x} u(x, x_0)] ds(x) = \\ &= \int_{\Gamma} [u^s(x, x_0) \partial_{\nu_x} G(x, z) - G(x, z) \partial_{\nu_x} u^s(x, x_0)] ds(x) + \\ &+ \int_{\Gamma} [G_b(x, x_0) \partial_{\nu_x} G(x, z) - G(x, z) \partial_{\nu_x} G_b(x, x_0)] ds(x). \end{aligned} \quad (3.79)$$

We now observe that, for $x \in \Gamma = \partial\Omega$ and $x_0 \in C$, $G_b(\cdot, x_0)$ solves equation (3.24) in Ω , while the Green's function for (3.24) is just $G(\cdot, z)$: then, by applying Green's representation formula³⁰ to $G_b(\cdot, x_0)$, we find:

$$\mathcal{R}(u(\cdot, x_0), G_z) = \int_{\Gamma} [u^s(x, x_0) \partial_{\nu_x} G(x, z) - G(x, z) \partial_{\nu_x} u^s(x, x_0)] ds(x) - G_b(x_0, z). \quad (3.80)$$

Now, for $x_0 \in \mathbb{R}^2 \setminus \bar{D}$, let us define

$$v(x_0) := \int_{\Gamma} [u^s(x, x_0) \partial_{\nu_x} G(x, z) - G(x, z) \partial_{\nu_x} u^s(x, x_0)] ds(x). \quad (3.81)$$

By reciprocity, for all $x \in \Gamma$, $u^s(x, \cdot)$ is a radiating solution of

$$\Delta u + k_b^2(x_0)u = 0 \quad (3.82)$$

in $\mathbb{R}^2 \setminus \bar{D}$ with respect to the variable x_0 ; as a consequence, v too is a radiating solution in $\mathbb{R}^2 \setminus \bar{D}$ of the same equation. Moreover, by virtue of (3.80) and (3.81), it holds that:

$$\mathcal{R}(u(\cdot, x_0), G_z) = v(x_0) - G_b(x_0, z) \quad \forall x_0 \in C. \quad (3.83)$$

Since we have supposed that $\Lambda_z \in \text{range}(P)$, there exists $w \in K_1^0$ such that

$$\mathcal{R}(u(\cdot, x_0), G_z) = \int_D [k_1^2 - k_D^2(x)] w(x) u(x, x_0) dx \quad \forall x_0 \in C. \quad (3.84)$$

Now, let \tilde{v} be the function defined for all $x_0 \in \mathbb{R}^2 \setminus \bar{D}$ as

$$\tilde{v}(x_0) := \int_D [k_1^2 - k_D^2(x)] w(x) u(x, x_0) dx. \quad (3.85)$$

Then, by reciprocity, \tilde{v} is a radiating solution of (3.82) in $\mathbb{R}^2 \setminus \bar{D}$. Moreover, by (3.84) and (3.85), we have

$$\mathcal{R}(u(\cdot, x_0), G_z) = \tilde{v}(x_0) \quad \forall x_0 \in C. \quad (3.86)$$

³⁰See e.g. [75], integral representation (7.16) p. 226, or, equivalently, (7.24) p. 229.

Now, from (3.83) and (3.86), it follows that \tilde{v} and $v - G_b(\cdot, z)$ coincide on C . Moreover, since \tilde{v} and $v - G_b(\cdot, z)$ are radiating solutions of (3.82) in $\mathbb{R}^2 \setminus \bar{V}$, by Theorem 3.8.1 they coincide in $\mathbb{R}^2 \setminus \bar{V}$. Then, by virtue of the unique continuation principle, they coincide in $\mathbb{R}^2 \setminus (\bar{D} \cup \{z\})$. Nonetheless, \tilde{v} is regular in z whereas $v - G_b(\cdot, z)$ is not, which is a contradiction. ■

Point 5.

We can now carry out the last point of our workplan, by proving in the next theorem the existence of approximate (in $L^2(C)$) solutions of equation (3.16).

Theorem 3.4.9. *Suppose that k_0 is not a transmission eigenvalue of problem (3.57) and let $z \in \Omega$. Then:*

a) *if $z \in D$, for any given $\epsilon > 0$ there exists a $g_z^\epsilon \in H^{-\frac{1}{2}}(C)$ such that*

$$\left\| \mathcal{R}(u(\cdot, \cdot), s_{g_z^\epsilon}) - \mathcal{R}(u(\cdot, \cdot), G_z) \right\|_{L^2(C)} < \epsilon \quad (3.87)$$

(where $u(\cdot, \cdot)$ is simply obtained by $u(\cdot, x_0) \in U$ when $x_0 \in C$ is regarded as a variable) and $s_{g_z^\epsilon}$ converges in $L^2(D)$ as $\epsilon \rightarrow 0$; moreover, for any fixed $\epsilon > 0$ and for all $z^ \in \partial D$, every $g_z^\epsilon \in H^{-\frac{1}{2}}(C)$ verifying inequality (3.87) is such that*

$$\lim_{z \rightarrow z^*} \|s_{g_z^\epsilon}\|_{L^2(D)} = \infty \quad \text{and} \quad \lim_{z \rightarrow z^*} \|g_z^\epsilon\|_{H^{-\frac{1}{2}}(C)} = \infty; \quad (3.88)$$

b) *if $z \in \Omega \setminus \bar{D}$, for any given $\epsilon > 0$ there exists a $g_z^\epsilon \in H^{-\frac{1}{2}}(C)$ such that*

$$\left\| \mathcal{R}(u(\cdot, \cdot), s_{g_z^\epsilon}) - \mathcal{R}(u(\cdot, \cdot), G_z) \right\|_{L^2(C)} < \epsilon; \quad (3.89)$$

moreover, every $g_z^\epsilon \in H^{-\frac{1}{2}}(C)$ verifying inequality (3.89) is such that

$$\lim_{\epsilon \rightarrow 0} \|s_{g_z^\epsilon}\|_{L^2(D)} = \infty \quad \text{and} \quad \lim_{\epsilon \rightarrow 0} \|g_z^\epsilon\|_{H^{-\frac{1}{2}}(C)} = \infty. \quad (3.90)$$

Proof. a) Let $z \in D$: then, according to Theorem 3.4.8, $\Lambda_z \in \text{range}(P)$: in fact, $\Lambda_z = P(-\tilde{v})$, see (3.78). Since the range of H is dense in K_1^0 with respect to the $L^2(D)$ -norm (by Theorem 3.4.2) and $\tilde{v} \in K_1^0$ (see the first equation of (3.77)), for any given $\epsilon' > 0$ there exists $g_z^{\epsilon'} \in H^{-\frac{1}{2}}(C)$ such that

$$\left\| Hg_z^{\epsilon'} - \tilde{v} \right\|_{L^2(D)} < \epsilon'. \quad (3.91)$$

Hence, recalling the factorization $F = -PH$ given by Theorem 3.4.1, the boundedness of P and the equality $\Lambda_z = P(-\tilde{v})$, we have

$$\left\| Fg_z^{\epsilon'} - \Lambda_z \right\|_{L^2(C)} = \left\| -PHg_z^{\epsilon'} + P\tilde{v} \right\|_{L^2(C)} \leq \|P\| \left\| Hg_z^{\epsilon'} - \tilde{v} \right\|_{L^2(D)} \quad (3.92)$$

and then, by using (3.91), (3.92) and choosing $\epsilon' = \epsilon/\|P\|$, we find

$$\|Fg_z^\epsilon - \Lambda_z\|_{L^2(C)} < \epsilon. \quad (3.93)$$

If we now remember definitions (3.19) and (3.76), we immediately realize that (3.93) is exactly thesis (3.87). The convergence of $s_{g_z^\epsilon}$ in $L^2(D)$ as $\epsilon \rightarrow 0$ immediately follows from the definition (3.20) of H and inequality (3.91).

In order to prove limits (3.88), we first remember equality (3.78), i.e., $\Lambda_z = P(-\tilde{v})$, where (\tilde{v}, \tilde{w}) is the solution of (3.77). Then, we define the function \tilde{u} as

$$\tilde{u} = \begin{cases} \tilde{v} - \tilde{w} & \text{in } D \\ G_z & \text{in } \mathbb{R}^2 \setminus \bar{D}. \end{cases} \quad (3.94)$$

Since $\tilde{v} - \tilde{w} = G_z$ and $\partial_\nu(\tilde{v} - \tilde{w}) = \partial_\nu G_z$ on ∂D , then \tilde{u} is in $H_{\text{loc}}^1(\mathbb{R}^2)$ and is the solution of the following scattering problem:

$$\begin{cases} \Delta u + \tilde{k}^2(x)u = [\tilde{k}^2(x) - k^2(x)]\tilde{v} & \text{in } \mathbb{R}^2 \\ \lim_{r \rightarrow \infty} \sqrt{r}(\partial_r u - ik_0 u) = 0; \end{cases} \quad (3.95)$$

we recall that $k^2(x)$ and $\tilde{k}^2(x)$ are defined in (3.4) and (3.5) respectively. Moreover, by continuity of the solution with respect to initial data, for all $R > 0$ such that D is included in the open ball of centre O and radius R , there exists a constant $\alpha_R \in \mathbb{R}_+^*$ (which depends on R and $\tilde{k}(x)$) such that for all $h \in L^2(D)$, the solution u of the scattering problem

$$\begin{cases} \Delta u + \tilde{k}^2 u = h & \text{in } \mathbb{R}^2 \\ \lim_{r \rightarrow \infty} \sqrt{r}(\partial_r u - ik_0 u) = 0 \end{cases} \quad (3.96)$$

verifies $\|u\|_{H^1(B_R)} \leq \alpha_R \|h\|_{L^2(D)}$. Then, coming back to problem (3.95), we can easily deduce that

$$\|G_z\|_{H^1(B_R \setminus \bar{D})} \leq \alpha_R \|\tilde{v}\|_{L^2(D)}. \quad (3.97)$$

Although the Green's function G_z describes the inhomogeneous background in Ω , by superposition (analogously to relation (3.6)) its singularity in z is only determined by the Green's function of the medium (in our case, the tumour) in which z is located: in particular³¹, $G_z \notin H^1(A)$ for any $A \subset \mathbb{R}^2$ such that $z \in \bar{A}$. Hence, from (3.97), we find that $\lim_{z \rightarrow z^*} \|\tilde{v}\|_{L^2(D)} = \infty$ and consequently, by virtue of (3.91), $\lim_{z \rightarrow z^*} \|Hg_z^\epsilon\|_{L^2(D)} = \infty$, which, remembering definition (3.20), is just the first limit in (3.88). Finally, the boundedness of

³¹See e.g. [35], p. 72.

H (i.e., of the single layer potential³²) implies that $\lim_{z \rightarrow z^*} \|g_z^\epsilon\|_{H^{-\frac{1}{2}}(C)} = \infty$, i.e., the second limit in (3.88).

b) Let $z \in \Omega \setminus \bar{D}$. Since P has a dense range and $\Lambda_z \in \overline{\text{range}(P)} \setminus \text{range}(P)$, we can use Tikhonov regularization [89] to show that there exists a sequence $\{f_{z,p}\}_{p=1}^\infty \subset K_1^0$ such that³³

$$\lim_{p \rightarrow \infty} \|-Pf_{z,p} - \Lambda_z\|_{L^2(C)} = 0 \quad \text{and} \quad \lim_{p \rightarrow \infty} \|f_{z,p}\|_{L^2(D)} = \infty. \quad (3.98)$$

In particular, the first limit in (3.98) implies that, for each $\epsilon > 0$, there exists $\tilde{p} \equiv \tilde{p}(\epsilon)$ such that $f_z^\epsilon := f_{z,\tilde{p}} \in K_1^0$ satisfies

$$\|-Pf_z^\epsilon - \Lambda_z\|_{L^2(C)} < \frac{\epsilon}{2}. \quad (3.99)$$

Moreover, since H has a dense range, for each $\epsilon > 0$ there exists $g_z^\epsilon \in H^{-\frac{1}{2}}(C)$ such that

$$\|Hg_z^\epsilon - f_z^\epsilon\|_{L^2(D)} < \frac{\epsilon}{2\|P\|}. \quad (3.100)$$

Then, by using the triangle inequality, relations (3.99), (3.100) and recalling that $F = -PH$, we get:

$$\begin{aligned} \|Fg_z^\epsilon - \Lambda_z\|_{L^2(C)} &= \|PHg_z^\epsilon + \Lambda_z\|_{L^2(C)} \leq \\ &\leq \|Pf_z^\epsilon - PHg_z^\epsilon\|_{L^2(C)} + \|Pf_z^\epsilon + \Lambda_z\|_{L^2(C)} < \\ &< \|P\| \frac{\epsilon}{2\|P\|} + \frac{\epsilon}{2} = \epsilon, \end{aligned} \quad (3.101)$$

so that inequality (3.89) is verified. Now, let us assume, by contradiction, that there exists a non-divergent sequence $\{f_{z,p}\}_{p=1}^\infty \subset K_1^0$ verifying the first limit in (3.98). Then, we can extract from $\{f_{z,p}\}_{p=1}^\infty$ a subsequence $\{f_{z,q} \equiv f_{z,p(q)}\}_{q=1}^\infty$ that is bounded in $L^2(D)$. Since $\{f_{z,q}\}_{q=1}^\infty$ is bounded, we can in turn extract from it a subsequence $\{f_{z,r} \equiv f_{z,q(r)}\}_{r=1}^\infty$ that is weakly convergent to a certain element $f_z^* \in K_0^1$. The continuity of P then implies that $-Pf_{z,r}$ weakly converges to $-Pf_z^*$; on the other hand, from the first limit in (3.98) we know that $-Pf_{z,r}$ strongly converges to Λ_z in $L^2(C)$: as a consequence, we obtain that $-Pf_z^* = \Lambda_z$, i.e., Λ_z is in the range of P , in contradiction with Theorem 3.4.8. If we now use this argument with a sequence of the kind $\{f_{z,p}\}_{p=1}^\infty := \{s_{g_{z,p}}\}_{p=1}^\infty$ (as made possible by the density of the range of $F = -PH$, see Corollary 3.4.7), we can easily prove the first limit in (3.90). Finally, as in the previous case a), the boundedness of the operator H implies the second limit in (3.90). ■

³²See e.g. [75], p. 203.

³³For details, see [4], p. 30 and p. 131.

Remark 3.4.1. By using the denseness³⁴ of $L^2(C)$ in $H^{-1/2}(C)$ and the boundedness of the operator H , it is easy to realize that Theorem 3.4.9 holds unchanged when the approximate solution g_z^ϵ is taken in $L^2(C)$ instead of $H^{-1/2}(C)$. \square

3.5 The visualization algorithm

The goal of the present section is to show how breast tumours can be visualized by using the RGF equation (3.16) as a tool to compute an indicator function (as suggested by Theorem 3.4.9 and Remark 3.4.1). The traditional pointwise algorithm presented in [36, 44] takes inspiration from blowing-up limits analogous to those in (3.88) and (3.90), and consists in plotting, for each z belonging to a numerical grid covering the sampling region Ω , a Tikhonov regularized solution of (3.16).

We first observe that in real experiments one needs to perform an angular discretization involving the positions of both the antennas on C sending the incident waves and the antennas on Γ measuring the total electric field and its normal derivative (i.e., the tangential component of the total magnetic field³⁵). For the sake of simplicity, we discretize the continuous parameters x_Γ on Γ and y_C on C with the same number N of equispaced knots, choosing C and Γ as concentric circles of radii R_C and R_Γ respectively; in particular, we now have $\Omega = \{z \in \mathbb{R}^2 : |z| < R_\Gamma\}$. Moreover, each of the pairs of discretization points $\{(x_0, y_0), \dots, (x_{N-1}, y_{N-1})\}$ is assumed to belong to a radius of C , i.e., the (pointlike) emitting and receiving antennas are in a radial symmetry (we notice that relaxing these assumptions would not change the general scheme of the following visualization algorithm, but would make the new formulation more complicated). The discretized form of (3.16) can be written in a compact form by establishing the following notations for each $i, j = 0, \dots, N-1$ and for each $z \in \Omega$:

$$U_{ij} := u(x_i, y_j), \quad L_{ij} := \frac{\partial G}{\partial \nu(x)}(x_i, y_j), \quad g_j := g(y_j), \quad G_{ij} := G(x_i, y_j), \quad (3.102)$$

$$V_{ij} := \frac{\partial u}{\partial \nu(x)}(x_i, y_j), \quad l_i(z) := \frac{\partial G}{\partial \nu(x)}(x_i, z), \quad q_i(z) := G(x_i, z).$$

We now regard the quantities U_{ij} , L_{ij} , G_{ij} , V_{ij} as the entries of the square $N \times N$ matrices \mathbf{U} , \mathbf{L} , \mathbf{G} , \mathbf{V} respectively, while we consider g_j , $l_i(z)$, $q_i(z)$ as the N components of the column vectors \mathbf{g} , $\mathbf{l}(z)$, $\mathbf{q}(z)$; finally, using the common matrix transposition and the rows

³⁴See e.g. [75], p. 98.

³⁵Cf. footnote no. 21, p. 52.

\times columns product, we set, for all $z \in \Omega$,

$$\mathbf{\Delta s} := \text{diag}(\Delta s_j) \equiv \frac{2\pi R_C}{N} \mathbf{I}_N, \quad \mathbf{D} := \mathbf{U}^T \mathbf{L} - \mathbf{V}^T \mathbf{G}, \quad \mathbf{b}(z) := \mathbf{U}^T \mathbf{l}(z) - \mathbf{V}^T \mathbf{q}(z), \quad (3.103)$$

where \mathbf{I}_N is the identity matrix of order N and $\frac{2\pi R_C}{N}$ is the (constant) discretization step $\Delta s_j > 0$ over $C \forall j = 0, \dots, N-1$. With the previous notations, the discretized version of (3.16) is the one-parameter family of linear systems in the (z -dependent) unknown $\mathbf{g} = \mathbf{g}(z)$

$$\mathbf{D} \mathbf{\Delta s} \mathbf{g}(z) = \mathbf{b}(z) \quad \forall z \in \Omega. \quad (3.104)$$

From now on, we shall denote by $\mathbb{C}_{\mathbf{\Delta s}}^N$ the vector space \mathbb{C}^N equipped with the $\mathbf{\Delta s}$ -weighted scalar product, defined as $(\mathbf{x}, \mathbf{y})_{\mathbf{\Delta s}, \mathbb{C}^N} := \sum_{j=1}^N x_j \Delta s_j \bar{y}_j$ for all $\mathbf{x}, \mathbf{y} \in \mathbb{C}^N$; this scalar product naturally induces a norm denoted by $\|\cdot\|_{\mathbf{\Delta s}, \mathbb{C}^N}$. Then we shall regard the matrix $\mathbf{A} := \mathbf{D} \mathbf{\Delta s}$ as the matrix representation of the linear operator $\mathcal{A} : \mathbb{C}_{\mathbf{\Delta s}}^N \rightarrow \mathbb{C}_{\mathbf{\Delta s}}^N$ such that $\mathcal{A}(\mathbf{x}) = \mathbf{D} \mathbf{\Delta s} \mathbf{x}$ for all $\mathbf{x} \in \mathbb{C}_{\mathbf{\Delta s}}^N$. We now point out that our simplified model for the healthy breast allows an analytic knowledge of the matrices \mathbf{L} and \mathbf{G} , as well as of the column vectors $\mathbf{l}(z)$ and $\mathbf{q}(z)$, but for the sake of brevity we shall omit these laborious computations. In the case of more complex models for the healthy breast, \mathbf{L} , \mathbf{G} , $\mathbf{l}(z)$ and $\mathbf{q}(z)$ can be determined numerically. On the other hand, the experimental data are collected in the matrices \mathbf{U} and \mathbf{V} : then, in general, only their noisy versions $\tilde{\mathbf{U}}$ and $\tilde{\mathbf{V}}$ are known. As a consequence of definitions (3.103), both the matrix \mathbf{D} and the column vector $\mathbf{b}(z)$ should be replaced by their noisy versions \mathbf{D}_h and $\mathbf{b}_\delta(z)$ in equation (3.104), which then becomes

$$\mathbf{A}_h \mathbf{g}(z) = \mathbf{b}_\delta(z) \quad \forall z \in \Omega, \quad (3.105)$$

having denoted by $\mathbf{A}_h := \mathbf{D}_h \mathbf{\Delta s}$ the matrix representation of the noisy version \mathcal{A}_h of the linear operator \mathcal{A} . Here the subscripts h and δ refer to bounds on the noise level, as specified in the following.

To implement the same no-sampling³⁶ approach already developed for the LSM, we replace (3.105) with the functional equation in $[L^2(\Omega)]^N := \bigoplus_{i=1}^N L^2(\Omega)$

$$[\mathbf{A}_h \mathbf{g}(\cdot)](\cdot) = \mathbf{b}_\delta(\cdot), \quad (3.106)$$

where the linear operator $\mathbf{A}_h : [L^2(\Omega)]^N \rightarrow [L^2(\Omega)]^N$ is defined as

$$[\mathbf{A}_h \mathbf{g}(\cdot)](\cdot) := \left\{ \sum_{j=0}^{N-1} (A_h)_{ij} g_j(\cdot) \right\}_{i=0}^{N-1} \quad \forall \mathbf{g}(\cdot) = \{g_j(\cdot)\}_{j=0}^{N-1} \in [L^2(\Omega)]^N \quad (3.107)$$

³⁶See Chapter 2, or [7, 27].

and $(A_h)_{ij}$ are the entries of the noisy matrix \mathbf{A}_h previously introduced. Here, we are regarding $[L^2(\Omega)]^N$ as a Hilbert space with the scalar product

$$(\mathbf{f}(\cdot), \mathbf{g}(\cdot))_{2,N} := \int_{\Omega} (\mathbf{f}(z), \mathbf{g}(z))_{\Delta_{\mathbf{s}}, \mathbb{C}^N} dz \quad \forall \mathbf{f}(\cdot), \mathbf{g}(\cdot) \in [L^2(\Omega)]^N, \quad (3.108)$$

and the induced norm

$$\|\mathbf{f}(\cdot)\|_{2,N} := \sqrt{\int_{\Omega} \|\mathbf{f}(z)\|_{\Delta_{\mathbf{s}}, \mathbb{C}^N}^2 dz} \quad \forall \mathbf{f}(\cdot) \in [L^2(\Omega)]^N. \quad (3.109)$$

According to our discretization, if $\mathbf{f}(\cdot) = \{f_i(\cdot)\}_{i=0}^{N-1}$ and $\mathbf{g}(\cdot) = \{g_i(\cdot)\}_{i=0}^{N-1}$, the scalar product (3.108) can be equivalently defined as

$$(\mathbf{f}(\cdot), \mathbf{g}(\cdot))_{2,N} := \frac{2\pi R_C}{N} \sum_{i=0}^{N-1} (f_i(\cdot), g_i(\cdot))_2, \quad (3.110)$$

where $(\cdot, \cdot)_2$ denotes the canonical scalar product in $L^2(\Omega)$.

The Tikhonov regularized solution $\mathbf{g}_{\alpha}(\cdot)$ of equation (3.106) can be explicitly computed by using the singular representation of the linear operator \mathcal{A}_h , whose singular system $\{\sigma_p^h; \mathbf{u}_p^h, \mathbf{v}_p^h\}_{p=0}^{r^h-1}$ is strictly related³⁷ to that of the matrix \mathbf{A}_h (r^h is the rank of \mathbf{A}_h). By means of an argument analogous to the proof of Theorem 2.5.2, p. 25, we find

$$\mathbf{g}_{\alpha}(\cdot) = \sum_{p=0}^{r^h-1} \frac{\sigma_p^h}{(\sigma_p^h)^2 + \alpha} \langle \mathbf{b}_{\delta}(\cdot), \mathbf{v}_p^h \rangle_{\Delta_{\mathbf{s}}, \mathbb{C}^N} \mathbf{u}_p^h, \quad (3.111)$$

where, for any $\mathbf{f}(\cdot) \in [L^2(\Omega)]^N$ and $\mathbf{w} \in \mathbb{C}_{\Delta_{\mathbf{s}}}^N$, we have denoted by $\langle \mathbf{f}(\cdot), \mathbf{w} \rangle_{\Delta_{\mathbf{s}}, \mathbb{C}^N}$ the element of $L^2(\Omega)$ defined as

$$\begin{aligned} \langle \mathbf{f}(\cdot), \mathbf{w} \rangle_{\Delta_{\mathbf{s}}, \mathbb{C}^N} : \Omega &\longrightarrow \mathbb{C} \\ z &\longmapsto (\mathbf{f}(z), \mathbf{w})_{\Delta_{\mathbf{s}}, \mathbb{C}^N} \quad \text{f.a.a. } z \in \Omega. \end{aligned} \quad (3.112)$$

The visualization method based on the analysis of the RGF equation is therefore:

1. compute (3.111) by using the singular system of \mathcal{A}_h ;
2. fix a value α^* for the regularization parameter α by applying some optimality criterion;

³⁷See Section 2.9, p. 39.

3. choose a suitable continuous monotonic function $J : [0, \infty) \rightarrow \mathbb{R}$ and plot the indicator function $\Psi(z) = J\left(\|\mathbf{g}_{\alpha^*}(z)\|_{\Delta\mathbf{s}, \mathbb{C}^N}^2\right)$ for $z \in \Omega$, where

$$\|\mathbf{g}_{\alpha^*}(z)\|_{\Delta\mathbf{s}, \mathbb{C}^N}^2 = \sum_{p=0}^{r^h-1} \frac{(\sigma_p^h)^2}{[(\sigma_p^h)^2 + \alpha^*]^2} \left| (\mathbf{b}_\delta(z), \mathbf{v}_p^h)_{\Delta\mathbf{s}, \mathbb{C}^N} \right|^2. \quad (3.113)$$

From now on this algorithm will be called ‘RGFM’ (in the present implementation we have chosen $J = -\ln$).

Item No. 2 is a critical step. It can be implemented by applying the generalized discrepancy principle [89], i.e., by finding the zero α^* of the generalized discrepancy function

$$\rho(\alpha) := \|\mathbf{A}_h \mathbf{g}_\alpha(\cdot)(\cdot) - \mathbf{b}_\delta(\cdot)\|_{2,N}^2 - (\delta + h \|\mathbf{g}_\alpha(\cdot)\|_{2,N})^2, \quad (3.114)$$

where we assume that noise bounds δ , h are known, such that

$$\|\mathbf{b}_\delta(\cdot) - \mathbf{b}(\cdot)\|_{2,N} \leq \delta, \quad \|\mathbf{A}_h - \mathbf{A}\| \leq h. \quad (3.115)$$

In the second inequality of (3.115), \mathbf{A} denotes the noise-free version of \mathbf{A}_h and $\|\cdot\|$ the operator norm: as in [7, 27], it is possible to prove that $\|\mathbf{A}_h - \mathbf{A}\| = \|\mathcal{A}_h - \mathcal{A}\| = |\sigma_0^h - \sigma_0|$, where σ_0 is the largest singular value of \mathcal{A} . Taking into account definitions (3.109) and (3.112), we can make the expression (3.114) of $\rho(\alpha)$ more explicit, i.e.,

$$\begin{aligned} \rho(\alpha) = & \sum_{p=0}^{r^h-1} \frac{\alpha^2 - h^2(\sigma_p^h)^2}{[(\sigma_p^h)^2 + \alpha]^2} \int_{\Omega} dz \left| (\mathbf{b}_\delta(z), \mathbf{v}_p^h)_{\Delta\mathbf{s}, \mathbb{C}^N} \right|^2 - \delta^2 + \\ & - 2\delta h \sqrt{\sum_{p=0}^{N-1} \frac{(\sigma_p^h)^2}{[(\sigma_p^h)^2 + \alpha]^2} \int_{\Omega} dz \left| (\mathbf{b}_\delta(z), \mathbf{v}_p^h)_{\Delta\mathbf{s}, \mathbb{C}^N} \right|^2}. \end{aligned} \quad (3.116)$$

Remark 3.5.1. The regularization procedure for this no-sampling RGFM is more difficult than the same procedure for the no-sampling LSM, since here we have two noisy terms, i.e., that containing the operator and that on the right-hand side of equation (3.106): in the case of the LSM, the right-hand side of the far-field equation is exactly known (i.e., $\delta = 0$). \square

3.6 Applications to data

The purpose of this section is to validate the RGF visualization algorithm described above against synthetic near-fields in a microwave tomography experiment for breast cancer

detection. The direct scattering data are computed by means of a standard method of moments code [81]. A set of $N = 16$ emitting antennas are placed on a circle surrounding the breast at a distance of $4.00 \cdot 10^{-2}$ m from the skin. The incident fields are TM-polarized cylindrical waves at a fixed frequency of 1.00 GHz. The total electric field and its normal derivative on Γ are computed by the code, corrupted by 10% random Gaussian noise and then collected by $N = 16$ receiving antennas placed in a radial symmetry with respect to the emitters, on a circle Γ at a distance of $3.00 \cdot 10^{-2}$ m from the skin. For all simulations, the computational time of the RGFM is very short, i.e., around 1 s.

In order to perform our simulations, the values of the geometric and electrical parameters characterizing the biological tissues (at a frequency of 1.00 GHz) are chosen in agreement with the realistic models given in [64], i.e., skin: $\varepsilon_r = 4.09 \cdot 10^1$, $\sigma = 9.00 \cdot 10^{-1}$ S/m; fat: $\varepsilon_r = 1.00 \cdot 10^1$, $\sigma = 1.50 \cdot 10^{-1}$ S/m; tumour: $\varepsilon_r = 5.39 \cdot 10^1$, $\sigma = 7.00 \cdot 10^{-1}$ S/m; vein: $\varepsilon_r = 5.00 \cdot 10^1$, $\sigma = 1.70 \cdot 10^{-1}$ S/m; gland: $\varepsilon_r = 1.15 \cdot 10^1$, $\sigma = 1.70 \cdot 10^{-1}$ S/m. Our simplified model of the healthy breast consists of a disk representing the fat tissue, surrounded by a circular corona representing the skin: the radius of the disk is $4.00 \cdot 10^{-2}$ m and the thickness of the skin layer is $2.00 \cdot 10^{-3}$ m.

In the first numerical example, we place into the fat a circular tumour with a diameter of $1.00 \cdot 10^{-2}$ m: the corresponding phantom is represented in Fig. 5.8(a). Then, the RGFM is applied to the direct scattering data computed for this phantom, thus providing the visualization in Fig. 5.8(b).

The second simulation considers the same phantom as in Fig. 5.8, but now a square scatterer (with $\varepsilon_r = 2.00$, $\sigma = 1.50$ S/m) is placed outside the breast, as represented in Fig. 5.9(a). The visualization provided by the RGFM is shown in Fig. 5.9(b): the algorithm is robust with respect to the presence of outer scatterers, although their presence is not encoded in the Green's function used to implement it.

In the third example, two circular tumours having the same diameter of $1.50 \cdot 10^{-2}$ m are placed at a distance of $3.16 \cdot 10^{-2}$ m between their centres, as illustrated in Fig. 5.10(a); the corresponding RGF visualization is shown in Fig. 5.10(b).

In the fourth experiment, the more realistic phantom of Fig. 5.11(a) is considered. Here the electrical parameters of the healthy fat are perturbed with components randomly drawn from a uniform distribution within 10% around the unperturbed values; moreover, six veins and one gland are placed into the breast. Two veins are in the imaging plane, while the other four flow in the orthogonal direction; the gland is just along one of the two veins (the vertical one, on the right) in the imaging plane. Of course, this perturbation is not coded into the Green's function, which then remains the same as in the previous cases. Finally, a circular tumour with a diameter of $1.50 \cdot 10^{-2}$ m is placed into this phantom.

The application of the RGFM leads to the visualization of Fig. 5.11(b), where the tumour is clearly visible, although the limited resolution of the procedure is pointed out by an increase of its apparent diameter, as shown by a comparison with the visualization of Fig. 5.8(b).

As one could expect, the perturbation of the healthy background becomes increasingly important as the size of the tumour diminishes. This effect is highlighted by the fifth simulation, in which a circular tumour with a diameter of $1.00 \cdot 10^{-2}$ m is placed into the same perturbed background as before: the phantom is shown in Fig. 5.12(a). In the visualization provided by the RGFM and represented in Fig. 5.12(b), the tumour is still detectable, but, mainly due to the veins in the imaging plane, its size tends to be overestimated and an artefact appears on the right. Therefore, under these conditions, the distinction between the tumour and the artefact can be obtained by means of a different imaging modality providing some quantitative information on the different kinds of tissue.

Although, *a priori*, the RGFM can visualize a tumour only if $G(\cdot, y)$ is exactly known, the previous simulations show that reliable visualizations can be obtained even with an incomplete knowledge of $G(\cdot, y)$, i.e., when only the Green's function corresponding to fat, skin and free space is available.

3.7 Conclusions and hints for future developments

In this chapter we generalize the formulation and improve the implementation of a linear qualitative method, based on the so-called 'reciprocity gap functional', for solving inverse scattering problems that are, in general, genuinely non-linear, i.e., allow no realistic linearizing approximation. Furthermore, we apply this approach for the first time to the visualization of breast cancer in a microwave tomography setting. From the theoretical viewpoint, the generalization consists of developing a formulation that takes into account the possible heterogeneity of the background medium inside the array of receiving antennas: in particular, if this background is lossy, an interior transmission problem with complex wave numbers needs to be discussed, in order to show that transmission eigenvalues form a discrete set. Although our focus is on the inverse problem of microwave tomography for breast cancer detection, other scattering situations (for penetrable targets) are easily incorporated in our framework by considering the proper Green's function; moreover, an analogous generalization could also be carried out in the case of impenetrable scatterers. From the viewpoint of implementation, the improvement consists of adopting a no-sampling approach, which provides very fast 2D visualizations of the breast: indeed, the computational times of the RGFM are around 1 s.

Of course, a weak point of the RGFM is that the physical and geometric properties of the healthy breast should be known *a priori*. This prior knowledge could be available, at least approximately, from previous clinical exams (e.g., MRI) of the same patient. In any case, future research should be devoted to assessing the stability and reliability of the RGFM with respect to uncertainties in the Green's function describing the healthy breast: in this context, our first results, as shown in Fig. 5.11 and Fig. 5.12, seem to highlight a promising robustness of the RGFM.

The real impact of the RGFM-based imaging technique should be evaluated by comparing it with other existing inversion methods, both qualitative (such as the LSM for near-field measurements, used for breast cancer detection in [21, 24]) and quantitative (such as the algorithms proposed in [68] or in [85]): to this aim, it would be interesting to perform a theoretical and operative analysis of the RGFM in order to assess the resolution achievable and to estimate the optimal number of antennas surrounding the breast, i.e., the minimum number of measurements needed to collect all the retrievable information. Since these issues were already discussed in Section 2.8 of Chapter 2 for the LSM, we shall not repeat here our considerations.

Of course, for segmentation purposes, an important step is to extract, in an automatic way and in short computational times, the profile of the tumoural masses from the visualization map provided by the RGFM. Moreover, although in some applications a fast visualization of the support of the tumour might be sufficient, a deeper analysis is often desirable: then, knowing the pointwise electrical parameters of the (possibly) cancerous tissue is an important information. To this end, it is necessary to use an iterative algorithm, which needs to be properly initialized. An accurate initialization requires the approximate knowledge of the geometric and physical properties of the tumour: the geometric information can be obtained from the profile automatically determined by post-processing the RGFM visualization, as just recalled, while a good initial guess for the electrical parameters is given by the typical or average values (easily available in literature) characterizing the tumoural masses of the female breast. Again, we refer to Section 2.8 of Chapter 2 for a discussion of these post-processing and hybridization issues.

Finally, we point out that each step of the overall approach proposed here should be tested against both simulated and real data. Then, a twofold effort is necessary: developing an efficient software that can generate, invert and (post-)process the direct scattering data, and constructing (or, at least, having at disposal) a reliable microwave tomograph.

3.8 Addenda to Chapter 3

3.8.1 Complementary theorems

In this subsection we want to prove two theorems previously used in the current chapter. The first theorem is the generalization for k not constant of Theorem 2.12 in [48].

Theorem 3.8.1. *Let W be an open and bounded Lipschitz domain such that $\mathbb{R}^2 \setminus \overline{W}$ is connected; let $k \in L^\infty(\mathbb{R}^2 \setminus \overline{W})$ and $R > 0$ be such that $k(x) = k_0 \in \mathbb{R}_+^* = (0, +\infty)$ for $|x| \geq R$. Moreover, let u be the unique solution of the following problem:*

$$\begin{cases} \Delta u + k^2(x)u = 0 & \text{in } \mathbb{R}^2 \setminus \overline{W} \\ u = 0 & \text{on } \partial W \\ \lim_{r \rightarrow \infty} \sqrt{r}(\partial_r u - ik_0 u) = 0. \end{cases} \quad (3.117)$$

Then, it holds that $u = 0$ in $\mathbb{R}^2 \setminus \overline{W}$.

Proof. Let $r \geq R$ be such that the open ball B_r with centre at the origin O and radius r contains \overline{W} . If we set $S_r := \partial B_r$ and we remember the first two equations in (3.117), as well as the hypothesis $k(x) = k_0$ for $|x| \geq R$, then the first Green's identity³⁸ shows that

$$\int_{S_r} u(x) \partial_\nu \bar{u}(x) ds(x) = \int_{B_r \setminus \overline{W}} |\nabla u(x)|^2 dx - \int_{B_r \setminus \overline{W}} k_0^2 |u(x)|^2 dx. \quad (3.118)$$

Taking the imaginary part of each term in this equation, we get

$$\operatorname{Im} \left\{ \int_{S_r} u(x) \partial_\nu \bar{u}(x) ds(x) \right\} = 0. \quad (3.119)$$

Hence, by virtue of Theorem 2.12 in [48], we deduce that $u = 0$ in $\mathbb{R}^2 \setminus \overline{B_r}$ and then the unique continuation principle ensures that $u = 0$ in $\mathbb{R}^2 \setminus \overline{W}$. ■

The second theorem links the injectivity of the single layer operator on the boundary of a domain to the solvability of the Dirichlet problem.

Theorem 3.8.2. *Let W be a bounded Lipschitz domain and let $W' \subset W$ be an open subset of W ; if $k \in L^\infty(W)$ is such that $\operatorname{Im} \{k^2(x)\} \geq 0$ f.a.a. $x \in W$ and $\operatorname{Im} \{k^2(x)\} \geq c > 0$ f.a.a. $x \in W'$, then the single layer operator $S_{\partial W} : H^{-\frac{1}{2}}(\partial W) \rightarrow H^{\frac{1}{2}}(\partial W)$ is bijective.*

Proof. Let $\varphi \in H^{-\frac{1}{2}}(\partial W)$ be such that $S_{\partial W} \varphi = 0$ and let v be the single layer potential of density φ , i.e.,

$$v(x) := \int_{\partial W} G(x, y) \varphi(y) ds(y) \quad \forall x \in \mathbb{R}^2 \setminus \partial W. \quad (3.120)$$

³⁸See e.g. [75], p. 118.

Then, in particular, v solves the following Dirichlet problem:

$$\begin{cases} \Delta v + k^2(x)v = 0 & \text{in } W \\ v = 0 & \text{on } \partial W. \end{cases} \quad (3.121)$$

By using the first Green's identity in W and remembering both the equation and the boundary condition in (3.121), we get:

$$-\int_W |\nabla v(x)|^2 dx + \int_W k^2(x)|v(x)|^2 dx = 0. \quad (3.122)$$

By taking the imaginary part of each term in (3.122), we obtain

$$\int_W \operatorname{Im} \{k^2(x)\} |v(x)|^2 dx = 0. \quad (3.123)$$

By virtue of the hypotheses made on $\operatorname{Im} \{k^2(x)\}$, we find $\int_W |v(x)|^2 dx = 0$: hence $v = 0$ in W' and by the unique continuation principle $v = 0$ in W . Then, in particular, $\partial_\nu v^- = 0$. Moreover v is a solution of problem (3.117) and Theorem 3.8.1 ensures that $v = 0$ in $\mathbb{R}^2 \setminus \overline{W}$: then $\partial_\nu v^+ = 0$. Now, according to the jump relations³⁹ for the single layer potentials, it holds that $-\varphi = \partial_\nu v^+ - \partial_\nu v^-$: hence $\varphi = 0$ and this shows the injectivity of $S_{\partial W}$. Since $S_{\partial W}$ is a Fredholm operator⁴⁰ of index 0, it is also bijective. ■

3.8.2 The interior transmission problem

In this subsection we discuss an interior transmission problem that plays an important role in the framework of the current chapter.

Let D be an open bounded Lipschitz domain and let us consider the following interior transmission problem: for all $h \in H_\Delta^1(D)$, find $u, v \in H_\Delta^0(D)$ such that $u - v \in H_\Delta^1(D)$ and

$$\begin{cases} \Delta u + k^2 n_1(k)u = 0 & \text{in } D \\ \Delta v + k^2 n_D(k)(x)v = 0 & \text{in } D \\ (u - v) = h & \text{on } \partial D \\ \partial_\nu(u - v) = \partial_\nu h & \text{on } \partial D, \end{cases} \quad (3.124)$$

where $k \in \mathbb{R}_+^* = (0, +\infty)$, $n_1 : \mathbb{R}_+^* \rightarrow \mathbb{C}$ is a complex-valued function of the real variable k and $n_D : \mathbb{R}_+^* \rightarrow L^\infty(D)$ is a function of the real variable k with values in the space $L^\infty(D)$. We now want to show that under some assumptions the problem (3.124) has a unique solution.

³⁹See e.g. [75], p. 203.

⁴⁰See e.g. [75], p. 33 and p. 227.

We first consider the homogeneous version of problem (3.124), i.e., the case in which the function h is identically zero, and we want to show that this problem has only the trivial solution, except for a discrete set of values for k . Then, if we call ‘set of transmission eigenvalues’ the set of values of k such that the homogeneous transmission problem has a non trivial solution, this means that the set of transmission eigenvalues is a discrete subset of \mathbb{R}_+^* .

Following the same steps as in [83], the following lemma for the homogeneous interior transmission problem can be easily proved.

Lemma 3.8.3. *Set $m(k) := n_1(k) - n_D(k)$ for all $k \in (0, \infty)$; if k is such that $m^{-1}(k) \in L^\infty(D)$, then the homogeneous transmission problem has a non trivial solution if and only if there exists a nontrivial function $w \in H_{\Delta,0}^1(D)$ such that*

$$F_k(w, \psi) = 0 \quad \forall \psi \in H_{\Delta,0}^1(D), \quad (3.125)$$

where $H_{\Delta,0}^1(D)$ is the Hilbert space (with respect to the norm given by (3.13)) defined as

$$H_{\Delta,0}^1(D) := \{u \in H_\Delta^1(D) : u = \partial_\nu u = 0 \text{ on } \partial D\}, \quad (3.126)$$

and F_k is the bounded sesquilinear form defined on $H_{\Delta,0}^1(D)$ as

$$\begin{aligned} F_k(\phi, \psi) &:= \int_D m^{-1}(k)(x) [\Delta + k^2 n_1(k)] \phi(x) [\Delta + k^2 n_D(k)] \bar{\psi}(x) dx = \\ &= (m^{-1}(k) [\Delta + k^2 n_1(k)] \phi, [\Delta + k^2 \bar{n}_D(k)] \psi)_0 \quad \forall \phi, \psi \in H_{\Delta,0}^1(D), \end{aligned} \quad (3.127)$$

having denoted by $(\cdot, \cdot)_0$ the scalar product in $L^2(D)$.

Now, for all $k \in \mathbb{R}_+^*$ such that $m^{-1}(k) \in L^\infty(D)$, let us define the following sesquilinear forms: $\forall \phi, \psi \in H_{\Delta,0}^1(D)$,

$$\begin{aligned} F_k^0(\phi, \psi) &:= (m^{-1}(k) \Delta \phi, \Delta \psi)_0, & F_k^1(\phi, \psi) &:= k^2 (m^{-1}(k) n_1(k) \phi, \Delta \psi)_0, \\ F_k^D(\phi, \psi) &:= k^2 (m^{-1}(k) \Delta \phi, \bar{n}_D(k) \psi)_0, & F_k^{1D}(\phi, \psi) &:= k^4 (m^{-1}(k) n_1(k) \phi, \bar{n}_D(k) \psi)_0. \end{aligned} \quad (3.128)$$

$$(3.129)$$

Then, for all $k \in \mathbb{R}_+^*$ such that $m^{-1}(k) \in L^\infty(D)$, it obviously holds that

$$F_k = F_k^0 + F_k^1 + F_k^D + F_k^{1D}. \quad (3.130)$$

Moreover, it can be easily shown that the following sesquilinear form on $H_{\Delta,0}^1(D)$

$$\forall u, v \in H_{\Delta,0}^1(D), \quad (u, v)_{\Delta,0} := (\Delta u, \Delta v)_0 \quad (3.131)$$

defines a scalar product on $H_{\Delta,0}^1(D)$ equivalent to the H_{Δ}^1 scalar product. Then, according to the Lax-Milgram theorem, for all $k \in \mathbb{R}_+^*$ such that $m^{-1}(k) \in L^\infty(D)$ we can introduce the operators associated with the previous forms (3.127), (3.128), (3.129), i.e., the operators in $H_{\Delta,0}^1(D)$ defined as

$$(S_k \phi, \psi)_{\Delta,0} := F_k(\phi, \psi), \quad (S_k^0 \phi, \psi)_{\Delta,0} := F_k^0(\phi, \psi), \quad (S_k^1 \phi, \psi)_{\Delta,0} := F_k^1(\phi, \psi), \quad (3.132)$$

$$(S_k^D \phi, \psi)_{\Delta,0} := F_k^D(\phi, \psi), \quad (S_k^{1D} \phi, \psi)_{\Delta,0} := F_k^{1D}(\phi, \psi) \quad \forall \phi, \psi \in H_{\Delta,0}^1(D). \quad (3.133)$$

Then, we clearly have

$$S_k = S_k^0 + S_k^1 + S_k^D + S_k^{1D}. \quad (3.134)$$

We now make the following assumptions (we shall shortly discuss their consistency with physics in the final Remark 3.8.1):

- 1) n_1 and n_D are analytic functions of k on \mathbb{R}_+^* : in this case we know that there exists an open and connected set $W \subset \mathbb{C}$ containing \mathbb{R}_+^* such that n_1 and n_D can be continued to analytic functions in W and for all such sets W the continuation is unique;
- 2) among the previous sets W , there exists a set \tilde{W} such that the set $Sing(m) := \{z \in \tilde{W} : m^{-1}(z) \notin L^\infty(D)\}$ is discrete;
- 3) there exists an open connected subset X of $\tilde{W} \setminus Sing(m)$ containing $\mathbb{R}_+^* \setminus Sing(m)$ such that, for all $z \in X$, either $\text{Re}\{m^{-1}(z)\} > c_z > 0$ on D , or $\text{Im}\{m^{-1}(z)\} > c_z > 0$ on D , or $\text{Re}\{m^{-1}(z)\} < -c_z < 0$ on D , or $\text{Im}\{m^{-1}(z)\} < -c_z < 0$ on D , where, for all $z \in X$, c_z is a positive constant, depending on z and verifying $\|m^{-1}(z)\|_\infty = o\left(\frac{c_z}{z^2}\right)$ as $z \rightarrow 0$;
- 4) n_1 and n_D are bounded when $k \in \mathbb{R}_+^*$ goes to 0.

As in [83], by exploiting the previous decomposition (3.134), we can prove that S_k is a Fredholm operator of index 0. Then, by using the analytic Fredholm theory, we can show that S_k is non-singular except for a discrete set of values of k : this task is accomplished by the following three theorems.

Theorem 3.8.4. *Let $z \in X$: then the operators S_z^1 , S_z^D and S_z^{1D} are compact.*

Proof. For all $\phi \in H_{\Delta,0}^1(D)$, from definitions (3.128), (3.129), (3.131), (3.132) and (3.133)

we have:

$$\begin{aligned}
(\Delta S_z^1 \phi, \Delta S_z^1 \phi)_0 &= (S_z^1 \phi, S_z^1 \phi)_{\Delta,0} = F_z^1(\phi, S_z^1 \phi) = z^2 (m^{-1}(z)n_1(z)\phi, \Delta S_z^1 \phi)_0, \\
(\Delta S_z^D \phi, \Delta S_z^D \phi)_0 &= (S_z^D \phi, S_z^D \phi)_{\Delta,0} = F_z^D(\phi, S_z^D \phi) = z^2 (m^{-1}(z)\Delta\phi, \bar{n}_D(z)S_z^D \phi)_0, \\
(\Delta S_z^{1D} \phi, \Delta S_z^{1D} \phi)_0 &= (S_z^{1D} \phi, S_z^{1D} \phi)_{\Delta,0} = F_z^{1D}(\phi, S_z^{1D} \phi) = \\
&= z^4 (m^{-1}(z)n_1(z)\phi, \bar{n}_D(z)S_z^{1D} \phi)_0,
\end{aligned}$$

whence we respectively get, for all $\phi \in H_{\Delta,0}^1(D)$,

$$\|S_z^1 \phi\|_{\Delta,0} \leq |z|^2 \|m^{-1}(z)\|_{\infty} |n_1(z)| \|\phi\|_0, \quad (3.135)$$

$$\|S_z^D \phi\|_{\Delta,0}^2 \leq |z|^2 \|m^{-1}(z)\|_{\infty} \|n_D(z)\|_{\infty} \|\phi\|_{\Delta,0} \|S_z^D \phi\|_0, \quad (3.136)$$

$$\|S_z^{1D} \phi\|_{\Delta,0}^2 \leq |z|^4 \|m^{-1}(z)\|_{\infty} \|n_D(z)\|_{\infty} |n_1(z)| \|\phi\|_0 \|S_z^{1D} \phi\|_0. \quad (3.137)$$

Since the injection $H_{\Delta,0}^1(D) \hookrightarrow L^2(D)$ is compact, inequalities (3.135), (3.136) and (3.137) prove the compactness of S_z^1 , S_z^D and S_z^{1D} respectively. ■

Theorem 3.8.5. *For all $z \in X$, the operator S_z^0 is non-singular.*

Proof. For all $\phi \in H_{\Delta,0}^1(D)$, by virtue of definitions (3.128) and (3.132) we have

$$(S_z^0 \phi, \phi)_{\Delta,0} = F_z^0(\phi, \phi) = (m^{-1}(z)\Delta\phi, \Delta\phi)_0. \quad (3.138)$$

Hence, by using the previous assumption No. 3 on $m^{-1}(z)$, we can deduce that either $\pm S_k^0$ or $\pm iS_k^0$ is positive and bounded from below, and then S_k^0 is non-singular. ■

Theorem 3.8.6. *The operator S_k is non-singular except for a discrete set of values of $k \in \mathbb{R}_+^*$.*

Proof. Let $\eta \in \mathbb{R}_+^*$ be such that $\|\phi\|_0 \leq \eta \|\phi\|_{\Delta,0}$ for all $\phi \in H_{\Delta,0}^1(D)$. According to assumptions 3 and 4, we can consider $k \in (0, 1) \setminus \text{Sing}(m)$ such that

$$|n_1(k)| \|m^{-1}(k)\|_{\infty} \leq \frac{c_k}{4\eta}, \quad (3.139)$$

$$\|n_D(k)\|_{\infty} \|m^{-1}(k)\|_{\infty} \leq \frac{c_k}{4\eta}, \quad (3.140)$$

$$|n_1(k)| \|n_D(k)\|_{\infty} \|m^{-1}(k)\|_{\infty} \leq \frac{c_k}{4\eta^2}. \quad (3.141)$$

Without loss of generality, replacing S_k by $-S_k$ or $\pm iS_k$ if needed, we can suppose that $\text{Re}\{m^{-1}(k)\} > c_k > 0$. Then, by using inequalities (3.135), (3.136), (3.137), (3.139), (3.140) and (3.141), for all $\phi \in H_{\Delta,0}^1(D)$ we get $\text{Re}\{(S_k \phi, \phi)_{\Delta,0}\} \geq \frac{c_k}{4} \|\phi\|_{\Delta,0}$. Thus S_k is positive and bounded below and then invertible. Hence, by using the analytic Riesz-Fredholm theory, it turns out that S_z is non-singular except for a discrete subset of X : as a consequence, S_k is non-singular except for a discrete set of values of $k \in \mathbb{R}_+^*$. ■

Corollary 3.8.7. *The set of transmission eigenvalues is a discrete subset of \mathbb{R}_+^* .*

Proof. It follows from Lemma 3.8.3 that the set of transmission eigenvalues in $k \in \mathbb{R}_+^* \setminus \text{Sing}(m)$ is the set of k such that S_k is non injective. Now, by Theorem 3.8.4 and Theorem 3.8.5, S_k is a Fredholm operator of index 0 for all $k \in \mathbb{R}_+^* \setminus \text{Sing}(m)$, so that $k \in \mathbb{R}_+^* \setminus \text{Sing}(m)$ is a transmission eigenvalue if and only if S_k is singular, but by Theorem 3.8.6 this holds only for a discrete set. Finally, since we supposed that the set $\text{Sing}(m)$ is discrete, the transmission eigenvalues form a discrete subset of \mathbb{R}_+^* . ■

We can now state the main and last theorem of this section, which can be proved analogously to Theorem 4.1 in [83].

Theorem 3.8.8. *If $k \in \mathbb{R}_+^* \setminus \text{Sing}(m)$ is not a transmission eigenvalue, then for all $h \in H_{\Delta}^1(D)$ the inhomogeneous transmission problem (3.124) has a unique solution.*

Remark 3.8.1. We now want to briefly discuss the consistency of the previous assumptions No. 1-4 with physics. To this end, we first observe that assumptions No. 2 and No. 3 are non-trivial only when $n_D(k)$ does depend on $x \in D$ for some $k \in \mathbb{R}_+^*$: indeed, it is easy to prove that if $n_D(k)$ is constant on D and different from n_1 for all $k \in \mathbb{R}_+^*$, then assumption No. 1 implies assumptions No. 2 and No. 3. Then, at least in the case of constant $n_D(k)$, only assumptions No. 1 and No. 4 require a physical justification. The latter is given by the model of Havriliak-Negami dielectric relaxation: according to this model, the complex electrical permittivity $\hat{\varepsilon}$ of a medium at an angular frequency ω is given by⁴¹

$$\hat{\varepsilon} = \varepsilon_{\infty} + \frac{\varepsilon_s - \varepsilon_{\infty}}{[1 + (-i\omega\tau)^{\alpha}]^{\beta}}, \quad (3.142)$$

where ε_{∞} is the permittivity at high frequency, ε_s is the static or low frequency permittivity, τ is the characteristic relaxation time and $\alpha, \beta \in (0, 1]$. In particular, model (3.142) gives the Cole-Davidson model for $\alpha = 1$, the Cole-Cole model for $\beta = 1$ and the Debye model for $\alpha = \beta = 1$. If we now observe that (cf. (3.1)) $n(k) = \hat{\varepsilon}/\varepsilon_0$, where the generic wave number in free space is given by $k = \omega/c$ (with $c = 1/\sqrt{\varepsilon_0\mu_0}$), we can easily realize that assumptions No. 1 and No. 4 are verified.

A similar discussion can be carried out when n_D is assumed to be piecewise constant on D : in this case, however, assumption No. 3 does not hold in general as a consequence of model (3.142), and has to be explicitly required. We shall not discuss more general

⁴¹See e.g. [53], or chapter 1 of [79]. However, in these two references the harmonic dependence on time is assumed to be ruled by $e^{i\omega t}$, while we follow the opposite sign convention, i.e., $e^{-i\omega t}$: this explains the mismatch in sign ($\pm i$) between [53, 79] and the formula (3.142).

cases: our purpose is to show that assumptions No. 1-4 are far from being empty, since they are satisfied for rather general classes of propagation media. \square

Chapter 4

The LSM explained by energy conservation

In general, qualitative methods pose some problems from the viewpoint of their theoretical foundation, since the equations at their basis are artificially formulated, i.e., do not follow from physical laws. In particular, as far as the linear sampling method (LSM) is concerned, a satisfactory understanding of the reason why it should work at all is still an open issue¹. This is due to a missing link between the general theorem inspiring the method and the method itself. Indeed, the general theorem shows that, for each sampling point z in the physical space, a far-field equation exists that admits approximate solutions whose L^2 -norm is bounded when z is inside the scatterer, tends to blow up when z approaches the boundary of the scatterer from inside and can be made arbitrarily large when z is outside. On the other hand, there is no *a priori* guarantee that the regularized solution of the far-field equation, as computed by the algorithm and exploited to characterize the domain of the scatterer, should behave like one of those approximate solutions. However, many numerical simulations, performed under very different scattering conditions and with various noise levels, show that there is generally² a good agreement between theory and practice, i.e., that the computed regularized solution behaves as indicated by the general theorem. Then, the main (and still open) issue is to explain such agreement.

However, owing to its very technical nature, this problem should be described more precisely before reviewing the existing literature on it. Then, unlike the previous chapters, the section entitled ‘State of the art’ will follow that entitled ‘The problem’: in the latter (i.e., the next one), we are going to give a rather detailed account of the issue we want to

¹See [10, 11, 34, 65] and also [35], p. 131, or [69], p. 168.

²See footnote no. 5 at p. 6.

address. To fix ideas and notations, we shall focus on the 2D electromagnetic scattering problem for a penetrable and isotropic cylinder, by assuming that the measurements are taken in the far-field region of a lossless and homogeneous background. In any case, the same theoretical problem affects the LSM in all scattering frameworks which it can be formulated for.

4.1 The problem

We first consider the following direct scattering problem: a plane, electromagnetic and time-harmonic wave, propagating in a homogeneous and non-conducting background medium, is scattered by an inhomogeneity consisting of a penetrable, isotropic and infinitely long cylinder. The geometric and physical properties of the cylinder are invariant with respect to translations along its axis: in particular, its cross section is the closure of an open and C^2 -domain $D \subset \mathbb{R}^2$. The material properties of the cylinder and of the background are described by the (normalized) refractive index³

$$n(x) := \frac{1}{\varepsilon_B} \left[\varepsilon(x) + i \frac{\sigma(x)}{\omega} \right] \quad \forall x \in \mathbb{R}^2, \quad (4.1)$$

where $i = \sqrt{-1}$ and ω denotes the angular frequency of the wave; $\varepsilon(x)$ and $\sigma(x)$ are the electrical permittivity and conductivity, respectively. We assume that $\varepsilon(x)$ is uniform in $\mathbb{R}^2 \setminus \bar{D}$ and equal to the background value $\varepsilon_B > 0$, while $\sigma = 0$ in the same region. We consider a non-magnetic scatterer, i.e., we require that the magnetic permeability is a positive constant μ_B everywhere in \mathbb{R}^2 .

Starting from the time-harmonic and rescaled Maxwell equations⁴

$$\operatorname{curl} E - ikH = 0, \quad \operatorname{curl} H + ikn(x)E = 0 \quad (4.2)$$

(where k is the wave number in the background), and assuming that the incident plane wave is TM-polarized, i.e., the incident electric field is parallel to the axis of the cylinder, the scattering problem under exam can be formulated in a 2D framework as follows⁵. Let $n(x)$ be such that $n|_{\bar{D}} \in C^1(\bar{D})$ and let $\hat{d} = \hat{d}(\theta) := (\cos \theta, \sin \theta)$ any incidence direction: then, given the incident field $u^i(x, \theta) := e^{ikx \cdot \hat{d}}$, find the total field $u = u(\cdot, \theta) \in$

³See [48], p. 251.

⁴See [48], p. 251.

⁵See [46] and [48], pp. 307-308.

$C^2(\mathbb{R}^2 \setminus \partial D) \cap C^1(\mathbb{R}^2)$ such that

$$\begin{cases} \Delta u(x) + k^2 n(x) u(x) = 0 & \text{for } x \in \mathbb{R}^2 \setminus \partial D & \text{(a)} \\ u(x) = e^{ikx \cdot \hat{d}} + u^s(x) & \text{for } x \in \mathbb{R}^2 & \text{(b)} \\ \lim_{r \rightarrow \infty} \left[\sqrt{r} \left(\frac{\partial u^s}{\partial r} - ik u^s \right) \right] = 0, & & \text{(c)} \end{cases} \quad (4.3)$$

where the limit in (4.3)(c), with $r := |x|$, expresses the Sommerfeld radiation condition, holding uniformly in $\hat{x} := \frac{x}{|x|}$, for the scattered field u^s .

For each incidence direction \hat{d} , there exists a unique solution⁶ to problem (4.3), and the corresponding scattered field $u^s = u^s(\cdot, \theta)$ has the following asymptotic behaviour (which holds uniformly in all directions \hat{x}):

$$u^s(x, \theta) = \frac{e^{ikr}}{\sqrt{r}} u_\infty(\varphi, \theta) + O(r^{-3/2}) \quad \text{as } r = |x| \rightarrow \infty, \quad (4.4)$$

where (r, φ) are the polar coordinates of the observation point x and the function $u_\infty = u_\infty(\cdot, \theta) \in L^2[0, 2\pi]$ is known as the *far-field pattern* of the scattered field u^s .

In this chapter we consider the qualitative problem of determining the support \bar{D} of the scatterer under the assumption that the far-field pattern $u_\infty(\varphi, \theta)$ is known for all observation and incidence angles $\varphi, \theta \in [0, 2\pi]$. A procedure for its solution is provided by the LSM.

Define the linear and compact *far-field operator* $F : L^2[0, 2\pi] \rightarrow L^2[0, 2\pi]$ corresponding to the inhomogeneous scattering problem (4.3) as⁷

$$(Fg)(\varphi) := \int_0^{2\pi} u_\infty(\varphi, \theta) g(\theta) d\theta \quad \forall g \in L^2[0, 2\pi]. \quad (4.5)$$

The operator F is injective with a dense range if k^2 is not a transmission eigenvalue⁸. By the superposition principle⁹, Fg is the far-field pattern of the scattered field

$$u_g^s(x) := \int_0^{2\pi} u^s(x, \theta) g(\theta) d\theta \quad \forall x \in \mathbb{R}^2 \setminus D \quad (4.6)$$

corresponding to the incident field u^i given by the *Herglotz wave function* v_g with kernel g , i.e.,

$$u^i(x) = v_g(x) := \int_0^{2\pi} e^{ikx \cdot \hat{d}(\theta)} g(\theta) d\theta \quad \text{for } x \in \mathbb{R}^2. \quad (4.7)$$

⁶See [48], pp. 307-308.

⁷See e.g. [35], p. 107.

⁸See e.g. [35], p. 108.

⁹See e.g. [48], p. 224.

Next consider the outgoing scalar field

$$\Phi(x, z) = \frac{i}{4} H_0^{(1)}(k|x - z|) \quad \forall x \neq z, \quad (4.8)$$

generated by a point source located at $z \in \mathbb{R}^2$, where $H_0^{(1)}(\cdot)$ denotes the Hankel function of the first kind and of order zero¹⁰. The corresponding far-field pattern is given by¹¹

$$\Phi_\infty(\varphi, z) = \frac{e^{i\pi/4}}{\sqrt{8\pi k}} e^{-ik\hat{x}(\varphi) \cdot z}, \quad \text{with } \hat{x}(\varphi) := (\cos \varphi, \sin \varphi) \quad \forall \varphi \in [0, 2\pi]. \quad (4.9)$$

For each $z \in \mathbb{R}^2$, the *far-field equation* is defined as¹²

$$(Fg_z)(\varphi) = \Phi_\infty(\varphi, z). \quad (4.10)$$

The LSM depends on what we shall call the *general theorem*¹³, concerning the existence of ϵ -approximate solutions to the far-field equation and their qualitative behaviour.

Theorem 4.1.1. (General theorem) *Let $D \subset \mathbb{R}^2$ be nonempty, open, bounded, with C^2 -boundary ∂D , and such that $\mathbb{R}^2 \setminus \bar{D}$ is connected; let $n : \mathbb{R}^2 \rightarrow \mathbb{C}$ be given by (4.1) and such that $n|_{\bar{D}} \in C(\bar{D})$; let $k := \omega\sqrt{\varepsilon_B \mu_B} > 0$ be such that k^2 is not a transmission eigenvalue and let F be the far-field operator (4.5) corresponding to the inhomogeneous scattering problem (4.3). Then:*

(i) *if $z \in D$, it follows that for every $\epsilon > 0$ there exists a solution $g_z^\epsilon \in L^2[0, 2\pi]$ of the inequality*

$$\|Fg_z^\epsilon - \Phi_\infty(\cdot, z)\|_{L^2[0, 2\pi]} \leq \epsilon \quad (4.11)$$

such that, for every $z^ \in \partial D$,*

$$\lim_{z \rightarrow z^*} \|g_z^\epsilon\|_{L^2[0, 2\pi]} = \infty \quad (\text{a}) \quad \text{and} \quad \lim_{z \rightarrow z^*} \|v_{g_z^\epsilon}\|_{H^1(D)} = \infty, \quad (\text{b}) \quad (4.12)$$

where $v_{g_z^\epsilon}$ is the Herglotz wave function with kernel g_z^ϵ ;

(ii) *if $z \notin D$, it follows that for every $\epsilon > 0$ and $\delta > 0$ there exists a solution $g_z^{\epsilon, \delta} \in L^2[0, 2\pi]$ of the inequality*

$$\|Fg_z^{\epsilon, \delta} - \Phi_\infty(\cdot, z)\|_{L^2[0, 2\pi]} \leq \epsilon + \delta \quad (4.13)$$

such that

$$\lim_{\delta \rightarrow 0} \|g_z^{\epsilon, \delta}\|_{L^2[0, 2\pi]} = \infty \quad (\text{a}) \quad \text{and} \quad \lim_{\delta \rightarrow 0} \|v_{g_z^{\epsilon, \delta}}\|_{H^1(D)} = \infty, \quad (\text{b}) \quad (4.14)$$

where $v_{g_z^{\epsilon, \delta}}$ is the Herglotz wave function with kernel $g_z^{\epsilon, \delta}$.

¹⁰See e.g. [35], p. 49.

¹¹See e.g. [35], p. 74.

¹²See e.g. [35], p. 125.

¹³See e.g. [35], p. 128.

On the basis of Theorem 4.1.1, the algorithm¹⁴ of the LSM can be shortly described as follows [52]. Consider a sampling grid that covers a region containing the scatterer. For each point z of the grid, compute the Tikhonov regularized solution g_z^α of the (angle-discretized) far-field equation (4.10) and fix the optimal value $\alpha^*(z)$ of the regularization parameter α by means of Morozov's generalized discrepancy principle [89]. Then, the boundary of the scatterer is visualized as the set of grid points where the (discretized) L^2 -norm of $g_{\alpha^*(z)} := g_z^{\alpha^*(z)}$ becomes mostly large.

Apart from noise and discretization issues, there is a logical gap between the content of Theorem 4.1.1 and the LSM. Indeed, the proof of the former gives no evidence that the approximate solutions g_z^ϵ and $g_z^{\epsilon,\delta}$ are just (or can be chosen as) the Tikhonov regularized solutions $g_{\alpha^*(z)}$ of the far-field equation (for $z \in D$ and $z \notin D$ respectively) exploited by the latter. Nevertheless, several numerical simulations¹⁵, although performed in very different scattering conditions and with various kinds of discretizations, noise levels (and even regularization procedures, as in [88]), show a behaviour of $\|g_{\alpha^*(z)}\|_{L^2[0,2\pi]}$ that is in reasonable agreement with limits (4.12)(a) and (4.14)(a), i.e., $\|g_{\alpha^*(z)}\|_{L^2[0,2\pi]}$ tends to grow up when z approaches the boundary from the inside of the scatterer and remains even larger when z is outside D . The open issue is then to explain such agreement. The next section is devoted to a discussion of some approaches proposed in the literature to tackle this problem.

4.2 State of the art

The papers¹⁶ that try to explain why or how the LSM works can be divided into two families:

1) a first set of papers [10, 11, 65] focuses on the restrictive¹⁷ case in which, in addition to the LSM, also the factorization method¹⁸ (FM) can be applied. In this framework, sophisticated tools of regularization theory play a major role;

2) a second set of papers [37, 86] uses physics-based arguments under restrictive hypotheses on the scattering conditions: in [37] the scatterer is assumed to be a dielectric

¹⁴The following description is concerned with the most popular implementation of the LSM. Of course, different regularization procedures can be considered to solve the (angle-discretized) far-field equation (4.10): see e.g. [88].

¹⁵See footnote no. 5 at p. 6.

¹⁶Of course, we are not considering [9] here, since this paper is the main source for the current chapter and will be presented in the next sections.

¹⁷The FM is, so far, significantly less general than the LSM (see e.g. [33], p. 247, or chapter 7 of [35]).

¹⁸See [69] and references therein.

target, while in [86] only perfectly electrical conducting objects (in the resonance regime) are taken into account. Although a regularization procedure is clearly necessary to (approximately) solve the far-field equation in a stable way, regularization theory in itself is not the core of these approaches.

In the following, we shall summarize and/or shortly discuss these papers: the result of our analysis will be that the problem under investigation cannot be considered solved.

4.2.1 FM-based approaches

In general, when Tikhonov regularization is applied to an inverse problem, the regularized solution may blow up only if the regularization parameter tends to zero. In particular, as far as the far-field equation (4.10) is concerned, a vanishing regularization parameter α is a necessary condition for $\|g_z^\alpha\|_{L^2[0,2\pi]}$ to blow up. Moreover, owing to the denseness of the range of F and to the fact that, in general, $\Phi_\infty(\cdot, z)$ does not belong to this range¹⁹, the fact that $\alpha \rightarrow 0^+$ is also a sufficient condition²⁰ for $\|g_z^\alpha\|_{L^2[0,2\pi]}$ to blow up for almost all $z \in \mathbb{R}^2$.

This is the reason why the approach proposed in [10] does not explain ‘why linear sampling works’, even in the restrictive case where also the FM is applicable. Indeed, Corollary 3.4 in [10] states that (with our notation²¹) 1) if $z \in D$, then $\|g_z^\alpha\|_{L^2[0,2\pi]}$ blows up as $\alpha \rightarrow 0^+$ and²² z approaches a point z^* of the boundary ∂D ; 2) if $z \notin D$, then $\|g_z^\alpha\|_{L^2[0,2\pi]}$ blows up as $\alpha \rightarrow 0^+$. But actually, for almost all $z \in \mathbb{R}^2$, the limit $\lim_{\alpha \rightarrow 0^+} \|g_z^\alpha\|_{L^2[0,2\pi]} = \infty$ holds. Then, the typical behaviour of $z \mapsto \|g_{\alpha^*(z)}\|_{L^2[0,2\pi]}$ as an indicator function cannot be explained by simply considering that $\alpha^*(z) \rightarrow 0^+$: at least one should prove a complementary property, whereby a vanishing regularization parameter is only enforced when $z \in D$ approaches the boundary ∂D , or when $z \notin D$. (In fact, our approach will provide such enforcement, as we shall see in Section 4.8.)

An analogous criticism would apply if one tried to tackle this problem by considering, for each $z \in \mathbb{R}^2$, a vanishing *discrepancy* $\|Fg_z^\alpha - \Phi_\infty(\cdot, z)\|_{L^2[0,2\pi]}$ instead of a vanishing

¹⁹I.e., the far-field equation is almost never solvable: see [35], p. 126; [34], p. 419; [47], p. 386; [48], p. 315; cf. also [73].

²⁰For details, see [4], p. 30 and p. 131.

²¹However, we point out that, according to [10], what we denote here by g_z^α is not necessarily the Tikhonov regularized solution of the far-field equation (4.10), but rather, and more generally, any regularized solution computed by means of a regularization procedure belonging to a set of regularization methods including Tikhonov regularization.

²²In the statement of Corollary 3.4, nothing is said about the order (if any) in which the two limits $\alpha \rightarrow 0^+$ and $z \rightarrow z^*$ are considered.

regularization parameter²³ α . Indeed, these two approaches are equivalent, as shown by Theorem 4.10.1 in Subsection 4.10.1, p. 119.

However, some results in [10] are used in [11] to obtain a new version of the LSM whose mathematical foundation can be considered satisfactory (of course, only in those cases where also the FM is applicable). For our purposes, we can summarize the results of [11] as follows: 1) the usual family²⁴ of indicator functions $z \mapsto \|g_z^\alpha\|_{L^2[0,2\pi]}$ is replaced by $z \mapsto |v_{g_z^\alpha}(z)|$, where g_z^α is the Tikhonov regularized solution of the far-field equation (4.10) and $v_{g_z^\alpha}$ is the Herglotz wave function of kernel g_z^α ; 2) the new indicator functions verify good convergence/divergence properties²⁵, i.e.,

$$\lim_{\alpha \rightarrow 0^+} |v_{g_z^\alpha}(z)| < \infty \text{ for } z \in D \quad (\text{a}) \quad \text{and} \quad \lim_{\alpha \rightarrow 0^+} |v_{g_z^\alpha}(z)| = \infty \text{ for } z \notin D \quad (\text{b}). \quad (4.15)$$

In this perspective, the unavoidable gap between the continuous framework and the numerical implementation of the new LSM-algorithm suggested by limits (4.15) can be reasonably filled in by assuming that discretization effects are negligible and that, for each $z \in \mathbb{R}^2$, the optimal value $\alpha^*(z)$ chosen for the regularization parameter α can be considered ‘small’ (typically due to a ‘small’ level of the noise affecting the far-field operator). However, it is worth noting that limits (4.15) do not explain the behaviour of the usual indicator function $z \mapsto \|g_{\alpha^*(z)}\|_{L^2[0,2\pi]}$, which is the problem we want to address here: they rather give rise to a rigorous, but alternative, version of the LSM.

The investigation proposed in [65] is too far from the context of this Ph.D. thesis to be even sketched here. For our purposes, the best that can be said about [65] is that, in the author’s words, the analysis provided there ‘may serve as a justification of the [linear sampling] method for problems where the Factorization Method is known to work’²⁶, which suffices to consider such analysis less general than desirable.

Summarizing, this set of papers can at most justify the LSM when the FM is also applicable, thus leaving unexplained the LSM itself in its full generality.

4.2.2 Physics-based approaches

The far-field equation (4.10) is neither a physical law, nor a consequence of physical laws: this is suggested by its ‘artificial’ formulation and confirmed by the fact that, in general,

²³Cf. e.g. the alternative version of part (ii) of Theorem 4.1.1 given in [69], p. 166.

²⁴‘Family’ means that here we do not need to consider a specific choice rule $\alpha^*(z)$ for the regularization parameter α .

²⁵Actually, a weaker result than limit (4.15)(b) is proved in [11], i.e., the following one: for any $z \in \mathbb{R}^2$, there exists a sequence $\{\alpha_n\}_{n=0}^\infty$ such that $\lim_{n \rightarrow \infty} \alpha_n = 0$ and $\lim_{n \rightarrow \infty} |v_{g_z^{\alpha_n}}(z)| = \infty$. However, this is not so important in our discussion.

²⁶Quoted from the abstract of [65].

it admits no exact solution for any location of the sampling point z . However, the LSM, which is strongly based on the far-field equation, can often provide reliable visualizations of unknown scatterer, thus highlighting some kind of link between this artificial equation and physics. Actually, nothing prevents from regarding the far-field equation as a condition, or a constraint that is added to the physical laws (e.g., Maxwell's equations) governing the scattering experiment, whereby the (approximate) fulfilment of such constraint involves the computation of a function whose L^2 -norm can serve as an indicator for the unknown scatterer.

In this perspective, the interest of a physical interpretation of the far-field equation or of the LSM is twofold: first, from a theoretical viewpoint, clarifying the undoubtable link between the LSM and physics would certainly be a major achievement; second, and equally important, a physical approach can be useful to understand the conditions under which the LSM performs best. Indeed, an explanation of the LSM in the spirit of regularization theory (as shortly outlined in the previous subsection) or, more generally, its explanation in terms of a mere agreement between the approximate solutions g_z^ϵ and $g_z^{\epsilon,\delta}$ exhibited by Theorem 4.1.1 (for $z \in D$ and $z \notin D$ respectively) with the Tikhonov regularized solutions $g_{\alpha^*(z)}$ of the far-field equation, can hardly explain why, in some typical situations, the visualization provided by the LSM is not good: e.g., too close²⁷ distinct objects tend to be merged (see e.g. [43], or Figure 5.16(a), p. 142, in the following), concave objects tend to be 'convexified' (see e.g. [37]), etc. These 'pathologies' highlight, in particular, some limitations of the LSM in terms of the resolution achievable, but these limitations, although reasonable, are not foreseen or explained by approaches such as the FM-based ones recalled above.

A preliminary step towards a physical interpretation of the far-field equation (4.10) is to observe (as already done soon below (4.5)) that its left-hand side Fg_z is the far-field pattern of the scattered field (4.6), corresponding to the incident field u^i (4.7) given by the Herglotz wave function v_{g_z} with kernel g_z . Since the right-hand side $\Phi_\infty(\cdot, z)$ of (4.10) is the far-field pattern of the field radiated by an elementary source placed at the sampling point z , it is clear that, in a physical perspective, the far-field equation can be paraphrased as follows: for each $z \in \mathbb{R}^2$, try to illuminate the target by a continuous superposition, weighted by g_z , of plane waves (i.e., by the incident field (4.7)) in such a way that the field scattered by the target is seen, at very large distances, as the field radiated by a point source placed at z .

Of course, the previous paraphrase of the far-field equation does not suffice to under-

²⁷With respect to the wavelength.

stand why the LSM works, and a much deeper investigation is needed²⁸. However, we can make a further step if we remember that 1) by Rellich's lemma²⁹, imposing the equality between the far-field patterns of two radiating fields amounts to imposing that the two fields are equal everywhere outside the scatterer; 2) no solution of the Helmholtz equation in an open C^2 -domain can be singular³⁰. Accordingly, if we pull back the far-field equation up to the near-field region, its impossibility for a sampling point z outside the scatterer is obvious, since it would enforce a singularity of the scattered field $u_{g_z}^s$ in $z \notin D$; on the other hand, its impossibility for $z \in D$ seems of somewhat more technical nature and less evident from a physical viewpoint. In other terms, the far-field equation seems to be endowed with two different 'degrees of impossibility', or better, of ill-posedness, depending on the fact that z is inside or outside D : a weak or mild ill-posedness for $z \in D$, and a strong one for $z \notin D$. This is in qualitative agreement with the well-known behaviour of the Tikhonov-Morozov regularization parameter $\alpha^*(z)$ in the LSM algorithm [52, 65], i.e., the values of $\alpha^*(z)$ are much larger for z inside than outside the scatterer. In other terms, the far-field equation seems to express a physical condition or constraint that, in the near-field region, can be at least approximately satisfied for $z \in D$, but not for $z \notin D$.

Remark 4.2.1. However, the previous discussion is purely heuristic, since any argument based on Rellich's lemma, i.e., on a pull-back of the far-field equation, should be formulated with great care. Indeed, the problem of recovering a radiating field from its far-field pattern is ill-posed³¹: in particular, continuity fails. Now, when the far-field equation (4.10) is approximately solved, e.g. via Tikhonov regularization, its left-hand side Fg_z^α will be only approximately equal to $\Phi_\infty(\cdot, z)$, and this does not imply any similarity between the field $u_{g_z^\alpha}^s$, having Fg_z^α as its far-field pattern, and the field $\Phi(\cdot, z)$ of the elementary source placed at z . In general, a regularization method for the far-field operator F (4.5) does not suffice to provide this kind of stability from the far-field to the near-field region, which can only be ensured by a regularization method for the operator

²⁸This is also the reason why we do not consider [2] fully pertinent to the problem we are dealing with. Indeed, in [2] the induced current inside the (penetrable and 2D) scatterer is represented via a multipole expansion, which corresponds to projecting the far-field equation onto a basis of multipole terms: then, such equation amounts to requiring that only the monopole term contributes to the scattered field. Although this equivalent reformulation (or 'physical paraphrase') of the far-field equation is interesting in that it inspires a family of possible modifications of the LSM (with some preliminary improvements with the respect to the standard LSM), the problem of understanding why the LSM works is not actually faced in [2].

²⁹See e.g. [48], p. 33.

³⁰See e.g. [35], p. 53.

³¹See e.g. [48], pp. 36-37.

mapping a radiating field into its far-field pattern³². However, this issue is ignored by the two papers we are going to shortly comment on. \square

From a chronological viewpoint, the first paper to address the problem of understanding the LSM from a physical viewpoint was [86]: here, the scatterer is assumed to be a 2D perfect conductor and the investigation is based on an analysis of the surface current induced on the boundary of the scatterer when illuminated by the incident field u^i (4.7) given by the Herglotz wave function $v_{g_z^\alpha}$ with kernel g_z^α . Moreover, most of this analysis is performed under the hypothesis that the time-harmonic field oscillates at an internal resonance frequency for the scatterer under exam. Then, although we disagree with some statements of [86], we do not need to discuss them: indeed, for our purposes, it suffices to observe that the approach of [86] is proposed under very restrictive assumptions on the material properties of the scatterer and on the frequencies of the fields, thus leaving unsolved, in its generality, the problem of understanding why the LSM works.

Few years later, another paper [37] appeared, which proposed a physical interpretation of the LSM in terms of a focusing problem for the (radiating component of the³³) current induced inside a 2D and dielectric scatterer. Similarly to [86], we think that some statements of [37] are ambiguous, or not properly justified, but for our purposes it suffices to observe that, in any case, the approach pursued in [37] can at most work for good dielectrics³⁴, i.e., (almost) lossless scatterers: indeed, owing to the well-known ‘skin effect’³⁵, in general no (even approximate) focusing of the induced current inside a lossy scatterer is possible. Again, the problem of understanding why the LSM works cannot be solved in its generality by the approach of [37].

On the other hand, the far-field equation (4.10) is independent of the material properties of the scatterer: indeed, one of the attractive features of the LSM is that no *a priori* information on the scatterer is needed (except that it is contained in the investigation domain). This suggests that also a physical interpretation of the far-field equation should require no assumption³⁶ on the physical parameters of the scatterer.

³²An interesting relation between these two kinds of regularization has been established in [10], for the particular case of 3D acoustic scattering by a sound-soft obstacle.

³³There seems to be some ambiguity on this point: according to Section II of [37], the far-field equation enforces, in general, a focusing in the sampling point z of the radiating component of the induced current, while in Section III only the (total) induced current is considered. This shift does not seem to be explicable in terms of the Tikhonov regularization procedure introduced in Section III: indeed, according to the authors, Tikhonov regularization avoids the existence of non-radiating *primary* sources, which *a priori* does not imply an analogous property of the total *induced* current.

³⁴For a definition of ‘good dielectric’, see e.g. [14], p. 80.

³⁵See e.g. [14], p. 149.

³⁶Of course, the usual hypotheses about D , n and k^2 (or analogous ones in the case of perfectly

4.3 Outline of our approach

The purpose of the present chapter is to conceive a physical interpretation of the far-field equation that does not depend on the penetrable or impenetrable nature of the scatterer. To this end, the principle of energy conservation, by virtue of its generality and simplicity, appears as a promising tool for investigating how the LSM works. Indeed, outside the scatterer, which can always be regarded as an equivalent source generating the scattered field³⁷, no sources are present³⁸ and no dissipation is possible, since the background is assumed to be lossless: then, the (time-averaged) power flux radiated by the scatterer is preserved both globally (i.e., on all the surfaces or, for 2D problems, all the curves surrounding the scatterer) and locally (i.e., along the flow tubes or, in 2D, the flow strips of a field that, in the electromagnetic case³⁹, is the Poynting vector).

More precisely, we shall split the problem of understanding why the LSM works into three steps:

1) we analyze the properties of the (time-averaged) Poynting vector associated with the field $u_z^{s,\epsilon}$ whose far-field pattern Fg_z^ϵ is the left-hand side of the far-field equation (4.10), for one of its ϵ -approximate solutions g_z^ϵ such that $\|Fg_z^\epsilon - \Phi_\infty(\cdot, z)\| \leq \epsilon$: this Poynting vector carries electromagnetic power from the scatterer up to infinity along its flow strips in the background medium. In particular, the far-field equation can be regarded as a constraint on the power flux transported by these flow strips up to the far-field region;

2) we numerically investigate the behaviour of the flow lines of the Poynting vector when the LSM is implemented and we interpret and formally describe such behaviour by appropriate definitions of ‘regularity’, ‘ramification point’, ‘far-field width’, etc.;

3) we prove that if the flow lines verify the properties formalized by these definitions, then energy conservation along a ‘regular’ flow strip from the boundary of the scatterer up to infinity, as well as the constraint on power fluxes expressed by the far-field equation, together imply that $\|g_z^\epsilon\|_{L^2[0,2\pi]}$ behaves as a good indicator function for the target. This result is then specified for the case where the approximate g_z^ϵ solution of the far-field equation is chosen as the Tikhonov regularized solution g_z^α .

conducting scatterers) in the general theorem 4.1.1 at the basis of the LSM could be maintained.

³⁷See e.g. [15], p. 215, or [14], p. 328.

³⁸Of course, some primary sources will be located in the far-field region to illuminate the scatterer, but insofar as the incident waves are taken as plane waves or, more generally, as entire solutions of the Helmholtz equation (such as Herglotz wave functions), these sources are ignored by the mathematical description, or idealization, of the scattering problem. In fact, the scattered field u^s verifies the Helmholtz equation in $\mathbb{R}^2 \setminus \bar{D}$, as shown by system (4.3).

³⁹For other kinds of waves, e.g. for acoustic ones, the analogous of the Poynting vector field should be considered: see Remark 4.4.2, p. 103, in the following.

However, it is clear from point 2) above that our explanation of the LSM is based on an *a posteriori* approach: i.e., the performance of the LSM is related to the behaviour of the flow lines of the Poynting vector, but such behaviour is numerically observed (in the particular scattering conditions considered here) and not theoretically predicted in general. This is also the reason why, at the current stage of advancement, our approach is incomplete and does not provide a mathematical justification of the LSM: to this end, it would be necessary to deduce the geometric properties of these flow lines *a priori*, i.e., starting from the knowledge of the scattering conditions. Such an investigation could be pursued by using sophisticated tools of topological dynamics⁴⁰, which is however beyond the purposes of this chapter. In any case, once the proper behaviour of the flow lines is assumed, the validity of our approach and, in particular, the results outlined in points 1) and 3) above are independent of the material properties of the scatterer.

In order to keep our investigation as simple as possible, we shall focus on the 2D electromagnetic scattering problem for a penetrable and isotropic cylinder, by assuming that the measurements are taken in the far-field region of a lossless and homogeneous background, as already specified in Section 4.1. However, the physical properties of the scatterer are irrelevant, and the key-ideas of our approach are still valid in different or more general situations: for example, the 3D acoustic scattering problem⁴¹ (possibly with aspect-limited measurements) has been addressed in [8], while the generalization to the case of an inhomogeneous and/or lossy background (possibly with near-field measurements) has been investigated in [5] for the 2D electromagnetic scattering problem.

4.3.1 Plan of the following sections

The remainder of this chapter is devoted to a detailed explanation of our energy-based approach to the LSM. More precisely, Section 4.4 introduces the Poynting vector of the scattered field and identifies some relevant features of its flow lines in the framework of energy (i.e., time-averaged power) conservation, thus allowing a physical interpretation of the far-field equation as a constraint on power fluxes. In Section 4.5 we perform a certain number of numerical simulations in order to visualize the behaviour of the flow lines of the Poynting vector when the sampling point is inside the scatterer or on its boundary. In Section 4.6 we prove that such behaviour, together with energy conservation along the flow strips and the energy constraint induced by the far-field equation, allows characterizing

⁴⁰As a general reference, see e.g. [1]; for more specific results concerning the Poynting vector, see e.g. [82].

⁴¹Cf. Remark 4.4.2, p. 103.

the ϵ -approximate solutions of the far-field equation in a fashion that is in agreement with the standard general theorem; in other terms, our main result is a new version of this general theorem based on the physical principle of energy conservation. Section 4.7 adapts the approach of Sections 4.5 and 4.6 to the case of a sampling point chosen outside the scatterer. Section 4.8 specifies the previous results to Tikhonov regularized solutions and compares the theoretical bounds on the discrepancy derived in Section 4.6 and 4.7 with its numerical values, as computed in Section 4.5. Finally, our conclusions and suggestions for future developments are proposed in Section 4.9.

4.4 The power flux of the scattered field and the far-field equation

In our interpretation of the LSM, a crucial role is played by the time-averaged Poynting vector \mathcal{S}^s associated with a scattered field u^s . In order to compute this vector, we need to restore, for a moment, a genuine 3D setting. If we refer \mathbb{R}^3 to an orthogonal Cartesian coordinate system (x_1, x_2, x_3) such that the x_3 -axis is parallel to the axis of the cylinder, we can express the scattered electric field as $E^s(x) = (0, 0, u^s(x))$. Then, from the first⁴² of eq.s (4.2), we find the corresponding magnetic field $H^s(x) = \frac{1}{ik} \left(\frac{\partial u^s}{\partial x_2}(x), -\frac{\partial u^s}{\partial x_1}(x), 0 \right)$. We now recall that, according to the notations of Sec. 9.1 in [48], these are *rescaled* fields, so that the actual complex spatial forms⁴³ of the scattered electric and magnetic fields are given by $\frac{1}{\sqrt{\epsilon_B}} E^s$ and $\frac{1}{\sqrt{\mu_B}} H^s$ respectively. Then, remembering that $k = \omega \sqrt{\epsilon_B \mu_B}$, we can compute the time-averaged Poynting vector \mathcal{S}^s associated with the scattered electromagnetic field $\left(\frac{1}{\sqrt{\epsilon_B}} E^s, \frac{1}{\sqrt{\mu_B}} H^s \right)$ as⁴⁴

$$\begin{aligned} \mathcal{S}^s(x) &= \frac{1}{2} \operatorname{Re} \left\{ \frac{1}{\sqrt{\epsilon_B}} E^s(x) \times \frac{1}{\sqrt{\mu_B}} \bar{H}^s(x) \right\} = \\ &= \operatorname{Re} \left\{ \frac{1}{2ik\sqrt{\epsilon_B \mu_B}} (0, 0, u^s(x)) \times \left(\frac{\partial \bar{u}^s}{\partial x_2}(x), -\frac{\partial \bar{u}^s}{\partial x_1}(x), 0 \right) \right\} = \\ &= \operatorname{Re} \left\{ \frac{1}{2i\omega \epsilon_B \mu_B} \left(u^s(x) \frac{\partial \bar{u}^s}{\partial x_1}(x), u^s(x) \frac{\partial \bar{u}^s}{\partial x_2}(x), 0 \right) \right\}. \end{aligned} \quad (4.16)$$

⁴²Of course, the Maxwell equations (4.2) are written for the total electromagnetic field; however, since we assume that the incident field satisfies the first one everywhere, by linearity this is also true for the scattered field.

⁴³Obtained by factoring out the temporal dependence $e^{-i\omega t}$, as in [48].

⁴⁴See e.g. [14], p. 29: although in [14] the complex spatial forms of the fields are obtained by factoring out the temporal dependence $e^{i\omega t}$ (i.e., with an opposite sign if compared to [48]), it is easy to realize that the expression of the time-averaged Poynting vector is the same in both cases.

In particular, $\mathcal{S}^s(x)$ is a vector with zero x_3 -component: then, we can come back to a 2D framework and write

$$\mathcal{S}^s(x) = \frac{1}{4i\omega \varepsilon_B \mu_B} [\bar{u}^s(x) \nabla u^s(x) - u^s(x) \nabla \bar{u}^s(x)]. \quad (4.17)$$

In general, the time-averaged Poynting vector is related to the mean flow (over a period) of power per unit area: accordingly, its flux over a given surface evaluates the time-averaged amount of power crossing that surface.

In our 2D framework, the flux of $\mathcal{S}^s(x)$ over any curve γ in $\mathbb{R}^2 \setminus D$ equals the average power radiated through γ (per unit x_3 -length) by the scatterer, modelled as an equivalent source of electromagnetic waves⁴⁵. Moreover, we consider only simple and (almost everywhere) regular curves. Then, for any such γ , we define the *power flux of the scattered field* u^s across γ as the power flux of the associated Poynting vector, namely

$$\mathcal{F}_\gamma(u^s) := \int_\gamma \mathcal{S}^s(x) \cdot \nu(x) dl(x), \quad (4.18)$$

where $\nu(x)$ denotes the unit normal to γ in x (chosen as outward when γ is closed) and $dl(x)$ indicates the standard measure defined on γ .

Since u^s satisfies the Helmholtz equation (with wave number $k > 0$) in $\mathbb{R}^2 \setminus \bar{D}$, the vector field $\mathcal{S}^s(x)$ is divergence free in $\mathbb{R}^2 \setminus \bar{D}$: indeed, from (4.3)(a) and (4.17), we have

$$\begin{aligned} \operatorname{div} \mathcal{S}^s(x) &= \frac{1}{4i\omega \varepsilon_B \mu_B} \{ |\nabla u^s(x)|^2 + \bar{u}^s(x) \Delta u^s(x) - |\nabla \bar{u}^s(x)|^2 - u^s(x) \Delta \bar{u}^s(x) \} = \\ &= \frac{1}{4i\omega \varepsilon_B \mu_B} \{ \bar{u}^s(x) [-k^2 u^s(x)] - u^s(x) [-\bar{k}^2 \bar{u}^s(x)] \} = \\ &= \frac{1}{4i\omega \varepsilon_B \mu_B} \{ -k^2 |u^s(x)|^2 + k^2 |\bar{u}^s(x)|^2 \} = 0 \quad \forall x \in \mathbb{R}^2 \setminus \bar{D}. \end{aligned} \quad (4.19)$$

Then, Gauss divergence theorem implies that

$$\mathcal{F}_\gamma(u^s) = 0 \quad (4.20)$$

for any closed curve in $\mathbb{R}^2 \setminus D$ not enclosing the scatterer (or any connected component of it). Furthermore

$$\mathcal{F}_{\gamma_1}(u^s) = \mathcal{F}_{\gamma_2}(u^s) \quad (4.21)$$

for any pair of closed curves γ_1 and γ_2 surrounding the whole scatterer.

In order to determine any of the integrals in (4.21), we introduce the circle $\Omega_R := \{x \in \mathbb{R}^2 : |x| = R\}$ and compute the *power flux at infinity of* u^s as

$$\mathcal{F}_\infty(u^s) := \lim_{R \rightarrow \infty} \mathcal{F}_{\Omega_R}(u^s). \quad (4.22)$$

⁴⁵Cf. footnote no. 37, p. 93.

We are now going to show, by means of the two following theorems, that this flux can be written in terms of the far-field pattern as

$$\mathcal{F}_\infty(u^s) = \frac{k}{2\omega \varepsilon_B \mu_B} \|u_\infty\|_{L^2[0,2\pi]}^2. \quad (4.23)$$

Theorem 4.4.1. *Let $R > 0$ and $B_R := \{x \in \mathbb{R}^2 : |x| < R\}$: then, any field u^s satisfying the Helmholtz equation in $\mathbb{R}^2 \setminus \bar{B}_R$ and the Sommerfeld radiation condition (4.3)(c) verifies the asymptotic behaviour*

$$\bar{u}^s \frac{\partial u^s}{\partial r}(r, \varphi) = \frac{ik}{r} |u_\infty(\varphi)|^2 + o(r^{-1}) \quad \text{as } r \rightarrow \infty. \quad (4.24)$$

Proof. The Sommerfeld radiation condition (4.3)(c) means nothing else than

$$\lim_{r \rightarrow \infty} \left(\sqrt{r} \sup_{\varphi \in [0,2\pi]} \left| \frac{\partial u^s}{\partial r}(r, \varphi) - ik u^s(r, \varphi) \right| \right) = 0, \quad (4.25)$$

which implies

$$\sup_{\varphi \in [0,2\pi]} \left| \frac{\partial u^s}{\partial r}(r, \varphi) - ik u^s(r, \varphi) \right| = o(r^{-1/2}) \quad \text{as } r \rightarrow \infty. \quad (4.26)$$

Moreover, the asymptotic behaviour (4.4), although concerning the particular case of a scattered field corresponding to an incident plane wave, also holds for generic radiating fields u^s satisfying the Helmholtz equation⁴⁶, i.e.,

$$u^s(x) = \frac{e^{ikr}}{\sqrt{r}} u_\infty(\varphi) + O(r^{-3/2}) \quad \text{as } r \rightarrow \infty, \quad (4.27)$$

which can be rewritten as

$$\sup_{\varphi \in [0,2\pi]} \left| u^s(r, \varphi) - \frac{e^{ikr}}{\sqrt{r}} u_\infty(\varphi) \right| = O(r^{-3/2}) \quad \text{as } r \rightarrow \infty. \quad (4.28)$$

Then, by (4.28) and the triangle inequality, we have

$$\begin{aligned} \sup_{\varphi \in [0,2\pi]} |u^s(r, \varphi)| &\leq \sup_{\varphi \in [0,2\pi]} \left| u^s(r, \varphi) - \frac{e^{ikr}}{\sqrt{r}} u_\infty(\varphi) \right| + \sup_{\varphi \in [0,2\pi]} \left| \frac{e^{ikr}}{\sqrt{r}} u_\infty(\varphi) \right| = \\ &= O(r^{-3/2}) + O(r^{-1/2}) = O(r^{-1/2}) \quad \text{as } r \rightarrow \infty, \end{aligned} \quad (4.29)$$

i.e.,

$$\sup_{\varphi \in [0,2\pi]} |u^s(r, \varphi)| = O(r^{-1/2}) \quad \text{as } r \rightarrow \infty. \quad (4.30)$$

⁴⁶See e.g. [48], p. 67.

Now, from (4.26) and (4.30), we find⁴⁷

$$\begin{aligned} \sup_{\varphi \in [0, 2\pi]} \left| \bar{u}^s(r, \varphi) \left[\frac{\partial u^s}{\partial r}(r, \varphi) - ik u^s(r, \varphi) \right] \right| &\leq \\ &\leq \sup_{\varphi \in [0, 2\pi]} |u^s(r, \varphi)| \sup_{\varphi \in [0, 2\pi]} \left| \frac{\partial u^s}{\partial r}(r, \varphi) - ik u^s(r, \varphi) \right| = \\ &= O(r^{-1/2}) o(r^{-1/2}) = o(r^{-1}) \quad \text{as } r \rightarrow \infty, \end{aligned} \quad (4.31)$$

i.e.,

$$\sup_{\varphi \in [0, 2\pi]} \left| \bar{u}^s \frac{\partial u^s}{\partial r}(r, \varphi) - ik |u^s(r, \varphi)|^2 \right| = o(r^{-1}) \quad \text{as } r \rightarrow \infty. \quad (4.32)$$

Hence, by virtue of the triangle inequality, we have

$$\begin{aligned} \sup_{\varphi \in [0, 2\pi]} \left| \bar{u}^s \frac{\partial u^s}{\partial r}(r, \varphi) - \frac{ik}{r} |u_\infty(\varphi)|^2 \right| &\leq \\ &\leq \sup_{\varphi \in [0, 2\pi]} \left| \bar{u}^s \frac{\partial u^s}{\partial r}(r, \varphi) - ik |u^s(r, \varphi)|^2 \right| + \sup_{\varphi \in [0, 2\pi]} \left| ik |u^s(r, \varphi)|^2 - \frac{ik}{r} |u_\infty(\varphi)|^2 \right|. \end{aligned} \quad (4.33)$$

The former supremum on the right-hand side of inequality (4.33) is ruled by (4.32); as regards the latter supremum, we have

$$\sup_{\varphi \in [0, 2\pi]} \left| ik |u^s(r, \varphi)|^2 - \frac{ik}{r} |u_\infty(\varphi)|^2 \right| = k \sup_{\varphi \in [0, 2\pi]} \left| |u^s(r, \varphi)|^2 - \frac{1}{r} |u_\infty(\varphi)|^2 \right|. \quad (4.34)$$

Simple algebraic computations yield

$$\begin{aligned} \left| |u^s(r, \varphi)|^2 - \frac{1}{r} |u_\infty(\varphi)|^2 \right| &= \left| |u^s(r, \varphi)| - \frac{1}{\sqrt{r}} |u_\infty(\varphi)| \right| \left(|u^s(r, \varphi)| + \frac{1}{\sqrt{r}} |u_\infty(\varphi)| \right) \leq \\ &\leq \left| u^s(r, \varphi) - \frac{e^{ikr}}{\sqrt{r}} u_\infty(\varphi) \right| \left(|u^s(r, \varphi)| + \frac{1}{\sqrt{r}} |u_\infty(\varphi)| \right). \end{aligned} \quad (4.35)$$

Hence, from (4.28), (4.30) and (4.35), we find⁴⁸

$$\begin{aligned} \sup_{\varphi \in [0, 2\pi]} \left| |u^s(r, \varphi)|^2 - \frac{1}{r} |u_\infty(\varphi)|^2 \right| &\leq \\ &\leq \sup_{\varphi \in [0, 2\pi]} \left| u^s(r, \varphi) - \frac{e^{ikr}}{\sqrt{r}} u_\infty(\varphi) \right| \sup_{\varphi \in [0, 2\pi]} \left(|u^s(r, \varphi)| + \frac{1}{\sqrt{r}} |u_\infty(\varphi)| \right) = \\ &= O(r^{-3/2}) [O(r^{-1/2}) + O(r^{-1/2})] = O(r^{-3/2}) O(r^{-1/2}) = O(r^{-2}). \end{aligned} \quad (4.36)$$

⁴⁷Cf. Prop. 3.5 p. 375 of [62] for the last passage in (4.31).

⁴⁸See also [62], p. 374-375, for the last line of passages.

Summing up, from (4.32), (4.33) and (4.36), we obtain⁴⁹

$$\sup_{\varphi \in [0, 2\pi]} \left| \bar{u}^s \frac{\partial u^s}{\partial r}(r, \varphi) - \frac{ik}{r} |u_\infty(\varphi)|^2 \right| = o(r^{-1}), \quad (4.37)$$

which is an equivalent restatement of thesis (4.24). ■

Theorem 4.4.2. *Under the same hypotheses of Theorem 4.4.1, the flux at infinity of u^s is given by equality (4.23).*

Proof. By virtue of relations (4.17) and (4.18), the flux of u^s across any curve γ is given by

$$\mathcal{F}_\gamma(u^s) = \frac{1}{4i\omega \varepsilon_B \mu_B} \int_\gamma \left[\bar{u}^s \frac{\partial u^s}{\partial \nu} - u^s \frac{\partial \bar{u}^s}{\partial \nu} \right] (x) dl(x). \quad (4.38)$$

If γ is a circle Ω_R of radius R , definition (4.38) becomes:

$$\mathcal{F}_{\Omega_R}(u^s) = \frac{1}{4i\omega \varepsilon_B \mu_B} \int_0^{2\pi} \left[\bar{u}^s \frac{\partial u^s}{\partial \nu} - u^s \frac{\partial \bar{u}^s}{\partial \nu} \right] (R, \varphi) R d\varphi. \quad (4.39)$$

Then, remembering the definition (4.22) of flux at infinity, it is clear that proving equality (4.23) amounts to proving that

$$\lim_{R \rightarrow \infty} \frac{1}{4i\omega \varepsilon_B \mu_B} \int_0^{2\pi} \left[\bar{u}^s \frac{\partial u^s}{\partial \nu} - u^s \frac{\partial \bar{u}^s}{\partial \nu} \right] (R, \varphi) R d\varphi = \frac{k}{2\omega \varepsilon_B \mu_B} \int_0^{2\pi} |u_\infty(\varphi)|^2 d\varphi, \quad (4.40)$$

or, equivalently,

$$\lim_{R \rightarrow \infty} \left| \frac{1}{4i\omega \varepsilon_B \mu_B} \int_0^{2\pi} \left[\bar{u}^s \frac{\partial u^s}{\partial \nu} - u^s \frac{\partial \bar{u}^s}{\partial \nu} \right] (R, \varphi) R d\varphi - \frac{k}{2\omega \varepsilon_B \mu_B} \int_0^{2\pi} |u_\infty(\varphi)|^2 d\varphi \right| = 0. \quad (4.41)$$

Now, simple computations yield

$$\begin{aligned} & \left| \frac{1}{4i\omega \varepsilon_B \mu_B} \int_0^{2\pi} \left[\bar{u}^s \frac{\partial u^s}{\partial \nu} - u^s \frac{\partial \bar{u}^s}{\partial \nu} \right] (R, \varphi) R d\varphi - \frac{k}{2\omega \varepsilon_B \mu_B} \int_0^{2\pi} |u_\infty(\varphi)|^2 d\varphi \right| = \\ & = \left| \frac{1}{4i\omega \varepsilon_B \mu_B} \left\{ \int_0^{2\pi} \left[\bar{u}^s \frac{\partial u^s}{\partial \nu}(R, \varphi) - \frac{ik}{R} |u_\infty(\varphi)|^2 \right] R d\varphi + \right. \right. \\ & \quad \left. \left. - \int_0^{2\pi} \left[u^s \frac{\partial \bar{u}^s}{\partial \nu}(R, \varphi) + \frac{ik}{R} |u_\infty(\varphi)|^2 \right] R d\varphi \right\} \right| \leq \\ & \leq \frac{1}{4\omega \varepsilon_B \mu_B} \left\{ \int_0^{2\pi} \sup_{\varphi \in [0, 2\pi]} \left| \bar{u}^s \frac{\partial u^s}{\partial \nu}(R, \varphi) - \frac{ik}{R} |u_\infty(\varphi)|^2 \right| R d\varphi + \right. \end{aligned} \quad (4.42)$$

⁴⁹Cf. the equation soon before (8.42) p. 231 in [48]: it is similar (but not analogous) to (4.24), and written for the 3D case.

$$\begin{aligned}
& + \int_0^{2\pi} \sup_{\varphi \in [0, 2\pi]} \left| u^s \frac{\partial \bar{u}^s}{\partial \nu}(R, \varphi) + \frac{ik}{R} |u_\infty(\varphi)|^2 \right| R d\varphi \Big\} = \\
& = \frac{2\pi R}{4\omega \varepsilon_B \mu_B} \left\{ \sup_{\varphi \in [0, 2\pi]} \left| \bar{u}^s \frac{\partial u^s}{\partial \nu}(R, \varphi) - \frac{ik}{R} |u_\infty(\varphi)|^2 \right| + \sup_{\varphi \in [0, 2\pi]} \left| u^s \frac{\partial \bar{u}^s}{\partial \nu}(R, \varphi) + \frac{ik}{R} |u_\infty(\varphi)|^2 \right| \right\}.
\end{aligned}$$

Moreover, relation (4.37) or, equivalently, (4.24), can be more explicitly rewritten as

$$\lim_{r \rightarrow \infty} \left[r \sup_{\varphi \in [0, 2\pi]} \left| \bar{u}^s \frac{\partial u^s}{\partial r}(r, \varphi) - \frac{ik}{r} |u_\infty(\varphi)|^2 \right| \right] = 0, \quad (4.43)$$

or also as

$$\lim_{r \rightarrow \infty} \left[r \sup_{\varphi \in [0, 2\pi]} \left| u^s \frac{\partial \bar{u}^s}{\partial r}(r, \varphi) + \frac{ik}{r} |u_\infty(\varphi)|^2 \right| \right] = 0. \quad (4.44)$$

The two previous limits (4.43) and (4.44) show that the last side in the chain of inequalities (4.42) vanishes as $R \rightarrow \infty$. This concludes the proof. ■

Having proved equality (4.23), we now want to show that this relation, when applied to specific scattered fields related to the far-field equation, 1) implies a technical consequence very helpful for a new formulation of the general theorem; 2) suggests a conceptual remark that naturally inspires a physical interpretation of the far-field equation, as well as a near-field version of it.

To this end, we first observe that if $g_z^\epsilon \in L^2[0, 2\pi]$ is such that $\|Fg_z^\epsilon - \Phi_\infty(\cdot, z)\|_{L^2[0, 2\pi]} \leq \epsilon$ and $\varphi_1, \varphi_2 \in [0, 2\pi]$ are any two angles such that $\varphi_1 \leq \varphi_2$, we have

$$\left| \|Fg_z^\epsilon\|_{L^2[\varphi_1, \varphi_2]} - \|\Phi_\infty(\cdot, z)\|_{L^2[\varphi_1, \varphi_2]} \right| \leq \|Fg_z^\epsilon - \Phi_\infty(\cdot, z)\|_{L^2[\varphi_1, \varphi_2]} \leq \epsilon. \quad (4.45)$$

Since, in general, the following implications hold:

$$a, b \geq 0, \quad |a - b| \leq \epsilon \Rightarrow a + b \leq 2b + \epsilon \Rightarrow |a^2 - b^2| = |a - b|(a + b) \leq \epsilon(2b + \epsilon), \quad (4.46)$$

setting $a = \|Fg_z^\epsilon\|_{L^2[\varphi_1, \varphi_2]}$ and $b = \|\Phi_\infty(\cdot, z)\|_{L^2[\varphi_1, \varphi_2]}$ yields

$$\left| \|Fg_z^\epsilon\|_{L^2[\varphi_1, \varphi_2]}^2 - \|\Phi_\infty(\cdot, z)\|_{L^2[\varphi_1, \varphi_2]}^2 \right| \leq \epsilon'(\varphi_1, \varphi_2), \quad (4.47)$$

where

$$\epsilon'(\varphi_1, \varphi_2) := \epsilon \left(2 \|\Phi_\infty(\cdot, z)\|_{L^2[\varphi_1, \varphi_2]} + \epsilon \right) \quad (4.48)$$

does not depend on z , since $\|\Phi_\infty(\cdot, z)\|_{L^2[\varphi_1, \varphi_2]}$ does not. Now, Fg_z^ϵ is the far-field pattern of the scattered field

$$u_z^{s, \epsilon}(x) := \int_0^{2\pi} u^s(x, \theta) g_z^\epsilon(\theta) d\theta \quad \forall x \in \mathbb{R}^2 \setminus D. \quad (4.49)$$

Therefore, a comparison between (4.23) and (4.47) implies that, for any observation interval $[\varphi_1, \varphi_2]$ in the far-field region, the flux of the scattered field $u_z^{s,\epsilon}$ can be made arbitrarily close to the flux of the field radiated by a pointlike source placed at the sampling point $z \in \mathbb{R}^2$. This result will play a crucial role in the proof of the new version of the general theorem based on energy conservation arguments, which will be discussed in Section 4.6.

Equation (4.23) has also the important physical consequences described in the following remark.

Remark 4.4.1. Let us consider the radiating field $w_z^{s,\epsilon}(x) = u_z^{s,\epsilon}(x) - \Phi(x, z)$, having $w_{z,\infty}^{s,\epsilon} = Fg_z^\epsilon - \Phi_\infty(\cdot, z)$ as its far-field pattern. Then, equations (4.21) and (4.23) applied to $w_z^{s,\epsilon}$, together with inequality (4.11), imply

$$\mathcal{F}_\gamma(w_z^{s,\epsilon}) = \mathcal{F}_\infty(w_z^{s,\epsilon}) = \frac{k}{2\omega \varepsilon_B \mu_B} \|w_{z,\infty}^{s,\epsilon}\|_{L^2[0,2\pi]}^2 \leq \frac{k \epsilon^2}{2\omega \varepsilon_B \mu_B}, \quad (4.50)$$

for any $z \in \mathbb{R}^2$ and any γ enclosing $D \cup \{z\}$. This may be regarded as the physical content of inequality (4.11) in the statement of the general theorem: the power flux of the difference field $u_z^{s,\epsilon}(x) - \Phi(x, z)$ across any closed curve is bounded according to (4.50). More importantly, equation (4.50) naturally inspires the near-field equation

$$\mathcal{F}_\gamma(w_z^{s,\epsilon}) = 0, \quad (4.51)$$

which is characterized by a certain similarity⁵⁰ with the integral equation at the basis of the reciprocity gap functional method [44]. As in that case, also here information on boundary values of both the field and its normal derivative are needed to qualitatively solve the problem. But here the physical interpretation is much more natural. In fact, it is known that, in L^2 , a small far-field pattern does not necessarily correspond to a small scattered field⁵¹. Instead, equation (4.50) shows that a small flux at infinity of $w_z^{s,\epsilon}$ remains small also close to the scatterer. Therefore the far-field equation can be pulled back to a near-field region, provided that the gap between its two sides is estimated in terms of power fluxes instead of L^2 -norms. \square

On the basis of equations (4.21) and (4.23), we have examined global conservation properties of the (time-averaged) power flux and their connection with the far-field equation. In view of the further developments, we complete the discussion with an analysis of how power is radiated along flow strips, possibly emanating from parts of the boundary of the scatterer.

⁵⁰However, we point out that the RGF equation (3.16), p. 53, is linear in the unknown g , while eq. (4.51) is not.

⁵¹See e.g. [48], p. 37.

We introduce the flow lines of the time-averaged Poynting vector $\mathcal{S}^s(x)$ by recalling that they are defined as the solutions to the initial value problem

$$\begin{cases} \frac{dx}{d\tau}(\tau) = \mathcal{S}^s(x(\tau)) & \text{(a)} \\ x(0) = x_0, & \text{(b)} \end{cases} \quad (4.52)$$

where x_0 is a point in $\mathbb{R}^2 \setminus D$. Since u^s (and, consequently, $\mathcal{S}^s(x)$) is real-analytic⁵² in $\mathbb{R}^2 \setminus \bar{D}$, for each $x_0 \in \mathbb{R}^2 \setminus \bar{D}$ there exists a unique solution $\zeta_{x_0}(\tau)$ of the problem (4.52), which will be called the *flow line of the scattered field u^s starting from x_0* . We are interested in considering the flow lines for $\tau \geq 0$. Henceforth, we assume that $\zeta_{x_0}(\tau)$ is defined for every $\tau \geq 0$ and that there are no critical points⁵³ x_0 of \mathcal{S}^s , such that the flow line starting from x_0 collapses into the point x_0 itself. By definition (4.18), the average power crossing a flow line is zero, thus showing that power is carried by the scattered field along its *flow strips*: the latter are open, connected and (almost everywhere) regular domains in $\mathbb{R}^2 \setminus D$ delimited by (infinite) flow lines, or by (semi-)finite portions of them and by (one or) two transverse sections.

Now we can follow the power flux of u^s from the near-field to the far-field region along its flow strips in the background medium. Accordingly, we consider a flow strip $E \subset \mathbb{R}^2 \setminus D$ delimited by two (different and semi-infinite) flow lines $\zeta_{x_0}(\tau)$ and $\zeta_{x_1}(\tau)$. We require that $\zeta_{x_0}(\tau)$ and $\zeta_{x_1}(\tau)$ are indefinitely outgoing toward the far-field region and that each of them approaches a definite direction at infinity: this is consistent with the Silver-Müller radiation condition⁵⁴, in that the radiating electric and magnetic fields tend to be transverse in the far-field region, which implies that the corresponding Poynting vector becomes radial. More precisely, we fix these requirements by means of the following definition.

Definition 4.4.1. *Let $x_0 \in \mathbb{R}^2 \setminus D$. A flow line $\zeta_{x_0}(\tau)$ is called ‘regular’ if:*

(i) $\zeta_{x_0}(\tau) \cap D = \emptyset \quad \forall \tau \geq 0;$

(ii) *there exists $R_0 > 0$ such that $\forall R > R_0$ the flow line $\zeta_{x_0}(\tau)$ intersects Ω_R in one and only one point $P_{x_0}(R)$ of polar coordinates $(R, \varphi[P_{x_0}(R)])$;*

(iii) $\exists \lim_{R \rightarrow \infty} \varphi[P_{x_0}(R)] =: \varphi_\infty(x_0).$

Moreover, a flow strip $E \subset \mathbb{R}^2 \setminus D$ of u^s is called ‘regular’ if it is bounded by two different regular flow lines.

⁵²See e.g. [35], p. 53.

⁵³Cf. e.g. chapter 2 in [1].

⁵⁴See e.g. [48], p. 160.

We point out in particular that no critical point of the Poynting vector is allowed to belong to a regular flow line. For an analysis of such points and their effects on the flow lines, see e.g. [82]. For future purpose, we also give the following definition.

Definition 4.4.2. *Let $\zeta_{x_0}(\tau)$ and $\zeta_{x_1}(\tau)$ be two regular flow lines with $x_0, x_1 \in \mathbb{R}^2 \setminus D$; let $\varphi_\infty(x_0)$ and $\varphi_\infty(x_1)$ be the corresponding asymptotic polar angles. Then, $\psi_\infty(x_0, x_1) := |\varphi_\infty(x_0) - \varphi_\infty(x_1)|$ is called the ‘asymptotic angular width’ of the flow strip bounded by $\zeta_{x_0}(\tau)$ and $\zeta_{x_1}(\tau)$.*

We can now describe how energy conservation is realized along regular flow strips. Indeed, let $x_0, x_1 \in \mathbb{R}^2 \setminus D$, not belonging to the same flow line. Consider the flow lines $\zeta_{x_0}(\tau)$, $\zeta_{x_1}(\tau)$ starting from x_0 , x_1 respectively, and assume that they are regular. Next choose $x_2 \in \zeta_{x_0}(\tau)$ and $x_3 \in \zeta_{x_1}(\tau)$ and draw two non-intersecting curves in $\mathbb{R}^2 \setminus D$, γ_1 and γ_2 , connecting x_0 to x_1 , and x_2 to x_3 , respectively. Then, the closed curve γ resulting from the union of γ_1 , γ_2 and the arcs of the flow lines with endpoints x_0 , x_2 and x_1 , x_3 is the boundary of a finite flow strip $E \subset \mathbb{R}^2 \setminus D$ with transverse sections γ_1 , γ_2 . According to (4.20), the power flux across γ is zero. As a consequence, if the unit normals to both γ_1 and γ_2 are oriented ‘towards infinity’, then $\mathcal{F}_{\gamma_1}(u^s) = \mathcal{F}_{\gamma_2}(u^s)$: the last equation is the ‘local’ counterpart of (4.21).

Finally, if $\zeta_{x_0}(\tau)$ and $\zeta_{x_1}(\tau)$ are regular flow lines identifying a (semi-infinite) regular flow strip with asymptotic angular width $\psi_\infty(x_0, x_1)$, then a ‘local’ version of (4.21)-(4.23) holds⁵⁵ in the form

$$\mathcal{F}_{\gamma_1}(u^s) = \mathcal{F}_{\gamma_2}(u^s) = \frac{k}{2\omega \varepsilon_B \mu_B} \|u_\infty\|_{L^2[\varphi_\infty(x_0), \varphi_\infty(x_1)]}^2. \quad (4.53)$$

In particular, equation (4.53) shows that the power flux of a scattered field through an outwardly oriented arc is positive.

Remark 4.4.2. The analysis performed so far is easily adapted to the acoustic case [48]. In particular, the role of the time-averaged Poynting vector (4.17) is now played by the vector [8]

$$\mathcal{S}^s(x) = \frac{1}{4i\omega \rho_0} [\bar{p}^s(x) \nabla p^s(x) - p^s(x) \nabla \bar{p}^s(x)], \quad (4.54)$$

where ρ_0 is the constant equilibrium density of the background and $p^s(x)$ is the acoustic scattered pressure field in the inviscid background fluid. \square

⁵⁵Cf. also Subsection 4.10.3, p. 125 (and, in particular, footnote no. 83, p. 125), for further details.

4.5 Behaviour of the flow lines

In the present section we consider some numerical simulations showing the behaviour of the flow lines for sampling points inside the scatterer or on its boundary. The implementation of the LSM used for our simulations is the same as in [52]. Specifically, the regularized solution $\mathbf{g}_{\alpha(z)}(z) \in \mathbb{C}^N$ of a noisy and discretized version $\frac{2\pi}{N}\mathbf{F}_h\mathbf{g}(z) = \Phi_\infty(z)$ of the far-field equation is accomplished by means of Tikhonov method, where the regularization parameter $\alpha(z)$ is fixed to an optimal value $\alpha^*(z)$ by the generalized discrepancy principle. This regularized solution is used in (4.49) and in the associated Poynting vector (4.17) to obtain a discretized version of $u_z^{s,\epsilon}$ and $\mathcal{S}_z^{s,\epsilon}$, respectively.

Our numerical simulations are performed by choosing a frequency $\nu = 1$ GHz, corresponding to a wavelength $\lambda = 0.30$ m in vacuum, which is the background medium (i.e., $\varepsilon_B = \varepsilon_0$, $\sigma_B = 0$), and by using the same number $N = 15$ of incidence and observation angles. The far-field patterns are computed by a 2D TM direct code based on the method of moments [81], then are corrupted by 3% Gaussian noise and used as entries of the noisy far-field matrix \mathbf{F}_h . The investigation domain T is a square of minimum side 1.50 m, i.e., 5.00λ .

In the first numerical example we consider an ellipse centred at the origin, with semi-axes of length $a = 0.40\lambda$ and $b = 0.20\lambda$: this scatterer is characterized by constant relative electrical permittivity $\varepsilon_r = 2.0$ and electrical conductivity $\sigma = 0.20$ S/m. In this case, the LSM provides a satisfactory visualization, shown in Figure 5.13(a) together with the actual profile (solid black line). For future purpose, in Figure 5.13(b) we plot the point-values of the discretized discrepancy $d(z) := \left\| \frac{2\pi}{N}\mathbf{F}_h\mathbf{g}_{\alpha^*(z)}(z) - \Phi_\infty(z) \right\|_{\mathbb{C}^N}$, which is a numerical estimate of $\epsilon \geq \|Fg_z^\epsilon - \Phi_\infty(\cdot, z)\|_{L^2[0,2\pi]}$.

Figure 5.14 shows the behaviour of the flow lines of $u_z^{s,\epsilon}$ for a sampling point placed at the centre of the ellipse: more precisely, the arrows represent the unit vector $\hat{\mathcal{S}}_z^{s,\epsilon}$ obtained by discretizing and normalizing⁵⁶ the time-averaged Poynting vector field $\mathcal{S}_z^{s,\epsilon}$. The behaviour of the flow lines is essentially radial with respect to z , in this resembling the field generated by a point source located at z : in other terms, the scattered field $u_z^{s,\epsilon}$ reproduces, at least qualitatively, the features of the fundamental solution $\Phi(\cdot, z)$. Such a radial behaviour of the flow lines with respect to z is maintained for any z inside the scatterer or on its boundary, as shown e.g. in Figure 5.15 for $z = (0.00\lambda, 0.20\lambda)$: in particular, the flow lines are regular in the sense of Definition 4.4.1.

The second example is concerned with a case in which the visualization of the unknown scatterer is unsatisfactory. We consider two penetrable ellipses with the same dimensions

⁵⁶The normalization is performed in order to avoid scale effects impairing the visualization.

as the previous one: the upper ellipse is centred at the point $(0.00\lambda, 0.50\lambda)$ and characterized by constant relative electrical permittivity $\varepsilon_{r,1} = 10$ and electrical conductivity $\sigma_1 = 0.38\text{ S/m}$; the lower ellipse is centred at $(0.00\lambda, -0.50\lambda)$ and its electrical parameters are $\varepsilon_{r,2} = 20$ and $\sigma_2 = 0.50\text{ S/m}$. Figure 5.16(a) shows the visualization provided by the LSM, together with the true profile of the scatterer (solid black lines). In Figure 5.16(b) we plot the point-values of the discretized discrepancy $d(z)$.

As in the previous case, for a sampling point z inside the scatterer, or on its boundary, the behaviour of the flow lines of $u_z^{s,\epsilon}$ resembles that of $\Phi(\cdot, z)$: see Figure 5.17 (for $z = (0.00\lambda, 0.50\lambda)$), Figure 5.18 (for $z = (0.00\lambda, 0.70\lambda)$) and Figure 5.19 (for $z = (0.00\lambda, 0.30\lambda)$). We point out that in the case of Figure 5.18 the flow lines starting from a neighbourhood of z are regular in the sense of Definition 4.4.1; instead, this is not true in the case of Figure 5.19, since these flow lines cannot reach the far-field region without crossing the lower ellipse: notably, in this case the visualization provided by the LSM is bad in the region around z .

From this first set of simulations, we can conclude that, if $z \in D$, the flow lines of the scattered field (4.49) resemble those of the field $\Phi(\cdot, z)$ radiated by a pointlike source placed at z : this fact, as we shall see in the next section, suffices to explain the growing of $\|g_z^\epsilon\|_{L^2[0,2\pi]}$ as z approaches the boundary ∂D . A second set of simulations will be performed in Section 4.7 to study the behaviour of the flow lines when z is outside D .

Remark 4.5.1. As anticipated in Sections 1.4 and 4.3, here we shall not try to justify, from a mathematical viewpoint, the behaviour of the flow lines, as observed in numerical simulations. However, the fact that, for $z \in D$, the (normalized) Poynting vector field $\hat{\mathcal{S}}_z^{s,\epsilon}$ associated with the scattered field $u_z^{s,\epsilon}$ very closely resembles that of the pointlike source placed at z is remarkable: then, we want to sketch a heuristic explanation for this similarity, by assuming that the scattering conditions allow applying the FM.

To this end, we recall Remark 4.2.1, p. 91, where we pointed out that the problem of recovering a radiating field from its far-field pattern is ill-posed. This issue motivates a significant part of the investigation pursued by [10]⁵⁷: here, it is shown in detail, for the particular case of 3D acoustic scattering by a sound-soft obstacle, how and under what (sufficient) conditions a regularization method \tilde{R}_α for the far-field operator F naturally yields a regularization method $R_\alpha := -H\tilde{R}_\alpha$ for the solution operator G of the direct scattering problem (i.e., G maps the boundary values φ on ∂D into the far-field pattern u_∞ of the scattered field). In this case, for $z \in D$, the Tikhonov regularized solution $g_z^\alpha = \tilde{R}_\alpha \Phi_\infty(\cdot, z)$ of the far-field equation (4.10) is such that not only Fg_z^α is ‘close’⁵⁸ to

⁵⁷See, in particular, Theorem 3.3 of [10].

⁵⁸In this paragraph, ‘close’ is clearly intended, at any one time, with respect to an appropriate norm:

$\Phi_\infty(\cdot, z)$, but also the boundary values $\varphi_z^\alpha := R_\alpha \Phi_\infty(\cdot, z)$ of the scattered field $u_{g_z^\alpha}^s$ having Fg_z^α as its far-field pattern are ‘close’ to the boundary values⁵⁹ of $\Phi(\cdot, z)$ on ∂D . Then, by virtue of the well-posedness of the direct scattering problem, the scattered field $u_{g_z^\alpha}^s$ will be ‘close’ to $\Phi(\cdot, z)$ also in the near-field region, which suggests that the flow lines of these two fields may have a similar behaviour⁶⁰.

It is clear that such discussion should be made much more precise and, hopefully, independent of any assumption on the applicability of the FM. \square

4.6 A new version of the general theorem: $z \in D$

In the present section we shall provide a new version of the general theorem for the LSM when the sampling point is inside the scatterer. This new version exploits the considerations on the fluxes of the Poynting vector described in Section 4.4, as well as the numerical behaviour of its flow lines shown in Section 4.5. In the next section, we shall consider the case of z outside the scatterer.

According to the general theorem, for every $\epsilon > 0$ there exists a solution g_z^ϵ of the inequality (4.11) such that $\|g_z^\epsilon\|_{L^2[0, 2\pi]} \rightarrow \infty$ if $z \rightarrow z^* \in \partial D$. We prove that, under appropriate assumptions on the flow lines, the norm of *any* approximate solution of the far-field equation blows up for a *non-vanishing* (although small enough) bound ϵ on the discrepancy.

Theorem 4.6.1. *Under the same hypotheses of Theorem 4.1.1, consider a point $z^* \in \partial D$ and a neighbourhood U_{z^*} of z^* . If $z \in U_{z^*} \cap D$ and $\epsilon > 0$, let $g_z^\epsilon \in L^2[0, 2\pi]$ be such that*

$$\|Fg_z^\epsilon - \Phi_\infty(\cdot, z)\|_{L^2[0, 2\pi]} \leq \epsilon. \quad (4.55)$$

For each $z \in U_{z^} \cap D$, denote by $C_z(z^*)$ the circle of centre z^* and radius $r := |z - z^*|$, and by $\tilde{C}_z(z^*)$ the intersection $C_z(z^*) \cap (\mathbb{R}^2 \setminus D)$. Suppose that U_{z^*} is so small that $\tilde{C}_z(z^*)$ is an arc with endpoints $y_z^1, y_z^2 \in \partial D$ for each $z \in U_{z^*} \cap D$. Moreover, assume that the flow lines $\zeta_{y_z^1}(\tau)$ and $\zeta_{y_z^2}(\tau)$ of $u_{g_z^\epsilon}^s$ are regular and identify a regular flow strip with the asymptotic angular width $\psi_\infty(z) := |\varphi_\infty(y_z^1) - \varphi_\infty(y_z^2)|$; finally, assume that $\lim_{z \rightarrow z^*} \varphi_\infty(y_z^1)$ and $\lim_{z \rightarrow z^*} \varphi_\infty(y_z^2)$ exist finite and are different. Then, for any such $g_z^\epsilon \in L^2[0, 2\pi]$,*

$$\lim_{z \rightarrow z^*} \|g_z^\epsilon\|_{L^2[0, 2\pi]} = \infty \quad (4.56)$$

we refer to [10] and Sec. 3.2 in [48] for details.

⁵⁹See Corollary 3.4 of [10].

⁶⁰However, it is worth pointing out that *a priori* such similarity might hold even if the two fields are not ‘close’ to each other: in this sense, the mathematical justification of the behaviour of the flow lines, as assumed by our approach, might not require the applicability of the FM.

if ϵ is small enough.

Proof. We preliminarily note that the existence of $g_z^\epsilon \in L^2[0, 2\pi]$ satisfying inequality (4.55) follows from the denseness⁶¹ of the range of F .

Let $z^* \in \partial D$. Since the boundary ∂D is C^2 , the condition that $\tilde{C}_z(z^*)$ is an arc is satisfied provided that $|z - z^*|$ is small enough (see Figure 5.20).

Next we assume, by contradiction, that the limit (4.56) does not hold. Then, there exist a constant $K > 0$ and a sequence $\{z_n\}_{n=0}^\infty \subset U_{z^*} \cap D$ such that $\lim_{n \rightarrow \infty} |z_n - z^*| = 0$ and

$$\|g_{z_n}^\epsilon\|_{L^2[0, 2\pi]} \leq K \quad \forall n \in \mathbb{N}. \quad (4.57)$$

Now, let $B_1 := \{x \in \mathbb{R}^2 \mid |x| < R_1\}$ be the open disk centred at the origin and with radius R_1 large enough, so that $B_1 \supset \bar{D}$, and set $G := B_1 \setminus \bar{D}$. To show the contradiction, we need a common bound for the fields $u_{z_n}^{s, \epsilon}(x)$ (defined as in (4.49)) for any $x \in \bar{G}$ and $n \in \mathbb{N}$, as well as for their partial derivatives.

The continuity in \bar{G} of $u^s(\cdot, \theta)$ for each $\theta \in [0, 2\pi]$ is obvious, while the continuity in $[0, 2\pi]$ of $u^s(x, \cdot)$, uniformly with respect to $x \in \bar{G}$, i.e., the property

$$\lim_{\theta \rightarrow \theta_0} \max_{x \in \bar{G}} |u^s(x, \theta) - u^s(x, \theta_0)| = 0 \quad \forall \theta_0 \in [0, 2\pi], \quad (4.58)$$

follows⁶² from the well-posedness of the direct scattering problem⁶³ with respect to the maximum norm in $C(\bar{B}_1)$ and from the fact that

$$\lim_{\theta \rightarrow \theta_0} \max_{x \in \bar{B}_1} |e^{ikx \cdot \hat{d}(\theta)} - e^{ikx \cdot \hat{d}(\theta_0)}| = 0 \quad \forall \theta_0 \in [0, 2\pi]. \quad (4.59)$$

It is possible to show⁶⁴ that the two previous continuity properties imply that u^s is a continuous function of both the variables x and θ , i.e., $u^s \in C(A)$, where $A := \bar{G} \times [0, 2\pi]$. Since A is compact, we can define

$$M_1 := \max_{(x, \theta) \in A} |u^s(x, \theta)|. \quad (4.60)$$

As a consequence, by using the Cauchy-Schwarz inequality and comparing with (4.49) and (4.57), we have

$$|u_{z_n}^{s, \epsilon}(x)| \leq \int_0^{2\pi} |u^s(x, \theta) g_{z_n}^\epsilon(\theta)| d\theta \leq M_1 \sqrt{2\pi} \|g_{z_n}^\epsilon\|_{L^2[0, 2\pi]} \leq \sqrt{2\pi} M_1 K =: Q_1, \quad (4.61)$$

⁶¹See e.g. [35], p. 108.

⁶²A detailed explanation of this implication is given in Subsection 4.10.2, p. 121.

⁶³See [48], p. 222 and pp. 307-308.

⁶⁴For details, see again Subsection 4.10.2, p. 121.

for all $n \in \mathbb{N}$ and for all $x \in \bar{G}$.

By a similar procedure, we can bound the incident field $u_{z_n}^{i,\epsilon}(x) = v_{g_{z_n}^\epsilon}$ for all $n \in \mathbb{N}$ and for all $x \in \bar{G}$:

$$|v_{g_{z_n}^\epsilon}(x)| \leq \int_0^{2\pi} \left| e^{ikx \cdot \hat{d}(\theta)} g_{z_n}^\epsilon(\theta) \right| d\theta \leq \sqrt{2\pi} \|g_{z_n}^\epsilon\|_{L^2[0,2\pi]} \leq \sqrt{2\pi} K. \quad (4.62)$$

From (4.61) and (4.62), we find an upper bound for the total field $u_{z_n}^\epsilon = u_{z_n}^{i,\epsilon} + u_{z_n}^{s,\epsilon}$, i.e.,

$$|u_{z_n}^\epsilon(x)| \leq Q_1 + \sqrt{2\pi} K \quad \forall x \in \bar{G}, \quad \forall n \in \mathbb{N}. \quad (4.63)$$

To find a similar bound for the derivatives, we recall⁶⁵ that the direct scattering problem for an incident field $u^i(x)$ is equivalent to the Lippmann-Schwinger equation

$$u(x) = u^i(x) - k^2 \int_B \Phi(x, y) m(y) u(y) dy, \quad x \in \bar{B}, \quad (4.64)$$

where $m := 1 - n$, and $B := \{x \in \mathbb{R}^2 : |x| < R\}$ is any open disk such that $\bar{B} \supset \bar{D}$; in particular, by taking $R > R_1$, we can assume that $B \supset \bar{G}$. As a consequence of (4.64), we find that

$$\frac{\partial u_{z_n}^{s,\epsilon}}{\partial x_i}(x) = -k^2 \int_B \frac{\partial \Phi}{\partial x_i}(x, y) m(y) u_{z_n}^\epsilon(y) dy, \quad x \in B \supset \bar{G}, \quad (4.65)$$

where the partial derivative with respect to x_i (with $i = 1, 2$) can be brought inside the integral because of the boundedness of $m(y)u_{z_n}^\epsilon(y)$ [61]. If we denote by M an upper bound for $|m(y)|$, from (4.63) and (4.65) we get

$$\left| \frac{\partial u_{z_n}^{s,\epsilon}}{\partial x_i}(x) \right| \leq k^2 M \left(Q_1 + \sqrt{2\pi} K \right) \int_B \left| \frac{\partial \Phi}{\partial x_i}(x, y) \right| dy \quad \forall x \in \bar{G}, \quad \forall n \in \mathbb{N}. \quad (4.66)$$

By the same arguments used in [61], it is possible to show that the integral on the right-hand side of (4.66) is a continuous function of x : then it takes its maximum value, say M_2 , on \bar{G} . As a consequence, we find an upper bound for the derivatives of the scattered field, i.e.,

$$\left| \frac{\partial u_{z_n}^{s,\epsilon}}{\partial x_i}(x) \right| \leq k^2 M \left(Q_1 + \sqrt{2\pi} K \right) M_2 =: Q_2 \quad \forall x \in \bar{G}, \quad \forall n \in \mathbb{N}. \quad (4.67)$$

(If the scatterer is impenetrable, inequalities analogous to (4.61) and (4.67) can be proved more easily, by exploiting the well-posedness of the direct problem: for details, see the second part of Subsection 4.10.2, p. 123).

Now, let us evaluate the flux $\mathcal{F}_{\tilde{C}_{z_n}(z^*)}(u_{z_n}^{s,\epsilon})$ as $n \rightarrow \infty$ in two ways:

⁶⁵See [48], p. 216 and pp. 307-308.

a) *near the boundary ∂D , i.e., across $\tilde{C}_{z_n}(z^*)$.* In view of (4.18), we have

$$\mathcal{F}_{\tilde{C}_{z_n}(z^*)}(u_{z_n}^{s,\epsilon}) = \frac{1}{4i\omega \varepsilon_B \mu_B} \int_{\tilde{C}_{z_n}(z^*)} \left[\bar{u}_{z_n}^{s,\epsilon} \frac{\partial u_{z_n}^{s,\epsilon}}{\partial \nu} - u_{z_n}^{s,\epsilon} \frac{\partial \bar{u}_{z_n}^{s,\epsilon}}{\partial \nu} \right] (x) dl(x). \quad (4.68)$$

Then, by observing that $\tilde{C}_{z_n}(z^*) \subset \bar{G}$ for n large enough, and by applying inequalities (4.61), (4.67), we have

$$\left| \mathcal{F}_{\tilde{C}_{z_n}(z^*)}(u_{z_n}^{s,\epsilon}) \right| \leq \frac{1}{2\omega \varepsilon_B \mu_B} \int_{\tilde{C}_{z_n}(z^*)} \left| \bar{u}_{z_n}^{s,\epsilon}(x) \frac{\partial u_{z_n}^{s,\epsilon}}{\partial \nu}(x) \right| dl(x) \leq \sqrt{2} \frac{|\tilde{C}_{z_n}(z^*)|}{2\omega \varepsilon_B \mu_B} Q_1 Q_2, \quad (4.69)$$

where $|\tilde{C}_{z_n}(z^*)|$ denotes the length of the arc $\tilde{C}_{z_n}(z^*)$. Since $|\tilde{C}_{z_n}(z^*)| \rightarrow 0$ as $n \rightarrow \infty$ (i.e., as $z_n \rightarrow z^*$), we find that

$$\lim_{n \rightarrow \infty} \left| \mathcal{F}_{\tilde{C}_{z_n}(z^*)}(u_{z_n}^{s,\epsilon}) \right| = 0; \quad (4.70)$$

b) *in the far-field region.* To this end, we consider the regular flow strip delimited by the two regular flow lines $\zeta_{y_{z_n}^1}(\tau)$ and $\zeta_{y_{z_n}^2}(\tau)$ of $u_{z_n}^{s,\epsilon}$, so that the power flux outgoing from $\tilde{C}_{z_n}(z^*)$ is preserved along the flow strip itself up to infinity. Hence, recalling (4.18), (4.22), (4.23), (4.47), following the notations introduced by Definition 4.4.1 and assuming (it is not restrictive) that $\varphi_\infty(y_{z_n}^1) \leq \varphi_\infty(y_{z_n}^2)$, we have⁶⁶

$$\begin{aligned} \mathcal{F}_{\tilde{C}_{z_n}(z^*)}(u_{z_n}^{s,\epsilon}) &= \frac{1}{4i\omega \varepsilon_B \mu_B} \int_{\tilde{C}_{z_n}(z^*)} \left[\bar{u}_{z_n}^{s,\epsilon} \frac{\partial u_{z_n}^{s,\epsilon}}{\partial \nu} - u_{z_n}^{s,\epsilon} \frac{\partial \bar{u}_{z_n}^{s,\epsilon}}{\partial \nu} \right] (x) dl(x) = \quad (4.71) \\ &= \frac{1}{4i\omega \varepsilon_B \mu_B} \lim_{R \rightarrow \infty} \int_{\varphi_{[P_{y_{z_n}^1}^1(R)]}}^{\varphi_{[P_{y_{z_n}^2}^2(R)]}} \left[\bar{u}_{z_n}^{s,\epsilon} \frac{\partial u_{z_n}^{s,\epsilon}}{\partial r} - u_{z_n}^{s,\epsilon} \frac{\partial \bar{u}_{z_n}^{s,\epsilon}}{\partial r} \right] (R, \varphi) R d\varphi = \\ &= \frac{k}{2\omega \varepsilon_B \mu_B} \|Fg_{z_n}^\epsilon\|_{L^2[\varphi_\infty(y_{z_n}^1), \varphi_\infty(y_{z_n}^2)]}^2 \geq \\ &\geq \frac{k}{2\omega \varepsilon_B \mu_B} \left\{ \|\Phi_\infty(\cdot, z_n)\|_{L^2[\varphi_\infty(y_{z_n}^1), \varphi_\infty(y_{z_n}^2)]}^2 - \epsilon' [\varphi_\infty(y_{z_n}^1), \varphi_\infty(y_{z_n}^2)] \right\}. \end{aligned}$$

According to our assumptions, we have

$$\lim_{n \rightarrow \infty} \varphi_\infty(y_{z_n}^1) =: \varphi_\infty^1 \quad \text{and} \quad \lim_{n \rightarrow \infty} \varphi_\infty(y_{z_n}^2) =: \varphi_\infty^2; \quad (4.72)$$

then, from the chain of inequalities (4.71), we easily get

$$\liminf_{n \rightarrow \infty} \mathcal{F}_{\tilde{C}_{z_n}(z^*)}(u_{z_n}^{s,\epsilon}) \geq \frac{k}{2\omega \varepsilon_B \mu_B} \left[\|\Phi_\infty(\cdot, z^*)\|_{L^2[\varphi_\infty^1, \varphi_\infty^2]}^2 - \epsilon'(\varphi_\infty^1, \varphi_\infty^2) \right]. \quad (4.73)$$

⁶⁶A detailed explanation of the passage from the second to the third line of relations (4.71) is given in Subsection 4.10.3, p. 125.

Since, by hypothesis,

$$\psi_\infty(z^*) := |\varphi_\infty^1 - \varphi_\infty^2| \neq 0, \quad (4.74)$$

the inequality $\|\Phi_\infty(\cdot, z^*)\|_{L^2[\varphi_\infty^1, \varphi_\infty^2]}^2 > 0$ holds; hence, by taking ϵ small enough, we can make $\epsilon'(\varphi_\infty^1, \varphi_\infty^2)$ small enough too, so that the right-hand side of (4.73) is strictly positive, and a contradiction between (4.70) and (4.73) is obtained. More precisely, according to definition (4.48), it suffices to take

$$0 < \epsilon < (\sqrt{2} - 1) \|\Phi_\infty(\cdot, z^*)\|_{L^2[\varphi_\infty^1, \varphi_\infty^2]} = (\sqrt{2} - 1) \sqrt{\frac{\psi_\infty(z^*)}{8\pi k}}. \quad (4.75)$$

This concludes the proof. ■

Remark 4.6.1. An explicit computation of bound (4.75) requires the knowledge of the asymptotic angular width $\psi_\infty(z^*)$. Since numerical simulations show that, for $z \in D$, the behaviour of the flow lines of $u_z^{s,\epsilon}$ is essentially radial with respect to z , we can identify $\psi_\infty(z^*)$ with the limit amplitude of the Euclidean angle $y_{z_n}^1 \widehat{z_n} y_{z_n}^2$ having its vertex at z_n and subtended by the arc $\tilde{C}_{z_n}(z^*)$ as $n \rightarrow \infty$. Now, it is easily seen that $y_{z_n}^1 \widehat{z_n} y_{z_n}^2$ is an angle at the circumference $C_{z_n}(z^*)$ whose corresponding angle at the centre tends to π as $n \rightarrow \infty$, owing to the existence of the tangent t^* in z^* to the C^2 -boundary ∂D (see Figure 5.20). As a consequence, we find that $\psi_\infty(z^*) = \pi/2$, and then bound (4.75) becomes

$$0 < \epsilon < (\sqrt{2} - 1) \frac{1}{4\sqrt{k}}. \quad (4.76)$$

We shall come back to this point later. □

Remark 4.6.2. Of course, Theorem 4.6.1 only identifies *sufficient* conditions ensuring the validity of limit (4.56), which can then hold under weaker assumptions. The core of the proof of this theorem consists of finding a contradiction with limit (4.70), for example by showing that

$$\liminf_{n \rightarrow \infty} \mathcal{F}_{\tilde{C}_{z_n}(z^*)}(u_{z_n}^{s,\epsilon}) > 0. \quad (4.77)$$

To this end, we could replace assumptions (4.72) and (4.74) with the following (and weaker) one: for each sequence $\{z_n\}_{n=0}^\infty \subset D$ such that $\lim_{n \rightarrow \infty} |z_n - z^*| = 0$, the asymptotic angular width $\psi_\infty(z_n)$ of the regular flow strip starting from $\tilde{C}_{z_n}(z^*)$ is such that $\liminf_{n \rightarrow \infty} \psi_\infty(z_n) > 0$. □

4.7 A new version of the general theorem: $z \notin D$

Let us first observe that, if $x_0 \in \partial D$, uniqueness issues for the initial value problem (4.52) may arise. Indeed, the scattered field u^s is real-analytic in $\mathbb{R}^2 \setminus \bar{D}$ but is only in $C^1(\mathbb{R}^2 \setminus D)$

(or in $C^{1,\alpha}(\mathbb{R}^2 \setminus D)$, with $0 < \alpha < 1$, in the case of perfect conductors⁶⁷). Accordingly, its first derivatives are only in $C^0(\mathbb{R}^2 \setminus D)$ (or in $C^{0,\alpha}(\mathbb{R}^2 \setminus D)$), i.e., they are not necessarily Lipschitz up to ∂D . Hence the field \mathcal{S}^s defined in (4.17) is not necessarily Lipschitz up to ∂D : as a consequence, an initial point x_0 taken on ∂D may be a *ramification point*, i.e., a point whence several flow lines start. A clear example of this is provided by Figures 5.15 and 5.18. Indeed, as observed in Section 4.5, the radially of flow lines is approximately verified for sampling points z in D and even on ∂D : then, in the latter case, z is also a ramification point.

A situation where no ramification point is allowed occurs when a penetrable scatterer stands out from the background in a smooth way, i.e., when n is in $C^1(\mathbb{R}^2)$: indeed, in this case⁶⁸ $u^s \in C^2(\mathbb{R}^2)$. However, this smoothness property is seldom verified in practice; moreover, numerical simulations show that the support of such a smooth scatterer is significantly underestimated by the LSM, as expected. Hence, we shall not explicitly investigate this situation in the following.

In the case of sampling points z chosen in regions outside the scatterer where the visualization is good, ramification points on ∂D systematically show up in our numerical experiments and the behaviour of the flow lines, in general, is far from being radial with respect to z or any other point in the plane.

With reference to the same experiments of Section 4.5, in Figure 5.21 we consider a sampling point $z = (1.17 \lambda, 0.70 \lambda)$: notably, two ramification points (represented by red square boxes) are detectable on the boundary of the scatterer.

In Figure 5.22 the sampling point is $z = (0.70 \lambda, 1.17 \lambda)$: again, two ramification points show up on the boundary ∂D . Finally, Figure 5.23 shows the behaviour of the flow lines for a sampling point z placed at the origin of the investigation domain: except for the region between the two ellipses, the field has a radial behaviour with respect to the sampling point. However, we notice that no ramification point is detectable and the visualization of the scatterer around z is bad.

The occurrence of ramification points is supported not only by numerics but also by theory, since assuming their existence allows proving that $\|g_z^\epsilon\|_{L^2[0,2\pi]}$ must blow up for $z \notin D$, and therefore provides a coherent theoretical framework whereby the numerical simulations can be interpreted.

To this aim we introduce a definition describing the behaviour of the flow lines starting from a ramification point and reaching the far-field region. Of course, this definition is inspired by the radial behaviour of the flow lines of the Green's function $\Phi(\cdot, z)$ with

⁶⁷See [48], p. 51 and pp. 64-67.

⁶⁸See [48], pp. 212-222 and pp. 307-308.

respect to the point source z and generalizes some of its relevant features by using the concepts of regularity and asymptotic angular width introduced in Definitions 4.4.1 and 4.4.2.

Definition 4.7.1. *A radiating solution u of the Helmholtz equation in $\mathbb{R}^2 \setminus \bar{D}$ is said to be ‘partially pseudo-radial’ with respect to a ramification point $z_0 \in \partial D$ if there exist at least two regular flow lines $\zeta_{z_0}^1(\tau)$ and $\zeta_{z_0}^2(\tau)$ starting from z_0 such that their asymptotic polar angles $\varphi_\infty^1(z_0)$ and $\varphi_\infty^2(z_0)$ are different, i.e., $\varphi_\infty^1(z_0) \neq \varphi_\infty^2(z_0)$, and the flow strip delimited by $\zeta_{z_0}^1(\tau)$ and $\zeta_{z_0}^2(\tau)$ is regular. If $\{\zeta_{z_0}^i(\tau)\}_{i \in I}$ denotes the set of all such flow lines and $\{\varphi_\infty^i(z_0)\}_{i \in I}$ is the set of their asymptotic polar angles, the quantity $\psi_\infty(z_0) := \sup_{i,j \in I} |\varphi_\infty^i(z_0) - \varphi_\infty^j(z_0)| > 0$ is called the ‘asymptotic angular width’ of the beam of flow lines outgoing from z_0 .*

Theorem 4.7.1. *Under the same hypotheses of Theorem 4.1.1, consider a point $z \in \mathbb{R}^2 \setminus D$. If ϵ is small enough, then there cannot exist $g_z^\epsilon \in L^2[0, 2\pi]$ such that*

$$\|Fg_z^\epsilon - \Phi_\infty(\cdot, z)\|_{L^2[0, 2\pi]} \leq \epsilon \quad (4.78)$$

and the field $u_z^{s,\epsilon}$ is partially pseudo-radial with respect to some point $z_0 \in \partial D$.

Proof. Let $z \notin D$. Assume by contradiction that there exist $\epsilon > 0$ and $g_z^\epsilon \in L^2[0, 2\pi]$ such that the inequality (4.78) holds and the field $u_z^{s,\epsilon}$ is partially pseudo-radial with respect to a ramification point $z_0 \in \partial D$. Let $\psi_\infty(z_0) > 0$ be the asymptotic angular width of the beam of flow lines outgoing from z_0 . According to Definition 4.7.1, we can find two regular flow lines $\zeta_{z_0}^1(\tau)$, $\zeta_{z_0}^2(\tau)$ of asymptotic polar angles $\varphi_\infty^1(z_0)$, $\varphi_\infty^2(z_0)$ respectively, such that the corresponding regular flow strip has asymptotic angular width $\tilde{\psi}_\infty(z_0) := |\varphi_\infty^1(z_0) - \varphi_\infty^2(z_0)| > 0$, which can be made arbitrarily close to (but not greater than) $\psi_\infty(z_0)$.

Consider a family of circles $C_n(z_0)$ of centre z_0 and radius r_n , with $\lim_{n \rightarrow \infty} r_n = 0$, and let $y_n^1 := C_n(z_0) \cap \{\zeta_{z_0}^1(\tau)\}_{\tau \in [0, +\infty)}$, $y_n^2 := C_n(z_0) \cap \{\zeta_{z_0}^2(\tau)\}_{\tau \in [0, +\infty)}$. Finally, denote by $\tilde{C}_n(z_0) \subset \mathbb{R}^2 \setminus D$ the arc with end points y_n^1 and y_n^2 , resulting from the intersection between the circle $C_n(z_0)$ and the flow strip identified by the flow lines $\zeta_{z_0}^1(\tau)$ and $\zeta_{z_0}^2(\tau)$.

Following the procedure of the previous theorem, we evaluate the flux $\mathcal{F}_{\tilde{C}_n(z_0)}(u_z^{s,\epsilon})$ as $n \rightarrow \infty$ in two ways:

a) *close to the point z_0 , across $\tilde{C}_n(z_0)$:*

$$\mathcal{F}_{\tilde{C}_n(z_0)}(u_z^{s,\epsilon}) = \frac{1}{4i\omega \varepsilon_B \mu_B} \int_{\tilde{C}_n(z_0)} \left[\bar{u}_z^{s,\epsilon} \frac{\partial u_z^{s,\epsilon}}{\partial \nu} - u_z^{s,\epsilon} \frac{\partial \bar{u}_z^{s,\epsilon}}{\partial \nu} \right] (x) dl(x). \quad (4.79)$$

Then, by applying the mean-value theorem for integration, we have:

$$\begin{aligned} \left| \mathcal{F}_{\tilde{C}_n(z_0)}(u_z^{s,\epsilon}) \right| &\leq \frac{1}{2\omega \varepsilon_B \mu_B} \int_{\tilde{C}_n(z_0)} \left| \bar{u}_z^{s,\epsilon}(x) \frac{\partial u_z^{s,\epsilon}}{\partial \nu}(x) \right| dl(x) = \\ &= \frac{|\tilde{C}_n(z_0)|}{2\omega \varepsilon_B \mu_B} |\bar{u}_z^{s,\epsilon}(\tilde{x}_n)| \cdot \left| \frac{\partial u_z^{s,\epsilon}}{\partial \nu}(\tilde{x}_n) \right|, \end{aligned} \quad (4.80)$$

where \tilde{x}_n is an appropriate point of $\tilde{C}_n(z_0)$. Since

$$\lim_{n \rightarrow \infty} |\tilde{C}_n(z_0)| = 0, \quad \lim_{n \rightarrow \infty} |\tilde{x}_n - z_0| = 0, \quad (4.81)$$

by the continuity of $u_z^{s,\epsilon}$ and $\frac{\partial u_z^{s,\epsilon}}{\partial \nu}$ we have

$$\lim_{n \rightarrow \infty} |\bar{u}_z^{s,\epsilon}(\tilde{x}_n)| = |\bar{u}_z^{s,\epsilon}(z_0)|, \quad \lim_{n \rightarrow \infty} \left| \frac{\partial u_z^{s,\epsilon}}{\partial \nu}(\tilde{x}_n) \right| = \left| \frac{\partial u_z^{s,\epsilon}}{\partial \nu}(z_0) \right|. \quad (4.82)$$

As a result, from (4.80) and (4.82), we find

$$\lim_{n \rightarrow \infty} \left| \mathcal{F}_{\tilde{C}_n(z_0)}(u_z^{s,\epsilon}) \right| = 0; \quad (4.83)$$

b) *in the far-field region.* Following the proof of Theorem 4.6.1, we consider the regular flow strip bounded by the flow lines $\zeta_{z_0}^1(\tau)$ and $\zeta_{z_0}^2(\tau)$ of $u_z^{s,\epsilon}$, outgoing from z_0 , and track the power flux outgoing from $\tilde{C}_n(z_0)$ up to the far-field region. As in the proof of (4.71), we obtain, for each $n \in \mathbb{N}$:

$$\begin{aligned} \mathcal{F}_{\tilde{C}_n(z_0)}(u_z^{s,\epsilon}) &= \frac{1}{4i\omega \varepsilon_B \mu_B} \int_{\tilde{C}_n(z_0)} \left[\bar{u}_z^{s,\epsilon} \frac{\partial u_z^{s,\epsilon}}{\partial \nu} - u_z^{s,\epsilon} \frac{\partial \bar{u}_z^{s,\epsilon}}{\partial \nu} \right] (x) dl(x) = \\ &= \frac{1}{4i\omega \varepsilon_B \mu_B} \lim_{R \rightarrow \infty} \int_{\varphi[P_{z_0}^1(R)]}^{\varphi[P_{z_0}^2(R)]} \left[\bar{u}_z^{s,\epsilon} \frac{\partial u_z^{s,\epsilon}}{\partial r} - u_z^{s,\epsilon} \frac{\partial \bar{u}_z^{s,\epsilon}}{\partial r} \right] (R, \varphi) R d\varphi = \\ &= \frac{k}{2\omega \varepsilon_B \mu_B} \|F g_z^\epsilon\|_{L^2[\varphi_\infty^1(z_0), \varphi_\infty^2(z_0)]}^2 \geq \\ &\geq \frac{k}{2\omega \varepsilon_B \mu_B} \left\{ \|\Phi_\infty(\cdot, z)\|_{L^2[\varphi_\infty^1(z_0), \varphi_\infty^2(z_0)]}^2 - \epsilon' [\varphi_\infty^1(z_0), \varphi_\infty^2(z_0)] \right\}. \end{aligned} \quad (4.84)$$

Since $\tilde{\psi}_\infty(z_0) = |\varphi_\infty^1(z_0) - \varphi_\infty^2(z_0)| > 0$, we have $\|\Phi_\infty(\cdot, z)\|_{L^2[\varphi_\infty^1(z_0), \varphi_\infty^2(z_0)]}^2 > 0$; this leads to a contradiction between (4.83) and (4.84) for ϵ such that

$$0 < \epsilon < (\sqrt{2} - 1) \|\Phi_\infty(\cdot, z)\|_{L^2[\varphi_\infty^1(z_0), \varphi_\infty^2(z_0)]} = (\sqrt{2} - 1) \sqrt{\frac{\tilde{\psi}_\infty(z_0)}{8\pi k}}. \quad (4.85)$$

This concludes the proof. ■

Remark 4.7.1. Analogously to Remark 4.6.1, we note that an explicit computation of bound (4.85) is only possible by knowing the asymptotic angular width $\tilde{\psi}_\infty(z_0)$. In our framework, this knowledge can only be obtained *a posteriori*, by looking in each case at the flow lines provided by the numerical simulations, as we shall do in the next section, in order to compare bounds (4.75) and (4.85) with the values of the discrepancy. However, as observed in Section 4.5, for sampling points z on ∂D the flow lines still have a radial behaviour: then, bound (4.76) is even an underestimate of the maximum ϵ allowed by (4.85) for such points, at least in those cases (like in Figures 5.15 and 5.18) where the flow lines can reach the far-field region without intersecting the scatterer. \square

Remark 4.7.2. The proof of Theorem 4.7.1 is developed by considering a single ramification point z_0 , but it is easily adapted to account for two or more such points. For example, if we assume the existence of two ramification points z_0 and z'_0 , we can consider two flow strips with asymptotic angular widths $\tilde{\psi}_\infty(z_0) = |\varphi_\infty^1(z_0) - \varphi_\infty^2(z_0)|$ and $\tilde{\psi}_\infty(z'_0) = |\varphi_\infty^1(z'_0) - \varphi_\infty^2(z'_0)|$. Then, our argument still holds by considering two vanishing sequences $\{r_n\}_{n=0}^\infty$, $\{r'_n\}_{n=0}^\infty$ and two corresponding families of collapsing circles $C_n(z_0)$, $C'_n(z'_0)$. Accordingly, the integral on $\tilde{C}_n(z_0)$ appearing in (4.79), (4.80) and (4.84) should be replaced by an integral on $\tilde{C}_n(z_0) \cup \tilde{C}'_n(z'_0)$, i.e., by the sum of two integrals, each of which behaves as shown in the proof. As a result, in bound (4.85) the norm of $\Phi_\infty(\cdot, z)$ in $L^2[\varphi_\infty^1(z_0), \varphi_\infty^2(z_0)]$ must be replaced by the norm of $\Phi_\infty(\cdot, z)$ in $L^2([\varphi_\infty^1(z_0), \varphi_\infty^2(z_0)] \cup [\varphi_\infty^1(z'_0), \varphi_\infty^2(z'_0)])$. Accordingly, in the same (4.85), $\tilde{\psi}_\infty(z_0)$ should be replaced by the *total asymptotic angular width*, defined as $\tilde{\psi}_\infty^T := \tilde{\psi}_\infty(z_0) + \tilde{\psi}_\infty(z'_0)$. \square

From Theorem 4.7.1 two natural issues arise, which we want to address. First, the statement of the theorem seems to be in contradiction with Figures 5.21 and 5.22, which rather seem to support the existence of a $g_z^\epsilon \in L^2[0, 2\pi]$ fulfilling the properties considered in the statement itself⁶⁹. This is apparently a paradox, since the theorem was formulated just taking inspiration from these figures. However, we should not forget that the correspondence between theory (i.e., continuous framework) and numerics (i.e., discrete and noisy framework) is not exact. In particular, the non-existence (in the former context) of a $g_z^\epsilon \in L^2[0, 2\pi]$ with the required properties will reflect upon a comparatively large value (in the latter one) of the \mathbb{C}^N -norm of the vector obtained from a discretization of g_z^ϵ itself. More specifically, we should expect that $\|\mathbf{g}_{\alpha^*(z)}(z)\|_{\mathbb{C}^N}$ (cf. Section 4.5) is much larger for z outside the scatterer than inside it (with a transition region across the boundary) and that $\alpha^*(z)$ is much smaller outside than inside it, at least when the visualization provided

⁶⁹We are going to verify, in the next section, that in the case of Figures 5.21 and 5.22 the value of ϵ is small enough, in the sense of bound (4.85) and Remark 4.7.2, as required by Theorem 4.7.1.

by the LSM is good. This is what actually happens, as we are going to see in the next section.

A second issue arises from an apparent self-contradiction in the statement of Theorem 4.7.1: the non-existence of $g_z^\epsilon \in L^2[0, 2\pi]$ with the required properties is established under the assumption of pseudo-radiality for the field $u_z^{s,\epsilon}$; but the non-existence of such $g_z^\epsilon \in L^2[0, 2\pi]$ seems to imply the non-existence of the corresponding field $u_z^{s,\epsilon}$ (and, consequently, of its flow lines). Accordingly, the requirement of pseudo-radiality is made about a field that does not apparently exist. This difficulty can be overcome by observing that the condition $g_z^\epsilon \in L^2[0, 2\pi]$ is not necessary for the existence of the field $u_z^{s,\epsilon}$, as given by (4.49).

To this purpose, we point out that the far-field operator F , given by (4.5), can be certainly regarded as defined on a space larger than $L^2[0, 2\pi]$: indeed, for each $\varphi \in [0, 2\pi]$, the far-field pattern $u_\infty(\varphi, \cdot)$ is real-analytic⁷⁰ on the interval $(0, 2\pi)$, and then $u_\infty(\varphi, \cdot) \in C^\infty(0, 2\pi)$. As a consequence, F can be easily defined, e.g., on the space of distributions having compact support, i.e.⁷¹, $\mathcal{E}^*(0, 2\pi) := \{g \in \mathcal{D}^*(0, 2\pi) : \text{supp } g \subset\subset (0, 2\pi)\}$, provided that the integral on the right-hand side of (4.5) is interpreted in the pairing sense, i.e., $\langle g, u_\infty(\varphi, \cdot) \rangle$. Analogous remarks can be made for the expression (4.7) of the superposed incident field $u^i = v_g$. This implies that, for any $g \in \mathcal{E}^*(0, 2\pi)$, Fg is actually the far-field pattern of a scattered field, which, by superposition, is given by the integral (4.49) in the pairing sense.

For example, the numerical/experimental set-up itself, involving a finite number N of incidence angles $\{\theta_0, \dots, \theta_{N-1}\}$, suggests enlarging the space to which g belongs in such a way that also g of the form

$$g(\theta) = \sum_{i=0}^{N-1} c_i \delta(\theta - \theta_i) \in \mathcal{E}^*(0, 2\pi) \quad (4.86)$$

(where, for each $i = 0, \dots, N-1$, $c_i \in \mathbb{C}$ and $\delta(\cdot - \theta_i)$ denotes the Dirac delta in \mathbb{R} concentrated at $\theta_i \in (0, 2\pi)$) can be considered as a candidate to be an approximate solution of the far-field equation (4.10): indeed, the form (4.86) for g is the only possibility for constructing an incident field v_g that is formally expressed by relation (4.7) but actually consists of a finite superposition of N plane waves with weights c_i .

Summarizing, the non-existence of a $g_z^\epsilon \in L^2[0, 2\pi]$ endowed with the properties required by Theorem 4.7.1 does not prevent us from considering the field $u_z^{s,\epsilon}$ and its flow lines.

⁷⁰See e.g. [48], p. 35.

⁷¹See e.g. [75], pp. 65-67.

A final comment is in order: so far we have only dealt with the full-view configuration of probes. Then, we conclude this section by sketching the extension of our approach to the aspect-limited case. Let $\Gamma_i, \Gamma_o \subset [0, 2\pi]$ be the sets of incidence and observation angles θ, φ respectively (for brevity, we consider Γ_o independent of θ). An ϵ -approximate solution of the modified far-field equation⁷² is a function $g_z^\epsilon \in L^2(\Gamma_i)$ such that

$$\left\| \int_{\Gamma_i} u_\infty(\cdot, \theta) g_z^\epsilon(\theta) d\theta - \Phi_\infty(\cdot, z) \right\|_{L^2(\Gamma_o)} \leq \epsilon. \quad (4.87)$$

In any case, the corresponding field $u_z^{s,\epsilon}(x) := \int_{\Gamma_i} u^s(x, \theta) g_z^\epsilon(\theta) d\theta$ and its flow lines are defined for all $x \in \mathbb{R}^2 \setminus D$; moreover, its far-field pattern, defined for $\varphi \in [0, 2\pi]$, satisfies condition (4.87) at least for $\varphi \in \Gamma_o$, and even in a larger set $\Gamma'_o \supset \Gamma_o$ if the left-hand side of (4.87) is strictly smaller than ϵ . Now, if $\Gamma'_o = [0, 2\pi]$, the situation is analogous to the full-view case; otherwise, Theorems 4.6.1 and 4.7.1 ensure that $\|g_z^\epsilon\|_{L^2(\Gamma_i)}$ blows up for each z approaching $z^* \in \partial D$ (or placed in $\mathbb{R}^2 \setminus D$), such that the flow lines starting from a neighbourhood of z^* (or from a ramification point z_0) reach, under the usual assumptions, the far-field region inside Γ'_o with a non-vanishing asymptotic angular width. Again, this is in qualitative agreement with numerical simulations, which show [42, 43, 44] that, when the emitters and receivers are placed in the same region, the scatterer is, in general, best visualized in its illuminated part.

4.8 Tikhonov regularization and numerical validation

Theorems 4.6.1 and 4.7.1 deal with generic ϵ -approximate solutions g_z^ϵ of the far-field equation. However, it is of interest to focus on Tikhonov regularized solutions, from both the theoretical and the numerical viewpoint, since they play a major role in the implementation of the LSM.

First of all, we observe that Theorem 4.6.1 does not state that $\|g_z^\epsilon\|_{L^2[0,2\pi]}$ is bounded for $z \in D$: rather, the existence of $g_z^\epsilon \in L^2[0, 2\pi]$, ensured by the denseness of the range of F , is a starting point of our argument. However, when Tikhonov regularized solutions $g_{\alpha^*(z)}$ of the far-field equation are considered, the boundedness of $\|g_{\alpha^*(z)}\|_{L^2[0,2\pi]}$ for $z \in D$ simply follows from the fact that $\alpha^*(z) > 0$. What Theorem 4.6.1 can establish is that, in spite of regularization, appropriate conditions on the flow lines as well as bound (4.75), which reads

$$\|Fg_{\alpha^*(z)} - \Phi_\infty(\cdot, z)\|_{L^2[0,2\pi]} < (\sqrt{2} - 1) \frac{1}{4\sqrt{k}} \quad \text{if } z \in D \quad (4.88)$$

⁷²See e.g. [35], p. 79.

in consequence of (4.76), force the norm $\|g_{\alpha^*(z)}\|_{L^2[0,2\pi]}$ to blow up when z tends to a point $z^* \in \partial D$, i.e., $\alpha^*(z)$ must vanish as $z \rightarrow z^*$. In other terms, inequality (4.88) suggests a criterion for choosing the regularization parameter $\alpha^*(z)$ for $z \in D$ in such a way that $g_{\alpha^*(z)}$ behaves as one of the approximate solutions of the far-field equation satisfying the condition described by limit (4.12)(a) of Theorem 4.1.1.

By a similar argument, Theorem 4.7.1 shows that, if $z \notin D$, the partial pseudo-radiality of $u_z^{s,\epsilon}$ with asymptotic angular width $\tilde{\psi}_\infty(z_0)$ and bound (4.85), i.e.,

$$\|Fg_{\alpha^*(z)} - \Phi_\infty(\cdot, z)\|_{L^2[0,2\pi]} < (\sqrt{2} - 1) \sqrt{\frac{\tilde{\psi}_\infty(z_0)}{8\pi k}} \quad \text{if } z \notin D, \quad (4.89)$$

cannot be simultaneously verified for a positive $\alpha^*(z)$. Accordingly, taking $\alpha^*(z) \rightarrow 0$ makes $\|g_{\alpha^*(z)}\|_{L^2[0,2\pi]}$ blow up, which corresponds to limit (4.14)(a) of Theorem 4.1.1.

Up to discretization and noise issues not explicitly addressed here, this behaviour of $\alpha^*(z)$ is in qualitative agreement with numerical simulations, which show, as well known [52, 65], that the values of $\alpha^*(z)$ are generally much smaller for z outside than for z inside the scatterer.

Moreover, although discretization and noise prevent an exact correspondence between numerical simulations and theoretical results, it is anyway interesting to compare, as a check of internal consistency for our framework, the theoretical bounds on ϵ , as given by (4.75) (i.e., (4.76)) and (4.85), with the values of the discretized discrepancy $d(z)$ (plotted in Figures 5.13(b) and 5.16(b)) at the sampling points z considered in the simulations of Sections 4.5 and 4.7. This comparison is non-trivial since, on the one hand, the physical interpretation formalized by Theorems 4.6.1 and 4.7.1 can be applied only if $d(z) \leq \epsilon$ and, on the other hand, the values of $d(z)$ are fixed by using the generalized discrepancy principle, while the bounds on ϵ are estimated in a completely different way, i.e., on the basis of the (total) asymptotic angular width of the flow lines.

For both the scattering experiments considered in Sections 4.5 and 4.7, the wave number k is the same, i.e., $k = \frac{2\pi}{\lambda} = 2.09 \cdot 10^6 \text{ m}^{-1}$. As a consequence, bound (4.76) for $z \rightarrow z^* \in \partial D$ reads $\epsilon < 2.3 \cdot 10^{-2}$. Figures 5.13(b) and 5.16(b), which plot the values of $d(z)$ for each z in the investigation domain, clearly show that, for both numerical experiments, $d(z) < 2.3 \cdot 10^{-2}$ for any z inside D and even on ∂D . However, while in the first experiment also the assumptions on the flow lines required by Theorem 4.6.1 are verified (see Figure 5.15), in the second one this only happens for a sampling point placed as in Figure 5.18, but not as in Figure 5.19: coherently with our approach, in the latter case the sampling point is placed in a region where the visualization of the scatterer is bad.

Let us now turn to the case of a sampling point external to the scatterer. For the single ellipse, the behaviour of the flow lines is shown in Figure 5.21. If we refer the square investigation domain T to the usual polar coordinates (r, φ) , from Figure 5.21 we can see that the asymptotic angular width $\tilde{\psi}_\infty(z_0)$ of the beam of flow lines outgoing from the left-upper ramification point z_0 is approximately given by $|\varphi_\infty^1(z_0) - \varphi_\infty^2(z_0)| \approx \pi$, since $\varphi_\infty^1(z_0) \approx 0$ and $\varphi_\infty^2(z_0) \approx \pi$. For the right-lower ramification point z'_0 , the asymptotic angular width $\tilde{\psi}_\infty(z'_0)$ can be estimated from $\varphi_\infty^1(z'_0) \approx 5\pi/4$ and $\varphi_\infty^2(z'_0) \approx 2\pi$, i.e., $\tilde{\psi}_\infty(z'_0) \approx 3\pi/4$. As a result, the total asymptotic angular width (see Remark 4.7.2) is $\tilde{\psi}_\infty^T \approx 7\pi/4$ and then bound (4.85) becomes $\epsilon < 4.2 \cdot 10^{-2}$. This bound is approximately fulfilled by the value of the discrepancy $d(z) = 4.4 \cdot 10^{-2}$ at the sampling point z chosen for Figure 5.21.

In the experiment with two ellipses, only the visualization of Figure 5.22 is worth discussing for the case of an external sampling point z : indeed, in Figure 5.23 no ramification point appears and the visualization around z is bad. For the upper ramification point z_0 of Figure 5.22, we can estimate $\varphi_\infty^1(z_0) \approx \pi/4$ and $\varphi_\infty^2(z_0) \approx \pi$, and then $\tilde{\psi}_\infty(z_0) \approx 3\pi/4$; for the right-lower ramification point z'_0 , Figure 5.22 suggests the values $\varphi_\infty^1(z'_0) \approx 3\pi/2$ and $\varphi_\infty^2(z'_0) \approx 2\pi$, i.e., $\tilde{\psi}_\infty(z'_0) \approx \pi/2$. Accordingly, the total asymptotic angular width is $\tilde{\psi}_\infty^T \approx 5\pi/4$ and then bound (4.85) reads $\epsilon < 3.6 \cdot 10^{-2}$, which is fulfilled by the value of the discrepancy $d(z) = 3.3 \cdot 10^{-2}$ at the sampling point of Figure 5.22.

Finally, it is interesting to observe that the maximum value of the theoretical bound on ϵ is obtained from relation (4.85) for a total asymptotic angular width $\tilde{\psi}_\infty^T = 2\pi$, which corresponds to $\epsilon < 4.5 \cdot 10^{-2}$: notably, this bound approximately coincides with the maximum values taken by the discrepancy $d(z)$, as plotted in Figures 5.13(b) and 5.16(b).

Remark 4.8.1. At the beginning of this section we saw that $\alpha^*(z) \rightarrow 0$ as $z \rightarrow z^* \in \partial D$ from the inside of D , and we recalled that such a behaviour of $\alpha^*(z)$ is in agreement with the results of numerical simulations [52, 65]. Hence, having in mind Theorem 4.10.1, one might expect an analogous behaviour of the (discretized) discrepancy $d(z)$; on the other hand, the plots of $d(z)$ shown in Figures 5.13(b) and 5.16(b) contradict such expectation, since they rather seem to highlight a slight increase (and certainly no decrease) of $d(z)$ as z approaches the boundary ∂D from inside. However, Theorem 4.10.1 simply states that, for each fixed $z \in \mathbb{R}^2$, the discrepancy $\beta(\alpha; z)$ is a vanishing function of α as $\alpha \rightarrow 0^+$, whence it does not follow that $\beta[\alpha^*(z); z]$ is a vanishing function of z as $z \rightarrow z^* \in \partial D$. Since $d(z)$ is a numerical estimate of $\beta[\alpha^*(z); z]$, we conclude that no expectation on $d(z)$ as $z \rightarrow z^*$ is *a priori* suggested⁷³ by Theorem 4.10.1. \square

⁷³The case of a fixed $z \notin D$ is different: here, taking a vanishing $\alpha^*(z)$ implies that the discrepancy also

4.9 Conclusions and hints for future developments

In this chapter we discuss a physical interpretation of the LSM based on energy conservation arguments. Our analysis considers the flow lines of the time-averaged Poynting vector field associated with the radiating field $u_z^{s,\epsilon}$, defined in terms of approximate solutions of the far-field equation as specified in (4.49). Our main theoretical result is that when the flow lines satisfy certain regularity properties (suggested by numerical simulations), then conservation of energy along the flow strips forces the approximate (and, in particular, Tikhonov regularized) solutions of the far-field equation to behave like indicator functions for the boundary of the scatterer. Moreover, numerical simulations confirm that, when a bad performance of the LSM occurs, the assumptions on the flow lines are not fulfilled, as is to be expected.

Possible future developments of our approach concern both theoretical and numerical issues. For example, it would be interesting to perform an *a priori* analysis of the flow lines of the Poynting vector from the viewpoint of topological dynamics, by assuming that the physical and geometric properties of the scatterer and the background are known: this would be a necessary step for making our physical interpretation a mathematical justification of the LSM.

Other issues deserving investigation are concerned with extending or adapting our physical interpretation to different or more general scattering conditions (cf. e.g. [5, 8]), as well as to other qualitative methods, like the factorization method⁷⁴ [69] and the reciprocity gap functional method [36, 44].

4.10 Addenda to Chapter 4

4.10.1 A technical result about the discrepancy

In the following theorem, we prove that when Tikhonov regularization is applied to the far-field equation (4.10), considering a vanishing regularization parameter amounts to considering a vanishing discrepancy.

vanishes by the same Theorem 4.10.1. However, as already pointed out, in the numerical implementation of the LSM we always find positive values of $\alpha^*(z)$ and, accordingly, positive values of $d(z)$: then, what the current remark points out is that the well-known behaviour of $\alpha^*(z)$ ('large' inside D and 'small' outside D) does not imply an analogous behaviour of $d(z)$.

⁷⁴In [8] this method is briefly considered from our perspective.

Theorem 4.10.1. *For each $z \in \mathbb{R}^2$, let g_z^α be the Tikhonov regularized solution of the far-field equation (4.10) and $\beta(\alpha; z) := \|Fg_z^\alpha - \Phi_\infty(\cdot, z)\|_{L^2[0, 2\pi]}$ the corresponding discrepancy. Then, under the hypotheses of Theorem 4.1.1, the limit*

$$\lim_{\alpha \rightarrow 0^+} \beta(\alpha; z) = 0 \quad \forall z \in \mathbb{R}^2 \quad (4.90)$$

holds. Moreover, for any fixed $z \in \mathbb{R}^2$, let $\alpha(\epsilon) > 0$ be such that

$$\beta[\alpha(\epsilon); z] \leq \epsilon \quad \forall \epsilon > 0; \quad (4.91)$$

then, the limit

$$\lim_{\epsilon \rightarrow 0^+} \alpha(\epsilon) = 0 \quad (4.92)$$

holds.

Proof. Under the hypotheses of Theorem 4.1.1, the range of the far-field operator F is dense⁷⁵ in $L^2[0, 2\pi]$. Then, the incompatibility measure⁷⁶ of the (noise-free) far-field equation (4.10) is zero, i.e.,

$$\mu[F, \Phi_\infty(\cdot, z)] := \inf_{g \in L^2[0, 2\pi]} \|Fg - \Phi_\infty(\cdot, z)\|_{L^2[0, 2\pi]} = 0. \quad (4.93)$$

Hence, limit (4.90) immediately follows from the well-known property⁷⁷

$$\lim_{\alpha \rightarrow 0^+} \beta(\alpha; z) = \mu[F, \Phi_\infty(\cdot, z)]. \quad (4.94)$$

Assume now that, for every $\epsilon > 0$, $\alpha(\epsilon) > 0$ verifies condition (4.91): this assumption is clearly non-empty by virtue of limit (4.90). Since the far-field operator F is compact⁷⁸, we can consider its singular system⁷⁹ $\{\sigma_p, u_p, v_p\}_{p=0}^\infty$. The latter is non-finite owing to the density of the range of F in $L^2[0, 2\pi]$: in particular, the set $\{v_p\}_{p=0}^\infty$ is an orthonormal basis of $L^2[0, 2\pi]$.

We can now write the explicit expression⁸⁰ of $\beta[\alpha(\epsilon); z]$ in terms of the singular system

⁷⁵See e.g. [35], p. 108.

⁷⁶See [89], p. 10.

⁷⁷See [89], p. 19.

⁷⁸See [35], pp. 124-125.

⁷⁹For basic concepts and notations, see e.g. Subsection 1.5.1 at pp. 16-20 of [4].

⁸⁰Cf. [4], p. 41 and p. 136.

of F as

$$\begin{aligned}
\beta[\alpha(\epsilon); z] &= \|Fg_z^\alpha - \Phi_\infty(\cdot, z)\|_{L^2[0, 2\pi]} = & (4.95) \\
&= \left\| \sum_{p=0}^{\infty} \frac{\sigma_p^2}{\sigma_p^2 + \alpha(\epsilon)} (\Phi_\infty(\cdot, z), v_p)_{L^2[0, 2\pi]} v_p - \sum_{p=0}^{\infty} (\Phi_\infty(\cdot, z), v_p)_{L^2[0, 2\pi]} v_p \right\|_{L^2[0, 2\pi]} = \\
&= \left\| \sum_{p=0}^{\infty} \frac{-\alpha(\epsilon)}{\sigma_p^2 + \alpha(\epsilon)} (\Phi_\infty(\cdot, z), v_p)_{L^2[0, 2\pi]} v_p \right\|_{L^2[0, 2\pi]} \leq \epsilon,
\end{aligned}$$

whence thesis (4.92) immediately follows, since $\Phi_\infty(\cdot, z) \neq 0$. ■

4.10.2 Continuity properties of scattered fields

Case 1. Penetrable scatterers

In this subsection, we want to justify in detail some statements made in the initial part of the proof of Theorem 4.6.1, i.e., from assumption (4.57) to definition (4.60). With the same notations used there, let us introduce the function $f : \bar{B}_1 \times [0, 2\pi] \rightarrow \mathbb{C}$ defined as $f(x, \theta) := e^{ikx \cdot \hat{d}(\theta)}$. This function is clearly continuous on the compact set $E := \bar{B}_1 \times [0, 2\pi]$, then⁸¹ f is uniformly continuous on E . Accordingly, given $\epsilon > 0$, it is possible to find $\delta > 0$, depending only on ϵ , such that

$$|f(x', \theta') - f(x, \theta)| < \epsilon \quad \forall (x', \theta'), (x, \theta) \in E : \|(x', \theta') - (x, \theta)\|_{\mathbb{R}^3} < \delta. \quad (4.96)$$

In particular, relation (4.96) implies that

$$|f(x, \theta') - f(x, \theta)| < \epsilon \quad \forall (x, \theta'), (x, \theta) \in E : \|(x, \theta') - (x, \theta)\|_{\mathbb{R}^3} < \delta, \quad (4.97)$$

and then

$$\max_{x \in \bar{B}_1} |f(x, \theta') - f(x, \theta)| < \epsilon \quad \forall \theta', \theta \in [0, 2\pi] : |\theta' - \theta| < \delta, \quad (4.98)$$

whence

$$\lim_{\theta' \rightarrow \theta} \max_{x \in \bar{B}_1} |f(x, \theta') - f(x, \theta)| = 0 \quad \forall \theta \in [0, 2\pi], \quad (4.99)$$

i.e., by replacing (θ', θ) with (θ, θ_0) and remembering the definition of f ,

$$\lim_{\theta \rightarrow \theta_0} \max_{x \in \bar{B}_1} |e^{ikx \cdot \hat{d}(\theta)} - e^{ikx \cdot \hat{d}(\theta_0)}| = 0 \quad \forall \theta_0 \in [0, 2\pi], \quad (4.100)$$

⁸¹See e.g. [63], p. 155.

which is limit (4.59) in the proof of Theorem 4.6.1. By virtue of Theorem 8.7 at p. 222 in [48], which states the well-posedness of the direct scattering problem with respect to the maximum norm in $C(\bar{B}_1)$, we find that the total field $u(x, \theta) = u^s(x, \theta) + e^{ikx \cdot \hat{d}(\theta)}$ verifies

$$\lim_{\theta \rightarrow \theta_0} \max_{x \in \bar{B}_1} |u(x, \theta) - u(x, \theta_0)| = 0 \quad \forall \theta_0 \in [0, 2\pi]. \quad (4.101)$$

Moreover, since $u^s(x, \theta) = u(x, \theta) - e^{ikx \cdot \hat{d}(\theta)}$, by the triangle inequality we have

$$|u^s(x, \theta) - u^s(x, \theta_0)| \leq |u(x, \theta) - u(x, \theta_0)| + \left| e^{ikx \cdot \hat{d}(\theta)} - e^{ikx \cdot \hat{d}(\theta_0)} \right| \quad \forall x \in \bar{B}_1, \quad \forall \theta, \theta_0 \in [0, 2\pi], \quad (4.102)$$

whence it follows that $\forall \theta, \theta_0 \in [0, 2\pi]$ the inequality

$$\max_{x \in \bar{B}_1} |u^s(x, \theta) - u^s(x, \theta_0)| \leq \max_{x \in \bar{B}_1} |u(x, \theta) - u(x, \theta_0)| + \max_{x \in \bar{B}_1} \left| e^{ikx \cdot \hat{d}(\theta)} - e^{ikx \cdot \hat{d}(\theta_0)} \right| \quad (4.103)$$

holds. Now, from limits (4.100), (4.101) and relation (4.103), we find

$$\lim_{\theta \rightarrow \theta_0} \max_{x \in \bar{B}_1} |u^s(x, \theta) - u^s(x, \theta_0)| = 0 \quad \forall \theta_0 \in [0, 2\pi], \quad (4.104)$$

which implies limit (4.58) in the proof of Theorem 4.6.1, since $\bar{G} \subset \bar{B}_1$.

We still need to prove the continuity in $A = \bar{G} \times [0, 2\pi]$ of u^s as a function of both the variables x and θ . More precisely, we need to prove that, given any $(x_0, \theta_0) \in A$, for every $\epsilon > 0$ there exists $\delta(\epsilon, x_0, \theta_0) > 0$ such that

$$|u^s(x, \theta) - u^s(x_0, \theta_0)| < \epsilon \quad \forall (x, \theta) \in A : \|(x, \theta) - (x_0, \theta_0)\|_{\mathbb{R}^3} < \delta(\epsilon, x_0, \theta_0). \quad (4.105)$$

To this end, we note that, by the triangle inequality, we have

$$|u^s(x, \theta) - u^s(x_0, \theta_0)| \leq |u^s(x, \theta) - u^s(x, \theta_0)| + |u^s(x, \theta_0) - u^s(x_0, \theta_0)| \quad \forall (x, \theta), (x_0, \theta_0) \in A. \quad (4.106)$$

Now, by virtue of (4.104), there exists $\delta_1(\epsilon, \theta_0) > 0$ such that

$$|u^s(x, \theta) - u^s(x, \theta_0)| < \frac{\epsilon}{2} \quad \forall x \in \bar{G}, \quad \forall \theta : |\theta - \theta_0| < \delta_1(\epsilon, \theta_0). \quad (4.107)$$

Moreover, $u^s(\cdot, \theta_0)$ is (uniformly) continuous on the compact set \bar{G} : then, there exists $\delta_2(\epsilon, \theta_0) > 0$ such that⁸²

$$|u^s(x, \theta_0) - u^s(x_0, \theta_0)| < \frac{\epsilon}{2} \quad \forall x \in \bar{G} : \|x - x_0\|_{\mathbb{R}^2} < \delta_2(\epsilon, \theta_0). \quad (4.108)$$

⁸²Exploiting the uniform continuity of $u^s(\cdot, \theta_0)$ on \bar{G} is not necessary: its mere continuity is sufficient, since no problem arises from the possible dependence of $\delta_2(\epsilon, \theta_0)$ on x_0 .

Taking into account (4.106), (4.107) and (4.108), we have

$$|u^s(x, \theta) - u^s(x_0, \theta_0)| < \epsilon \quad \forall (x, \theta) \in A : \|x - x_0\|_{\mathbb{R}^2} < \delta_2(\epsilon, \theta_0) \wedge |\theta - \theta_0| < \delta_1(\epsilon, \theta_0). \quad (4.109)$$

Let us define $\tilde{\delta}(\epsilon, \theta_0) := \min \{\delta_1(\epsilon, \theta_0), \delta_2(\epsilon, \theta_0)\}$: from (4.109) we get

$$|u^s(x, \theta) - u^s(x_0, \theta_0)| < \epsilon \quad \forall (x, \theta) \in A : \|x - x_0\|_{\mathbb{R}^2} < \tilde{\delta}(\epsilon, \theta_0) \wedge |\theta - \theta_0| < \tilde{\delta}(\epsilon, \theta_0), \quad (4.110)$$

which implies

$$|u^s(x, \theta) - u^s(x_0, \theta_0)| < \epsilon \quad \forall (x, \theta) \in A : \|x - x_0\|_{\mathbb{R}^2}^2 + |\theta - \theta_0|^2 < \tilde{\delta}^2(\epsilon, \theta_0). \quad (4.111)$$

If we now remember that

$$\|(x, \theta) - (x_0, \theta_0)\|_{\mathbb{R}^3} = [\|x - x_0\|_{\mathbb{R}^2}^2 + |\theta - \theta_0|^2]^{1/2}, \quad (4.112)$$

we can rewrite (4.111) as

$$|u^s(x, \theta) - u^s(x_0, \theta_0)| < \epsilon \quad \forall (x, \theta) \in A : \|(x, \theta) - (x_0, \theta_0)\|_{\mathbb{R}^3} < \tilde{\delta}(\epsilon, \theta_0). \quad (4.113)$$

Relation (4.113) now shows that condition (4.105) is fulfilled with $\delta(\epsilon, x_0, \theta_0) := \tilde{\delta}(\epsilon, \theta_0)$.

Case 2. Impenetrable scatterers

We now want to adapt the proof of Theorem 4.6.1 to the case of impenetrable scatterers: to this end, it suffices to prove inequalities analogous to (4.61) and (4.67). As we are going to see, this can be made by exploiting the well-posedness of the direct scattering problem: indeed, in this case the solution operator is bounded from $C^{1,\alpha}(\partial D)$ into $C^{1,\alpha}(\mathbb{R}^2 \setminus D)$, as shown in [48], p. 51.

Similarly to the previous case 1, let $f : \partial D \times [0, 2\pi] \rightarrow \mathbb{C}$ (with $\partial D \subset \mathbb{R}^2$) be defined as $f(x, \theta) := e^{ikx \cdot \hat{d}(\theta)}$. Let us denote by $\partial_i f$ and $\partial_{ij} f$ (where $i, j = 1, 2$) the first and second partial derivatives of f with respect to x_i, x_j . It is clear that $f, \partial_i f$ and $\partial_{ij} f$ are continuous on the compact set $A' := \partial D \times [0, 2\pi]$, and then uniformly continuous on A' itself. Accordingly, given $\epsilon > 0$, it is possible to find $\delta > 0, \delta_i > 0$ and $\delta_{ij} > 0$ depending only on ϵ , such that, for all $i, j = 1, 2$, it holds that

$$|f(x', \theta') - f(x, \theta)| < \epsilon \quad \forall (x', \theta'), (x, \theta) \in A' : \|(x', \theta') - (x, \theta)\|_{\mathbb{R}^3} < \delta, \quad (4.114)$$

$$|\partial_i f(x', \theta') - \partial_i f(x, \theta)| < \epsilon \quad \forall (x', \theta'), (x, \theta) \in A' : \|(x', \theta') - (x, \theta)\|_{\mathbb{R}^3} < \delta_i, \quad (4.115)$$

$$|\partial_{ij} f(x', \theta') - \partial_{ij} f(x, \theta)| < \epsilon \quad \forall (x', \theta'), (x, \theta) \in A' : \|(x', \theta') - (x, \theta)\|_{\mathbb{R}^3} < \delta_{ij}. \quad (4.116)$$

In particular, by taking $\delta_m := \min_{i,j=1,2} \{\delta, \delta_i, \delta_{ij}\}$, relations (4.114), (4.115) and (4.116) imply that

$$|f(x, \theta') - f(x, \theta)| < \epsilon \quad \forall (x, \theta'), (x, \theta) \in A' : \|(x, \theta') - (x, \theta)\|_{\mathbb{R}^3} < \delta_m, \quad (4.117)$$

$$|\partial_i f(x, \theta') - \partial_i f(x, \theta)| < \epsilon \quad \forall (x, \theta'), (x, \theta) \in A' : \|(x, \theta') - (x, \theta)\|_{\mathbb{R}^3} < \delta_m, \quad (4.118)$$

$$|\partial_{ij} f(x, \theta') - \partial_{ij} f(x, \theta)| < \epsilon \quad \forall (x, \theta'), (x, \theta) \in A' : \|(x, \theta') - (x, \theta)\|_{\mathbb{R}^3} < \delta_m. \quad (4.119)$$

Hence, if we define the C^2 -norm of a C^2 function $g : X \rightarrow \mathbb{C}$, where $X \subset \mathbb{R}^2$, as

$$\|g\|_{\infty,2,X} := \sup_{x \in X} |g(x)| + \sum_{i=1}^2 \sup_{x \in X} |\partial_i g(x)| + \sum_{i,j=1}^2 \sup_{x \in X} |\partial_{ij} g(x)|, \quad (4.120)$$

from (4.117), (4.118) and (4.119) we find that

$$\|f(x, \theta') - f(x, \theta)\|_{\infty,2,\partial D} < 7\epsilon \quad \forall \theta', \theta \in [0, 2\pi] : |\theta' - \theta| < \delta_m, \quad (4.121)$$

whence

$$\lim_{\theta' \rightarrow \theta} \|f(x, \theta') - f(x, \theta)\|_{\infty,2,\partial D} = 0 \quad \forall \theta \in [0, 2\pi], \quad (4.122)$$

i.e., by replacing (θ', θ) with (θ, θ_0) and remembering the definition of f ,

$$\lim_{\theta \rightarrow \theta_0} \left\| e^{ikx \cdot \hat{d}(\theta)} - e^{ikx \cdot \hat{d}(\theta_0)} \right\|_{\infty,2,\partial D} = 0 \quad \forall \theta_0 \in [0, 2\pi]. \quad (4.123)$$

Of course, the C^2 -norm is stronger than the $C^{1,\alpha}$ -norm: then (4.123) implies (with the notations of [48], p. 40)

$$\lim_{\theta \rightarrow \theta_0} \left\| e^{ikx \cdot \hat{d}(\theta)} - e^{ikx \cdot \hat{d}(\theta_0)} \right\|_{1,\alpha,\partial D} = 0 \quad \forall \theta_0 \in [0, 2\pi]. \quad (4.124)$$

Accordingly, Theorem 3.11 at p. 51 in [48] allows concluding that

$$\lim_{\theta \rightarrow \theta_0} \|u^s(\cdot, \theta) - u^s(\cdot, \theta_0)\|_{1,\alpha,\mathbb{R}^2 \setminus D} = 0 \quad \forall \theta_0 \in [0, 2\pi]. \quad (4.125)$$

In particular, if $\bar{G} \subset \mathbb{R}^2 \setminus D$ is the compact set defined at the previous case 1, we have

$$\lim_{\theta \rightarrow \theta_0} \max_{x \in \bar{G}} |u^s(\cdot, \theta) - u^s(\cdot, \theta_0)| = 0 \quad \forall \theta_0 \in [0, 2\pi], \quad (4.126)$$

$$\lim_{\theta \rightarrow \theta_0} \max_{x \in \bar{G}} |\partial_i u^s(\cdot, \theta) - \partial_i u^s(\cdot, \theta_0)| = 0 \quad \forall \theta_0 \in [0, 2\pi], \quad \forall i \in \{1, 2\}. \quad (4.127)$$

By means of the same argument used for passing from (4.104) to (4.113), we can prove that u^s and $\partial_i u^s$ (for $i = 1, 2$) are continuous on $A = \bar{G} \times [0, 2\pi]$: hence, there exist $M_1, M_2 \geq 0$ such that

$$|u^s(x, \theta)| \leq M_1, \quad |\partial_i u^s(x, \theta)| \leq M_2 \quad \forall (x, \theta) \in A, \quad \forall i \in \{1, 2\}. \quad (4.128)$$

If we now remember the definition (4.49) of $u_z^{s,\epsilon}$ and the assumption (4.57) on the boundedness of $\|g_{z_n}^\epsilon\|_{L^2[0,2\pi]}$, we can apply the Cauchy-Schwarz inequality and Lebesgue's dominated convergence theorem to obtain, $\forall x \in \bar{G}$ and $\forall n \in \mathbb{N}$,

$$|u_{z_n}^{s,\epsilon}(x)| \leq \int_0^{2\pi} |u^s(x, \theta) g_{z_n}^\epsilon(\theta)| d\theta \leq M_1 \sqrt{2\pi} \|g_{z_n}^\epsilon\|_{L^2[0,2\pi]} \leq \sqrt{2\pi} M_1 K =: Q_1 \quad (4.129)$$

and

$$\left| \frac{\partial u_{z_n}^{s,\epsilon}}{\partial x_i}(x) \right| \leq \int_0^{2\pi} \left| \frac{\partial u^s(x, \theta)}{\partial x_i} g_{z_n}^\epsilon(\theta) \right| d\theta \leq M_2 \sqrt{2\pi} \|g_{z_n}^\epsilon\|_{L^2[0,2\pi]} \leq \sqrt{2\pi} M_2 K =: Q_2, \quad (4.130)$$

which correspond exactly to inequalities (4.61) and (4.67) in the proof of Theorem 4.6.1. The remainder of the proof itself can be left unchanged.

4.10.3 A technical detail concerning relations (4.71)

A justification of the passage from the second to the third line of relations (4.71) is similar to (but more difficult than) the proof of Theorem 4.4.2. Indeed, in the latter the integration domain is $[0, 2\pi]$, i.e., independent of R , while now the integration domain is the interval $[\varphi[P_{y_{z_n}^1}(R)], \varphi[P_{y_{z_n}^2}(R)]]$ and then depends on⁸³ R .

Let us remember that, by assumption, the following two limits hold:

$$\lim_{R \rightarrow \infty} \varphi[P_{y_{z_n}^1}(R)] = \varphi_\infty(y_{z_n}^1), \quad \lim_{R \rightarrow \infty} \varphi[P_{y_{z_n}^2}(R)] = \varphi_\infty(y_{z_n}^2). \quad (4.131)$$

Hence, if we define the two functions

$$h_n^1(R) := \varphi[P_{y_{z_n}^1}(R)] - \varphi_\infty(y_{z_n}^1), \quad h_n^2(R) := \varphi[P_{y_{z_n}^2}(R)] - \varphi_\infty(y_{z_n}^2), \quad (4.132)$$

we have

$$\lim_{R \rightarrow \infty} h_n^1(R) = 0 = \lim_{R \rightarrow \infty} h_n^2(R). \quad (4.133)$$

We now define, as a shorthand notation, the function

$$f_n^{s,\epsilon}(R, \varphi) := \frac{1}{4i\omega \varepsilon_B \mu_B} \left[\bar{u}_{z_n}^{s,\epsilon} \frac{\partial u_{z_n}^{s,\epsilon}}{\partial r} - u_{z_n}^{s,\epsilon} \frac{\partial \bar{u}_{z_n}^{s,\epsilon}}{\partial r} \right] (R, \varphi). \quad (4.134)$$

Then, we want to prove that

$$\lim_{R \rightarrow \infty} \left| \int_{\varphi[P_{y_{z_n}^1}(R)]}^{\varphi[P_{y_{z_n}^2}(R)]} f_n^{s,\epsilon}(R, \varphi) R d\varphi - \frac{k}{2\omega \varepsilon_B \mu_B} \|F g_{z_n}^\epsilon\|_{L^2[\varphi_\infty(y_{z_n}^1), \varphi_\infty(y_{z_n}^2)]}^2 \right| = 0. \quad (4.135)$$

⁸³A completely analogous problem arises about the second equality in (4.53), p. 103, and the same procedure proposed here to justify (4.71) also applies to (4.53).

To this end, we observe that, by remembering definitions (4.132), we can write

$$\begin{aligned} & \left| \int_{\varphi[P_{y_{z_n}^1}(R)]}^{\varphi[P_{y_{z_n}^2}(R)]} f_n^{s,\epsilon}(R, \varphi) R d\varphi - \frac{k}{2\omega \varepsilon_B \mu_B} \|Fg_{z_n}^\epsilon\|_{L^2[\varphi_\infty(y_{z_n}^1), \varphi_\infty(y_{z_n}^2)]}^2 \right| = \\ & = \left| \int_{\varphi_\infty(y_{z_n}^1) + h_n^1(R)}^{\varphi_\infty(y_{z_n}^2) + h_n^2(R)} f_n^{s,\epsilon}(R, \varphi) R d\varphi - \frac{k}{2\omega \varepsilon_B \mu_B} \int_{\varphi_\infty(y_{z_n}^1)}^{\varphi_\infty(y_{z_n}^2)} \frac{|Fg_{z_n}^\epsilon(\varphi)|^2}{R} R d\varphi \right|. \end{aligned} \quad (4.136)$$

Of course, it holds that

$$\begin{aligned} & \int_{\varphi_\infty(y_{z_n}^1) + h_n^1(R)}^{\varphi_\infty(y_{z_n}^2) + h_n^2(R)} f_n^{s,\epsilon}(R, \varphi) R d\varphi = \\ & \int_{\varphi_\infty(y_{z_n}^1) + h_n^1(R)}^{\varphi_\infty(y_{z_n}^1)} f_n^{s,\epsilon}(R, \varphi) R d\varphi + \int_{\varphi_\infty(y_{z_n}^1)}^{\varphi_\infty(y_{z_n}^2)} f_n^{s,\epsilon}(R, \varphi) R d\varphi + \int_{\varphi_\infty(y_{z_n}^2)}^{\varphi_\infty(y_{z_n}^2) + h_n^2(R)} f_n^{s,\epsilon}(R, \varphi) R d\varphi. \end{aligned} \quad (4.137)$$

Then, by inserting (4.137) into (4.136) and using the triangle inequality, we find

$$\begin{aligned} & \left| \int_{\varphi[P_{y_{z_n}^1}(R)]}^{\varphi[P_{y_{z_n}^2}(R)]} f_n^{s,\epsilon}(R, \varphi) R d\varphi - \frac{k}{2\omega \varepsilon_B \mu_B} \|Fg_{z_n}^\epsilon\|_{L^2[\varphi_\infty(y_{z_n}^1), \varphi_\infty(y_{z_n}^2)]}^2 \right| \leq \\ & \leq \left| \int_{\varphi_\infty(y_{z_n}^1)}^{\varphi_\infty(y_{z_n}^2)} f_n^{s,\epsilon}(R, \varphi) R d\varphi - \frac{k}{2\omega \varepsilon_B \mu_B} \int_{\varphi_\infty(y_{z_n}^1)}^{\varphi_\infty(y_{z_n}^2)} \frac{|Fg_{z_n}^\epsilon(\varphi)|^2}{R} R d\varphi \right| + \\ & + \left| \int_{\varphi_\infty(y_{z_n}^1) + h_n^1(R)}^{\varphi_\infty(y_{z_n}^1)} f_n^{s,\epsilon}(R, \varphi) R d\varphi + \int_{\varphi_\infty(y_{z_n}^2)}^{\varphi_\infty(y_{z_n}^2) + h_n^2(R)} f_n^{s,\epsilon}(R, \varphi) R d\varphi \right|. \end{aligned} \quad (4.138)$$

Now, the two integrals in the second line of (4.138) involve the same integration domain $[\varphi_\infty(y_{z_n}^1), \varphi_\infty(y_{z_n}^2)]$, which is independent of R : accordingly, we can apply to them the same arguments presented in the proof of Theorem 4.4.2 (with $[0, 2\pi]$ replaced by $[\varphi_\infty(y_{z_n}^1), \varphi_\infty(y_{z_n}^2)]$) and conclude that the term in the second line of (4.138) vanishes as $R \rightarrow \infty$.

Then, in order to show that limit (4.135) holds, i.e., that the right-hand side of (4.136) tends to zero as $R \rightarrow \infty$, it suffices to prove that the contribution in the third line of (4.138) vanishes as $R \rightarrow \infty$. Actually, it suffices to prove that

$$\lim_{R \rightarrow \infty} \left| \int_{\varphi_\infty(y_{z_n}^1) + h_n^1(R)}^{\varphi_\infty(y_{z_n}^1)} \left[\bar{u}_{z_n}^{s,\epsilon} \frac{\partial u_{z_n}^{s,\epsilon}}{\partial r} \right] (R, \varphi) R d\varphi \right| = 0, \quad (4.139)$$

and

$$\lim_{R \rightarrow \infty} \left| \int_{\varphi_\infty(y_{z_n}^1) + h_n^1(R)}^{\varphi_\infty(y_{z_n}^1)} \left[u_{z_n}^{s,\epsilon} \frac{\partial \bar{u}_{z_n}^{s,\epsilon}}{\partial r} \right] (R, \varphi) R d\varphi \right| = 0, \quad (4.140)$$

since the remaining terms can be treated in the same way.

In order to prove limit (4.139), we first observe that

$$\lim_{R \rightarrow \infty} \left| \int_{\varphi_\infty(y_{z_n}^1) + h_n^1(R)}^{\varphi_\infty(y_{z_n}^1)} \frac{ik}{R} |Fg_{z_n}^\epsilon(\varphi)|^2 R d\varphi \right| = 0, \quad (4.141)$$

since the integrand is bounded (and independent of R), while, by limits (4.133), the measure of the integration domain vanishes for $R \rightarrow \infty$. Moreover, from (4.43) and other trivial properties, we have

$$\begin{aligned} & \left| \int_{\varphi_\infty(y_{z_n}^1) + h_n^1(R)}^{\varphi_\infty(y_{z_n}^1)} \left[\bar{u}_{z_n}^{s,\epsilon} \frac{\partial u_{z_n}^{s,\epsilon}}{\partial r} \right] (R, \varphi) R d\varphi - \int_{\varphi_\infty(y_{z_n}^1) + h_n^1(R)}^{\varphi_\infty(y_{z_n}^1)} \frac{ik}{R} |Fg_{z_n}^\epsilon(\varphi)|^2 R d\varphi \right| \leq \quad (4.142) \\ & \leq \left| \int_{\varphi_\infty(y_{z_n}^1) + h_n^1(R)}^{\varphi_\infty(y_{z_n}^1)} \sup_{\varphi \in [0, 2\pi]} \left| \bar{u}_{z_n}^{s,\epsilon} \frac{\partial u_{z_n}^{s,\epsilon}}{\partial r} (R, \varphi) - \frac{ik}{R} |Fg_{z_n}^\epsilon(\varphi)|^2 \right| R d\varphi \right| = \\ & = R \sup_{\varphi \in [0, 2\pi]} \left| \bar{u}_{z_n}^{s,\epsilon} \frac{\partial u_{z_n}^{s,\epsilon}}{\partial r} (R, \varphi) - \frac{ik}{R} |Fg_{z_n}^\epsilon(\varphi)|^2 \right| |h_n^1(R)| \rightarrow 0 \quad \text{as } R \rightarrow \infty. \end{aligned}$$

Finally, from the triangle inequality, we obtain

$$\begin{aligned} & \left| \int_{\varphi_\infty(y_{z_n}^1) + h_n^1(R)}^{\varphi_\infty(y_{z_n}^1)} \left[\bar{u}_{z_n}^{s,\epsilon} \frac{\partial u_{z_n}^{s,\epsilon}}{\partial r} \right] (R, \varphi) R d\varphi \right| \leq \quad (4.143) \\ & \leq \left| \int_{\varphi_\infty(y_{z_n}^1) + h_n^1(R)}^{\varphi_\infty(y_{z_n}^1)} \left[\bar{u}_{z_n}^{s,\epsilon} \frac{\partial u_{z_n}^{s,\epsilon}}{\partial r} \right] (R, \varphi) R d\varphi - \int_{\varphi_\infty(y_{z_n}^1) + h_n^1(R)}^{\varphi_\infty(y_{z_n}^1)} \frac{ik}{R} |Fg_{z_n}^\epsilon(\varphi)|^2 R d\varphi \right| + \\ & \quad + \left| \int_{\varphi_\infty(y_{z_n}^1) + h_n^1(R)}^{\varphi_\infty(y_{z_n}^1)} \frac{ik}{R} |Fg_{z_n}^\epsilon(\varphi)|^2 R d\varphi \right|. \end{aligned}$$

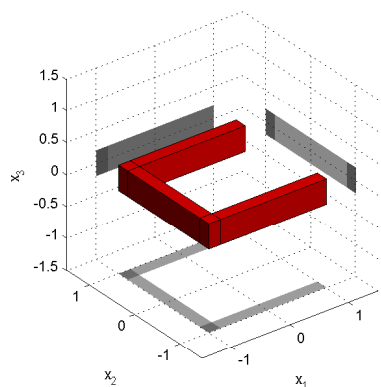
By virtue of (4.141), (4.142) and (4.143), limit (4.139) follows. As regards limit (4.140), it suffices to adapt the previous argument by using relation (4.44) instead of (4.43). This concludes the proof.

Chapter 5

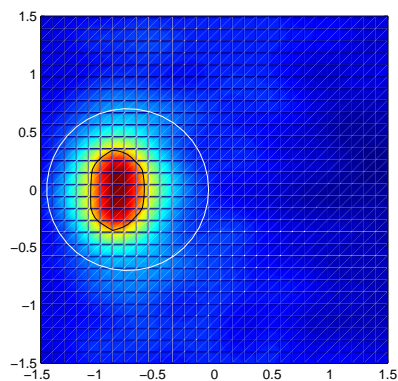
Figures and tables

As anticipated in the Preface, this chapter collects all the figures and tables of the thesis, according to the following criterion: each section contains the figures and tables referred to in a specific section of Chapters 2-4 and has just the same title (and, between square brackets, the same number) of such section.

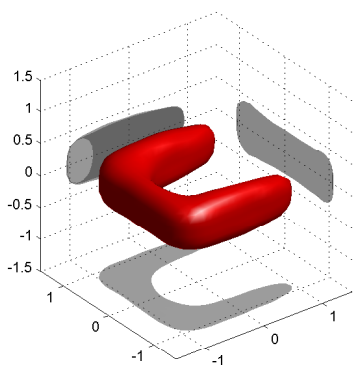
5.1 [2.6] Numerical applications



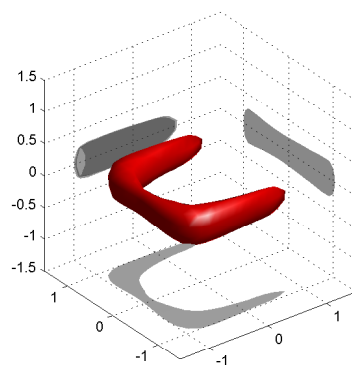
(a)



(b)



(c)



(d)

Figure 5.1: Visualization performance of the 3D no-sampling LSM: (a) the scatterer; (b) application of active contours to the restriction of the indicator function to the plane of Cartesian equation $x_2 = 0$ (white line: initialization; black line: final profile); (c) visualization provided by the no-sampling LSM in around 90s of CPU time (the threshold value for the surface equation is computed by using (2.84)); (d) visualization provided by the traditional LSM in around 1600s of CPU time (the threshold value for the surface equation is obtained by means of a heuristic trial-and-error procedure).

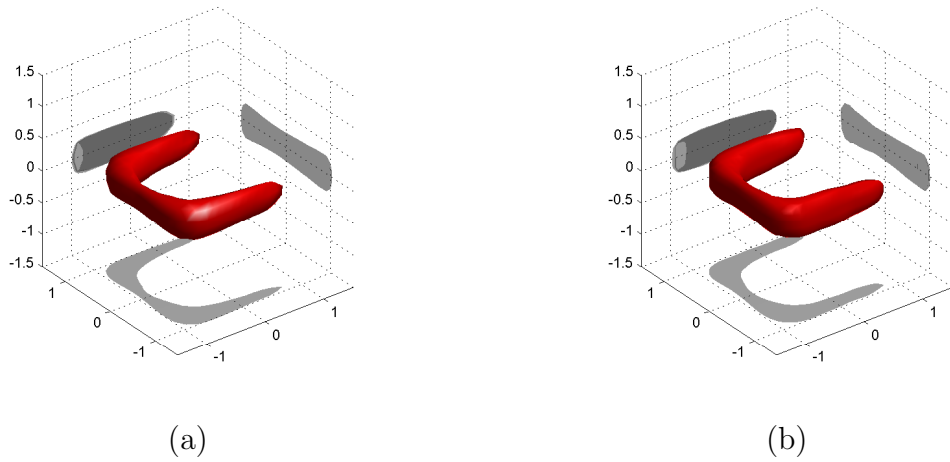


Figure 5.2: Comparison between the traditional and the no-sampling LSM for the scatterer shown in Figure 5.1(a): (a) visualization provided by the traditional LSM; (b) visualization provided by the no-sampling LSM. In both cases the threshold value for the surface equation is obtained by means of a heuristic trial-and-error procedure. The difference between the two visualizations is negligible.

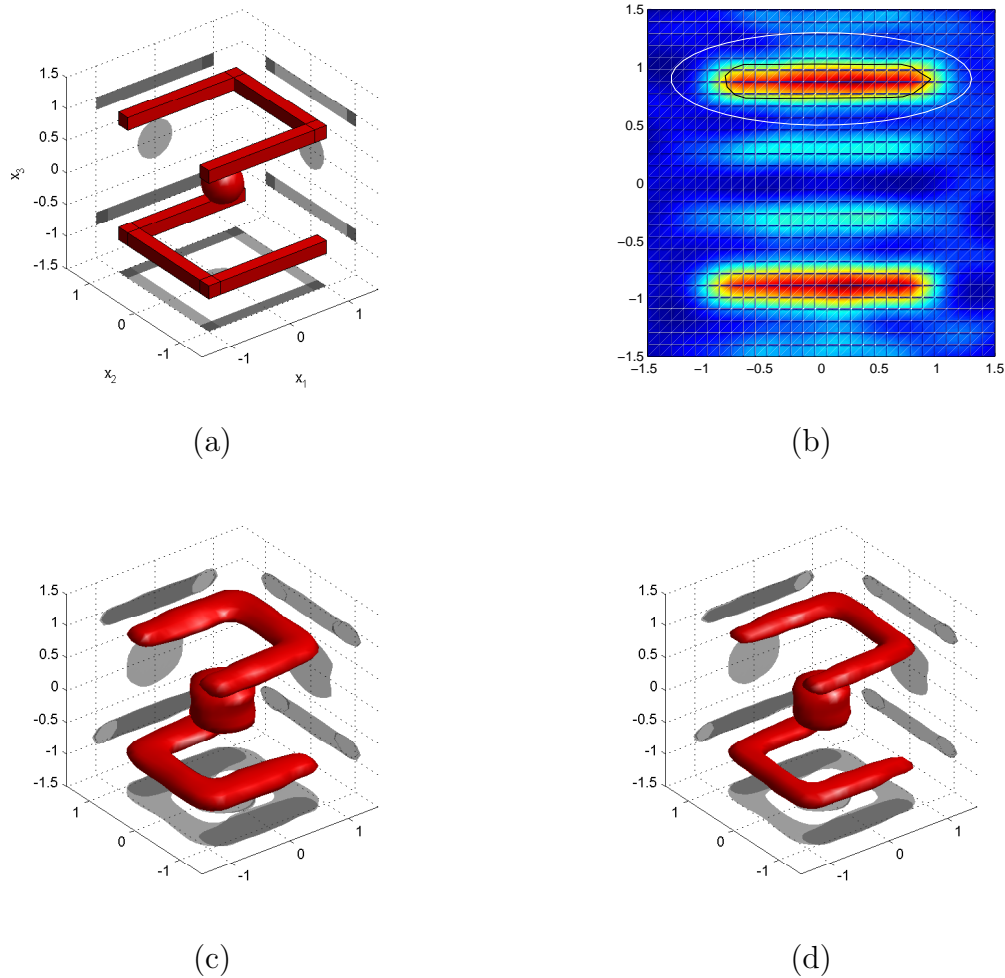


Figure 5.3: Visualization performance of the 3D no-sampling LSM: (a) the scatterer; (b) application of active contours to the restriction of the indicator function to the plane of Cartesian equation $x_2 = 0.9$ (white line: initialization; black line: final profile); (c) visualization provided by the no-sampling LSM in around 90s of CPU time (the threshold value for the surface equation is computed by using (2.84)); (d) visualization provided by the traditional LSM in around 1600s of CPU time (the threshold value for the surface equation is obtained by means of a heuristic trial-and-error procedure).

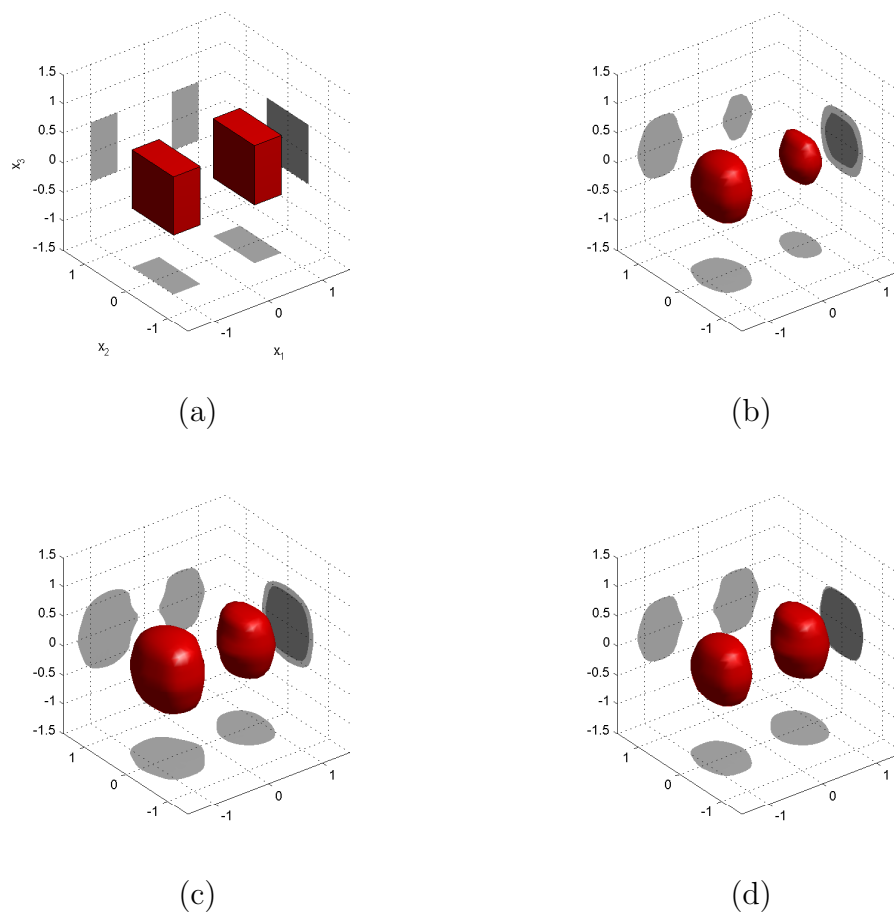
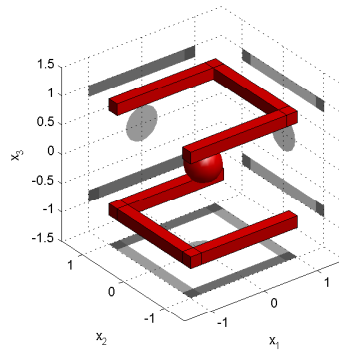


Figure 5.4: Visualization of two objects with different permittivity by means of the no-sampling LSM: (a) the two scattering objects; (b) visualization obtained by using a unique threshold value $C = C_1$ computed as in (2.84) by cutting the non-connected scatterer with the plane $x_1 = -0.75$; (c) visualization obtained by using a unique threshold value $C = C_2$ computed as in (2.84) by cutting the non-connected scatterer with the plane $x_1 = 0.75$; (d) visualization obtained by using the two different threshold values C_1 and C_2 for the two objects. In each case, the visualization time is around 90s of CPU time.

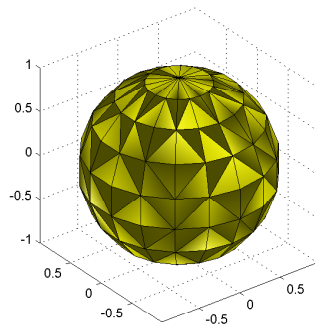
	Figure 5.1	Figure 5.3	Figure 5.4
Traditional	$[5.3 \cdot 10^{-6}, 4.4 \cdot 10^{-5}]$	$[9.3 \cdot 10^{-8}, 2.8 \cdot 10^{-7}]$	$[1.7 \cdot 10^{-7}, 5.2 \cdot 10^{-6}]$
No-sampling	$7.2 \cdot 10^{-6}$	$9.3 \cdot 10^{-8}$	$2.8 \cdot 10^{-7}$

Table 5.1: Values of the regularization parameter α provided by the generalized discrepancy principle in the traditional and the no-sampling LSM for the three previous experiments. First row: interval $[\alpha_{\min}^*, \alpha_{\max}^*]$ defined by the minimum and maximum values of α for all sampling points in the traditional implementation. Second row: the unique value α^* of α in the no-sampling implementation.

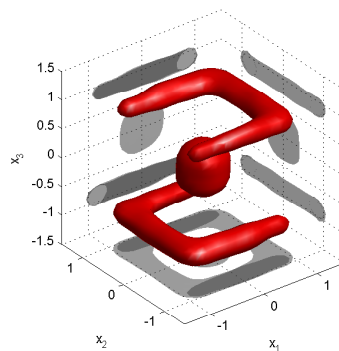
5.2 [2.7] First-order discretization



(a)

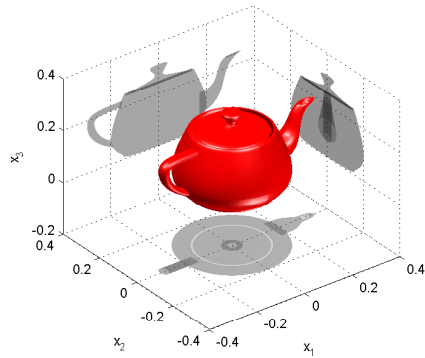


(b)

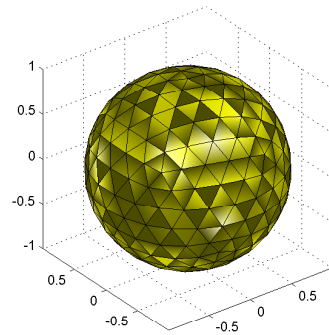


(c)

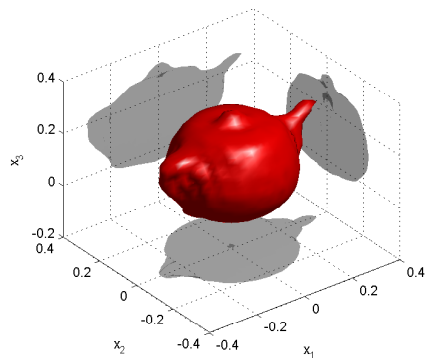
Figure 5.5: Visualization performance of the 3D no-sampling LSM: (a) the scatterer; (b) non-uniform triangular mesh formed on the unit sphere by the 144 views chosen to implement a first-order discretization of the far-field equation; (c) no-sampling LSM visualization of the scatterer.



(a)



(b)



(c)

Figure 5.6: Visualization performance of the 3D no-sampling LSM: (a) exact geometry of the scatterer (perfectly conducting teapot); (b) uniform triangular mesh formed on the unit sphere by the 252 views chosen to implement a first-order discretization of the far-field equation; (c) no-sampling LSM visualization of the teapot.

5.3 [3.3] Notations

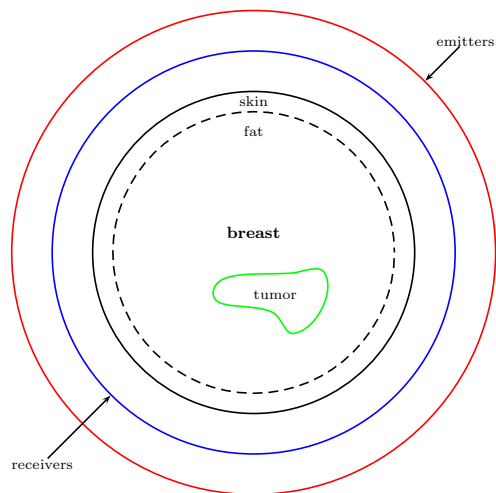


Figure 5.7: Scheme of the 2D microwave tomography experiment for breast cancer detection.

5.4 [3.6] Applications to data

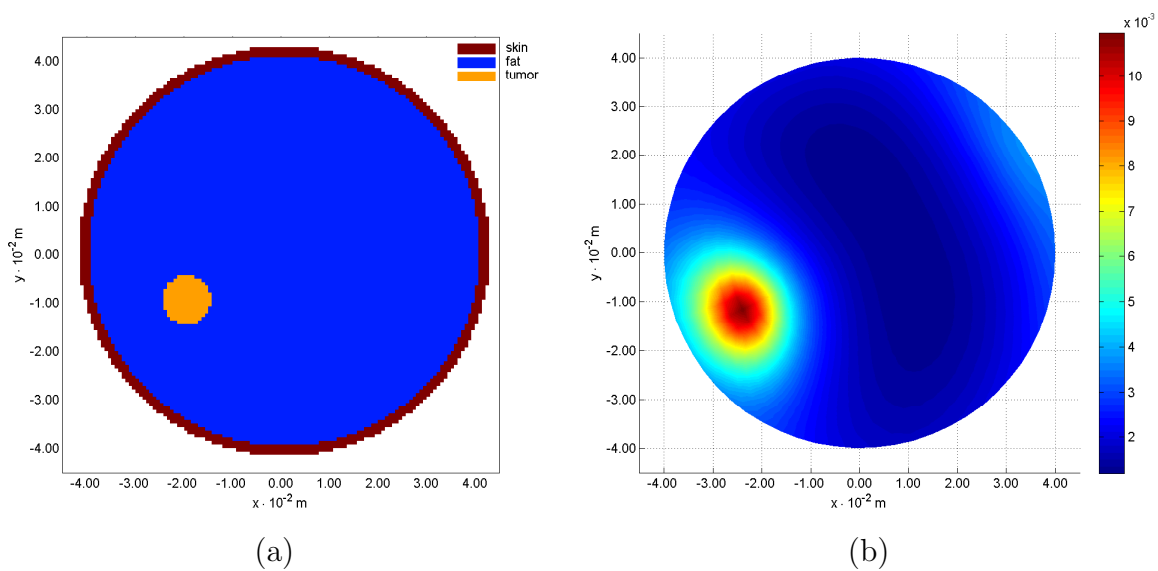


Figure 5.8: (a) Phantom of the breast: a circular tumour, centred at $(-2.00, -1.00) \cdot 10^{-2}$ m and with a diameter of $1.00 \cdot 10^{-2}$ m, is placed in the fat tissue. (b) Visualization provided by the RGFM.

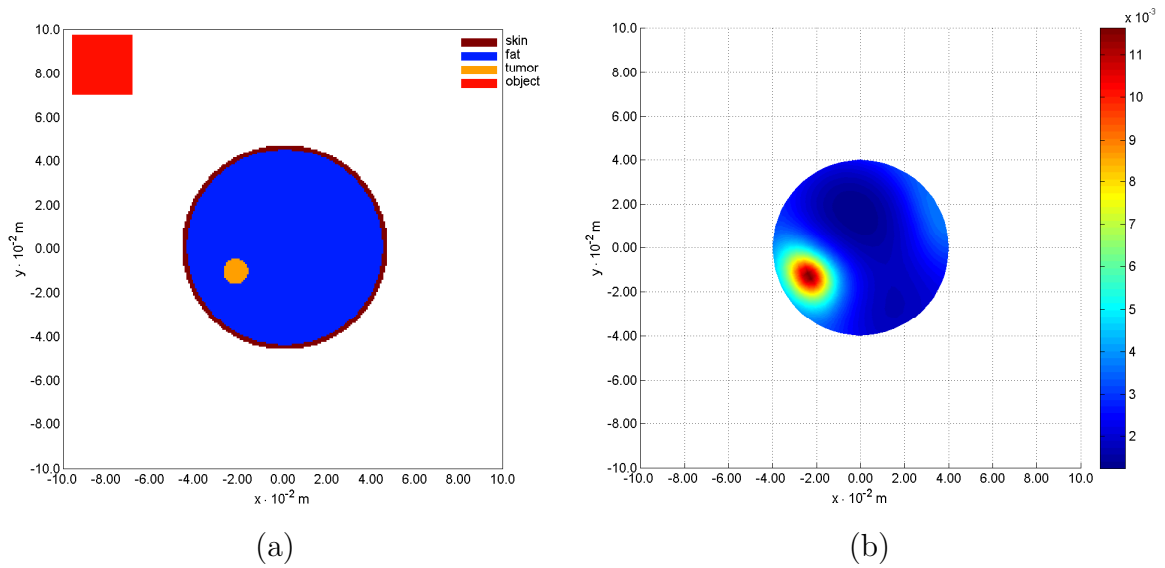


Figure 5.9: (a) Phantom of the breast: a circular tumour, centred at $(-2.00, -1.00) \cdot 10^{-2} \text{ m}$ and with a diameter of $1.00 \cdot 10^{-2} \text{ m}$, is placed in the fat tissue; a square scatterer, centred at $(-8.20, 8.20) \cdot 10^{-2} \text{ m}$ and with a side of $2.75 \cdot 10^{-2} \text{ m}$ is put outside the breast. (b) Visualization provided by the RGFM.

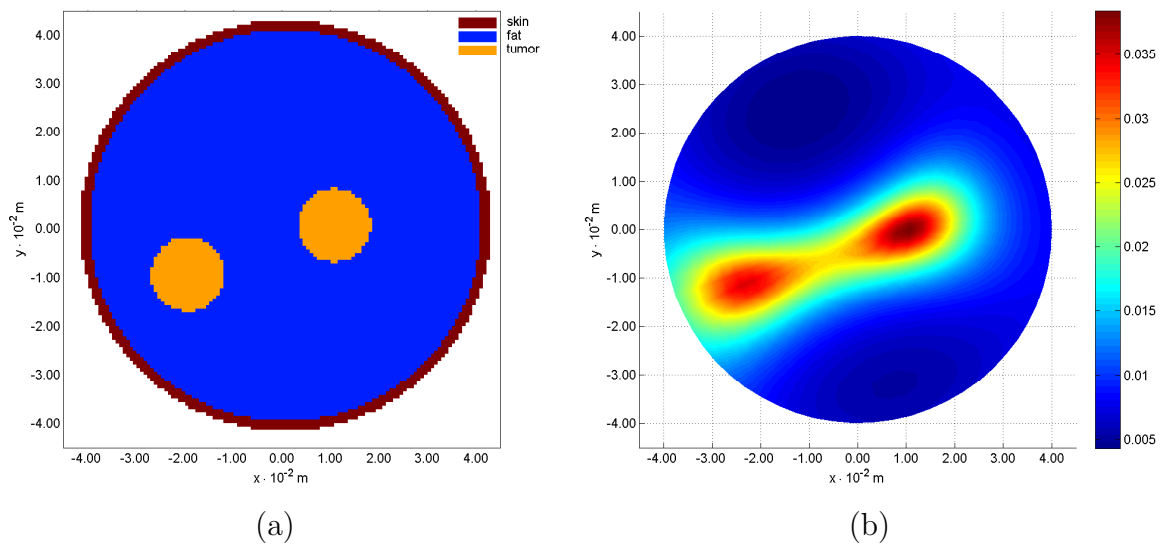


Figure 5.10: (a) Phantom of the breast: two circular tumours, with the same diameter of $1.50 \cdot 10^{-2} \text{ m}$, are placed in the fat tissue: one is centred at $(-2.00, -1.00) \cdot 10^{-2} \text{ m}$, the other in $(1.00, 0.00) \cdot 10^{-2} \text{ m}$. (b) Visualization provided by the RGFM.

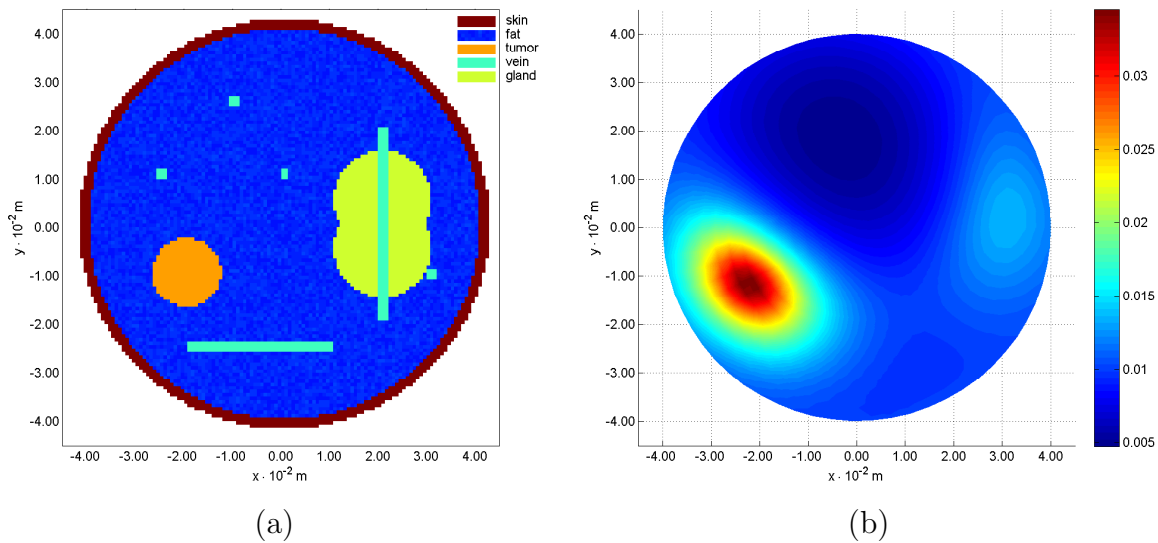


Figure 5.11: (a) Phantom of the breast: the healthy fat is perturbed with components randomly drawn from a uniform distribution within 10% around the unperturbed values; moreover, six veins and one gland are added inside the fat tissue. A circular tumour, centred at $(-2.00, -1.00) \cdot 10^{-2}$ m and with a diameter of $1.50 \cdot 10^{-2}$ m is also placed in the breast. (b) Visualization provided by the RGFM.

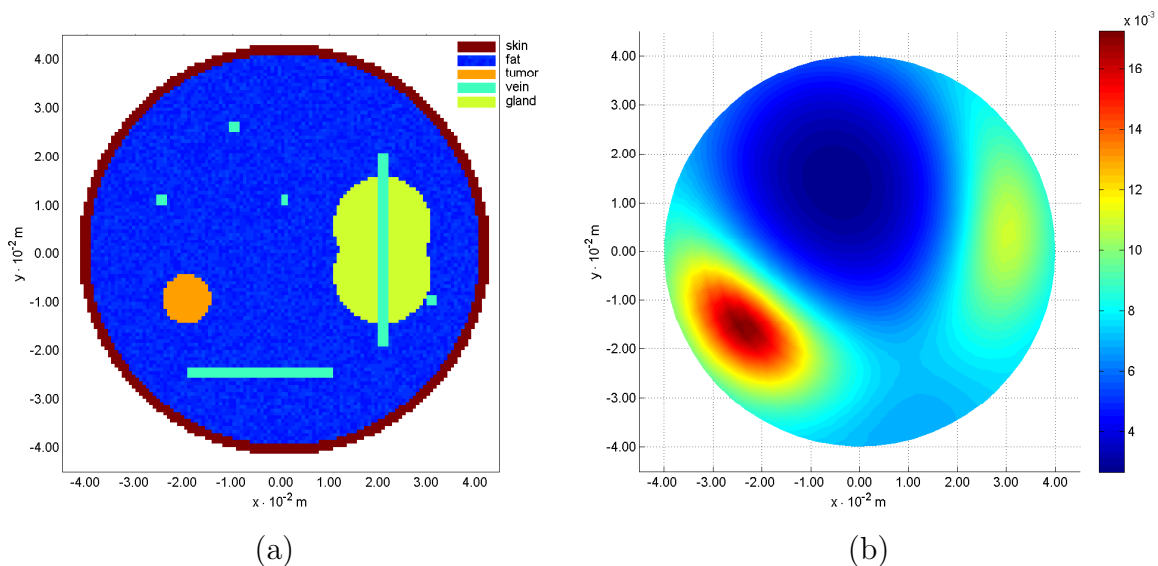
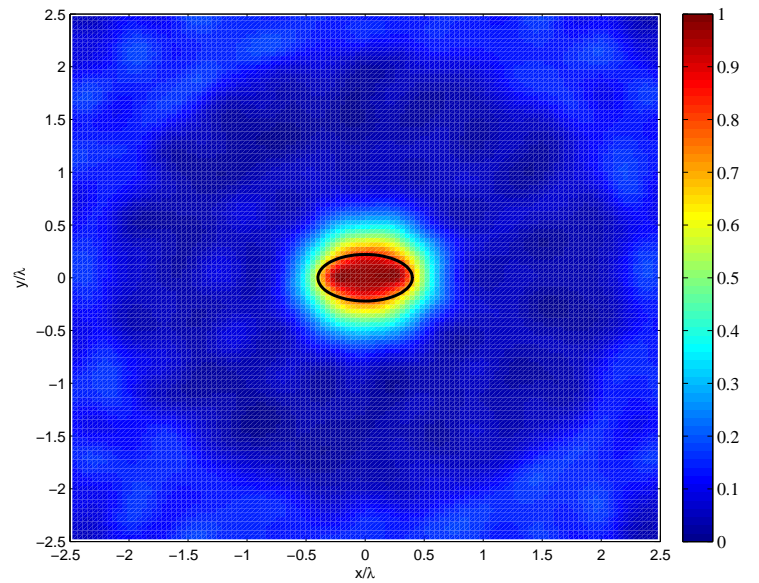
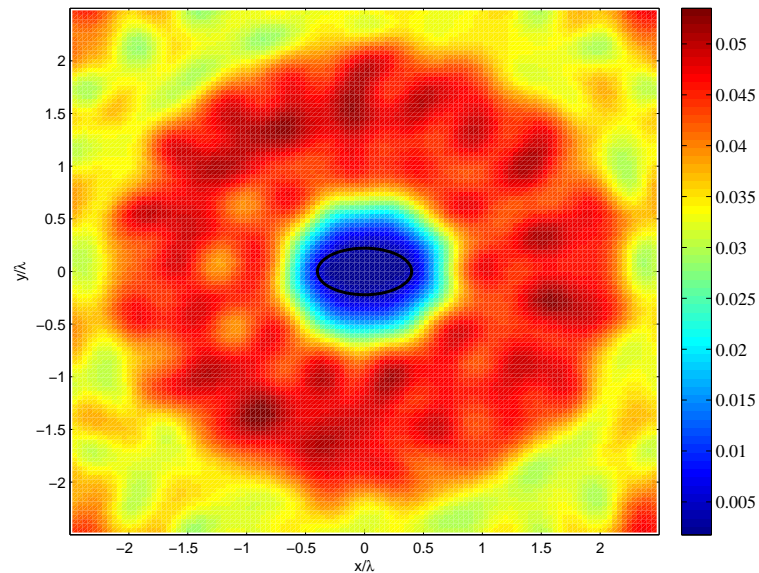


Figure 5.12: (a) Phantom of the breast: the healthy fat is perturbed with components randomly drawn from a uniform distribution within 10% around the unperturbed values; moreover, six veins and one gland are added inside the fat tissue. A circular tumour, centred at $(-2.00, -1.00) \cdot 10^{-2}$ m and with a diameter of $1.00 \cdot 10^{-2}$ m is also placed in the breast. (b) Visualization provided by the RGFM.

5.5 [4.5] Behaviour of the flow lines



(a)



(b)

Figure 5.13: Implementation of the LSM: (a) visualization of an elliptic scatterer with, superimposed, its true profile (solid black line); (b) values of the discretized discrepancy $d(z)$.

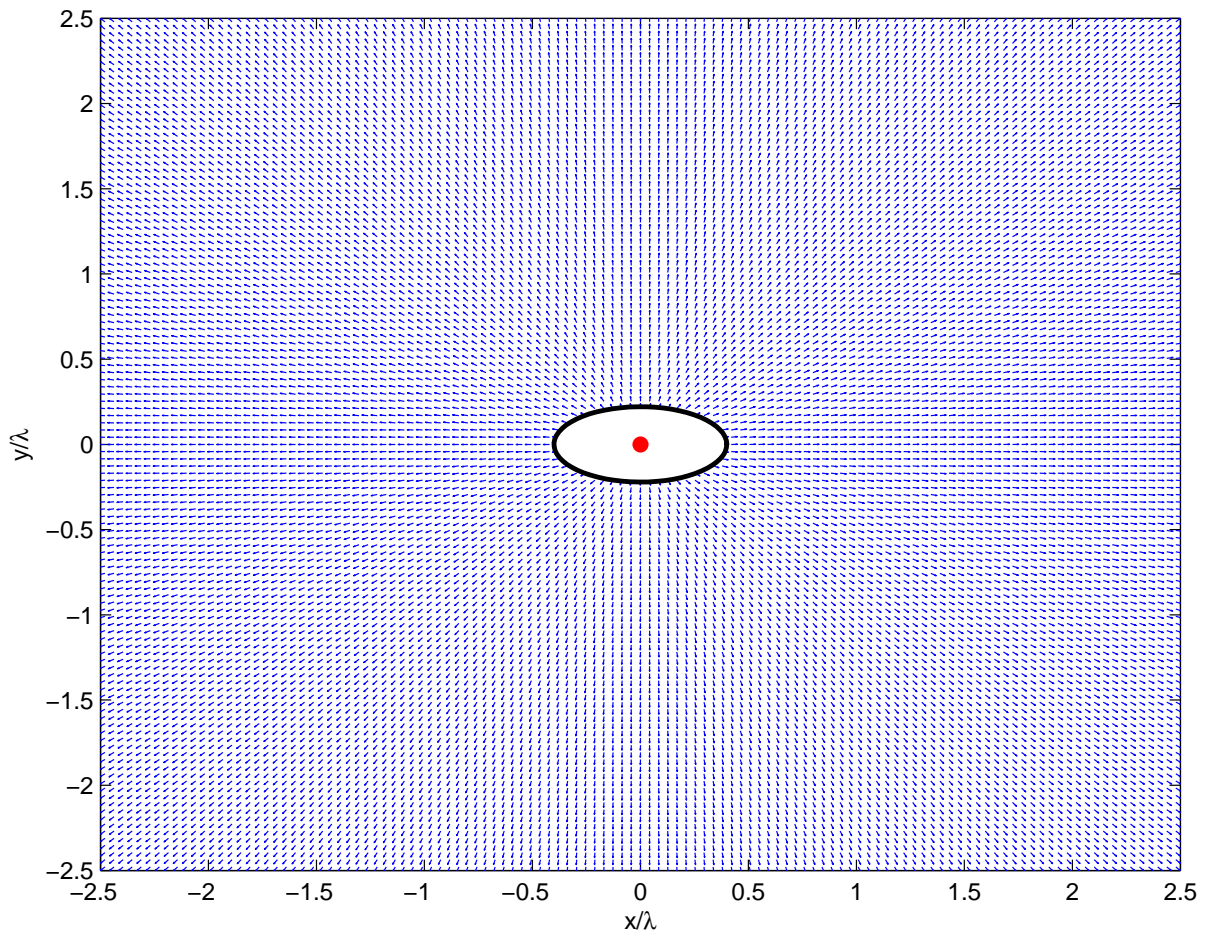


Figure 5.14: Behaviour of the unit vector field $\hat{S}_z^{s,\epsilon}$ for a sampling point z (represented by a red bullet) placed at the centre of the ellipse.

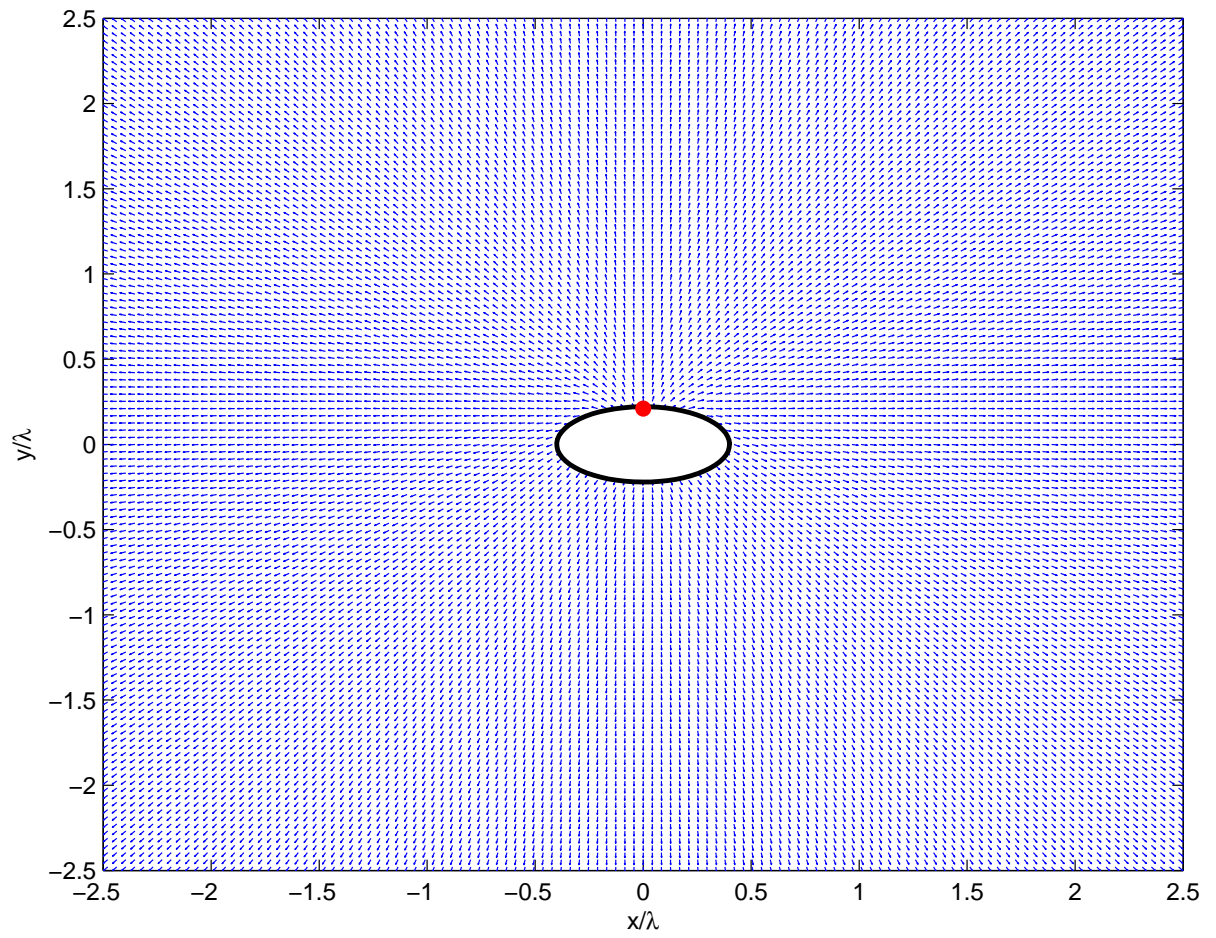


Figure 5.15: Behaviour of the unit vector field $\hat{\mathcal{S}}_z^{s,\epsilon}$ for a sampling point z (represented by a red bullet) placed at the top of the ellipse.

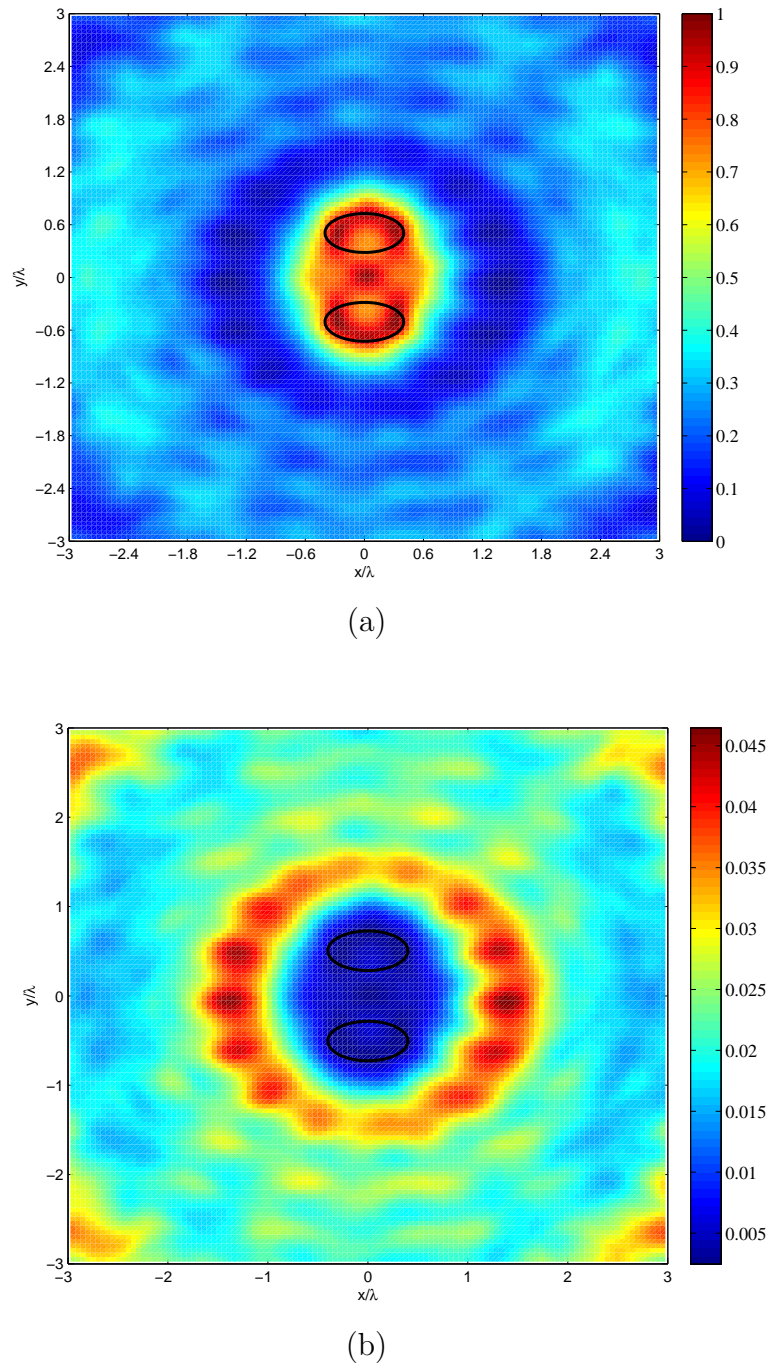


Figure 5.16: Implementation of the LSM: (a) visualization of a double-elliptic scatterer with, superimposed, its true profile (solid black lines); (b) values of the discretized discrepancy $d(z)$.

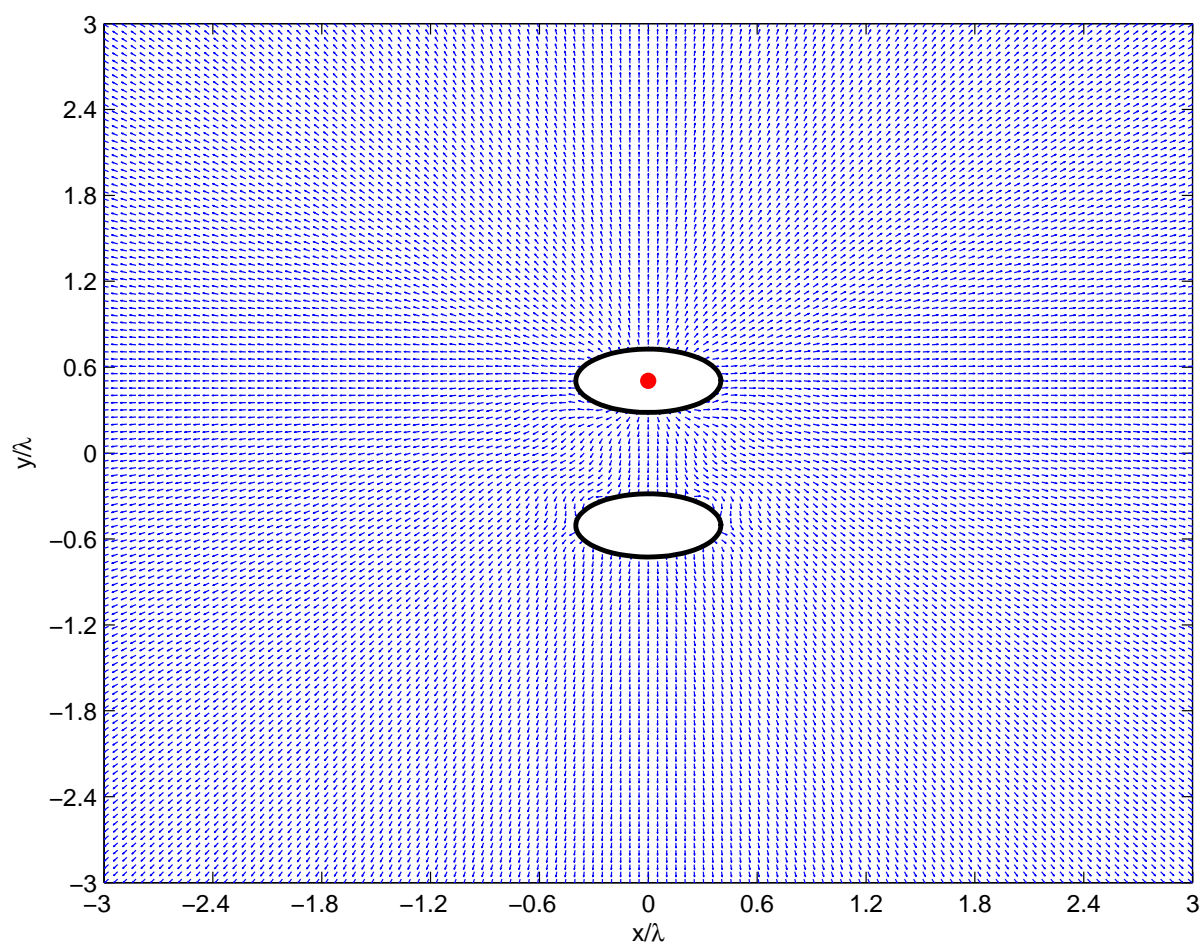


Figure 5.17: Behaviour of the unit vector field $\hat{\mathcal{S}}_z^{s,\epsilon}$ for a sampling point z (represented by a red bullet) placed at the centre of the upper ellipse.

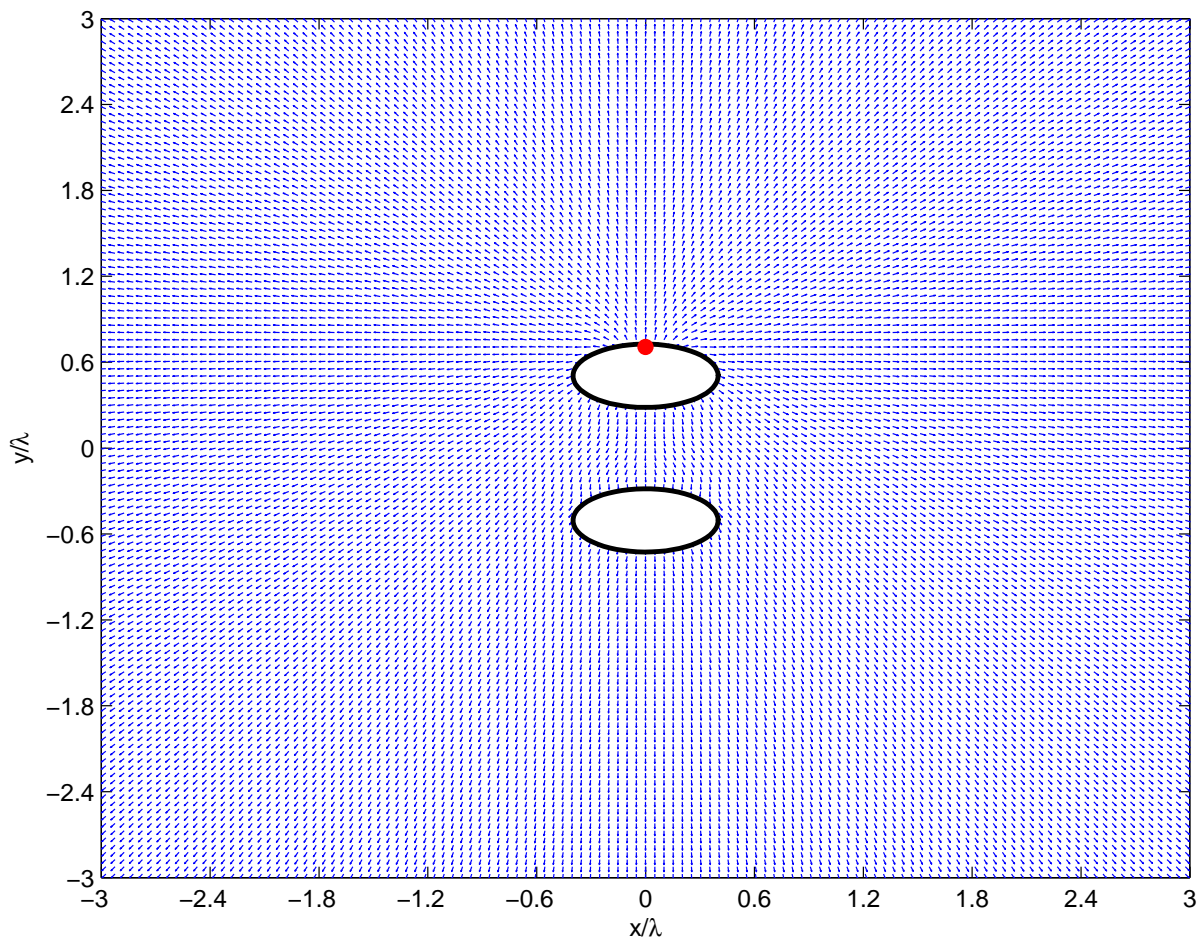


Figure 5.18: Behaviour of the unit vector field $\hat{S}_z^{s,\epsilon}$ for a sampling point z (represented by a red bullet) placed at the top of the upper ellipse.

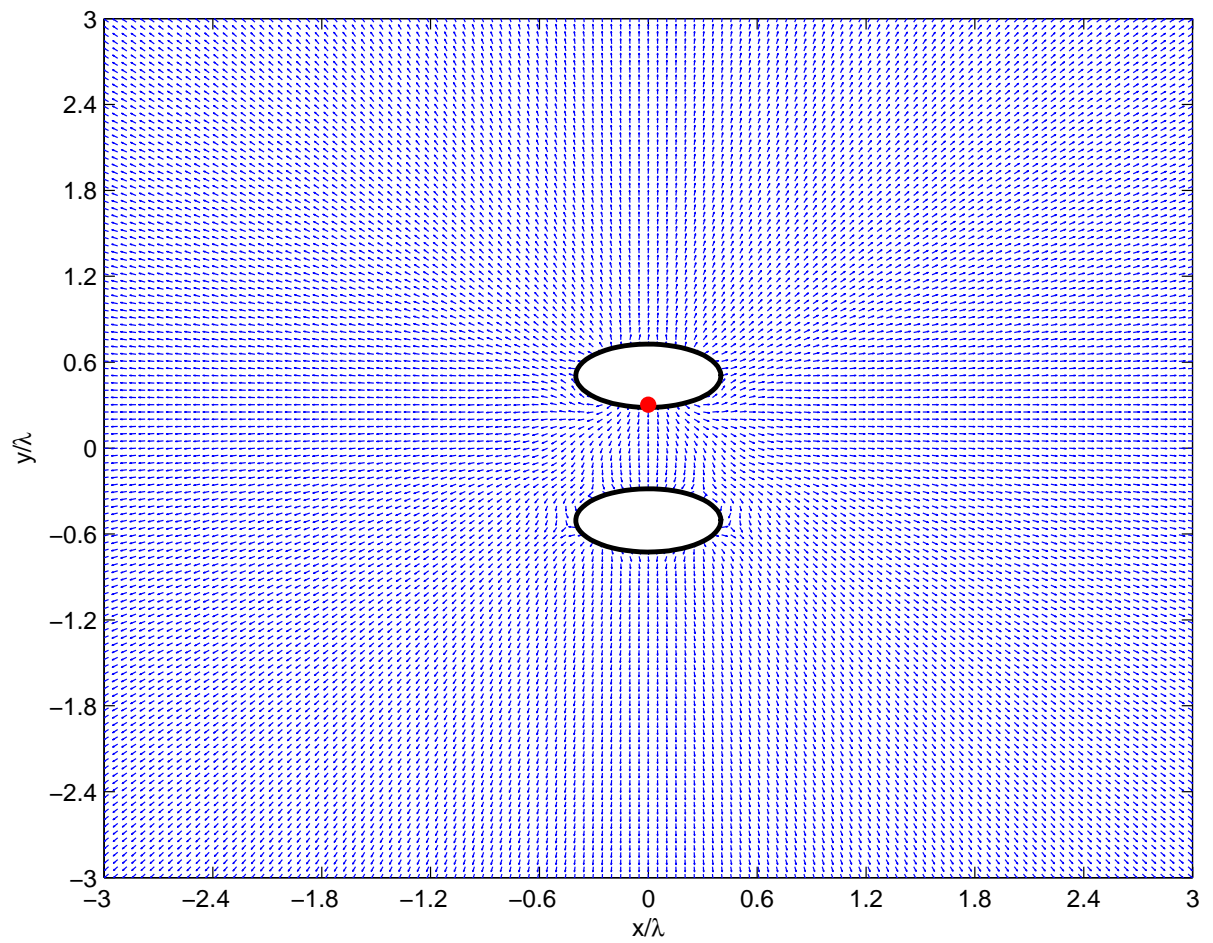


Figure 5.19: Behaviour of the unit vector field $\hat{\mathcal{S}}_z^{s,\epsilon}$ for a sampling point z (represented by a red bullet) placed at the bottom of the upper ellipse.

5.6 [4.6] A new version of the general theorem: $z \in D$

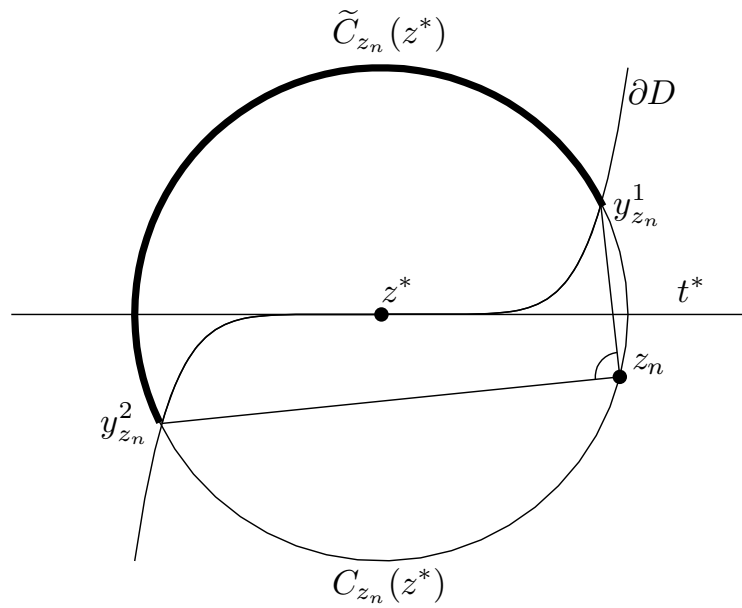


Figure 5.20: Geometric construction considered in the proof of Theorem 4.6.1, for a point $z_n \in D$ approaching $z^* \in \partial D$.

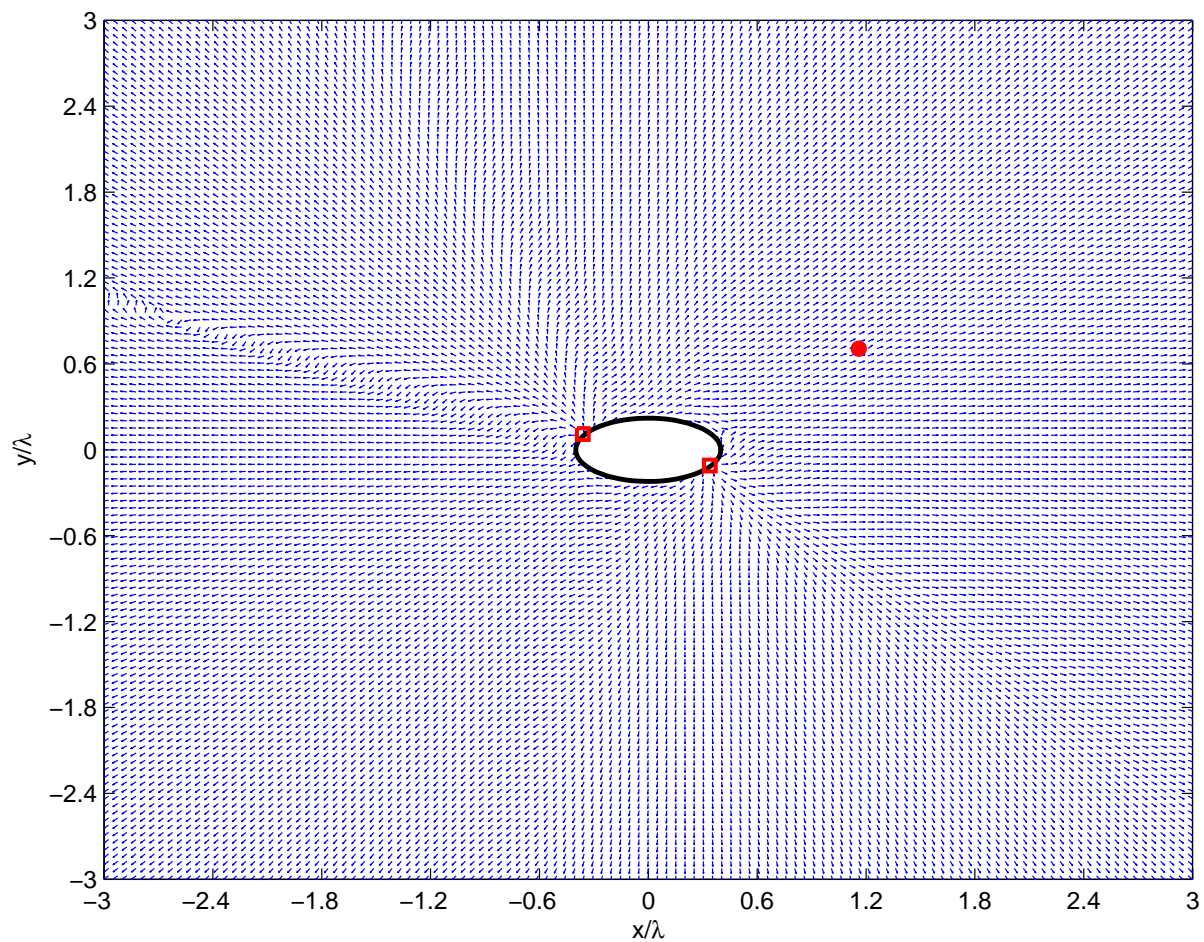
5.7 [4.7] A new version of the general theorem: $z \notin D$ 

Figure 5.21: Behaviour of the unit vector field $\hat{S}_z^{s,\epsilon}$ for a sampling point z (represented by a red bullet) placed outside the scatterer. Two ramification points (square boxes) are detectable.

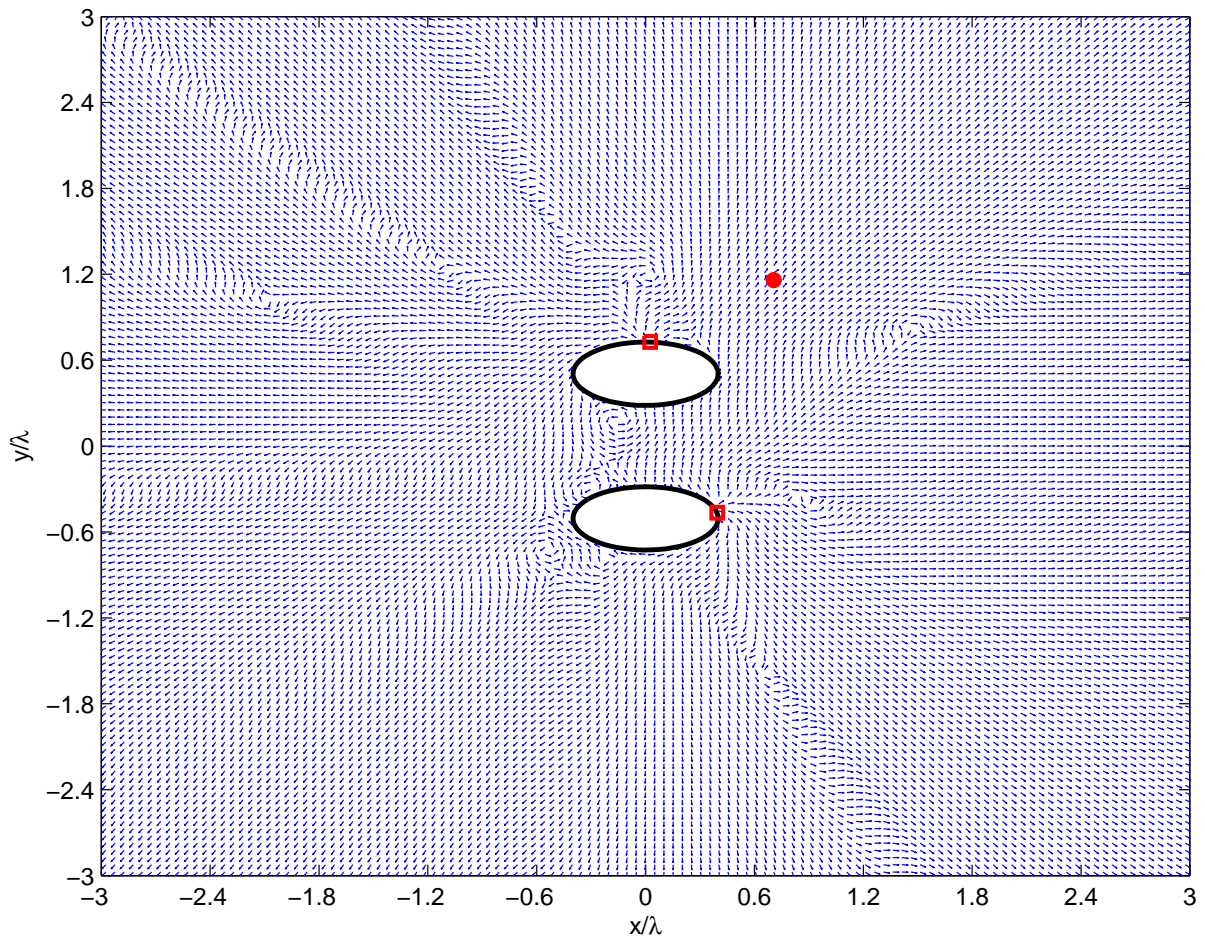


Figure 5.22: Behaviour of the unit vector field $\hat{S}_z^{s, \epsilon}$ for a sampling point z (represented by a red bullet) placed outside the scatterer. Two ramification points (square boxes) are detectable.

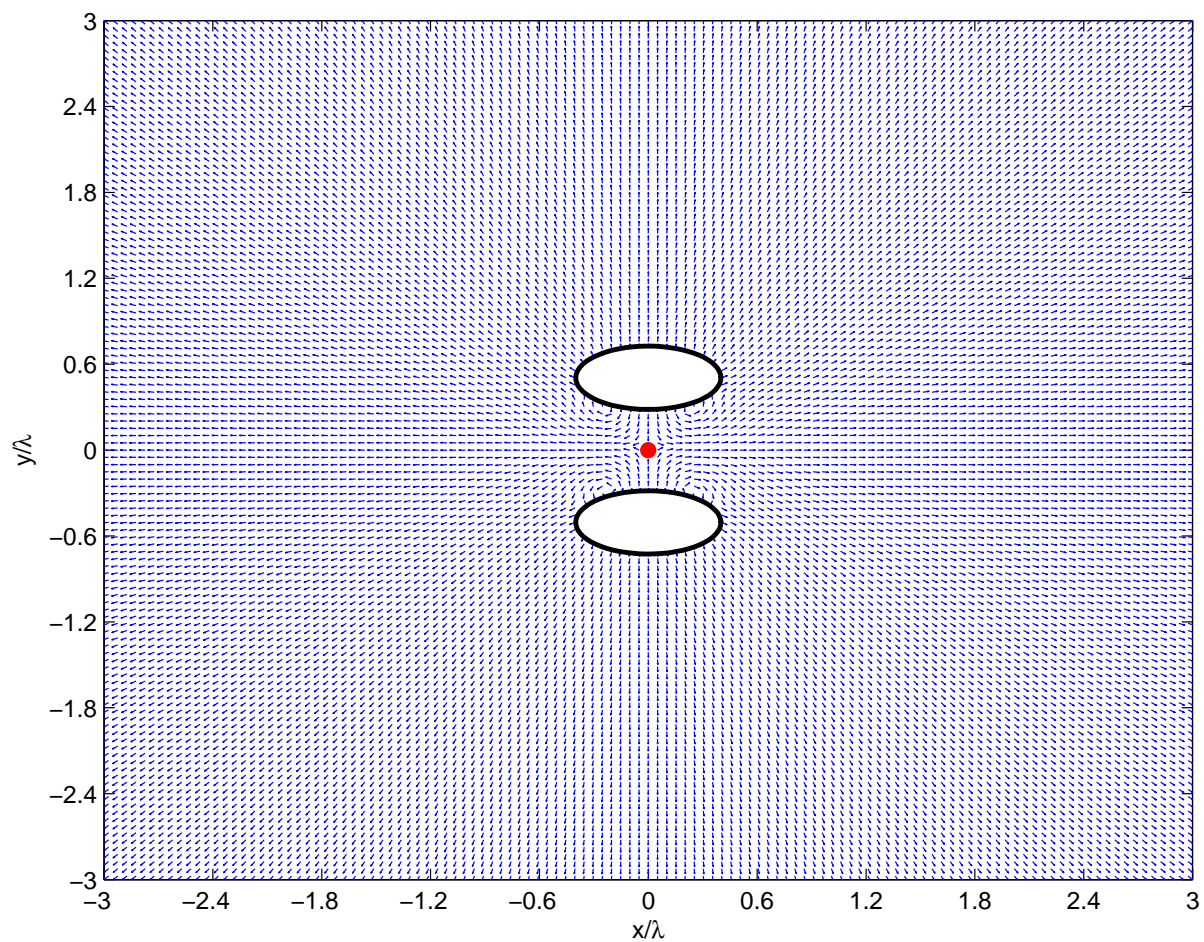


Figure 5.23: Behaviour of the unit vector field $\hat{\mathcal{S}}_z^{s, \epsilon}$ for a sampling point z (represented by a red bullet) placed outside the scatterer.

Bibliography

- [1] R. Abraham and J. E. Marsden. *Foundations of Mechanics*. The Addison-Wesley Publishing Company, Inc., Reading, Massachusetts, second edition, 1987.
- [2] K. Agarwal, X. Chen, and Y. Zhong. Interpretation of linear sampling method in terms of induced multiples. In *Proc. of the Asia-Pacific Microwave Conference, December 7-10 2009. APMC 2009*, pages 500–503, Singapore, 2009.
- [3] R. A. Albanese, R. L. Medina, and J. W. Penn. Mathematics, medicine and microwaves. *Inverse Problems*, 10:995–1007, 1994.
- [4] R. Aramini. *On Some Open Problems in the Implementation of the Linear Sampling Method*. PhD thesis in mathematics, Università degli Studi di Trento, Dipartimento di Matematica, 2007.
- [5] R. Aramini, M. Brignone, G. Caviglia, A. Massa, and M. Piana. The linear sampling method in a lossy background: an energy perspective. *Inverse Problems in Science and Engineering*. In press.
- [6] R. Aramini, M. Brignone, J. Coyle, and M. Piana. Postprocessing of the linear sampling method by means of deformable models. *SIAM J. Sci. Comput.*, 30(5):2613–2634, 2008.
- [7] R. Aramini, M. Brignone, and M. Piana. The linear sampling method without sampling. *Inverse Problems*, 22:2237–2254, 2006.
- [8] R. Aramini, G. Caviglia, and G. Giorgi. The role of point sources and their power fluxes in the linear sampling method. *SIAM J. Appl. Math.* In press.
- [9] R. Aramini, G. Caviglia, A. Massa, and M. Piana. The linear sampling method and energy conservation. *Inverse Problems*, 26:055004, 2010.
- [10] T. Arens. Why linear sampling works. *Inverse Problems*, 20:163–173, 2004.

-
- [11] T. Arens and A. Lechleiter. The linear sampling method revisited. *J. Integral Equations Appl.*, 21(2):179–202, 2009.
- [12] S. R. Arridge. Optical tomography in medical imaging. *Inverse Problems*, 15:R41–R93, 1999.
- [13] A. B. Bakushinsky and M. Yu. Kokurin. *Iterative Methods for Approximate Solution of Inverse Problems*. Springer, Dordrecht, 2004.
- [14] C. A. Balanis. *Advanced Engineering Electromagnetics*. John Wiley & Sons, Inc., New York, 1989.
- [15] M. Bertero and P. Boccacci. *Introduction to Inverse Problems in Imaging*. Institute of Physics Publishing, Bristol, 1998.
- [16] G. Bindu, A. Lonappan, V. Thomas, C. K. Aanandan, and K. T. Mathew. Active microwave imaging for breast cancer detection. *Prog. Electromagn. Res. (PIER)*, 58:149–169, 2006.
- [17] G. Bindu, A. Lonappan, V. Thomas, C. K. Aanandan, and K. T. Mathew. Dielectric studies of corn syrup for applications in microwave breast imaging. *Prog. Electromagn. Res. (PIER)*, 59:175–186, 2006.
- [18] E. J. Bond, X. Li, S. C. Hagness, and B. D. Van Veen. Microwave imaging via space-time beamforming for early detection of breast cancer. *IEEE Trans. Ant. Prop.*, 51(8):1690–1705, 2003.
- [19] L. Borcea. Electrical impedance tomography. *Inverse Problems*, 18:R99–R136, 2002.
- [20] G. Bozza. *Numerical methods for inverse and ill-posed problems in electromagnetics*. PhD thesis in electronic and computer engineering and telecommunications, Università degli Studi di Genova, 2009.
- [21] G. Bozza, M. Brignone, and M. Pastorino. Application of the no-sampling linear sampling method to breast cancer detection. *IEEE Trans. Biomed. Eng.*, 57(10):2525–2534, 2010.
- [22] G. Bozza, M. Brignone, M. Pastorino, M. Piana, and A. Randazzo. Integration of linear sampling and newton-like schemes in inverse scattering. In *Proc. of the IEEE Antennas and Propagation Society International Symposium, June 1-5 2009. APSURSI '09*, pages 1–4, Charleston, SC (USA), 2009.

- [23] G. Bozza, M. Brignone, M. Pastorino, M. Piana, and A. Randazzo. An inverse scattering based hybrid method for the measurement of the complex dielectric permittivities of arbitrarily shaped homogenous targets. In *Proc. of the IEEE Instrumentation and Measurement Technology Conference, 5-7 May 2009. I2MTC '09*, pages 719–723, Singapore, 2009.
- [24] G. Bozza, M. Brignone, M. Pastorino, A. Randazzo, and M. Piana. Imaging of unknown targets inside inhomogeneous backgrounds by means of qualitative inverse scattering. *Inverse Problems and Imaging (IPI)*, 3(2):231–241, 2009.
- [25] G. Bozza, M. Brignone, M. Piana, M. Pastorino, and A. Randazzo. A fast and efficient microwave method for detecting dielectric and conducting bodies inside complex structures. In *Proc. of the 39th European Microwave Conference, Sept. 29 - Oct. 1 2009. EuMC 2009*, pages 1618–1621, Rome, Italy, 2009.
- [26] M. Brignone, R. Aramini, G. Bozza, and M. Piana. No sampling linear sampling for 3d inverse scattering problems. In E. De Bernardis, R. Spigler, and V. Valente, editors, *Applied and Industrial Mathematics in Italy III. Selected Contributions from the 9th SIMAI Conference, Rome, Italy, 15-19 September 2008*, volume 82 of *Series on Advances in Mathematics for Applied Sciences*, pages 146–155. World Scientific Publishing Co. Pte. Ltd., Singapore, 2010.
- [27] M. Brignone, G. Bozza, R. Aramini, M. Pastorino, and M. Piana. A fully no-sampling formulation of the linear sampling method for three-dimensional inverse electromagnetic scattering problems. *Inverse Problems*, 25:015014, 2009.
- [28] M. Brignone, G. Bozza, A. Randazzo, R. Aramini, M. Piana, and M. Pastorino. Hybrid approach to the inverse scattering problem by using ant colony optimization and no-sampling linear sampling. In *Proc. of the IEEE Antennas and Propagation Society International Symposium, July 5-11 2008. AP-S 2008*, pages 1–4, San Diego, CA (USA), 2008.
- [29] M. Brignone, G. Bozza, A. Randazzo, M. Piana, and M. Pastorino. A hybrid approach to 3d microwave imaging by using linear sampling and aco. *IEEE Trans. Ant. Prop.*, 56(10):3224–3232, 2008.
- [30] O. M. Bucci and G. Franceschetti. On the degrees of freedom of scattered fields. *IEEE Trans. Ant. Prop.*, 37(7):918–926, 1989.

-
- [31] A. E. Bulyshev, S. Y. Semenov, A. E. Souvorov, R. H. Svenson, A. G. Nazarov, Y. E. Sizov, and G. P. Tatsis. Computational modeling of three-dimensional microwave tomography of breast cancer. *IEEE Trans. Biomed. Eng.*, 48(9):1053–1056, 2001.
- [32] A. E. Bulyshev, A. E. Souvorov, S. Yu Semenov, V. G. Posukh, and Y. E. Sizov. Three-dimensional vector microwave tomography: theory and computational experiments. *Inverse Problems*, 20:1239–1259, 2004.
- [33] F. Cakoni. Recent developments in the qualitative approach to inverse electromagnetic scattering theory. *J. Comput. Appl. Math.*, 204:242–255, 2007.
- [34] F. Cakoni and D. Colton. Open problems in the qualitative approach to inverse electromagnetic scattering theory. *Europ. J. Appl. Math.*, 16:411–425, 2005.
- [35] F. Cakoni and D. Colton. *Qualitative Methods in Inverse Scattering Theory*. Springer, Berlin, 2006.
- [36] F. Cakoni, M. Fares, and H. Haddar. Analysis of two linear sampling methods applied to electromagnetic imaging of buried objects. *Inverse Problems*, 22:845–867, 2006.
- [37] I. Catapano, L. Crocco, and T. Isernia. On *simple methods* for shape reconstruction of unknown scatterers. *IEEE Trans. Ant. Prop.*, 55(5):1431–1436, 2007.
- [38] Q. Chen, H. Haddar, A. Lechleiter, and P. Monk. A sampling method for inverse scattering in the time domain. *Inverse Problems*, 26:085001, 2010.
- [39] M. Cheney, D. Isaacson, and J. C. Newell. Electrical impedance tomography. *SIAM Review*, 41(1):85–101, 1999.
- [40] L. D. Cohen. On active contour models and balloons. *CVGIP Image understanding*, 53:211–218, 1991.
- [41] L. D. Cohen and I. Cohen. Finite-element methods for active contour models and balloons for 2-d and 3-d images. *IEEE Trans. Pattern Anal. Machine Intell.*, 15:1131–1147, 1993.
- [42] F. Collino, M'B. Fares, and H. Haddar. On the validation of the linear sampling method in electromagnetic inverse scattering problems. Rapport de recherche n. 4665, Institut National de Recherche en Informatique et en Automatique (INRIA), Rocquencourt, December 2002.

- [43] F. Collino, M'B. Fares, and H. Haddar. Numerical and analytical studies of the linear sampling method in electromagnetic inverse scattering problems. *Inverse Problems*, 19:1279–1298, 2003.
- [44] D. Colton and H. Haddar. An application of the reciprocity gap functional to inverse scattering theory. *Inverse Problems*, 21:383–398, 2005.
- [45] D. Colton, H. Haddar, and P. Monk. The linear sampling method for solving the electromagnetic inverse scattering problem. *SIAM J. Sci. Comput.*, 24(3):719–731, 2003.
- [46] D. Colton, H. Haddar, and M. Piana. The linear sampling method in inverse electromagnetic scattering theory. *Inverse Problems*, 19:S105–S137, 2003.
- [47] D. Colton and A. Kirsch. A simple method for solving inverse scattering problems in the resonance region. *Inverse Problems*, 12:383–383, 1996.
- [48] D. Colton and R. Kress. *Inverse Acoustic and Electromagnetic Scattering Theory*. Springer, Berlin, second edition, 1998.
- [49] D. Colton and P. Monk. A linear sampling method for the detection of leukemia using microwaves. *SIAM J. Appl. Math.*, 58(3):926–941, 1998.
- [50] D. Colton and P. Monk. A linear sampling method for the detection of leukemia using microwaves ii. *SIAM J. Appl. Math.*, 60(1):241–255, 1999.
- [51] D. Colton and P. Monk. Target identification of coated objects. *IEEE Trans. Ant. Prop.*, 54(4):1232–1242, 2006.
- [52] D. Colton, M. Piana, and R. Potthast. A simple method using morozov's discrepancy principle for solving inverse scattering problems. *Inverse Problems*, 13:1477–1493, 1997.
- [53] D. K. Das-Gupta and P. C. N. Scarpa. Modeling of dielectric relaxation spectra of polymers in the condensed phase. *IEEE El. Insul. Mag.*, 15(2):23–37, 1999.
- [54] R. Dautray and J. L. Lions. *Spectral Theory and Applications*, volume 3 of *Mathematical Analysis and Numerical Methods for Science and Technology*. Springer, New York, 2000.

- [55] F. Delbary, M. Brignone, G. Bozza, R. Aramini, and M. Piana. A visualization method for breast cancer detection by using microwaves. *SIAM J. Appl. Math.*, 70(7):2509–2533, 2010.
- [56] A. J. Devaney. Diffraction tomography. In W. M. Boerner et al., editor, *Inverse Methods in Electromagnetic Imaging*, Part 2, pages 1107–1135. D. Reidel Publishing, Boston, 1985.
- [57] M. Donelli, G. Franceschini, A. Martini, and A. Massa. An integrated multiscaling strategy based on a particle swarm algorithm for inverse scattering problems. *IEEE Trans. Geosc. Rem. Sens.*, 44(2):298–312, 2006.
- [58] J. G. Elmore, M. B. Barton, V. M. Moceris, S. Polk, P. J. Arena, and S. W. Fletcher. Ten-year risk of false positive screening mammograms and clinical breast examinations. *N. Engl. J. Med.*, 338(16):1089–1096, 1998.
- [59] H. W. Engl, M. Hanke, and A. Neubauer. *Regularization of Inverse Problems*. Kluwer Academic Publishers, Dordrecht, 1996.
- [60] C. Eyraud, J.-M. Geffrin, A. Litman, P. Sabouroux, and H. Giovannini. Drift correction for scattering measurements. *Appl. Phys. Lett.*, 89(24):244104, 2006.
- [61] A. Gamliel, K. Kim, A. I. Nachman, and E. Wolf. A new method for specifying nonradiating, monochromatic, scalar sources and their fields. *J. Opt. Soc. Am.*, 6:1388–1393, 1989.
- [62] G. Gilardi. *Analisi uno*. McGraw-Hill Libri Italia, Milano, 1991.
- [63] D. H. Griffel. *Applied Functional Analysis*. Dover Publications, Inc., New York, 2002.
- [64] S. C. Hagness, A. Taflove, and J. E. Bridges. Two-dimensional fdtd analysis of a pulsed microwave confocal system for breast cancer detection: Fixed-focus and antenna-array sensors. *IEEE Trans. Biomed. Eng.*, 45(12):1470–1479, 1998.
- [65] M. Hanke. Why linear sampling really seems to work. *Inverse Problems and Imaging*, 2(3):373–395, 2008.
- [66] Ø. Hjelle and M. Dæhlen. *Triangulations and Applications*. Springer, Berlin, 2006.
- [67] P. T. Huynh, A. M. Jarolimek, and S. Daye. The false-negative mammogram. *RadioGraphics*, 18(5):1137–1154, 1998.

- [68] T. Rubæk, P. M. Meaney, P. Meincke, and K. D. Paulsen. Nonlinear microwave imaging for breast-cancer screening using gauss-newton's method and the cgls inversion algorithm. *IEEE Trans. Ant. Prop.*, 55(8):2320–2331, 2007.
- [69] A. Kirsch and N. Grinberg. *The Factorization Method for Inverse Problems*. Oxford University Press Inc., New York, 2008.
- [70] L. D. Landau and E. M. Lifshitz. *Electrodynamics of continuous media*, volume 8 of *Course of Theoretical Physics*. Pergamon Press, Oxford, second edition, 1984.
- [71] R. Leis. *Initial Boundary Value Problems in Mathematical Physics*. John Wiley, New York, 1986.
- [72] R. Lencredot, A. Litman, H. Tortel, and J.-M. Geffrin. Measurement strategies for a confined microwave circular scanner. *Inverse Problems in Science and Engineering*, 17(6):787–802, 2009.
- [73] A. Liseno and R. Pierri. Impossibility of recovering a scatterer's shape by the first version of the “linear sampling” method. *Int. J. Electron. Comm. (AEÜ)*, 57(1):70–73, 2003.
- [74] D. R. Luke and R. Potthast. The point source method for inverse scattering in the time domain. *Math. Meth. Appl. Sci.*, 29:1501–1521, 2006.
- [75] W. McLean. *Strongly Elliptic Systems and Boundary Integral Equations*. Cambridge University Press, Cambridge, 2000.
- [76] P. M. Meaney and Q. Fang. Microwave imaging: A model-based approach. In K. D. Paulsen, P. M. Meaney, and L. C. Gilman, editors, *Alternative Breast Imaging*, The Kluwer International Series in Engineering and Computer Science, pages 127–153. Springer Science + Business Media, Inc., Boston, 2005.
- [77] P. M. Meaney, M. W. Fanning, D. Li, S. P. Poplack, and K. D. Paulsen. A clinical prototype for active microwave imaging of the breast. *IEEE Trans. Microwave Theory Tech.*, 48(11):1841–1853, 2000.
- [78] P. M. Meaney, S. A. Pendergrass, M. W. Fanning, D. Li, and K. D. Paulsen. Importance of using a reduced contrast coupling medium in 2d microwave breast imaging. *J. of Electromagn. Waves and Appl.*, 17(2):333–355, 2003.
- [79] A. Moliton. *Applied Electromagnetism and Materials*. Springer, New York, 2007.

- [80] F. Natterer and F. Wübbeling. A propagation-backpropagation method for ultrasound tomography. *Inverse Problems*, 11:1225–1232, 1995.
- [81] J. H. Richmond. Scattering by a dielectric cylinder of arbitrary cross section shape. *IEEE Trans. Ant. Prop.*, 13:334–341, 1965.
- [82] A. A. Rizvi and C. H. Papas. Power flow structures in two dimensional electromagnetic fields. *Prog. Electromagn. Res. (PIER)*, 29:261–294, 2000.
- [83] B. P. Rynne and B. D. Sleeman. The interior transmission problem and inverse scattering from inhomogeneous media. *SIAM J. Math. Anal.*, 22(6):1755–1762, 1991.
- [84] J. A. Sethian. *Level Set Methods and Fast Marching Methods*. Cambridge University Press, Cambridge, 1999.
- [85] J. D. Shea, P. Kosmas, S. C. Hagness, and B. D. Van Veen. Three-dimensional microwave imaging of realistic numerical breast phantoms via a multiple-frequency inverse scattering technique. *Medical Physics*, 37(8):4210–4226, 2010.
- [86] N. Shelton and K. F. Warnick. Behavior of the regularized sampling inverse scattering method at internal resonance frequencies. *Prog. Electromagn. Res. (PIER)*, 38:29–45, 2002.
- [87] W. L. Stutzman and G. A. Thiele. *Antenna theory and design*. John Wiley & Sons, Inc., New York, 1981.
- [88] A. Tacchino, J. Coyle, and M. Piana. Numerical validation of the linear sampling method. *Inverse Problems*, 18:511–527, 2002.
- [89] A. N. Tikhonov, A. V. Gonchanski, V. V. Stepanov, and A. G. Yagola. *Numerical Methods for the Solution of Ill-posed Problems*. Kluwer Academic Publishers, Dordrecht, 1995.
- [90] Q. Z. Zhong, H. L. Qing, C. Xiao, E. Ward, G. Ybarra, and W. T. Joines. Microwave breast imaging: 3-d forward scattering simulation. *IEEE Trans. Biomed. Eng.*, 50(10):1180–1189, 2003.